

UNIVERSITÉ DE BORDEAUX
Centre de Recherche Paul Pascal

PH.D. THESIS

A dissertation presented in candidacy for the degree of:

Docteur de l'Université Bordeaux

Spécialité: Lasers, matière et nanosciences

École Doctorale Sciences Physiques et de l'Ingénieur

Defended on May 24th, 2017 by:

Bosi MAO

**Dynamics of agar-based gels
in contact with solid surfaces:
Gelation, Adhesion, Drying and Formulation**

Supervisors:

Patrick SNABRE & Thibaut DIVOUX

In front of the committee composed of :

Costantino CRETON	Directeur de recherche, ESPCI Paris	Rapporteur
Taeke NICOLAI	Directeur de recherche, IMMM Le Mans	Rapporteur
Sébastien MANNEVILLE	Professeur, ENS Lyon	Examineur
François VILLEVAL	Expert R&D milieux de culture, bioMérieux	Examineur
Cécile ZAKRI	Professeur, Université de Bordeaux	Examineur
Marguerite RINAUDO	Professeur, Université Joseph Fourier de Grenoble	Invité
Pierre-Yves BEZIAU	Responsable industrialisation, bioMérieux	Invité
Bruno TETART	Expert R&D microbiologie, bioMérieux	Invité
Patrick SNABRE	Directeur de recherche, CRPP Bordeaux	Directeur
Thibaut DIVOUX	Chargé de recherche, CRPP Bordeaux	Co-directeur

ARTICLES RELATED TO THE PH.D. THESIS

- [1] **Syneresis and delayed detachment in agar plates,**
T. Divoux, B. Mao, & P. Snabre,
Soft Matter **11**, 3677–3685 (2015)
- [2] **Normal force controlled rheology applied to agar gelation,**
B. Mao, T. Divoux & P. Snabre,
Journal of Rheology **60**, 473–489 (2016)
- [3] **Heat-induced aging of agar solutions:
Impact on the structural and mechanical properties of agar gels,**
B. Mao, A. Bentaleb, F. Louerat, T. Divoux & P. Snabre,
Food Hydrocolloids **64**, 59–69 (2017)
- [4] **Impact of saccharides on the drying kinetics of agarose gels measured
by *in-situ* interferometry,**
B. Mao, T. Divoux & P. Snabre,
Scientific Reports **7**, 41185 (2017)

– Remerciements –

Les travaux de thèse présentés dans ce manuscrit ont été réalisés sous la direction du Dr. Patrick SNABRE et du Dr. Thibaut DIVOUX, au sein du Centre de Recherche Paul Pascal et à l'initiative de l'entreprise bioMérieux dans le cadre de la convention CIFRE.

Je tiens, tout d'abord, à remercier mes directeurs de thèse Patrick et Thibaut qui m'ont choisie pour réaliser ce projet de recherche original et qui ont orienté mes travaux tout au long de ces 3 ans. Ils m'ont tous les deux soutenue du début jusqu'à la fin et m'ont insufflée la passion pour la science et le sujet sur lequel je travaillais.

Je remercie Patrick pour sa grande attention. Il s'est toujours rendu disponible quand j'avais la moindre question ou besoin d'aide. Il était aussi intéressant d'échanger nos points de vue sur la science et la vie lors de nos pauses café tous les matins.

Je remercie Thibaut pour son enthousiasme, son énergie ainsi que sa grande réactivité dans ses réponses à mes questions (parfois jusqu'à très tard le soir) bien que nous travaillions à distance. Je le remercie aussi de m'avoir invité et fait visiter Boston.

Je remercie François VILLEVAL, mon correspondant à bioMérieux, de m'avoir chaleureusement accueilli dans son équipe au début de thèse, d'avoir fait le lien avec les autres collègues de la société et finalement de m'avoir fait confiance ce qui m'a permis de mener à bien ce projet. Je lui souhaite une heureuse retraite.

Je tiens à remercier également les rapporteurs de cette thèse Costantino CRETON et Tacke NICOLAI pour l'intérêt qu'ils ont porté à mon travail ce qui a permis d'aboutir à des remarques et des discussions enrichissantes. Merci également aux autres membres du jury qui ont accepté de juger mon travail: Sébastien MANNEVILLE et Marguerite RINAUDO. Je remercie aussi Cécile ZAKRI, directrice du CRPP, pour m'avoir accueillie ces 3 dernières années au sein du laboratoire et d'avoir présidé mon jury. Enfin, je remercie particulièrement Pierre-Yves BEZIAU et Bruno TETARD, qui ont accepté d'assister à ma soutenance en tant qu'invités. Merci aussi à vous deux pour avoir assisté aux différentes réunions d'échange d'avancement de projet et toutes les discussions intéressantes et conseils qui en ont résulté.

Durant cette thèse je me suis formée à différentes techniques et ai testé mes échantillons sur de nombreux appareils au CRPP. Je tiens donc remercier tous ceux qui ont eu la gentillesse de m'accorder leur temps. Tout d'abord l'atelier mécanique avec Philippe et Manuel qui ont fabriqué beaucoup de pièces ce qui m'a permis d'adapter de nombreuses

expériences; Ahmed pour toutes les expériences au rayon X que nous avons souvent répétées ensemble; et Isabelle LY pour les expériences de cryo-fracture qui étaient délicates et difficiles à réaliser. Enfin, Je remercie aussi Éric pour toutes les discussions intéressantes qu'on a eues sur la vie, et la rhéologie.

Je remercie également Yuping GUO et Jérôme MARTINEZ de bioMérieux pour avoir effectué les mesures de chromatographie ionique et de chromatographie d'exclusion stérique sur mes échantillons.

Je souhaite remercier tous les membres du Centre de Recherche Paul Pascal que j'ai eu le plaisir de côtoyer durant ces quelques années, et tout particulièrement les membres de l'équipe M2SD.

Pendant ces trois années, j'ai eu la chance de rencontrer des personnes de grande valeur avec lesquelles j'ai passé des moments inoubliables et ai eu de nombreuses crises de fou rire.

Je pense à Mayada ma co-bureau qui m'a encouragée et soutenue pendant tous les moments du coup de blues aux moments de joie. Je lui souhaite une bonne fin de thèse que nous allons célébrer ensemble. Bonne rédaction! Merci à Cintia ma co-bureau numéro 2 avec laquelle je me suis toujours bien entendue, ton "corbatas de unquera" est vraiment délicieux.

Je pense aussi à Vincent pour les nombreuses soirées qu'il a organisées chez lui (son tapis s'en souvient encore) et pour son talent au bière pong. Nous nous reverrons à Lyon où toi et ta copine Mouna sont les bienvenus.

Je remercie Katerina et George les deux premiers amis que j'ai eus à Bordeaux. Katerina, merci pour ton optimisme et sourire rafraichissants. Merci aussi pour les bons plats grecs que t'as préparés quand j'étais malade, je m'en souviendrai toute ma vie. George, merci d'être revenu de l'Angleterre pour participer à ma soutenance, je te souhaite un bon voyage et une bonne chance pour ta nouvelle vie aux États-Unis.

Je n'ai pas oublié Kevin, Hélène, Artem, Maxime, Florian le bon dessinateur, Pierre-Etienne, Rafael et sa joyeuse femme Nathassia ainsi qu'Antoine et sa copine Valentine pour toutes les soirées que nous avons passées ensemble et les jeux auxquels nous avons participé.

Je remercie aussi mes chers compatriotes chinois : Cheng pour tous les déjeuners que nous avons pris ensemble; Xuan pour ton sourire et pour m'avoir appris à jouer au "ba shi fen" un jeu de carte chinois ; et Xiaoqing pour tous les supers repas que t'as fait, je te souhaite plein de joie pour ton petit fils duoduo.

Je remercie enfin ma famille et ma belle-famille de tous les soutiens moraux et attentions portées. Je tiens à mentionner mon mari Anthony qui s'est dévoué à faire toutes les tâches ménagères et repas pendant ces derniers mois, cela m'a libéré du temps pour travailler sur la thèse.

– Summary –

My PhD work was carried out in partnership with the company BioMérieux, a world leader in the *in-vitro* diagnostics market. The company commercializes agar-based plates, which are used as growth culture media for microorganisms and cells, and for routine diagnostic tests. Compared to individually made agar plate, mass-produced culture media tend to shrink and detach from the lateral wall of the Petri dish. The detachment may take place either a short time after the production, or later on during the incubation of the dish at constant temperature while monitoring the growth of microorganisms. In some rare occasions, the gel is even observed to fracture. In both cases, the plate cannot be used for its original purpose, which costs each year a fair share of money in customer return.

The problem of the gel contraction is extremely complex. First, the exact formulation of the culture media varies a lot with the intended application, and the gel may contain numerous additives such as nutriments, blood, salt, sugar, surfactants, etc. that will affect the water-holding capacity of the gel and therefore the shrinkage dynamics. Second, a large number of parameters might play a key role from the moment the agar powder is introduced into solution and brought to a boil to when the gel, cast in the dish, is used as a culture medium. Finally, being mainly composed of water ($> 95\%$ wt.), agar gels are naturally prone to water-loss by evaporation, either at rest or under external perturbation. Therefore, one needs to understand the kinetics of the water release in quiescent conditions, and identify the components in the gel formulation that may affect the water-holding capacity of the gel. Moreover, the interaction of the gel with the solid wall of the dish also appears as a key parameter since the adhesion of the gel on the bottom and/or the lateral wall may influence the detachment time. One should therefore understand the adhesion and static friction properties between an agar gel and a solid surface, and further study the thinning kinetics of an agar gel cast in a cylindrical dish.

To perform my PhD, I have used a wide array of experimental techniques: namely normal force controlled rheology to monitor the mechanical properties during the gelation and the drying of agar gels. Non-linear rheology and a novel test test-fixture build upon a modified spin coater have made it possible to quantify the adhesion properties of agar gels to various solid surfaces. Interferometric observations have been used to quantify the thinning rate of agar gels, and quantify the influence of the gel composition on its water-holding capacity. Finally, other techniques such as X-ray diffraction, optical profilometry and electronic microscopy have been used to characterize the structure of agar gels and that of the solid surfaces involved in that study.

Among other key results, I have unraveled and measured the contraction of the agar sample during the sol/gel transition of the solution, which depends on both the agarose concentration and the cooling rate. Furthermore, I have shown that a prolonged heating of the agar solution quickly leads to the degradation of the polysaccharides, which produce softer and more ductile gel for increasing cooking times. Finally, the adhesion of the gel to the dish depends essentially on the surface roughness of the walls, and is sensitive to the formulation of the gel. The presence of specific salts increases the adhesion of the gel to the plastic walls. Finally, the presence in a small quantity of non-gelling saccharides does not affect the gel mechanical properties, and increases the water-holding capacity of gel. This PhD work brings valuable answers to concrete industrial issues and should help optimizing the formulation of commercial culture media and their lines of production so as to produce faster, gels that are more stable during transport and their commercial use.

– Résumé –

Mon projet de thèse s’est effectué en partenariat avec l’entreprise BioMérieux, leader mondial des solutions de diagnostics *in vitro* pour le marché de la santé. Cette entreprise commercialise des gels à base d’agar sous forme de boîtes de Pétri servant de milieux de culture pour les microorganismes et les cellules. Ces gels utilisés depuis 1881 se comportent comme des solides mous poreux, sortes d’éponges dont la structure composée de polysaccharides auto-assemblés, est remplie d’eau à 95%. L’effet d’une contrainte extérieure (lors du transport des boîtes), ou du séchage lors de la phase d’incubation des boîtes de Pétri peut suffire à expulser l’eau du gel, lubrifiant ainsi le contact entre le gel et les parois de la boîte de Pétri. Le gel peut alors se détacher, glisser dans la boîte de Pétri ou encore se fracturer ce qui rend le milieu de culture inutilisable pour tout test de microbiologie.

L’objectif de la thèse a consisté en une étude minutieuse des divers paramètres pouvant influencer sur les propriétés mécaniques et le détachement du gel des parois de la boîte de Pétri. Ce travail a été mené au niveau (*i*) de la préparation du gel : influence du temps de chauffage de la solution d’agar, de la vitesse de refroidissement et de la température finale, (*ii*) du contact gel/boîte : influence sur le détachement du gel des spécificités des parois de la boîte comme la mouillabilité ou la rugosité de surface et (*iii*) de la formulation du gel: influence de l’origine de l’agar et de la présence de divers additifs généralement employés dans les milieux de culture cellulaire. Cette étude a été menée avec différentes techniques complémentaires : la rhéologie linéaire à force normale imposée a permis de suivre l’évolution des propriétés mécaniques du gel lors des phases de gélification et de séchage. La rhéologie non-linéaire et la centrifugation à l’aide d’un dispositif original de “tournette” développé au laboratoire ont permis de quantifier l’adhésion entre le gel et de nombreuses surfaces solides. Des observations interférométriques ont permis de mesurer précisément la vitesse d’amincissement du gel lors du séchage et de quantifier l’impact de la composition chimique du gel sur sa propension à perdre de l’eau. Enfin, d’autres techniques comme la diffraction des rayons X, la profilométrie optique et la microscopie électronique ont par ailleurs permis de caractériser la structure des gels d’agar et celles des surfaces solides étudiées.

Entre autres résultats marquants, j’ai mis en évidence la contraction des échantillons lors de la transition sol/gel induite par le refroidissement des solutions d’agar. Cette contraction, qui dépend à la fois de la concentration en agarose et de la vitesse de refroidissement de la solution joue un rôle important dans le détachement du gel de la boîte dans laquelle il est coulé. Par ailleurs, j’ai montré que le maintien à haute température d’une solution d’agar conduit rapidement à la dégradation des polysaccharides, produisant une fois refroidie, des gels d’autant plus mous et ductiles que la période de chauffage a été longue. Par ailleurs, l’adhésion du gel aux parois de la boîte dépend essentiellement de la rugosité de surface des parois et non de leur mouillabilité. Enfin, la formulation du gel permet de modifier à la fois la vitesse d’évaporation de l’eau du gel et l’adhésion du gel aux parois. La présence en faible quantité de sucres non gélifiants ne modifie pas les propriétés mécaniques des gels d’agarose et augmente leur capacité à retenir leur eau. La présence de sels spécifiques permet quant-à-elle d’améliorer l’adhésion du gel sur la surface plastique de la boîte. Cette thèse devrait permettre d’optimiser la formulation des milieux de culture et leurs lignes de production de façon à produire à plus haute cadence des gels plus stables lors du transport et de leur utilisation commerciale.

Contents

1	General introduction	13
1.1	Generalities on polymer gels	14
1.1.1	Generic features of gels	14
1.1.2	Mechanical properties of (bio)polymer gels	16
1.1.3	Specific properties of polysaccharide gels	16
1.2	Agar(ose) gels: a tentative review	17
1.2.1	Historical background	17
1.2.2	Chemical structure of agar	18
1.2.3	Gelation and microstructure of agar gels	19
1.2.4	Mechanical properties of agar gels	20
1.2.5	Industrial applications of agar(ose) gels	22
1.3	Framework and thesis outline	23
2	Samples and experimental techniques	25
2.1	Agar(ose) samples	26
2.1.1	Agarose and agarpectin content in agar samples	26
2.1.2	Polymer molecular weight	27
2.1.3	Additional chemical analysis	28
2.2	Gel structural properties	28
2.2.1	Cryo Scanning Electron Microscopy (cryo-SEM)	28
2.2.2	X-ray scattering experiments	30
2.3	Gel mechanical properties	31
2.3.1	Bulk rheology and Normal Force Controlled (NFC) rheology	31
2.3.2	Macro-indentation experiments	37
2.4	Gel adhesion, friction and slip	39
2.4.1	Strain sweep and gel debonding	39
2.4.2	Centrifugal stress and gel debonding	42
2.5	Gel drying	48
2.5.1	Interferometric observations	48
2.5.2	Spatio-temporal tracking	50
2.6	Properties of solid surfaces	55
2.6.1	3D scanning interferometry	55
2.6.2	Water contact angle measurements	56
3	Role of thermal history on agar gels	59
3.1	Incubation of agar solutions at 80°C	60

3.1.1	Heat-induced aging of agar sols	61
3.1.2	Impact on gelation kinetics and gel microstructure	63
3.1.3	Impact on gel adhesion and failure dynamics	65
3.1.4	Discussion and conclusion	70
3.2	Cooling kinetics of hot agar solutions	72
3.2.1	Impact of cooling rate	72
3.2.2	Impact of a temperature drop	73
3.2.3	Impact of a temperature plateau during cooling	75
3.2.4	Discussion and conclusion	76
4	Adhesion and debonding of agar gels from solid surfaces	79
4.1	Adhesion of hydrogels on solid surfaces: a short review of the literature	80
4.2	Gel adhesive properties determined by shear rheology	85
4.2.1	Influence of gel thickness (gap width)	85
4.2.2	Influence of the strain sweep-rate	86
4.2.3	Influence of agar concentration	87
4.2.4	Influence of the solid surface properties	88
4.3	Gel adhesion properties determined with a spinning centrifuge	89
4.3.1	Impact of contact duration between the gel and the plate	90
4.3.2	Impact of gel thickness	92
4.3.3	Impact of the rate of increase of the spinner rotation speed	93
4.3.4	Impact of agar concentration	94
4.3.5	Impact of the solid surface properties	95
4.4	Discussion and conclusion	98
	Appendix A Observations of agar gels under compression or shear	105
A.1	Water release at the air/gel interface of a gel under compression	105
A.2	Shear-induced debonding of the gel from a solid surface	107
5	Drying of agar gels	109
5.1	Drying of gels	110
5.2	Gel drying dynamics studied by tracking experiments	112
5.2.1	Drying of agar gel plates cast in a dish	113
5.2.2	Influence of agar concentration	116
5.2.3	Influence of solid surface properties	118
5.3	Gel local thinning-rate measured by interferometry	121
5.3.1	Influence of dish material and wall roughness	121
5.3.2	Drying of a thin agar gel cast in a glass dish	122
5.3.3	Influence of dish geometry	124
5.4	Mechanical and structural properties of agar gels during drying	126
5.5	Discussion and conclusion	128
	Appendix B Observations during the drying of a non-constrained agar gel	129
6	Role of additives on agar(ose) gel properties	131
6.1	Role of agaropectin on agarose gels	132
6.1.1	Impact on gelation and agarose gel debonding	133

6.1.2	Impact on the microstructure of agarose gels	135
6.1.3	Impact on agarose gel drying kinetics	135
6.2	Role of ionic species on agar gels	136
6.2.1	Anions: impact on gelation and gel debonding	137
6.2.2	Cations: impact on gelation and gel debonding	140
6.2.3	Impact of anions and cations on the drying kinetics of agar gels . . .	141
6.3	Effect of saccharides on agarose gels	141
6.3.1	Impact on gelation and gel debonding	143
6.3.2	Impact on the drying kinetics of agarose gels	144
6.3.3	Impact on agarose gel microstructure	145
6.4	Effect of surfactants on gel debonding	146
6.5	Discussion and conclusion	148
7	Conclusion and outlooks	151
	References	157

Chapter 1

General introduction

Contents

1.1	Generalities on polymer gels	14
1.1.1	Generic features of gels	14
1.1.2	Mechanical properties of (bio)polymer gels	16
1.1.3	Specific properties of polysaccharide gels	16
1.2	Agar(ose) gels: a tentative review	17
1.2.1	Historical background	17
1.2.2	Chemical structure of agar	18
1.2.3	Gelation and microstructure of agar gels	19
1.2.4	Mechanical properties of agar gels	20
1.2.5	Industrial applications of agar(ose) gels	22
1.3	Framework and thesis outline	23

1.1 Generalities on polymer gels

1.1.1 Generic features of gels

The term “gel” has been introduced in 1861 by a Scottish chemist, Thomas Graham and refers to a gelatinous substance. At first sight, it may appear as difficult to provide a clean-cut definition of gels since the term encompasses a wide category of systems as varied as protein gels, lamellar mesophases, inorganic clays, colloidal/polymer mixtures, microgels, etc. Yet, all these gels share the following common features: (i) a preponderance of solvent and (ii) the presence of a 3D network of connected molecules and/or particles, which translates into a storage modulus G' much larger than the loss modulus G'' (Larson, 1999). The elastic shear modulus of a gel is typically such as $G' \lesssim 10^7$ Pa and a few examples that span over the whole range of values accessible include: $G' \simeq 100$ Pa for commercial hair gels, $G' \simeq 10$ kPa for agar gels and $G' \simeq 1$ MPa for silicon rubber. In order to sort the wide amount of gels, Flory proposed a classification in 1974 based on the structural properties of gels (Flory, 1974). The latter classification has been adapted and modified over the years and can be summarized as follows (te Nijenhuis, 1997; Larson, 1999):

- **Polymer networks**, which are made of polymers and divided into two sub-categories: the covalent networks (e.g. rubber, epoxyresin, etc.) and the physically cross-linked networks (e.g. gelatin, agar, etc.). The former category involves the formation of chemical bonds via end groups or cross linkers during the gelation [Fig. 1.1(a) and (b)], whereas in the latter category the molecules are bound together by weak forces such as hydrogen bonds, van der Waals forces, electrostatic interactions, or simply by physical entanglements of the polymer chains. Most often, physically cross-linked networks display crystallites or organized domains that involve bundles of chains of multiple stranded helices [Fig. 1.2(a)–(c) and (e)]. The gelation of covalent networks is irreversible, whereas the physically crosslinked networks show a reversible gelation with respect to a well-defined control parameter, which can be the temperature (e.g. agar gels), the pH (e.g. casein gels), the ionic content (e.g. alginate gels), etc. Despite such differences, polymer gels usually exhibit a “true” solid-like behavior in the sense that their brittle failure is not reversible: once cut in half, a polymer gel cannot heal, at least not without varying the external control parameters described above.
- **Particulate networks**, which encompass gels of attractive particles (e.g. carbon black soot particles, polymer/colloid mixtures, etc.) and gels of densely packed soft particles (e.g. hair gel, thermo-sensitive microgels, etc.). In attractive gels the elasticity comes from the existence of a percolated network that forms even at very low volume fraction in particles [Fig. 1.2(d)], while in soft gels the elasticity results from a jammed collection of deformable objects. As a result, both types of particulate networks show a yield stress, i.e. a stress below which they display a solid-like mechanical behavior and above which they flow like liquids (Bonn, Denn, Berthier, Divoux, & Manneville, 2017). It is worth noting that contrarily to the polymer networks category, particulate networks behave as “fake solids” as the solid state can be erased by a large shear, and then fully rejuvenated by an adequate period of rest (Cloitre, Borrega, & Leibler, 2000; Viasnoff & Lequeux, 2002; Coussot, Nguyen, Huynh, & Bonn, 2002).

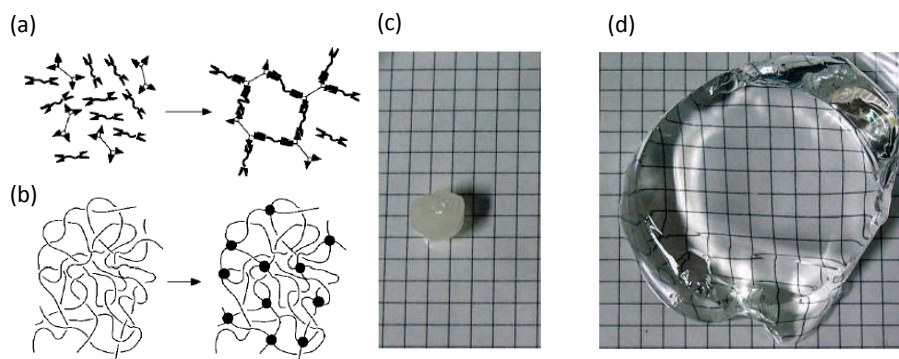


Figure 1.1: Examples of covalent networks - or *chemical gels*: (a) Reacting monomers (e.g. thermosetting resins, etc.), (b) Crosslinking polymer chains (e.g. vulcanized rubbers, etc.). Reprinted from (Rubinstein & Colby, 2003). (c-d) Super-absorbent lipophilic polyelectrolyte gel: dried (c) and swollen (d) in THF for 48 h. Reprinted from (Ono et al., 2007).

- **Well ordered lamellar structures**, in which lamellae are arranged in parallel giving rise to a long range order. Typical examples include gels of surfactants and phospholipids, etc.

In the present manuscript, I will focus on the first category: polymer networks filled with water. These *hydrogels* show a remarkable capacity to store large amount of water, up to more than several hundred times the weight of polymer for some superabsorbent gels [Fig. 1.1(c) and (d)]. Water-holding capacity makes polymer gels in general highly relevant for biomedical applications (Hoffman, 2002) such as cell encapsulation (Hunt & Grover, 2010) and tissue engineering (K.-Y. Lee & Mooney, 2001; Van Vlierberghe, Dubruel, & Schacht, 2011), as well as in food industry (Mezzenga, Schurtenberger, Burbidge, & Michel, 2005; Barham et al., 2010).

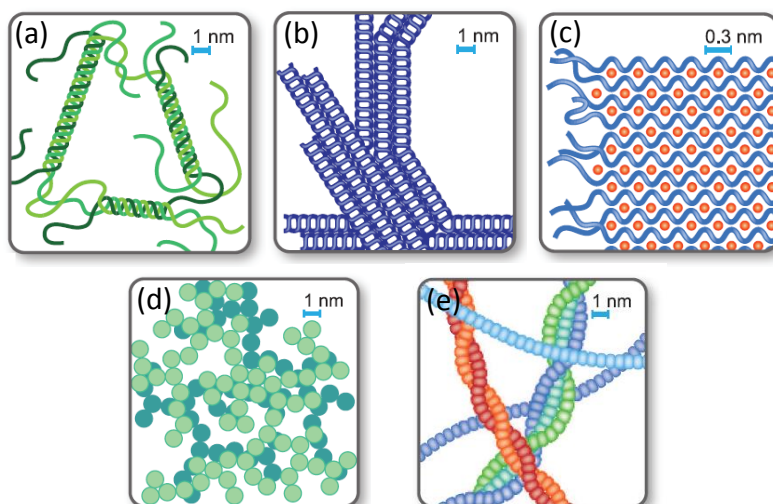


Figure 1.2: Sketch of the network formation and the various microstructures in physical gel systems: (a) helical association associated with gelation for gelatin and agarose; (b) helical formation in charged polysaccharides such as carrageenans; (c) egg-box complexation in Ca^{2+} alginate gels; (d) colloidal aggregation of proteins close to the iso-electric point; (e) fibrillar aggregation of proteins in amyloid type gels at low pH. Reprinted from (Djabourov et al., 2013).

1.1.2 Mechanical properties of (bio)polymer gels

Hydrogels commonly feature a porous and fibrillar microstructure that is filled with water, and therefore exhibit solid-like viscoelastic mechanical properties. Although hydrogels usually display a solid behavior, (bio)polymer gels are characterized by an elastic modulus of about a few kPa, which is relatively small compared to other solid materials (Oyen, 2014). Furthermore, while soft polymer gels share common features with hard materials including delayed failure under external stress (Bonn, Meunier, Greffier, Al-Kahwaji, & Kellay, 1998; Leocmach, Perge, Divoux, & Manneville, 2014), crack propagation (Baumberger, Caroli, & Martina, 2006; Daniels, Mukhopadhyay, Houseworth, & Behringer, 2007) and work-hardening (Schmoller, Fernández, Arevalo, Blair, & Bausch, 2010), the porous microstructure also confers upon them remarkable nonlinear viscoelastic properties. Indeed, such soft solids strongly stiffen upon increasing deformation, which stems from the inherent nonlinear elastic behavior of the polymer chains composing the gel network, and/or from the network itself (Storm, Pastore, MacKintosh, Lubensky, & Janmey, 2005; Pouzot, Nicolai, Benyahia, & Durand, 2006; Piechocka, Bacabac, Potters, MacKintosh, & Koenderink, 2010; Carrillo, MacKintosh, & Dobrynin, 2013). Finally, polymer gels hence endure large strains to failure and dissipate substantial mechanical work, leading to tough hydrogels and elastomers. In fact, the race for further improving hydrogels mechanical strength, and develop tough and highly stretchable materials has produced a wealth of crosslinking methods mainly based on the use of a double network or fancy crosslinkers (Gong & Katsuyama, 2003; Sun et al., 2012; Zhao, 2014; Grindy et al., 2015). The latter research topic represents a great deal of the current research activity on hydrogels.

1.1.3 Specific properties of polysaccharide gels

Polysaccharides are mostly from natural origin and encompass a wide variety of polymers divided into three categories: anionic polysaccharides, e.g. carrageenans, gellans, alginates and pectins, cationic polysaccharides, e.g. chitosan, and neutral polysaccharides such as agarose, which will be discussed more extensively in the next section (Djabourov et al., 2013). Polysaccharides form reversible physical gels: for instance, alginates gel in the presence of divalent counterions, whereas carrageenans form a thermo-reversible gel (Hermansson, Eriksson, & Jordansson, 1991). Polysaccharides play a key role as thickener, gelling, emulsifying, and hydrating polymers and the applications in biomedical, pharmaceutical and cosmetic industry are countless. We kindly refer the reader to a recent review for a detailed account of the current use of polysaccharides (Rinaudo, 2008). One specific property of polysaccharides that I would like to emphasize, and that is often ignored in the literature, is the volume variation associated with the gelation.

To our knowledge, the contraction of a polysaccharide gel during the sol-gel transition was first observed by K. Krishnamurti in 1934 on agar gels, as reported by (Heymann, 1935). To quote the author: “*The transformation, investigated at constant temperature, is accompanied by a decrease in volume and, consequently, it can be assumed that hydration increases. This assumption is in agreement with the experiments of A. Taffel and of Th. Svedberg, who found that the volume contraction, which occurs when gelatin is dissolved in water, is larger at lower temperatures, where a gel is formed, than at higher ones, where sol formation occurs.*” Volume contraction was also mentioned for the gelation of κ -carrageenan by (Payens & Snoeren, 1972) but not illustrated. Later on, gelation experiments monitored by small amplitude oscillatory shear and conducted on κ -carrageenan in a cone and plate geometry (Hermansson, 1989), and on Konjac glucomannan in a parallel-

plate geometry (H. Zhang et al., 2001) both revealed an interesting artifact: the elastic modulus G' showed an overshoot during the gel formation, that was merely interpreted as wall slip. This overshoot was rightfully interpreted only by (Moldenaers, Mewis, & Berghmans, 1988) who conducted gelation experiments on κ -carrageenan in a parallel plate geometry and concluded that “*Adhesion between platens and gel remains critical because of geometrical changes due to temperature effects and shrinkage of the gel.*” Experiments conducted in a cell composed of a perforated cylinder only partially solved the problem of the contraction (Richardson & Goycoolea, 1994), and we will see later on in the manuscript that rheological experiments conducted at constant normal force instead of constant volume, brings a long overdue answer to the problem and further allows to measure the gel contraction associated with the gelation.

1.2 Agar(ose) gels: a tentative review

Seaweed have been used as a natural resource for more than two thousand years for food, medical purposes, fertilizers, etc. (Newton, 1951). During the last century seaweed was introduced in the West and has been employed for the production of water-soluble polysaccharides or *phycocolloids*. Phycocolloids are widely used for manufacturing goods, because of their colloidal properties and gelling capacity. The most important phycocolloids, which are agar, carrageenan and alginate are now produced in industrial quantities. The former two classes are extracted from a red seaweed of class *Rhodophyceae* (Dixon, 1973), whereas the latter is extracted from a brown seaweed of class *Phaeophyceae* (Siberfeld, Rousseau, & Reviere, 2014). The present work is dedicated to the physical properties of agar-based gels. In this section, I will present briefly the historical background of the use of agar, before introducing the chemical structure of agar polymers and the properties of agar gels. I will finish by giving a short summary on the applications of agar gels.

1.2.1 Historical background

Agar, also called agar-agar, was the first phycocolloid used as a food additive in civilization, and it is considered to have been discovered accidentally in 1658 by a Japanese innkeeper, Tarazaemon Minoia (Naylor, 1976; Armisen & Galatas, 1987). During the eighteenth centuries, agar is introduced in the West. In 1882, Robert Koch introduced agar as a culture medium for bacteriological applications (Chapman, 1970). Agar is also one of the food ingredients first approved as Generally Recognized as Safe (GRAS) by the FDA in 1974 (Imeson, 2010).

In the middle of the seventeenth century, agar was produced in Japan, China and Korea from Genus *Gelidium amansii* exclusively. Later, as *Gelidium* was in short supply, other species of *Rhodophyceae* were used as substitutes for the agar production. Nowadays, most of the agar used for manufacturing goods comes from genus *Gelidium*, *Gracilaria*, *Pterocladia*, and *Gelidiella*, which are distributed geographically over the coastlines of all continents (Kim, 1970; Dawson, 1966; Whistler & BeMiller, 1993; Chapman, 1970). Agars produced from these different seaweeds lead to gels of distinct characteristics, with different strengths, different gelling and melting temperatures, and various synergies with other polymers. All these seaweeds are therefore developed to satisfy diverse applications. Furthermore, agar is a polysaccharide that accumulates in the cell walls of algae. For this reason, the agar content in seaweeds, and its characteristics vary with the seasons

and the hydrodynamic conditions of the environment where the algae grows¹. A series of other ecological factors such as the nutrient availability, the substrate composition on which the algae grows could also influence agar properties.

1.2.2 Chemical structure of agar

According to the US Pharmacopeia, agar is defined as a *hydrophilic colloid extracted from certain red seaweeds of the Rhodophyceae class*, but the agar composition is in fact more complex. In 1937, C. Araki showed that agar is formed by a mixture of at least two polysaccharides, whose basic monomer is galactose. The first one was named *agarose* and the second one *agaropectin* (Araki, 1937).

Agarose, which is a neutral polymer, is the gelling component of agar (Araki, 1956) and forms aqueous gels at concentrations as low as 0.1% wt. (Clark, Richardson, Ross-Murphy, & Stubbs, 1983; Clark & Ross-Murphy, 1985). In 1938, two research groups independently discovered the existence of 3-6, anhydro-L-galactose as part of the agar molecule (Percival, Somerville, & Forbes, 1938; Hands & Peat, 1938), and in 1979, the chemical structure of agarose was described as an idealized alternating di-saccharide (Liang, Stevens, Morris, & Rees, 1979). Since then, the structure of agarose is described as the repeating units of agarobiose represented $(AB)_n$, where A and B respectively denotes the β -1,3 linked D-galactose and the α -1,4 linked 3,6-anhydro-L-galactose residues pictured in Figure 1.3 (Clark & Ross-Murphy, 1987; Matsushashi, 1990). As a neutral galactan molecule, agarose contains a low degree of substitution with charged substitutes such as pyruvate and sulphate [the sulfate content is usually below 0.15% wt. (San Biagio, Madonia, Sciortino, Palma-Vittorelli, & Palma, 1984)] and varying amounts of methyl functions. Finally, agarose is polydisperse and shows a high average molecular weight \overline{M}_w , of about 1.2×10^5 Da, which corresponds to about 400 agarobiose units linked together (Hickson & Polson, 1968).

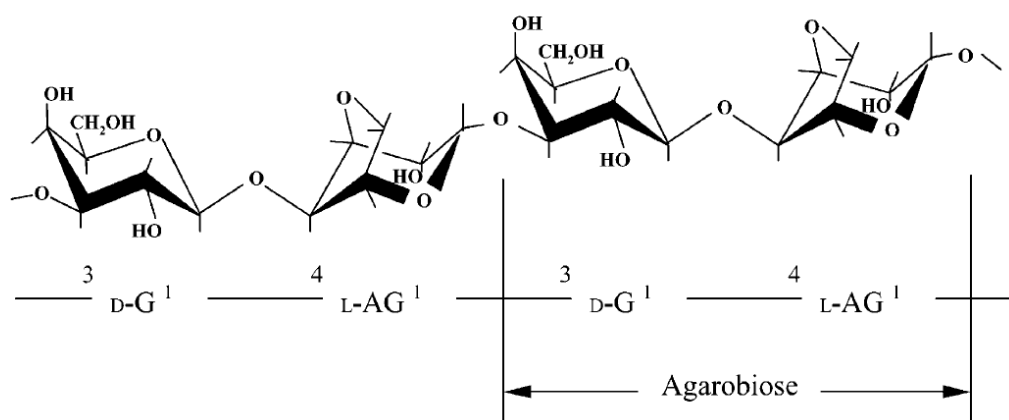


Figure 1.3: Illustration of the basic secondary structure of agarose molecules: D-G is β -D-galactopyranose and L-AG is 3,6-anhydro- α -L-galactopyranose. An agarobiose unit is indicated. Reprinted from (Labropoulos et al., 2002).

The other components of agar mostly consist in agaropectins, which are charged galactan molecules with much higher sulfate content than agarose (5% to 8% wt.) and very low gelling capacity (Armisen & Galatas, 2009). Agaropectin has been far less stud-

¹The number of agarose-contained rhizoidal cells is higher where the water movements are stronger. (Armisen & Galatas, 1987).

ied than agarose due to its lack of practical applications. The average molecular weight, \overline{M}_w of agaropectin, is still a matter for debate: values obtained through sedimentation, diffusion and viscosity experiments are typically below 2×10^4 Da (Hickson & Polson, 1968; Fuse & Suzuki, 1975), which is much lower than that of agarose. However, independent measurements on agaropectin extracted from agar and measured by Size Exclusion Chromatography coupled to Low Angle laser light scattering (SEC-LALLS) lead to values of about 4×10^5 Da, which is much higher than those of both the agarose and agar (Mitsuiki, Mizuno, & Motoki, 1999).

Finally, the relative content of agarose and agaropectin present in agar, and the individual molecular weight vary depending on the origin of the raw material (Araki, 1958; Tagawa, 1966) and the manufacturing extraction process considered (Fuse & Goto, 1971; Tagawa & Kojima, 1966).

1.2.3 Gelation and microstructure of agar gels

Agar is a thermo-reversible gel, i.e. the gelation can be induced by variations of temperature, without the addition of any other substance. Insoluble in cold water, agar becomes soluble in boiling water. Once cooled down below the gelation temperature, T_g that varies between 30°C and 40°C depending mostly on the methoxyl content (Guiseley, 1970; San Biagio et al., 1984), agar forms a thermoreversible gel that does not melt below 80°C (Dea, McLinnon, & Rees, 1972). Such hysteretic behavior is reproducible and can be repeated a great number of times (Dea et al., 1972). The higher melting temperature of the gel results from the very stable conformation of the ordered structures that form upon cooling (E. R. Morris, Rees, & Robinson, 1980). Note that the thermal hysteresis is used in the food industry and makes agar much more suitable for applications in microbiology than the low-melting-point gelatin (25°C to 30°C) (Armisen & Galatas, 2009).

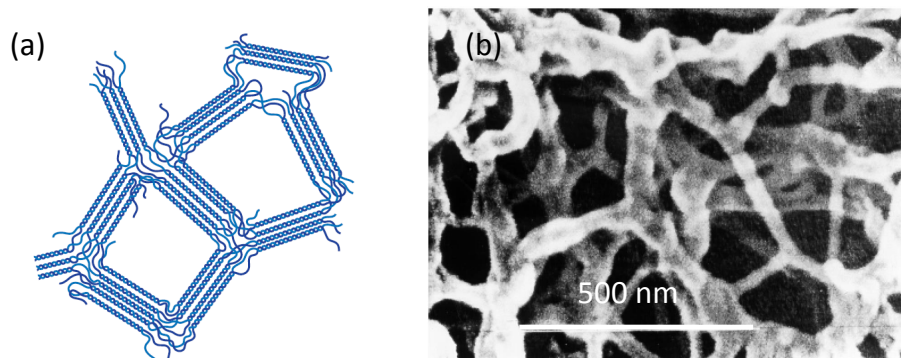


Figure 1.4: (a) Schematic representation of the agarose network structure composed of bundles of double helices. Reprinted from (Djabourov et al., 2013). (b) Electronic scanner microphotograph of 2% wt. agarose gel. The white bar represents 500 nm (100000 \times). Reprinted from (Medin, 1995).

The agar(ose) gelation starts with a liquid-liquid phase separation known as spinodal decomposition that corresponds to the formation of polymer-rich and solvent-rich regions (Feke & Prins, 1974; San Biagio, Bulone, Emanuele, Palma-Vittorelli, & Palma, 1996; Matsuo, Tanaka, & Ma, 2002), together with a conformational change of the agarose molecules, which self-associate via hydrogen bonds² (Tako & Nakamura, 1988; Braudo, 1992). The exact formation scenario of the gel results from a subtle competition between these distinct processes (Manno et al., 1999), which in turn strongly depends on the agarose

²For that reason, agar gels are part of the “physical gel” category discussed above.

concentration, agarose molecular weight, and the thermal history (Normand, Lootens, Amici, Plucknett, & Aymard, 2000; Aymard et al., 2001; Xiong et al., 2005). The spinodal demixion is favored for agarose concentrations lower than 2% wt., whereas the gelation occurs through a more direct scenario at larger concentrations.

Furthermore, although the exact conformation of the agarose molecules within the gel network is still debated (single aligned helices vs left-handed threefold double helices) (Arnott, Fulmer, & Scott, 1974; Clark & Ross-Murphy, 1987; Foord & Atkins, 1989; Djabourov, Clark, Rowlands, & Ross-Murphy, 1989; Schafer & Stevens, 1995; Guenet & Rochas, 2006), the microstructure of agar gels at a coarser scale is consensually described as a porous network made of bundles of agarose helices (Chui, Philips, & McCarthy, 1995; Pernodet, Maaloum, & Tinland, 1997; Nordqvist & Vilgis, 2011) [Fig. 1.4(a)]. The whole polymer network is filled with free water molecules (Woessner, Snowden, & Chiu, 1970) and the pores of the gel microstructure show a broad size distribution [Fig. 1.4(b)], while the mesh size varies from a few hundred nanometers to a few micrometers depending on the agarose concentration (Brigham, Gidley, Hoffmann, & Smith, 1994; Chui et al., 1995; Medin, 1995; Pernodet et al., 1997; Normand, Lootens, et al., 2000; Xiong et al., 2005; Narayanan, Xiong, & Liu, 2006; Rahbani, Behzad, Khashab, & Al-Ghoul, 2013).

Finally, agar gels exhibit a high exclusion limit, which is identified as the greatest size of globular protein that can cross the gel in an aqueous solution. For instance, in the case of a 2% wt. agarose gel, the exclusion limit is 3.0×10^7 Da. The presence of agaropectin reduces the exclusion limit as these molecules do not participate to the gel network and obstruct the pores, which is the reason why electrophoresis gels are prepared with pure agarose rather than agar (Medin, 1995).

1.2.4 Mechanical properties of agar gels

In the linear deformation regime, agar gels show an elastic shear modulus that is quite independent of the frequency (Mohammed, Hember, Richardson, & Morris, 1998; Piazza & Benedetti, 2010), as illustrated in Figure 1.5 for three gels of different agarose concentrations. Moreover, agar gels behave as viscoelastic soft solids, whose mechanical properties are mainly governed by the amount of agarose introduced: both the elastic shear modulus G' and the compression elastic modulus E of agar gels scale as power-laws of the agarose concentration. In Figure 1.6(a), we report our measurements of Young's modulus E together with data extracted from the literature. All the results are compatible within

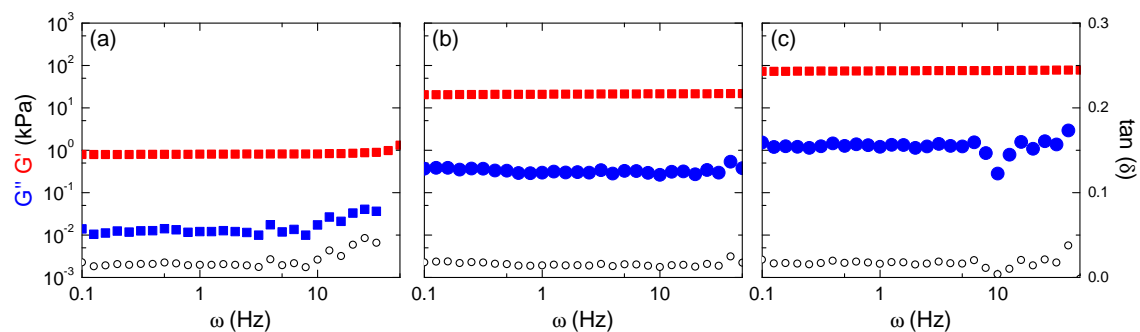


Figure 1.5: Storage and loss modulus G' , G'' (left axis) and loss tangent $\tan(\delta) = G''/G'$ (right axis) vs oscillatory frequency ω for agar-BM1 gels (see Chapter 2 for the different types of agar used in the manuscript) at different concentrations: 0.5% (a), 1.5% (b), and 3% wt. (c). Experiments conducted in a parallel-plate geometry after a gelation monitored with the zero normal force controlled protocol (see Chapter 2). Shear strain amplitude $\gamma = 0.1\%$ and initial gel thickness $e_0 = 500 \mu\text{m}$.

error bars and point towards two regimes: a first one with a power-law exponent of about 2.6 for agarose concentrations lower than 2%, and a second one with a power-law exponent of about 1.6 for larger agarose concentrations. The same data can also be plotted with respect to the distance $C - C_g$ to the critical gelation concentration, where $C_g \approx 0.1\%$ wt. denotes the critical agarose concentration below which no gelation is observed (Ramzi, Rochas, & Guenet, 1998).

Beyond the linear deformation regime, agar gels show a pronounced stress/strain hardening (Barrangou, Daubert, & Foegeding, 2006; Nakauma, Ishihara, Funami, Yamamoto, & Higashimori, 2014) and for even larger deformations display a brittle-like failure involving the formation of macroscopic fractures (Bonn, Kellay, Prochnow, Ben-Djemaa, & Meunier, 1998; Barrangou et al., 2006; Daniels et al., 2007; Spandagos, Goudoulas, Luckham, & Matar, 2012). The fractures grow perpendicularly to the shear direction beyond a critical strain, whose value is governed by the molecular weight of the polymer (Normand, Lootens, et al., 2000).

Finally, being mainly composed of water, agar gels are also subject to water loss and one should clearly distinguish between the spontaneous release of water (or syneresis) associated with aging, and the water that evaporates due to the difference between the chemical potential of water in the gel and the surrounding atmosphere. The syneresis phenomenon is attributed to the contraction of the polymer network by a slow further aggregation of the helices (Arnott et al., 1974; Dea & Rees, 1987). Syneresis decreases abruptly when increasing agarose concentration³, whereas water sweeping out from agar gels is enhanced under external deformation (Nakayama, Kawasaki, Niwa, & Hamada, 1978; Matsuhashi, 1990).

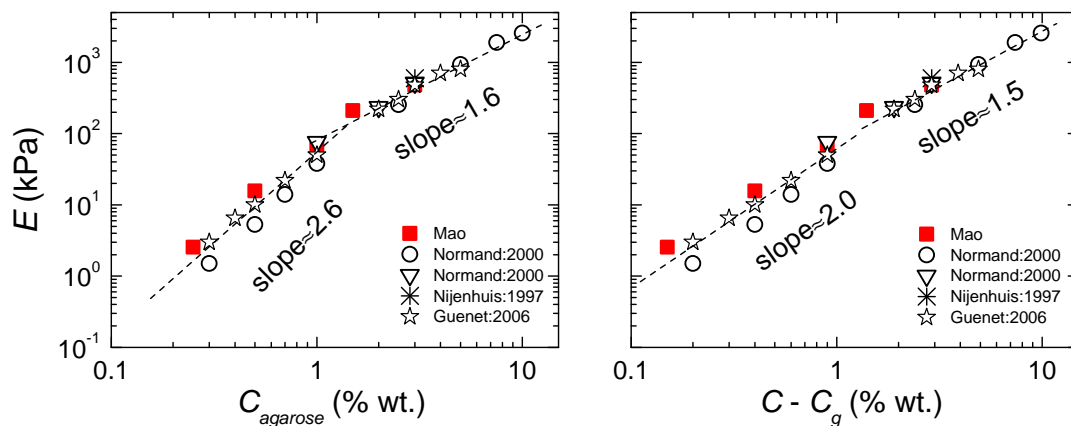


Figure 1.6: (a) Compression elastic modulus E vs. agarose concentration C for results obtained during this thesis work (■) by macro-indentation of agar gels and data compiled from the literature (Normand, Lootens, et al., 2000; te Nijenhuis, 1997; Guenet & Rochas, 2006). The data are well described by two power-laws of different exponents $\alpha \approx 2.6$ for $C < 1\%$ wt., and $\alpha \approx 1.6$ for $C > 1\%$ wt.. (b) Same data plotted as a function to the distance $C - C_g$, to the critical agarose concentration below which no agarose gelation is observed with $C_g \approx 0.1\%$ wt. (Fujii et al., 2000; Normand, Lootens, et al., 2000).

³The syneresis of agar gels becomes significant at around 1% or lower concentrations and the amount of water swept out from the gel network is roughly inversely proportional to the square of the concentration for most practical concentrations (Matsuhashi, 1990).

1.2.5 Industrial applications of agar(ose) gels

Agar shows unique gelling characteristics, which are not present in any other phyco-colloid, and makes it relevant for a wide range of applications. Agar is used as a thickener in foodstuff, and once gelled, plays a key role in numerous biotechnological applications ranging from growth medium for microorganisms to substitute for biological tissues (Glicksman, 1983; Stanley, 2006). About 80% of the agar worldwide production is used in the food industry, and the remaining 20% is used in biotechnology applications. Only 1% of the global agar production is used as a raw material to manufacture pure agarose products, such as agarose gels for electrophoresis or chromatography applications (Hjerten, 1962; Imeson, 2010).

Agar in the food industry

Over the past centuries, agar has been commonly used in the oriental cuisine as a gelling agent, known as “Qiongzhi” in Chinese, “Kanten” in Japanese (Glicksman, 1983) and “agar-agar” in western countries. Nowadays, agar is used in low metabolic energy therapies, and added to juice and to some alcoholic liqueurs as a stabilizing agent. Moreover, agar is used in bakery products to coat the surface of cakes and chocolate pralines to prevent dehydration, in yogurts to decrease the acidity level, in the meat industry and especially in the preparation of soft boiled sausages to reduce the fat content, etc. (Armisen & Galatas, 1987; Medin, 1995).

Agar in microbiology

In 1882, Robert Koch introduced agar as a culture medium for bacteriology after the suggestion by Dr Hesse, whose wife had used agar for many years to make fruit and vegetable jellies (Chapman, 1970). Since then, growth media have become a major application of agar and no other substance has come to replace it (Silverthorne & Sorensen, 1971; Callaway, 2015) since agar is indigestible by most microorganisms. Furthermore, agar gel is non-toxic for almost all microorganisms, and shows a huge resistance to degradation by enzymes that damage other gelling agents. Agar can be sterilized repeatedly without losing its properties, and the agar gels cast in Petri dishes can be kept at various incubation temperatures without any risk of liquefaction thanks to the temperature hysteresis discussed above. All these unique properties facilitate the manufacturing process and permit the incubation of microorganisms at ambient temperature. Finally, the osmotic pressure of agar-based culture medium is well adapted to cells such as red blood cells, bacteria or yeasts (Armisen & Galatas, 1987).

1.3 Framework and thesis outline

My PhD work is carried out in partnership with the company BioMérieux, a world leader of *in vitro* diagnostics for the human healthcare market. The company commercializes Petri dishes, which are used as culture media for the growth of microorganisms and cells, and for routine diagnostic tests. Since Fanny and Walter Hesse realized the relevance of agar for applications in microbiology, agar gels have been used without interruption for manufacturing culture media, and so far without any surrogate molecule or few competitor media. Further note that agar gels cast in Petri dishes provide an ideal ground for bacteria since the growth of microorganisms often requires an air/gel interface and microfluidic technologies based on flowing agar microspheres are not ready to replace Petri dishes.

And yet, the extensive manufacturing of agar gels through industrial processes has led to discover some limitations of that popular gel when cast in Petri dishes. Indeed, mass-produced culture media tend to shrink and detach from the lateral wall of the dish (Fig. 1.7). The detachment may take place either a short time after the gel production, or later on during the incubation of the Petri dish at constant temperature to monitor the growth of bacteria. In some rare occasions, the gel is even observed to fracture. In both cases, the agar gel cannot be used for its original purpose, which costs each year a fair share of money in customer return. The problem of the gel retraction is extremely complex. First, the exact formulation of the culture media varies a lot with the intended application, and the gel may contain nutriment, blood, etc. that will affect the water-holding capacity and therefore the shrinkage dynamics. Second, a large number of parameters might play a key role from the moment the agar powder is introduced into solution and brought to a boil to when the gel, cast in the dish, is used as a culture medium.

Being mainly composed of water (> 95 % wt.), agar gels are naturally prone to solvent-loss by evaporation, either at rest or under external deformation (Matsushashi, 1990). One can easily imagine that water loss promotes both gel shrinkage and the gel detachment from the sidewall of the dish. Therefore, one needs to understand the kinetics of the water release in quiescent conditions, and identify the components in the gel formulation (e.g. polymers, saccharides, salts, surfactants, etc.) that may affect the water-holding capacity of the gel. Moreover, the interaction of the gel with the solid walls of the dish also appears as a key parameter since the adhesion of the gel on the bottom and/or the lateral wall will influence the detachment time. One should therefore understand the adhesion and static friction properties between an agar gel and a solid surface, and further study the thinning kinetics of an agar gel cast in a cylindrical dish left to dry. To tackle such delicate issues, we have used a wide array of experimental techniques: rheology, macro-indentation, electron microscopy, X-ray scattering and interferometry and even developed original test fixtures such as a modified spin-coater to quantify the adhesion between the gel and a solid surface, and an optical flow method to detect with a high sensitivity the 2D motion of an agar gel cast in a dish and left to dry. All these methods are carefully



Figure 1.7: Pictures of a commercial agar plate at two different times. (left) View taken after unwrapping the plate from its original package and (right) view taken after a 24 h incubation at 25°C without cover lid on the dish. The gel has detached from the sidewall of the dish on the right side of the picture. The scale is set by the dish diameter of 8.5 cm. Extracted from (Divoux, Mao, & Snabre, 2015).

discussed in Chapter 2.

Historically, as I first joined the CRPP, Patrick Snabre and Thibaut Divoux had just realized that the free surface of commercial gels in Petri dishes were not flat, but slightly tilted, and that, as the gel was left to dry at ambient temperature, the detachment of the gel from the lateral wall of the dish was taking place at the very location where the gel thickness was minimal. We used direct observations and speckle pattern correlation analysis to rationalize the delayed detachment of an agar gel from the sidewall of the Petri dish, showing that the detachment time was controlled by the gel minimal thickness. The latter results published in (Divoux, Mao, & Snabre, 2015) convinced the company BioMérieux that the casting step of the agar gels into the dishes is critical, and that one should make sure to produce agar gels as flat as possible so as to postpone the detachment time.

From there, I investigated the influence of the key parameters associated with the gel preparation, and started with the influence of temperature. In the industrial process, hot agar-based solutions are prepared and maintained at high temperature for several hours before being cast in Petri dishes and cooled down at a rate of about 2 to 3°C/min. For these reasons, I carried out gelation experiments in a parallel-plate geometry connected to a rheometer so as to monitor agar gelation in well-controlled conditions. The results of these experiments are reported in Chapter 3, in which I also investigate the influence of the incubation duration of the hot agar solution on the gel properties, as well as the impact of the cooling rate and the role of a pause in the cooling process on the structural and mechanical properties of agar gels.

Chapter 4 is devoted to the study of the adhesion and debonding of agar gels in contact with solid surfaces. The goal was to determine the key parameters associated with the agar gel adhesion to a solid surface. Is it the surface roughness of the substrate, or the wettability that controls the agar gel adhesiveness? To answer these questions, I have determined the critical shear stress beyond which agar gels in contact with a solid surface, start sliding. For this purpose, I carried out two types of experiments: strain sweep experiments with a rheometer and centrifuge experiments using a modified spin-coater. Both techniques lead to consistent results and systematic tests on surfaces made of metal, glass, plastic (PS and PMMA), etc. of different surface roughness and wettability made it possible to rationalize the debonding of agar gels from solid surfaces.

Another important part of my PhD work concerns the drying kinetics of agar gels cast in dishes, which is presented in Chapter 5. An optical flow method is introduced so as to quantify the 2D motion of an agar gel cast in a cylindrical dish and left to dry. I further used an interferometer to determine the local thinning rate of an agar gel at different locations in a cylindrical dish and demonstrate how such a highly sensitive technique can be used to determine the influence of the gel composition on the drying kinetics.

Finally, in Chapter 6, I report the impact of additives such as salts, saccharides and surfactants on agar gel properties, including the influence on gel adhesion to solid surfaces and gel drying kinetics. On the one hand, agarose gels turn out to be highly sensitive to the presence of non-gelling saccharides in minute amounts, which can be used to slow down the water evaporation from the gel. On the other hand, minute amounts of salts or surfactants may strongly affect the adhesive properties of agar gels on plastic surfaces, without changing too much the drying rate. In that last chapter, we discuss how the additives can be used to tune the properties of agar gels.

Chapter 2

Samples and experimental techniques

Contents

2.1	Agar(ose) samples	26
2.1.1	Agarose and agarpectin content in agar samples	26
2.1.2	Polymer molecular weight	27
2.1.3	Additional chemical analysis	28
2.2	Gel structural properties	28
2.2.1	Cryo Scanning Electron Microscopy (cryo-SEM)	28
2.2.2	X-ray scattering experiments	30
2.3	Gel mechanical properties	31
2.3.1	Bulk rheology and Normal Force Controlled (NFC) rheology	31
2.3.2	Macro-indentation experiments	37
2.4	Gel adhesion, friction and slip	39
2.4.1	Strain sweep and gel debonding	39
2.4.2	Centrifugal stress and gel debonding	42
2.5	Gel drying	48
2.5.1	Interferometric observations	48
2.5.2	Spatio-temporal tracking	50
2.6	Properties of solid surfaces	55
2.6.1	3D scanning interferometry	55
2.6.2	Water contact angle measurements	56

Associated peer-reviewed articles:

▷ **Normal force controlled rheology applied to agar gelation,**

B. Mao, T. Divoux & P. Snabre,
Journal of Rheology **60**, 473–489 (2016)

▷ **Impact of saccharides on the drying kinetics of agarose gels measured by *in-situ* interferometry,**

B. Mao, T. Divoux & P. Snabre,
Scientific Reports **7**, 41185 (2017)

2.1 Agar(ose) samples

The present chapter concerns the different agar(ose) samples studied during my PhD work, as well as the various techniques and homemade methods used along the three years. The polymer samples consist in a commercial agarose provided by Sigma Aldrich and four different agar samples: one provided by Sigma Aldrich and three others provided by bioMérieux, whose respective properties are summarized in Table 2.1.

Nomination	Agarose	Agar			
	Agarose	Agar-SA	Agar-BM1	Agar-BM2	Agar-BM3
Provider	Sigma Aldrich	Sigma Aldrich	BioMérieux	BioMérieux	BioMérieux
CAS	9012-36-6	9002-18-0	–	–	–
Reference	A9539	A5306	03904185	03904185	<i>N.C.</i>
Batch number	SLBD2497V	SLBJ6279V	1002235510	1004167220	P14044
E (kPa, 1.5%wt. by default)	75 (for 1% wt.)	60 ± 10	50	60	<i>N.C.</i>
G' (kPa, 1.5%wt. by default)	19 (for 1% wt.)	22 ± 2	20	20	9
Agarose (%)	100	70	70	70	60
Agaropectin (%)	-	30	30	30	40
\overline{M}_{w_agar} (kDa)	-	85	130	100	140
$\overline{M}_{w_agarose}$ (kDa)	130	60	<i>N.C.</i>	60	70
$\overline{M}_{w_agaropectin}$ (kDa)	-	180	<i>N.C.</i>	180	170
Sulphur content (%wt.)	< 0.05	1	0.6	0.6	1.4
Azote content (%wt.)	< 0.05	0.5	0.4	0.4	0.4
Moisture	11.8%	<i>N.C.</i>	14.5%	12.7%	10.6%
NH ₄ ⁺ (mg/g)	-	-	-	-	-
Li ⁺ (mg/g)	-	-	-	-	-
Na ⁺ (mg/g)	4	17	18	17	13
K ⁺ (mg/g)	-	-	-	-	16
Mg ²⁺ (mg/g)	-	1	-	-	0.4
Ca ²⁺ (mg/g)	1	2.5	0.6	0.6	6
Cl ⁻ (mg/g)	1	8	5	7	2
SO ₄ ²⁻ (mg/g)	0.6	1	0.6	1	16

Table 2.1: Properties of agar(ose) samples. The symbol (-) stands for “not observed”, while E and G' represent respectively the Young’s modulus and the shear elastic (or storage) modulus. The Young’s modulus is measured through macro-indentation experiments (see Section 2.3.2 for technical details) and the storage modulus G' is determined by small-amplitude oscillatory shear rheology (see Section 2.3.1 for technical details).

2.1.1 Agarose and agaropectin content in agar samples

The storage modulus of gels was shown to increase as a power law of the polymer concentration for several biopolymers such as κ -carrageenan, gelatin, agarose, etc. (Meunier, Nicolai, Durand, & Parker, 1999; Normand, Muller, Ravey, & Parker, 2000; Mohammed et al., 1998). In the case of agar gels, only the agarose molecules contribute to the network elasticity as the agaropectin molecules do not gel. Therefore, the shear elastic modulus vs. the polymer concentration in a pure agarose sample was first determined and used as a calibration curve to estimate the agarose content in agar samples composed of both agarose and agaropectin molecules.

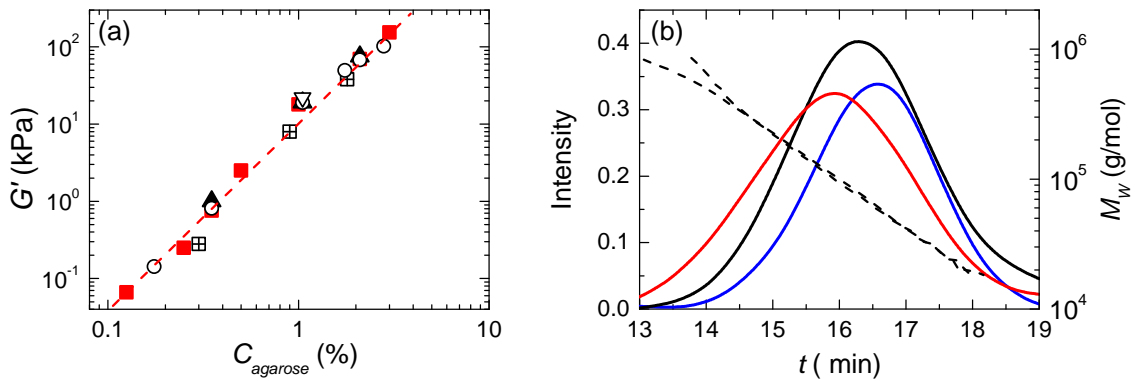


Figure 2.1: (a) Master curve for the shear elastic modulus G' of various agar gels vs the agarose concentration rescaled to match the calibration curve of the pure agarose sample (■). The scaling factor $\mathcal{W}_{agarose}$ is 0.7 for agar-SA (▽), agar-BM1 (○) and agar-BM2 (▲); and 0.6 for agar-BM3 (⊞). The power-law exponent for the pure agarose sample (■) is 2.42 ± 0.07 in good agreement with previous results reported in the literature (Normand, Lootens, et al., 2000; Mohammed et al., 1998; Guenet & Rochas, 2006). (b) Molecular weight distributions of agar-BM2 (black), agarose (blue) and agaropectin (red) molecules extracted from agar-BM2 and determined by size exclusion chromatography coupled with multi-angle light scattering (SEC/MALLS) considering a refractive index increment $dn/dc = 0.12$ measured independently by differential refractometry with dilute agar solutions of different concentrations (0.01% wt., 0.02% wt., 0.03% wt., 0.04% wt., 0.05% wt.).

For this purpose, the agar concentration is multiplied by a scaling factor $\mathcal{W}_{agarose}$ such that the shear elastic modulus of the agar gel coincides with that of the pure agarose gel [Fig. 2.1(a)]. The scaling factor $\mathcal{W}_{agarose}$ provides a good estimate of the agarose concentration in the agar samples: $\mathcal{W}_{agarose} = 70\%$ for Agar-SA, Agar-BM1, Agar-BM2 and $\mathcal{W}_{agarose} = 60\%$ for Agar-BM3.

2.1.2 Polymer molecular weight

To determine the distribution and the average molecular weight \overline{M}_w of agarose and agaropectin molecules in agar samples, the two components were separated using the method described in (Hjerten, 1962; Mitsuiki et al., 1999). By the addition in hot agar solution of cetylpyridinium chloride (CPC), a cationic surfactant, the charged agaropectin polymer is precipitated meanwhile the neutral agarose polymer still stays in the solution. The agarose gel is obtained by cooling the supernatant after the removal of the agaropectin precipitate, and then crushed/washed several times to remove the salts residues. The agaropectin precipitate is also washed several times. Finally, the extracts are frozen and lyophilized by freeze-drying for the determination of the molecular weight distribution. The M_w distributions of the agar, agarose and agaropectin molecules are characterized with size exclusion chromatography (SEC) coupled with multi-angle laser light scattering, refractive index detection and ultraviolet detection (SEC/MALLS+RI+UV, Wyatt) in collaboration with J. Martinez from the R&D Immunoassay department in BioMérieux. The molecular weight distributions of agar-BM2 sample are displayed in Figure 2.1(b). The average molecular weight of agaropectin molecules ($\overline{M}_w \approx 1.6 \times 10^5 - 2.0 \times 10^5$ g/mol) is found to be higher than that of agarose molecules ($\overline{M}_w \approx 6 \times 10^4 - 7 \times 10^4$ g/mol). Similar results have been obtained with the other agar samples (see Table 2.1) and in agreement with data from literature (Mitsuiki et al., 1999).

2.1.3 Additional chemical analysis

The additional results reported in table 2.1 are obtained as follows. Sulphur and azote contents are determined by elemental analysis. The moisture content is measured using Thermogravimetric analysis (TGA Q50, TA instrument) by monitoring the mass loss of the sample submitted to a temperature increase up to 200°C. Both experiments are performed directly on agar powder. Finally, the ion contents were characterized by ionic chromatography (ICS-1100, Thermo Scientific) on dilute agar solutions (0.05% wt.) in collaboration with Dr. Y. Guo from the R&D raw material department in BioMérieux.

We should emphasize that agar-BM1 and agar-BM2 samples originate from the same source and only differ from the batch number. Indeed, all the analysis performed on these samples lead to compatible data within error bars. On the other hand, the more expensive agar-BM3 originates from another source and its gels show better adhesion performance with less shrinking and detachment issues when cast in plastic dishes. A systematic characterization of the agar samples was performed since the origin of the better performance of agar-BM3 is still unclear. Compared to agar-BM1 and agar-BM2, agar-BM3 displays a slightly lower proportion of agarose and further shows significantly higher contents in K^+ , Ca^{2+} , and SO_4^{2-} ionic species.

2.2 Gel structural properties

Historically, the microstructure of agar gels have been studied with different methods: optical microscopy, transmission electron microscopy (TEM) (Pernodet et al., 1997), Scanning Electron Microscopy (SEM) (Rahbani et al., 2013), Atomic Force Microscopy (AFM) (Pernodet et al., 1997) and more recently confocal microscopy (Russ, Zielbauer, Koynov, & Vilgis, 2013). During my PhD, I investigated the microstructure of agar gels using two techniques: (i) cryo-Scanning Electron Microscopy (cryo-SEM) in collaboration with M. Martineau and P. Legros from the *Plateforme Aquitaine de Caractérisation des Matériaux* (PLACAMAT, UMR 3626), and (ii) X-ray scattering in collaboration with A. Bentaleb at CRPP. The cryo-SEM technique gives high-resolution images of agar gels, while X-ray scattering provides information on the local arrangement of the polysaccharides in the gel. Note that both techniques are invasive as the former requires to freeze the gel, while the latter is performed on a dried gel.

2.2.1 Cryo Scanning Electron Microscopy (cryo-SEM)

In practice, a sample is extracted from the agar gel with a plastic pipette and glued to a metallic pin stub of 12.5 mm diameter using a drop of commercial sugar solution (OCT Compound 4583, Scigen Tissus Plus). The sample and the stub are then immersed in a liquid nitrogen bath for about 5 min, before being placed in the low vacuum preparation chamber of the SEM microscope (Fig. 2.2), which is cooled down to $T = -90^\circ\text{C}$. The sample is “beheaded” in situ with a scalpel and the temperature is then increased up to $T = -50^\circ\text{C}$ at about $5^\circ\text{C}/\text{min}$ so as to sublime the frozen water enclosed inside the sample [Fig. 2.3(b)]. After 5 min, the temperature is decreased back to $T = -85^\circ\text{C}$ and the sample is coated with a nanolayer of gold-palladium (120 s at 5 mA). Finally, the sample is cooled down to $T = -160^\circ\text{C}$ and introduced inside the observation chamber of the microscope. Images are taken in standard detection mode, i.e. secondary electron imaging (SEI) mode at 5 kV.

Typical results on a 1.5% wt. agar-BM1 gel are pictured in figure 2.3. The sample

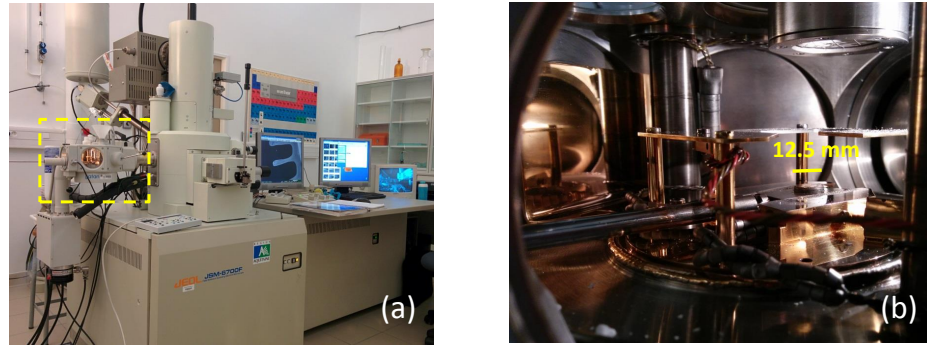


Figure 2.2: (a) Picture of the Scanning Electron Microscope JEOL 6700F available at PLACAMAT. The location of the preparation chamber is marked by a yellow square. (b) Picture of the preparation chamber where the sample is beheaded, sublimed and metalized. The scale is given by the metallic pin stub of diameter 12.5 mm.

displays different microstructures in different locations. In the center part, the gel shows a fibrous-like microstructure composed of interconnected strands delimiting pores with a broad size distribution up to a few micrometers [Fig. 2.3(d)], which is in agreement with cryo-SEM data reported in the literature for similar agarose concentration (Charlionet, Levasseur, & Malandrin, 1996; Brigham et al., 1994; Nishinari & Fang, 2016a). Near the edge of the sample, the gel displays a similar microstructure with that observed in the center region, except for the presence of large scale cellular structures [Fig. 2.3(c) and (e)].

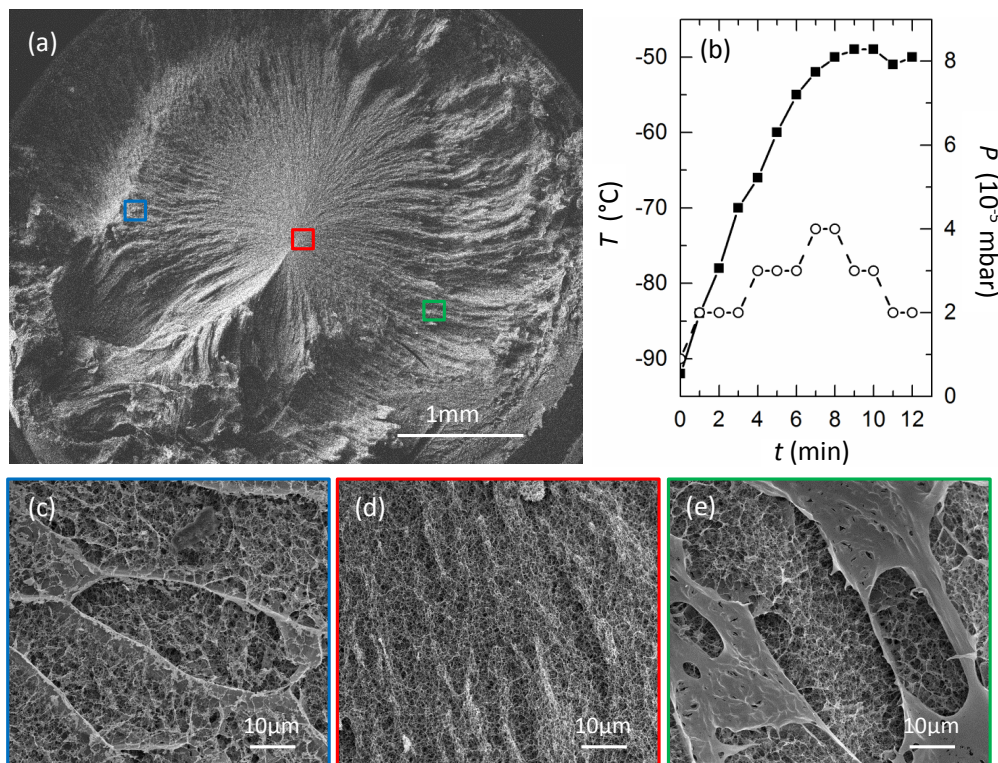


Figure 2.3: (a) Cryo-SEM picture of 1.5% wt. agar-BM1 gel. (b) Time variation of the temperature $T(t)$ of the gel sample during the sublimation step, and corresponding pressure P . (c)–(e) Pictures of the gel extracted from (a) at different locations highlighted by rectangles which color in (a) corresponds to the color of the frame outline.

Such alveoli are most likely an experimental artefact, which might either results from the sample preparation (stress-induced damages associated with the extraction of a piece of the gel with a pipette) or could be caused by the sublimation process. Therefore, all the cryo-SEM images presented in the rest of the manuscript always correspond to the center region of the gel samples.

2.2.2 X-ray scattering experiments

X-ray diffraction is a method widely used to characterize the microstructure of materials on scales ranging from a few tenths of an angstrom to a few hundred nanometers. The experimental setup available in the CRPP laboratory is illustrated in Figure 2.4(a): a monochromatic incident X-ray beam of wavelength $\lambda = 1.5418\text{\AA}$ and photon energy 8 keV is produced by a micro-source generator (Rigaku MicroMax 007HF) with a 1200 W rotating anode coupled to a confocal Max-Flux Osmic mirror (Applied Rigaku Technologies, Austin, USA) and focused on the sample. The interaction of the incident X-ray beam with the scattering sample produces a diffraction pattern with intense radiation peaks when the Bragg's condition $2d \sin \theta = \lambda$ is satisfied, where d is the spacing between diffracting planes, θ the scattering angle, and λ the beam wavelength. By scanning the sample through a range of 2θ angles, all possible diffraction directions are attained due to the random orientation of the scattering gel microstructure. The agar gel is irradiated with the X-ray beam for an hour and the powder diffraction pattern is recorded through a MAR345 image plate detector (MARResearch, Norderstedt, Germany) placed at 152 mm from the sample. The numerical aperture of the detector allows to probe wavenumbers $q = 4\pi \sin \theta / \lambda$ from 8 nm^{-1} up to 30 nm^{-1} . Raw data are processed with the software ©Fit2D: the background intensity diffracted by the surrounding air is first subtracted to

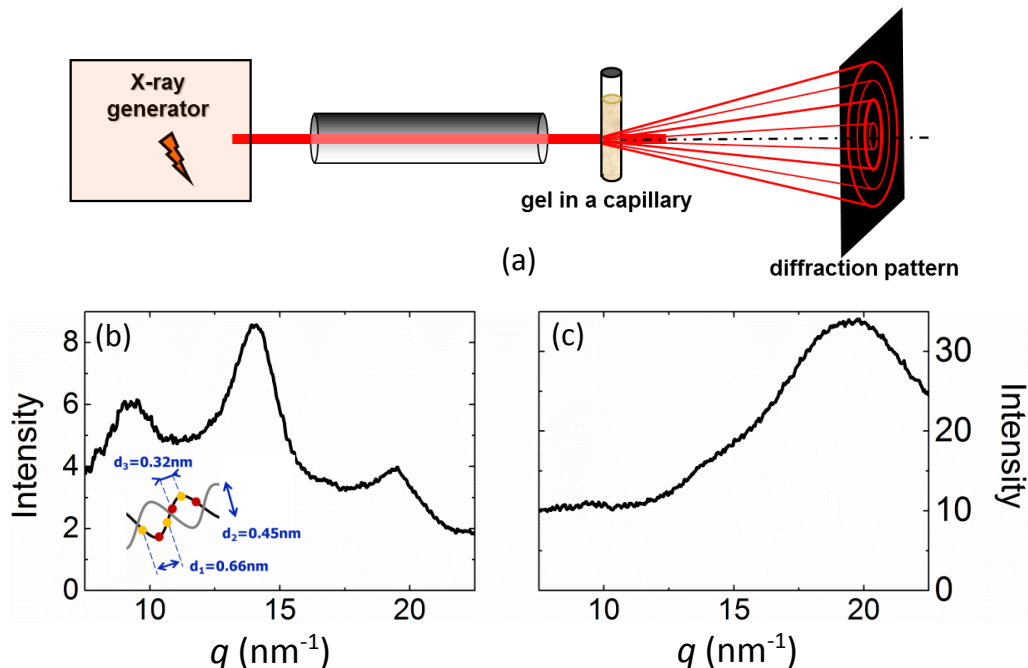


Figure 2.4: (a) Sketch of the X-ray diffraction experiment available at CRPP. Below, X-ray diffraction spectra $I(q)$, where q stands for the wavenumber, for a dried 1.5% wt. agar-SA gel (b) or an hydrated 1.5% wt. agar-SA gel (c).

the raw intensity, before a normalization to account for the exposure time and the beam intensity.

I have conducted experiments on both fully hydrated gels and dried gels, enclosed in sealed glass capillaries. In the latter case, gels are cast in smooth plastic dishes (diameter 55 mm) made of polystyrene and then left to dry for 3 days at ambient room temperature, i.e. $T = (22 \pm 2)^\circ\text{C}$, to obtain a dried and transparent agar(ose) film. The diffraction spectra of a dried 1.5% wt. agar-SA gel is reported in Figure 2.4(b). The intensity exhibits three maxima at the following wavenumbers: $q_1 = 9.45 \text{ nm}^{-1}$, $q_2 = 13.86 \text{ nm}^{-1}$ and $q_3 = 19.3 \text{ nm}^{-1}$, which correspond respectively to: $d_1 = 2\pi/q_1 = 0.66 \text{ nm}$, $d_2 = 0.45 \text{ nm}$ and $d_3 = 0.32 \text{ nm}$. Following the seminal work of (Foord & Atkins, 1989), such values can be interpreted as follows: the agarose chains are associated into 3-fold double helices [see inset in Fig. 2.4(b)], where d_1 and d_3 correspond respectively to the distance between two different and two identical saccharides, while d_2 stands for the helix diameter. Interestingly, the diffraction spectra obtained from hydrated gels and reported in Figure 2.4(c) shows only a single maximum at $q_3 = 19.3 \text{ nm}^{-1}$, whereas the two other maxima visible on dry gels are much less pronounced or absent. Indeed the water molecules in the agar gel dramatically lower the angular spectrum resolution. Therefore, X-ray spectra reported in the rest of the manuscript only concern dried gels.

2.3 Gel mechanical properties

2.3.1 Bulk rheology and Normal Force Controlled (NFC) rheology

Rheological setup

The bulk properties of viscous agar solutions and solid-like agar gels are monitored through rheological experiments with a stress-controlled rheometer DHR-2 from TA Instruments [Fig. 2.5(a)]. On the one hand, the viscosity $\eta = \sigma/\dot{\gamma}$ of hot agar solutions is measured by steady-shear rheology in a cone-and-plate geometry, where σ represents the imposed shear stress and $\dot{\gamma}$ the shear rate. The cone (diameter 60 mm, angle 2°) is made of stainless steel and the bottom plate consists in a Teflon coated Peltier unit, which allows to control the sample temperature. Viscosity measurements are performed at $T = 50^\circ\text{C}$ and the geometry is pre-heated before being filled with the agar liquid solution. The linear viscoelastic properties of agar gels, i.e. the storage (or elastic shear) modulus G' and loss modulus G'' are determined prior to, during and after agar gelation by Small Amplitude Oscillatory Shear (SAOS) experiments. SAOS experiments are performed with a

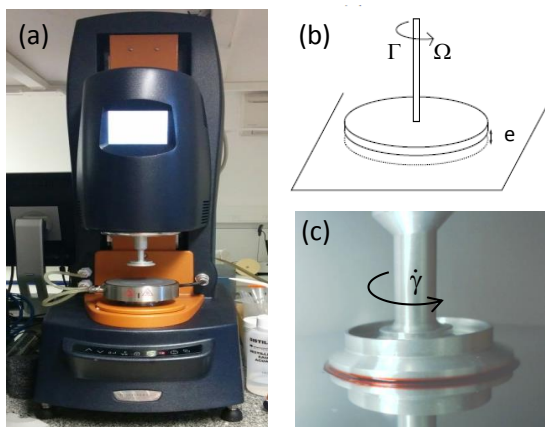


Figure 2.5: (a) View of the stress-controlled rheometer (DHR-2, TA instruments). (b) Sketch of a plate-plate geometry. The rheometer exerts a torque Γ on the upper plate and the rotational speed $\Omega(t)$ is monitored. Taking into account geometrical factors, both quantities are converted into a shear stress σ and a shear rate $\dot{\gamma}$ respectively. (c) View of the homemade plate-plate geometry of diameter 40 mm. The sample is surrounded with a rim of oil –here dyed in red for visualization purposes– so as to minimize the water evaporation.

homemade plate-plate geometry of diameter 40 mm [Fig. 2.5(c)]. The upper moving plate made of duralumin is sandblasted and displays a RMS surface roughness of $(4 \pm 2) \mu\text{m}$, as measured by 3D microscopy and Atomic Force Microscopy. The bottom plate consists in a smooth and teflon coated Peltier unit that allows for a precise temperature control during the agar gelation. Evaporation is minimized either by using a solvent trap containing deionized water and placed on top of the upper plate, or by adding a thin layer of sunflower seed oil¹ [the seed oil is colored with a red dye for a better visualization, see Fig. 2.5(c)] from *Helianthus annuus* (Sigma Aldrich) around the sample, depending on the duration of the experiment.

Gap compensation and zero normal force protocol

Gelation experiments performed with a rheometer are somewhat delicate as large temperature variation induces a non-negligible thermal dilation of the plates. To make sure that the gelation is monitored in the absence of any experimental artifact, a rigorous and robust protocol is followed step by step as detailed below.

I first consider the following experiment to illustrate the impact of the thermal dilation of the plates on the rheological measurements: the gap width is set to $e = 500 \mu\text{m}$ at $T = 20^\circ\text{C}$, before being heated up to 70°C . Due to the thermal dilation of the plates, the gap width decreases as the temperature increases, by $1.3 \mu\text{m}/^\circ\text{C}$, as determined by the calibration of the instrument. The gap width is therefore $435 \mu\text{m}$ at the moment the hot polymer solution is introduced inside the pre-heated geometry. Once the polymer solution is loaded, the temperature is decreased at a constant rate $\dot{T} = 1^\circ\text{C}/\text{min}$ down to $T_f = 20^\circ\text{C}$ while both the normal force [Fig. 2.6(a)] and the viscoelastic moduli G' and G'' [Fig. 2.6(d)] of the sample are monitored through small amplitude oscillations with a strain amplitude $\gamma = 0.01 \%$. During the first half hour, the agar solution remains liquid as long as $T \geq 35^\circ\text{C}$, and the normal force F_N is close to zero as the gap width increases back to the initial value of $500 \mu\text{m}$. After about 0.6 h, the agar gelation starts, as evidenced by the growth of the elastic shear modulus, which becomes larger than the loss modulus. Concomitantly, the normal force F_N shows negative values indicating that the gel is pulling down on the upper plate, until a significant upturn occurs at $t = 0.75$ h prior to the end of the cooling phase ($t = 0.8$ h), representative of a brutal change in the contact between the gel and the plates, as discussed below. Moreover, the elastic shear modulus G' goes through a maximum at $t = 0.88$ h after the temperature has reached the terminal value $T_f = 20^\circ\text{C}$, and further relaxes towards a steady-state terminal value $G'_f = 11.7$ kPa, while the normal force F_N remains negative. Agar gelation appears as over after 2.5 h, and the gel sample then displays a solid-like behavior as evidenced by $G' \gg G''$.

In fact, the above procedure does not compensate for the thermal dilation of the plates, leading to an artificially low estimate of the storage modulus G' . Indeed, repeating the same gelation experiment while taking into account the change in the gap width due to thermal dilation, leads to much larger values of the storage modulus G' [Fig. 2.6(e)]. In that case, later referred to as the “temperature compensation mode”, the gap width remains constant during the entire experiment and the terminal value of the elastic shear modulus is $G'_f = 28.0$ kPa [Fig. 2.6(e)], instead of 11.7 kPa in the absence of compensation for the

¹Sunflower seed oil was chosen since the diffusion coefficient $D \simeq 10^{-10} \text{ m}^2.\text{s}^{-1}$ of water in sunflower seed oil is an order of magnitude lower than the diffusivity of water in silicone oil. In sunflower seed oil, the polar moieties of triglycerides strongly interact with water through hydrogen bonds, resulting in a lower mobility of water molecules (Zieverink, de Rijke, de Kruijf, & de Kok, 2009).

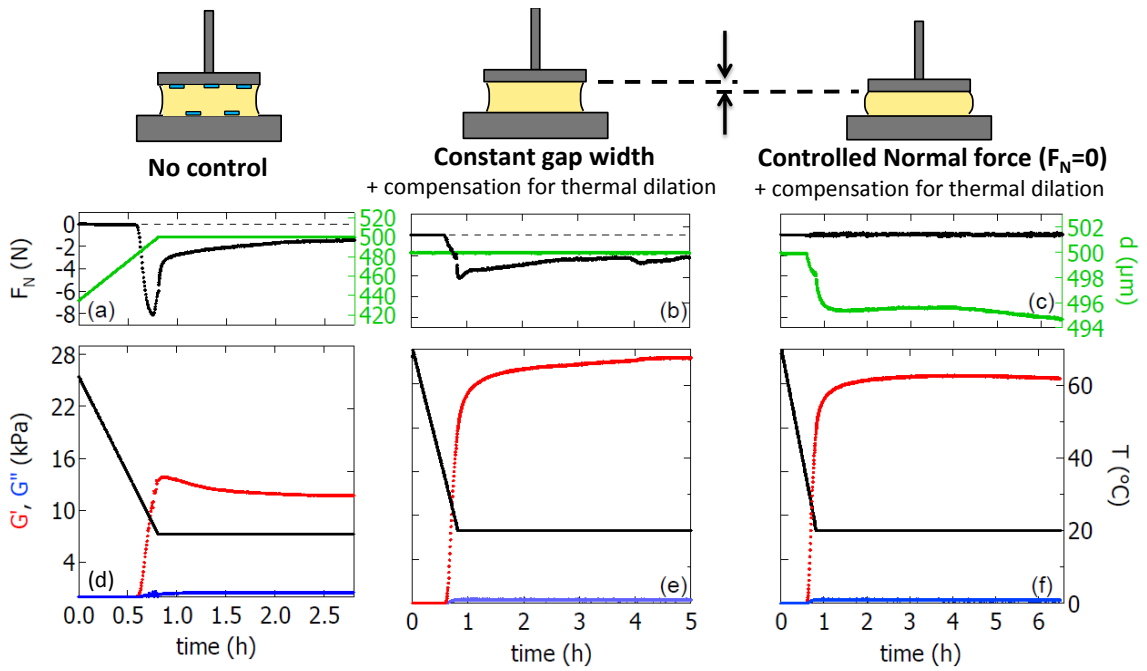


Figure 2.6: Time evolution of the normal force F_N and the gap width e (a)–(c) together with the storage and loss moduli (d)–(e) during the gelation of a 1.5% wt. agar-BM1 solution when decreasing the temperature from $T = 70^\circ\text{C}$ down to 20°C at a cooling rate $\dot{T} = 1^\circ\text{C}/\text{min}$. The gelation experiment is repeated three times with different protocols. The first column illustrates a gelation run performed without any particular precaution. Although the gap width is set initially at $e_0 = 500 \mu\text{m}$ at $T = 20^\circ\text{C}$, the true gap width varies by $65 \mu\text{m}$ due to the thermal dilation of the plates, resulting in a lower terminal value of the storage modulus $G'_f = 11.7 \text{ kPa}$. The second column shows a gelation experiment during which the temperature compensation mode is active and compensates for the thermal dilation of the plates. The gap width remains constant during the whole gelation process ($e_0 = 500 \mu\text{m}$). Yet, the normal force is still negative which proves that the sample contracts during the gel formation. Such a contraction leads to strain hardening effects as evidenced by the continuous increase of the storage modulus ($G'_f \simeq 28.0 \text{ kPa}$ at $t = 5 \text{ h}$). Finally, the third column illustrates a gelation run with a sample experiencing a constant normal force $F_N = (0.0 \pm 0.1) \text{ N}$, while the temperature compensation mode is active. The gap width of initial value $e_0 = 500 \mu\text{m}$, decreases by 1% which compensates for the sample contraction ($G'_f = 25.9 \text{ kPa}$). For the three experiments, the strain amplitude $\gamma = 0.01 \%$, the frequency $f = 1 \text{ Hz}$ and the solvent trap is filled with water.

thermal dilation of the plates [Fig. 2.6(d)]. Such a difference illustrates how dramatic and misleading can be the effect of the thermal dilation of the plates on the measurements of the gel linear viscoelastic properties. As a consequence, the abrupt upturn of the normal force observed in Figure 2.6(a) in the absence of any thermal compensation results from a partial loss of contact and/or the formation of local lubrication spots between the gel sample and the plates, due to the large negative value of the normal force F_N . Indeed, the maximum value of $F_N \sim -8 \text{ N}$ in Figure 2.6(a) gives an estimate of the tensile strain acting on a 1.5% wt. agar-BM1 gel with a Young's modulus of about 70 kPa [see Fig. 2.11 in Section 2.3.2] of about 10% which is large enough to trigger the release of solvent and induce a partial lubrication of the gel-plate interface.

At this stage the protocol is not yet satisfying. Indeed, the normal force still exhibits negative values during the gel formation although the thermal dilation of the plates is compensated [Fig. 2.6(b)]. A negative normal force reflects a downward force exerted by the sample on the upper plate, due to the contraction of the sample at the sol-gel

transition. As a result, the storage modulus G' displays a weak logarithmic increase even after the normal force F_N has reached a plateau [Fig. 2.6(b)(e)], which is representative of a strain hardening effect induced by the gel contraction. Such a slow drift of G' towards ever larger values was also reported in other studies conducted on gels containing agar(ose) (Goycoolea, Richardson, Morris, & Gidley, 1995; Labropoulos et al., 2002; Normand et al., 2003), but usually unnoticed as data are most often plotted in semi-logarithmic scale which flattens G' artificially.

To compensate for the effect of both the thermal dilation of the plates and the contraction of the sample during the phase transition, the gel formation is now monitored with the temperature compensation mode switched on, while imposing a controlled normal force $F_N = (0.0 \pm 0.1)$ N instead of a constant gap width. The gap width, which initial value is set to $e_0 = 500$ μm may now vary during the experiment and indeed, we observe a gap decrease of about 4 μm concomitantly to the growth of the storage modulus G' [Fig. 2.6(c)]. Such a gap width decrease of about 1% allows the upper plate to stay in contact with the gel while the latter contracts during the gelation. Furthermore, the storage modulus does not drift anymore and reaches a lower constant terminal value $G'_f = 25.9$ kPa [Fig. 2.6(f)] compared to the constant gap width experiment [Fig. 2.6(e)]. The latter observation also confirms the strain hardening scenario previously invoked in Figure 2.6(e). The error bar associated with the measurement of the terminal values G'_f of the storage modulus is mainly dependent upon the ability of the experimentalist to load the shear cell with the same amount of hot agar solution. Repeating about ten times the same experiment on agar solutions extracted from different batches leads to compatible results within 10%². In conclusion, monitoring the gelation process while imposing a constant normal force equals to zero prevents any strain hardening of the gel and appears as a more robust method to determine accurately the gel elastic properties. The latter method is further referred to as “the zero normal force protocol” in the rest of the manuscript.

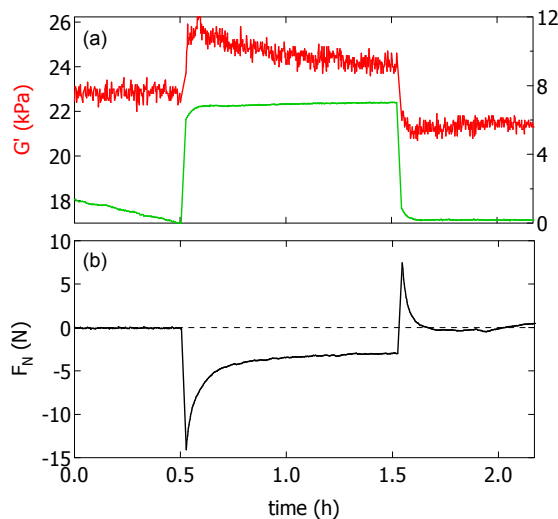


Figure 2.7: (a) Time evolution of the storage modulus G' of 1.5% wt. agar-BM1 gel in response to an increase $\Delta e = 6$ μm of the gap width triggered at $t = 0.5$ h and suppressed after waiting 1 hour. Δe denotes the excess gap width above the value reached at $t = 0.5$ h, after the end of the gelation process under the zero normal force protocol, and taken as an arbitrary reference. (b) Time evolution of the normal force F_N concomitant to the gel response.

Finally, I have performed a supplemental test to further demonstrate that the slow increase in the storage modulus G' reported when considering an experiment at a constant gap width [Fig. 2.6(e)] is indeed due to the strain hardening of the gel sample. An agar

²Note that repeating the gelation experiments under zero normal force with different initial gap values, i.e. $e_0 = 200$ μm and 1000 μm give compatible values of the terminal steady-state storage modulus G'_f within error bars, which demonstrates that the determination of gel viscoelastic properties using the zero normal force protocol is independent of the initial gap width e_0 .

gel is prepared between parallel plates (initial gap $e_0 = 500 \mu\text{m}$) using the zero normal force protocol, by decreasing the temperature from 70°C down to 20°C at $1^\circ\text{C}/\text{min}$. At the end of the gelation process, the gap width undergoes a 1% decrease while the normal force is still equal to zero, in agreement with the results reported in Figure 2.6(c) and (f). The rheometer is then switched to a controlled gap mode and the gap width is increased by $\Delta e = 6 \mu\text{m}$ at $0.1 \mu\text{m}/\text{s}$, which corresponds to a tensile strain acting on the gel of about 1%. In response, the gel elastic shear modulus shows a brutal increase of about 10% from 23 kPa to 25 kPa [Fig. 2.7(a)], while the normal force concomitantly becomes negative and relaxes towards a steady-state value $F_N \simeq -3\text{N}$ [Fig. 2.7(b)] indicating that the gel is pulling down on the upper plate. Such a behavior demonstrates that an increase of the gap width triggers an increase of the gel elastic shear modulus representative of the strain hardening of the gel under extension. We thus conclude that a contraction of the gel sample may also give rise to strain hardening effects and to ever increasing values of the storage modulus G' when performing the gelation experiment at constant gap [Fig. 2.6(e)]. Moreover, when the gap increase $\Delta e = 6 \mu\text{m}$ is suppressed after a time period of 1 h, the normal force relaxes back to zero, while the storage modulus G' decreases towards a value slightly lower than the initial one (Fig. 2.7). Such a lower value of the elastic shear modulus G' is likely due to the sharp initial increase of the gap, which triggers a partial loss of contact between the gel and the plates.

Strain adapted protocol

Here, I briefly discuss the role of the strain amplitude γ applied to the sample during a gelation experiment. Figure 2.8(a) displays in a semi-logarithmic plot the temporal evolution of the storage and loss moduli during a rheological experiment conducted under the zero normal force protocol with a constant strain amplitude $\gamma = 0.01 \%$ and a frequency $f = 1 \text{ Hz}$ [same protocol as in Fig. 2.6(f)]. Although the sample is liquid-like during the first half hour, such a small oscillatory deformation leads to noisy and comparable values of G' and G'' until both moduli exceed about 1 Pa. This experimental observation, which is commonly encountered in the literature (Altmann, Cooper-White, Dunstan, & Stokes, 2004; Russ, Zielbauer, & Vilgis, 2014), is related to a too low strain amplitude. Indeed, the minimum measurable value G'_{min} of the storage modulus is inversely proportional to

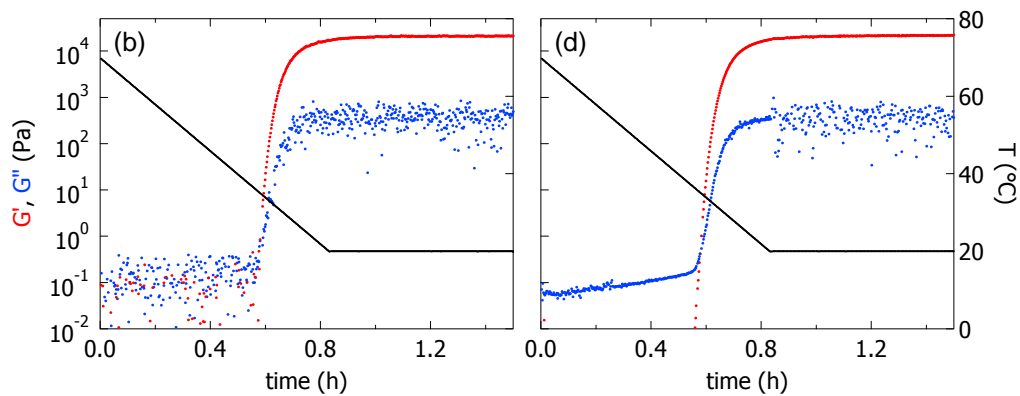


Figure 2.8: Time evolution of the storage and loss moduli in semi-logarithmic scale determined through small amplitude oscillations of frequency $f = 1 \text{ Hz}$ during the gelation of a 1.5% wt. agar-BM1 solution with constant strain amplitude $\gamma = 0.01 \%$ (a), or with γ values adapted to the value of the shear elastic modulus G' (b). For both experiments, “the zero normal force protocol” is applied and the solvent trap is filled with water.

the strain amplitude γ and given by the relation:

$$G'_{\min} = \frac{4\Gamma_{\min}}{3\pi R^3 \gamma} \quad (2.1)$$

where R denotes the plate radius and Γ_{\min} the smallest measurable torque (Ewoldt, Johnston, & Caretta, 2015). In the case of the DHR-2 rheometer ($\Gamma_{\min} = 2$ nN.m) and a strain amplitude $\gamma = 0.01$ %, the relation 2.1 gives $G'_{\min} = 1$ Pa, which is in excellent agreement with the minimal significant modulus observed in Figure 2.8(a). Imposing a larger strain amplitude before the start of the gelation, such as $\gamma = 1$ % allows to decrease G'_{\min} down to 0.01 Pa and to measure consistent values for the viscoelastic moduli during the first half hour, i.e. $G' = 0$ since the sample is still liquid [Fig. 2.8(b)]. The strain amplitude is then decreased when the storage modulus G' increases as the gelation starts, so as to remain in the linear regime and prevent any strain-induced release of the solvent and/or gel debonding from the plates. As a consequence, the following protocol leads to reproducible measurements: $\gamma = 1$ % for $G' < 1$ Pa, $\gamma = 0.1$ % for 1 Pa $< G' < 10$ Pa and $\gamma = 0.01$ % for $G' > 10$ Pa. After gelation, the terminal value $G'_f = 21.6$ kPa of the storage modulus is compatible within error bars with the value $G'_f = 21.0$ kPa measured with a constant strain amplitude $\gamma = 0.01$ %. Therefore adapting the value of the strain amplitude during agar gelation allows for a more accurate determination of the temperature crossover between G' and G'' that is often used as a good estimate of the gelation point³ and which occurs here at $T_g = 35.2^\circ$ C. Such a strain-adapted protocol is systematically applied for SAOS experiments reported in the rest of the manuscript.

Smooth or rough boundary conditions

Here, SAOS experiments are conducted with the zero normal force protocol to study the impact of the surface roughness of the plates on the monitoring of agar gel viscoelastic properties. The previous experiments reported in Figure 2.6 and Figure 2.8 have been performed with mixed boundary conditions (BC), namely a rough metallic upper plate and a smooth (teflon coated) bottom Peltier plate. To further test the robustness of the zero normal force protocol, we have performed gelation experiments with symmetric smooth or rough boundary conditions. On the one hand, the sandblasted duralumin rotor was replaced with a duralumin plate polished on a rotating wheel with a suspension of ultrafine aluminum oxide particles to produce a mirror like surface [Fig. 2.9(a)] of RMS surface roughness ($R_q = 6.9 \pm 4.4$) nm as determined from 3D microscopy and AFM measurements. The bottom plate used by default is the smooth and Teflon coated Peltier plate.

On the other hand, symmetrically rough boundary conditions are obtained by topping the Peltier plate with a sandblasted duralumin plate of typical RMS surface roughness of about $4 \mu\text{m}$, similar to that of the upper sandblasted duralumin plate and ensuring a good thermal conductivity between the Peltier plate and the sample. Both experiments reported in Figure 2.9(b) lead to compatible terminal values of the storage modulus G'_f within error bars (rough BC: $G'_f = 23.6$ kPa; smooth BC: $G'_f = 23.8$ kPa) and in quantitative agreement with the storage modulus determined with mixed boundary conditions [see Fig. 2.6(f)]. Such experiments demonstrate that the zero normal force protocol together

³Note that a proper definition of the gelation point is the instant when G' and G'' both scale as identical power laws of frequency, which corresponds to a value of the phase angle $\delta = \arctan(G''/G')$ that is independent of the frequency (Chambon & Winter, 1987). However, the dominant elastic behavior of agar gels as soon as the gelation starts makes the latter method unsuitable and only the temperature crossover of G' and G'' can give an estimation of the agar gelation temperature.

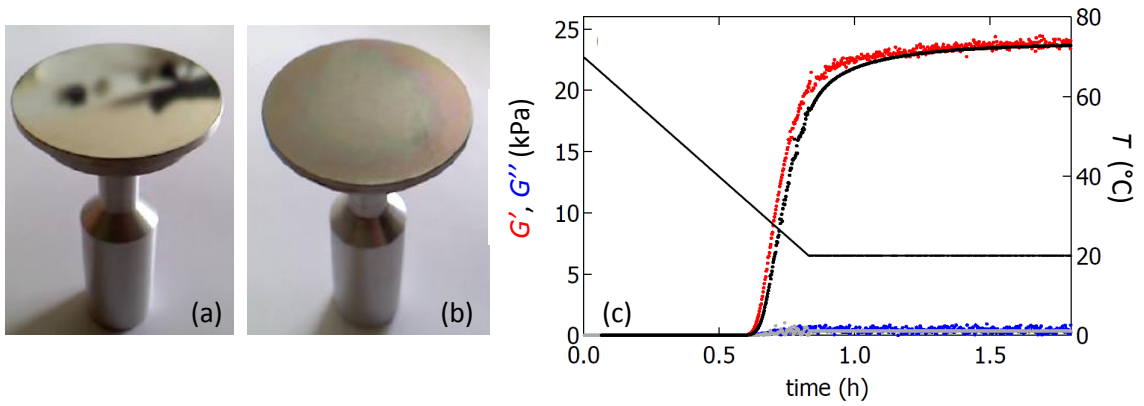


Figure 2.9: Pictures of a smooth polished duralumin plate (a), or a rough sandblasted duralumin plate (b). The scale is fixed by the plate diameter of 40 mm. (c) Time evolution of the viscoelastic moduli G' and G'' during the gelation of a 1.5% wt. agar-BM1 solution, under controlled normal force $F_N = (0.0 \pm 0.1)$ N. The experiment is performed twice, each time with symmetric boundary conditions: once with smooth surfaces, i.e. a polished duralumin upper plate pictured in (a) and a Teflon coated bottom plate (red and blue symbols) and once with rough walls, i.e. sandblasted duralumin plates (black and gray symbols). In both cases the relative gap width decrease is about 1%, the crossover temperature of G' and G'' is $T_g = 35.7^{\circ}\text{C}$, and the terminal values of the storage modulus are respectively $G'_f = 23.8$ kPa and 23.6 kPa. Both experiments are performed with a solvent trap filled with water.

with oscillations of small amplitude adapted to the value of the elastic shear modulus allows one to monitor the gelation dynamics between parallel plates with either smooth or rough boundary conditions. The zero normal force protocol further appears as more robust and more relevant than the traditional constant gap width protocol, which often requires the use of sandpaper. Indeed, sandpaper does not compensate for the sample contraction during gelation and is a poor thermal conductor. Moreover, sandpaper often displays adhesion issues to the Peltier plate at high temperature, hence inducing large error bars.

2.3.2 Macro-indentation experiments

Macro-indentation tests of agar gels with a flat-ended cylinder provide a way to characterize both the compression elastic properties and the mechanical resistance of the soft material. Agar gels, shaped as flat cylinders of (3.9 ± 0.2) mm thick, are prepared in smooth glass dishes (diameter 50 mm) and left to gel at room temperature, i.e. $T = (22 \pm 2)^{\circ}\text{C}$. Once the gel is formed, a disk of diameter $2R = 34$ mm is extracted by stamping the center of the gel plate with a circular punch tool, and removing the gel surrounding the tool. The glass dish with the gel are placed on a transparent base made of PMMA for the observation of the gel disk from below during the subsequent indentation run [Fig. 2.10(a)]. The indentation test is performed with a duralumin cylinder connected at one end to the stress-controlled rheometer, and presenting a circular flat surface on the other end (diameter 10 mm) [Fig. 2.10(b)]. The normal force sensor of the rheometer is used as a force gauge to determine the stress-strain $\sigma_N(\epsilon)$ relation during the sample indentation. In practice, the cylindrical indenter is positioned above the center region of the gel and lowered at a constant velocity $v = 100 \mu\text{m/s}$, down to a penetration depth corresponding to a compressive strain $\epsilon \approx 50\%$ with respect to the initial thickness e of the gel sample. A camera (Logitech HD C920) and a flat mirror placed at an angle of 45° with respect to the transparent PMMA plate are used to monitor the gel from below and record both the formation and the propagation of cracks that may occur at large enough

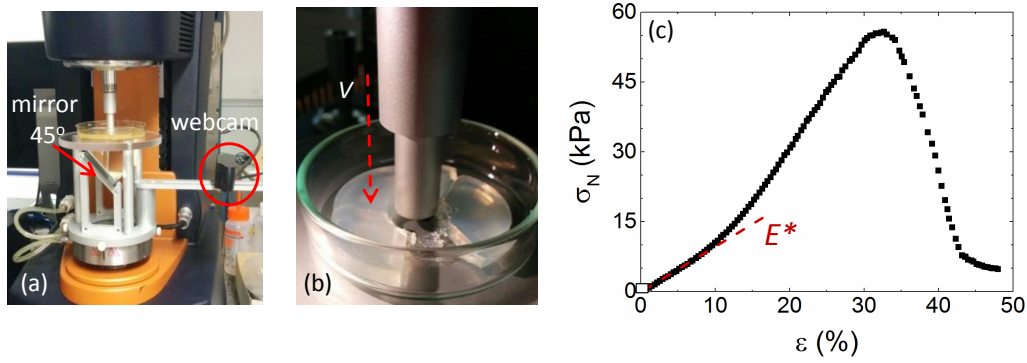


Figure 2.10: (a) Picture of the experimental set-up used for macro-indentation tests: the compressive deformation and the subsequent failure of the gel are monitored from below through a transparent PMMA bottom plate by means of a high resolution webcam, while the normal force sensor of the rheometer is used to record the stress-strain curve. (b) Disk of 1.5% wt. agar-SA gel in a smooth glass dish. The indentation run is conducted with a flat-ended cylinder (diameter 10 mm) at constant penetration speed $v = 100 \mu\text{m/s}$. (c) Normal stress σ_N vs. compressive strain ϵ during the indentation run of a 1.5% wt. agar-SA gel disk of thickness 3.9 mm and diameter 34 mm.

compressive strains.

Fig. 2.10(c) shows a typical indentation curve for a 1.5% wt. agar-SA gel. The stress increases linearly with the compressive strain up to a few percents, followed by a faster than linear increase associated with the strain hardening of the gel, up to a maximum value $\sigma_N^{(m)}$ at $\epsilon = \epsilon^{(m)}$. The linear low-strain regime provides a way to define an apparent elastic compression modulus $E^* = \partial\sigma/\partial\epsilon$ as the initial slope of the stress-strain curve. Taking into account the cylindrical shape of the indenter, the finite thickness e of the gel disk and the stress singularity at the sharp edge of the indenter, the Young's modulus E of the soft material obeys the following relation derived from previous analysis (Hayes, Keer, Herrmann, & Mockros, 1972; Haider & Holmes, 1997):

$$E = (1 - \nu^2) \frac{r}{e} \frac{\pi}{2\kappa} E^* \quad (2.2)$$

where ν is the Poisson coefficient of the gel, $r = 5 \text{ mm}$ the radius of the indenter, $e = 3.9 \text{ mm}$ the thickness of the gel disk and κ a numerical correction related to geometrical effects in relation with the variables r , e and ν . The only unknown is the Poisson coefficient ν that can be otherwise carefully determined through indentation runs performed on gel disks of different thicknesses. Figure 2.11(a) shows the apparent elastic modulus E^* as determined by the slope of the stress-strain experimental curves $\sigma(\epsilon)$ for compressive strains less than a few percents and for gel samples of thickness e ranging between 1 mm and 11 mm. The latter data $E^*(e)$ together with relation (2.2) are considered to compute the Young's modulus $E(e, \nu)$ for three different values ν of the Poisson coefficient, namely $\nu = 0.0$, 0.3 and 0.5 [see respectively Fig 2.11(b), (c) and (d)]. In each case, the $\kappa(r, e)$ value is determined using the integral expression proposed by (Haider & Holmes, 1997) for $\nu = 0$, and by (Hayes et al., 1972) for $\nu > 0$. Relying on the assumption that the Young's modulus E should neither depend on the gel thickness e , nor on the indentation speed, the value $\nu = 0.5$ can be ruled out [Fig. 2.11(d)]. Moreover, $E^*(e, \nu)$ data obtained with $\nu = 0.0$ also exhibit a significant dependence with the gel height e [Fig. 2.11(b)]. Finally, a Poisson coefficient $0.1 \leq \nu \leq 0.3$ provides a Young's modulus E independent of the gel thickness e as illustrated in Figure 2.11(c) for $\nu = 0.3$. Such a range of values for the Poisson coefficient leads to a correction factor $2.6 \leq \kappa \leq 3$

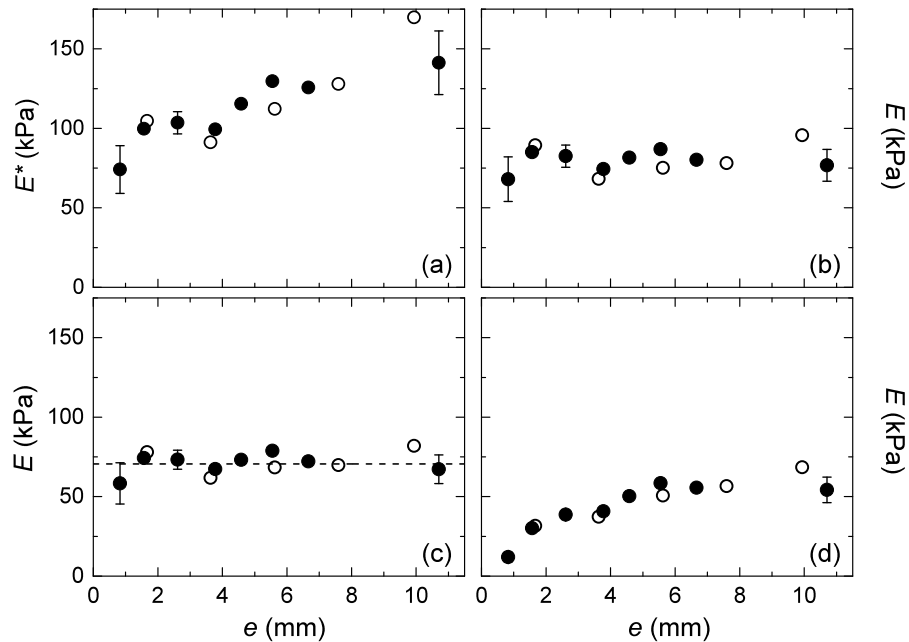


Figure 2.11: (a) Apparent compression elastic modulus $E^* = \partial\sigma/\partial\epsilon$ as determined during indentation experiments vs the gel thickness e . The two types of symbols are for experiments conducted at different indentation velocities: (\circ) $v = 50 \mu\text{m/s}$ and (\bullet) $v = 100 \mu\text{m/s}$. Each point corresponds to a gel prepared anew from a fresh agar sol incubated at $T = 80^\circ\text{C}$ for less than one day. (b)–(d) Young’s modulus E derived from the apparent compression elastic modulus E^* in (a) using the equation (2.2) with a Poisson coefficient $\nu = 0.0$ (b), $\nu = 0.3$ (c) and $\nu = 0.5$ (d). The black horizontal dashed line in (c) corresponds to the best linear fit of the data, leading to $E = (70 \pm 7)$ kPa.

using the integral relation provided by (Haider & Holmes, 1997), and therefore gives a Young’s modulus $E = (70 \pm 10)$ kPa for a 1.5% wt. agar-SA gel prepared from a fresh agar sol. Note that the latter value is in quantitative agreement with the elastic shear modulus $G' = (20 \pm 2)$ kPa measured through small amplitude oscillations since a compatible value $E(G') = (48 \pm 10)$ kPa within error bars can be derived from the relation $E(G') = 2G'(1 + \nu)$ (Landau & Lifshitz, 1970), showing that the agar disk behaves as an isotropic material during the indentation test.

2.4 Gel adhesion, friction and slip

During my PhD, two different methods were considered to quantify the adhesion between an agar gel and a solid surface, and to measure the shear stress necessary for the gel detachment from a solid substrate. The first method consists in imposing a strain sweep to a gel previously formed between two parallel plates. Beyond a critical strain, the gel detaches from the plates, which defines a critical shear stress for the gel debonding. The second method and the more original one, is based on a modified spin-coater that uses the centrifugal force to induce the detachment of several agar gel pellets adhering to a flat surface that is put into rotation.

2.4.1 Strain sweep and gel debonding

Concerning the first method, an agar gel is prepared in situ in a parallel-plate geometry connected to the stress controlled rheometer, using the zero normal force protocol (see

Section 2.3.1). Once the gel storage modulus G' and the gel thickness e show stationary values representative of a complete gelation, the rheometer is then switched from controlled normal force to constant gap width, maintaining the latest value e of the gap width. An oscillatory strain sweep test of frequency $f = 1$ Hz and strain amplitude logarithmically varying from $\gamma = 0.01\%$ up to 100% over a total duration of 2160 s is then applied to the gel sample.

An example of the agar gel response to an oscillatory strain sweep is pictured in Figure 2.12(a). In the low strain amplitude regime, the storage modulus G' remains constant, while the shear stress σ increases with time. As the shear strain amplitude reaches a critical value γ_c , corresponding to a critical stress σ_c , both the shear stress and the storage modulus drop abruptly. The values γ_c and σ_c respectively are defined as the critical shear strain amplitude and the critical shear stress above which the gel debonds from the plates of the shear cell. Indeed, the abrupt drop in shear stress likely results from the interfacial debonding of the gel from the plates, together with the release of water since no macroscopic fracture is visible when raising the upper plate after the end of the test. Water droplets are further visible on top of the agar gel, once the upper plate is slowly moved upward [Fig. 2.12(b)].

The impact of the gel preparation in the rheometer on the adhesion properties between the mature gel and the plates was also investigated. For this purpose, a series of gelation experiments was performed using the zero normal force protocol, while applying an oscillating shear strain of constant amplitude to monitor the gelation. Three different shear strain amplitudes $\gamma = 1\%$, 0.1% and 0.01% were considered. The results displayed in Figure 2.13 show quantitatively the same terminal values of the elastic shear modulus [$G'_f \simeq 22$ kPa in Fig. 2.13(d)–(f)] and a similar gel contraction [$\Delta e/e \simeq 1\%$ in Fig. 2.13(a)–(c)]. Therefore, an applied shear strain of amplitude lower than 1% has no significant influence upon the terminal viscoelastic properties and the gel microstructure when the agar gelation is monitored with the zero normal force protocol.

Yet, the shear strain amplitude applied during the gelation process may damage the adhesive contact between the agar gel and the plates. Indeed, an oscillatory strain sweep

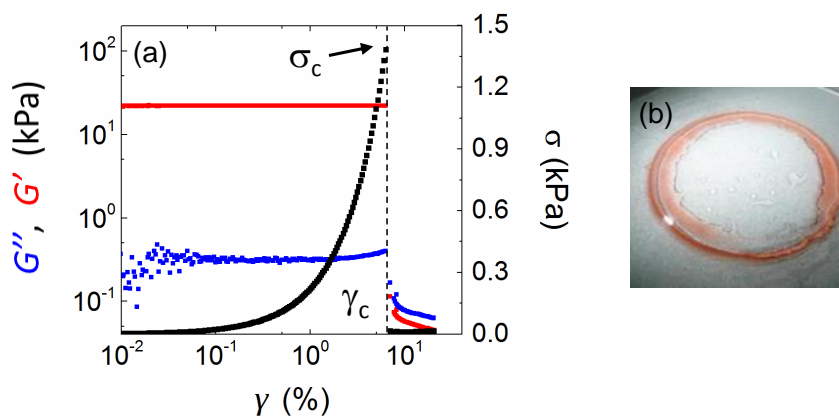


Figure 2.12: (a) Storage and loss moduli (resp. G' and G'' , primary vertical axis) together with the shear stress amplitude σ (secondary vertical axis) vs. shear strain amplitude γ during an oscillatory strain sweep test of frequency $f = 1$ Hz. The strain amplitude is increased logarithmically from $\gamma = 0.01\%$ to 100% over a duration of 2160 s (i.e. 9 s/point). (b) Picture of a 1.5% wt. agar-BM1 gel at the end of the oscillatory strain sweep experiment, after raising the upper plate. Water droplets can be clearly observed on the gel surface.

experiment was applied after the agar gelation, by increasing logarithmically the shear strain amplitude from $\gamma = 0.01\%$ up to 100% , so as to determine the critical shear strain γ_c beyond which the gel debonds. The agar gels prepared with different initial protocols show marked differences when submitted to larger shear strain amplitudes [Fig.2.13(g)–(i)]. In other words, the critical shear strain γ_c above which the storage modulus G' abruptly decreases is very sensitive to the shear strain amplitude applied during the gelation process. Agar gels, which formation was monitored with a low shear strain amplitude $\gamma = 0.01\%$, can resist and maintain contact with the plates up to a larger value of the critical shear strain γ_c . Such a result indicates that shear strain amplitudes as low as 0.01% during the gelation are indeed required to guarantee an optimal adhesion between the gel and the plates. Moreover, the evolution of the gel viscoelastic moduli when the interfacial failure occurs strongly depends on the strain amplitude γ applied during the gel formation. An agar gel prepared under a low strain amplitude $\gamma = 0.01\%$ shows a brutal drop in the storage modulus G' during the strain sweep run [Fig. 2.13(i)], which hints at an abrupt

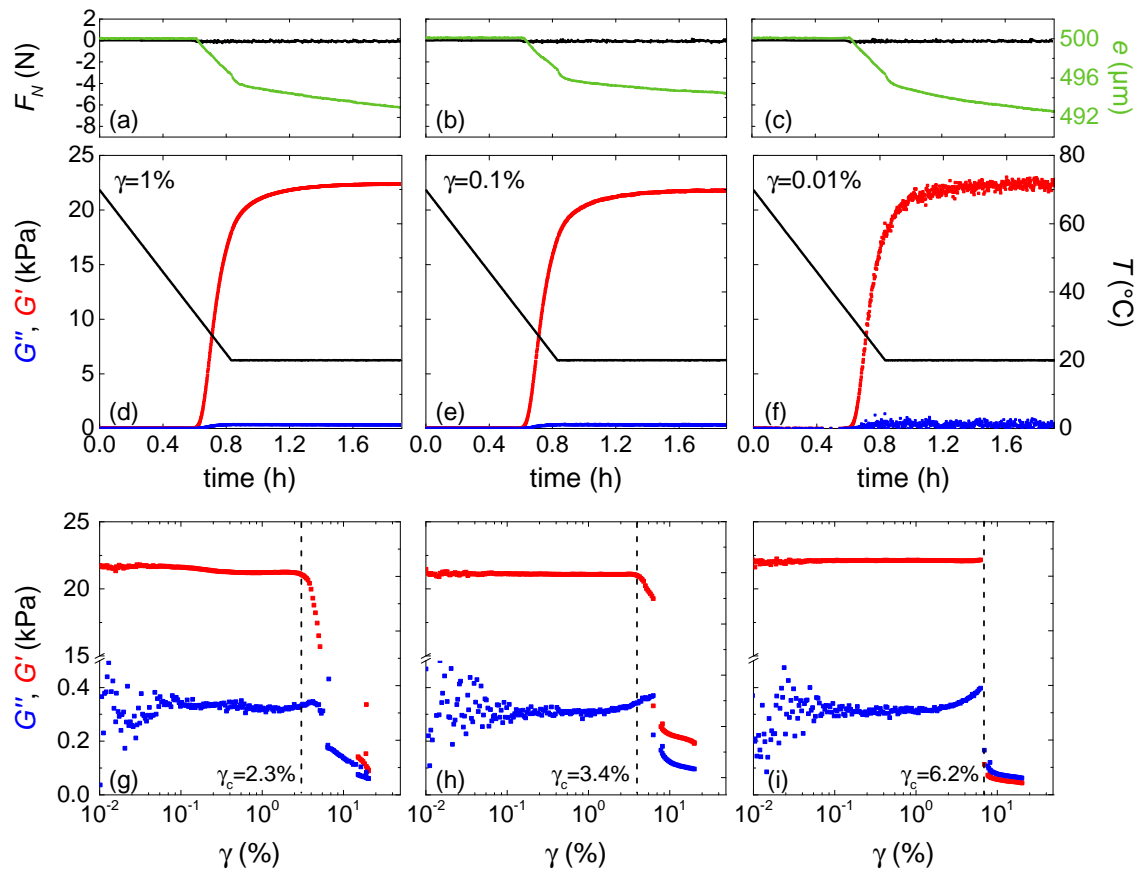


Figure 2.13: Temporal evolution of the normal force F_N and the gap width e (a)–(c) together with the storage and loss moduli (d)–(f) during the gelation of a 1.5% wt. agar-BMI solution when decreasing the temperature from $T = 70^\circ\text{C}$ to 20°C at a cooling rate $\dot{T} = 1^\circ\text{C}/\text{min}$ while using the zero normal force protocol and applying different constant shear strain amplitudes: $\gamma = 1\%$ (first column), $\gamma = 0.1\%$ (second column) and $\gamma = 0.01\%$ (third column). The terminal values of the gel storage modulus of 22.3 kPa, 21.8 kPa and 22.3 kPa respectively are compatible within error bars. (g)–(i) Oscillatory strain sweeps experiments performed on the three gels obtained in (d), (e) and (f), two hours after the agar gel gelation. The vertical dashed line indicates the critical shear strain γ_c above which the storage modulus G' decreases. For all the experiments the oscillatory frequency is 1Hz.

detachment of the gel from the plates. On the contrary, agar gels which formation has been monitored under larger strain amplitudes ($\gamma = 0.1\%$ and 1%) display a much smoother decrease in the storage modulus G' above the critical shear strain γ_c [Fig. 2.13(g) and (h)] that likely indicates a more progressive gel debonding associated with a somewhat initially damaged adhesive contact between the gel and the plates.

2.4.2 Centrifugal stress and gel debonding

The second method used to quantify the adhesion between a gel and a solid surface is based on a modified spin coater (spin 150, SDS-Europe) pictured in Figure 2.14(a). Agar gel pellets are placed on the bottom flat wall of a large horizontal circular dish (internal radius $R = 68$ mm) centered on the spinner axis. A gradual increase of the spinner rotation speed results in a centrifugal stress acting on the agar gel pellets varying from a few Pa up to several kPa. The bottom plate can be changed easily, which allows to explore a wide variety of solid substrates [Fig. 2.14(b)–(d)]. Moreover, the centrifugal force acts as a uniform bulk force on the gel volume, hence providing better-controlled stress conditions at the gel/substrate interface, in comparison with the complex stress field generated during a peel test or a probe-tack test. The first section concerns a validation of the centrifuge method through benchmark measurements of static friction coefficients between solid surfaces. The second section is dedicated to a recipe for preparing the agar gel pellets in a reproducible fashion for the centrifuge experiments.

Method validation - static friction between two solid surfaces

Benchmark experiments were performed with solid cylinders placed on solid surfaces so as to measure the static friction coefficient and validate the centrifuge method. Cylinders made of steel, duralumin and plastic (polyvinyl chloride or PVC) of diameter $d=20$ mm and thicknesses $e=2, 4, 8,$ and 16 mm were milled by the mechanics of the laboratory. Moreover, a homemade template illustrated in Figure 2.15(a) and (b), with the drawings of circular cross sections regularly spaced along the circumference of a circle coaxial with the dish axis, ensures a precise placement of 4 to 8 cylinders at a distance $r=40$ mm from the dish center. The spinner further allows a linear increase of the dish rotation speed $\omega(t)$ (in rpm) with a minimum increase rate $d\omega/dt=3.33$ rpm/s [Fig. 2.15(c), light gray

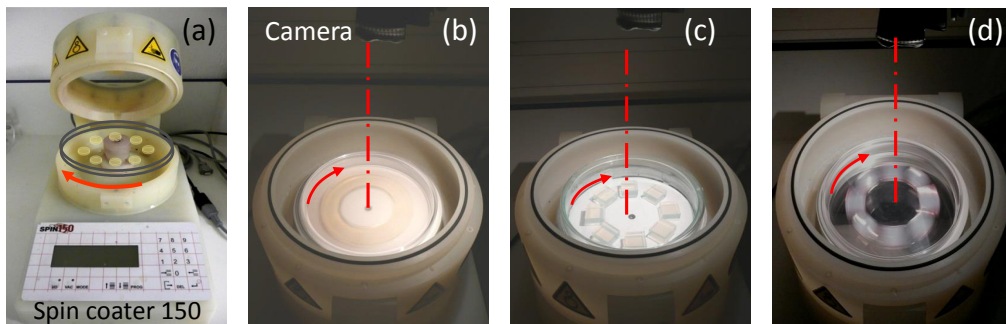


Figure 2.14: (a) Experimental set-up using a modified spin coater 150 (SPS-Europe) as a centrifuge to quantify the adhesion between a gel and a solid surface. Agar pellets cured in a smooth plastic dish (b), a smooth glass dish (c), or a dish with a polished duralumin bottom surface (d). The increase in the centrifugal force acting upon the gel pellets when increasing progressively the rotation speed of the spinner leads to an interfacial debonding of the agar gel pellets from the bottom solid wall.

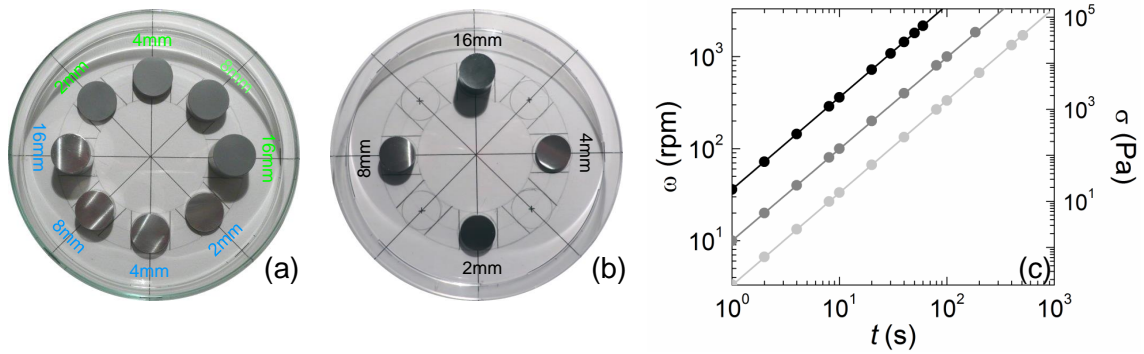


Figure 2.15: (a) Duralumin (blue color) and plastic (PVC, green color) cylinders placed at a distance $r = 40$ mm from the center of a smooth glass dish. (b) Steel cylinders placed at a distance $r = 40$ mm from the center of a smooth plastic dish made of PS. Cylinders with variable thicknesses $e = 2, 4, 8$ or 16 mm. (c) Time evolution of both the rotation speed $\omega(t)$ of the dish (primary vertical axis) and the shear stress $\sigma(t)$ (secondary vertical axis) acting on a steel cylinder ($d=20$ mm, $e=4$ mm, $\rho=7.8$ g/cm³) located at a distance $r=40$ mm from the dish center for different rates of increase of the rotation speed $d\omega/dt=3.33$ rpm/s (light gray), 10 rpm/s (gray) or 36 rpm/s (black) during the centrifuge experiment.

line] and a maximum increase rate $d\omega/dt=36$ rpm/s [Fig. 2.15(c), black line]. A cylinder located at a distance r from the dish axis experiences a centrifugal acceleration $\omega^2 r$ even for a non-uniform rotation motion. During a centrifuge experiment, the shear stress σ acting on a cylinder of mass m and thickness e in frictional contact with the bottom wall of the dish can be derived from the relation:

$$\sigma = \frac{m\omega^2 r}{A} = e\rho\omega^2 r \quad (2.3)$$

where A is the contact area of the cylinder with the bottom solid surface, and ρ denotes the density of the cylinder, which was measured with a pycnometer. The density of plastic (PVC), duralumin and steel cylinders were determined to be respectively $\rho=1.33, 2.8$ and 7.8 g/cm³. The shear stress σ acting on a steel cylinder therefore increases from a few Pa up to several kPa in a characteristic time ranging from a few seconds to about 5 minutes, depending on the rate of increase of the rotation speed $d\omega/dt$ [Fig. 2.15(c)].

A centrifuge experiment goes as follows: cylinders are placed on a glass or plastic dish with either smooth or rough bottom surfaces previously rinsed with ethanol. The dish is then carefully placed in the modified spin coater and the acceleration centrifuge experiment is started without any delay. A camera (Logitech HD C920) is placed above the spin coater [Fig. 2.14(b)] to record the motion and the debonding of the cylinders with an acquisition rate of 2 frames/s for $d\omega/dt=3.33$ rpm/s and 30 frames/s for $d\omega/dt=36$ rpm/s.

Results obtained with steel cylinders of different thicknesses are reported in Figure 2.16. Despite the different weights mg varying between 7 mN and 38 mN, the four steel cylinders debond at a critical rotation speed $\omega_c \approx 101$ rpm almost simultaneously [Figure 2.16(b) and (c)]. Moreover, the critical shear stress $\sigma_c = e\rho\omega_c^2 r$, characteristic of the cylinder debonding, increases linearly with the normal load $P = mg/A$ for both a smooth and a rough bottom plate [Fig. 2.16(d)]. Therefore, the static friction $\mu_s \equiv \sigma_c/P$ is constant and independent of the normal load in agreement with the first Amontons-Coulomb's law, predicting a static friction coefficient μ_s only dependent on the properties of the surfaces in contact (Bowden & Tabor, 1950; Gong, Iwasaki, & Osada, 1999). Furthermore, the static friction coefficient of steel cylinders is larger on rough surfaces ($\mu_s = 0.49 \pm 0.03$) than on smooth surfaces ($\mu_s = 0.36 \pm 0.05$), which likely results from

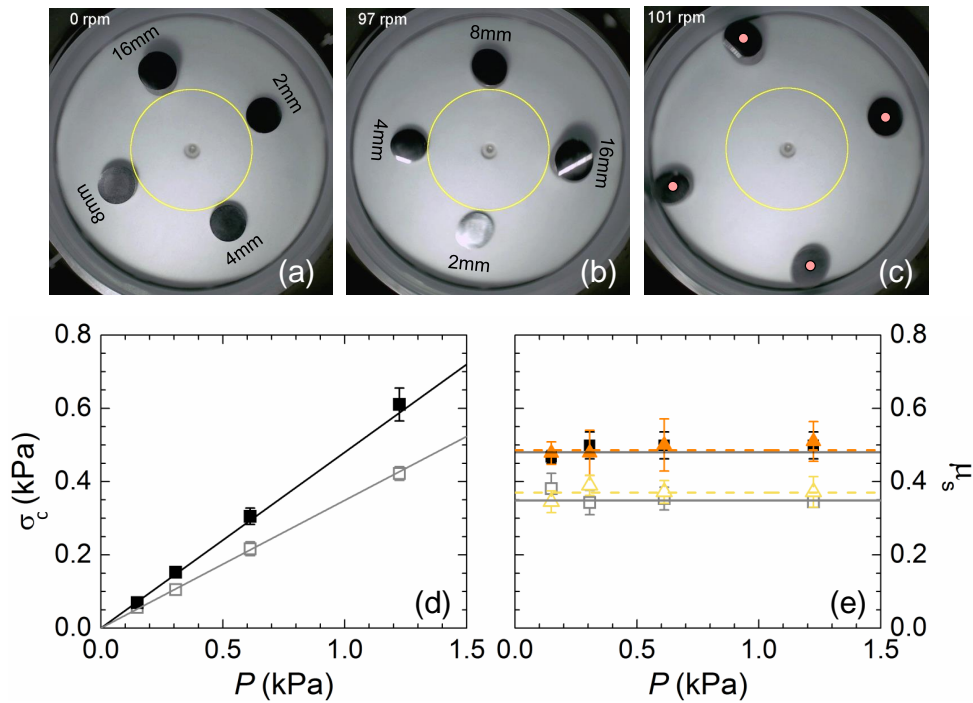


Figure 2.16: Centrifuge experiment ($d\omega/dt=3.33$ rpm/s) for steel cylinders of different thicknesses $e=2, 4, 8$ and 16 mm in frictional contact with a rough glass surface. Images (a), (b) and (c) are taken at different time of the experiment: (a) before centrifuge run, (b) at $\omega \approx 97$ rpm, and (c) at $\omega = \omega_c \approx 101$ rpm. The simultaneous detachment of the cylinders (marked with red points) is observed. The yellow circle of radius 30 mm, tangent to the inner position of each cylinder before detachment, serves as a guide to the eye. (d) Critical shear stress σ_c as a function of the normal pressure $P = mg/A$ for steel cylinders with different thicknesses on a smooth glass surface (open symbols) or a rough glass surface (filled symbols). (e) Average static friction coefficient μ_s versus the normal load P for steel cylinders in contact with smooth (open symbols) or rough surfaces (filled symbols) made of glass (gray or black colors) or plastic PS (yellow or orange colors). Error bars correspond to the average standard deviation associated with three independent measurements.

obstruction and interlocking effects associated with surface roughness.

Another series of centrifuge experiments performed with cylinders made of lighter materials such as plastic (PVC, $\rho=1.33$ g/cm³) and duralumin ($\rho=2.8$ g/cm³) show a more complex friction behavior. The detachment of the cylinders no more occurs simultaneously, but takes place over a somewhat more extended range of rotation speed [Fig. 2.17(b)–(d)]. The static friction coefficient further displays larger values in the limit of low normal loads ($P < 0.1$ kPa) for thin and light cylinders. In this regime, the adhesion effects may become dominant and the contact areas are no longer plastically deformed, which result in a higher static friction and a deviation from Amontons-Coulomb's law. When increasing the normal load, such as $P > 0.2$ kPa, the static friction coefficient is no more sensitive to the normal load and the Amontons-Coulomb's law is recovered. These experiments demonstrate both the validity and the power of the centrifuge method to measure the static friction properties of solid materials in contact, and study the debonding of agar gels weakly adhering onto solid substrates.

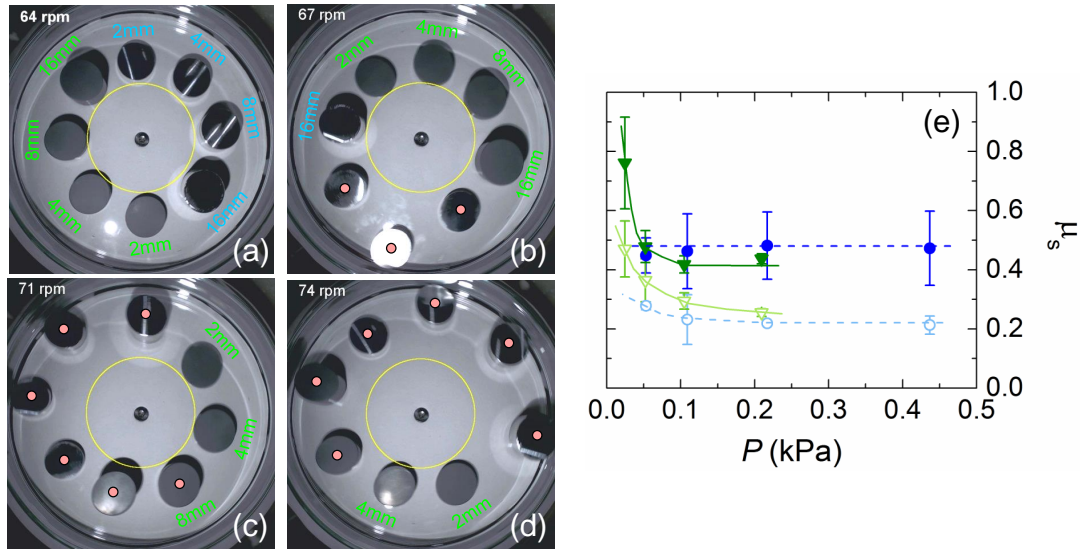


Figure 2.17: (a)-(d) Centrifuge experiments ($d\omega/dt=3.33$ rpm/s) for PVC (green color) and duralumin (blue color) cylinders with different thickness $e=2, 4, 8$ or 16 mm in contact with a rough glass surface at different rotation speed $\omega \approx 64$ rpm (a), 67 rpm (b), 71 rpm (c), 74 rpm (d). The cylinders (marked with red points) detach progressively over a rotation speed range 60 rpm $< \omega < 70$ rpm for duralumin cylinders, and 70 rpm $< \omega < 110$ rpm for PVC cylinders. The yellow circle of radius 30 mm, tangent to the inner position of each cylinder before detachment, serves as a guide to the eye. (e) Average static friction coefficient μ_s versus the normal pressure P for duralumin (blue) and PVC (green) cylinders in contact with smooth (open symbols) or rough (filled symbols) glass surfaces. Error bars correspond to average standard deviation associated with three independent measurements.

“Mikado” preparation and agar gel debonding

The manipulation of agar gels is much more delicate than solid cylinders, and therefore requires experimental precautions that are discussed in the present section. Agar gels plates are firstly prepared by pouring a hot solution of polysaccharides in dishes (diameter 136 mm) with specific smooth or rough bottom surfaces and left to gel at room temperature $T = (22 \pm 2)^\circ\text{C}$. After the gelation, gel plates are covered with a lid to prevent water evaporation and are cured during 1 hour before the preparation of gel pellets. The curing time of the agar gel cast in a dish may influence the adhesive contact and will be further discussed in Section 4.3.1, in Chapter 4. In the present work, the curing period of 1 hour is considered by default to quantify the “first debonding” of agar gels. The “first debonding” refers to the loss of the adhesive contact between the agar gel pellet cast in the dish and the bottom solid surface. Once the first centrifuge run is completed, one may replace the agar pellets at the same initial position, wait for a given time at ambient temperature covering the dish with a lid to suppress water evaporation, before starting a new centrifuge run. The gel detachment that occurs during a second centrifuge run is referred to as the “second debonding”.

As a first attempt, 8 pellets of 1.5% wt. agar-BM1 gels are obtained either by stamping the gel plate with a circular punch tool (inner diameter $d \approx 20$ mm) or by using a cutter blade [Fig. 2.18(a)] before carefully removing the gel around the pellets. The centrifuge experiment shows that the circular pellets stamped with the circular punch tool detach at lower rotation speeds ($\omega_c = 70$ - 110 rpm), than the square pellets cut by using a cutter blade ($\omega_c \approx 260$ rpm) [Fig. 2.18(b)]. The reason is most likely that the punch tool exerts

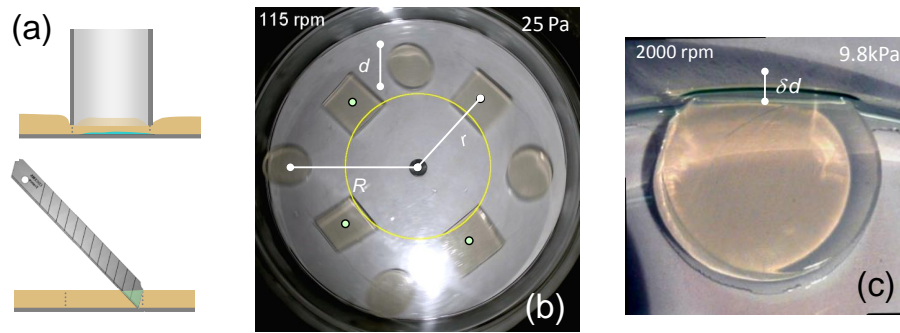


Figure 2.18: (a) Schematic representation of the preparation of agar pellets either by stamping the gel plate with a circular punch tool or by cutting the gel with a cutter blade. (b) Centrifuge run of 1.5% wt. agar-BM1 gel pellets of size $d = 20$ mm and thickness $e = 4$ mm, in frictional contact with a smooth plastic dish made of PS (rotation speed $\omega=115$ rpm). Note the premature detachment of stamped circular agar pellets over a rotation speed range $70 \text{ rpm} < \omega < 110 \text{ rpm}$ while square pellets cut with a cutter blade debond later (the green points symbolize no debonding of agar pellets). (c) Centrifuge deformation δd of a circular agar gel pellet (1.5% wt. agar-BM1) of diameter $d = 20$ mm in contact with the lateral circular wall of the dish at $\omega=2000$ rpm (compressive stress $\sigma \approx 9.8$ kPa and compressive strain $\delta d/d \approx 0.25$).

a normal pressure generating a compressive deformation of the soft material that is large enough to partially debond the gel from the bottom surface of the dish and thus weaken the adhesive contact between the gel and the solid substrate.⁴

A less invasive method for the preparation of the gel pellets was therefore developed and referred to as the “*Mikado*” protocol which goal is to avoid the gel deformation and any premature partial debonding of the agar gel pellets during the cutting phase. The so called “*Mikado*” protocol consists in using a homemade template and cutting precisely the gel plate with a cutter blade along both radial and orthoradial lines drawn on the template (Fig. 2.19). A careful removal of the peripheral parts of the gel followed by the removal of the central semi-circular half portions successfully prevents the premature detachment of the square agar gel pellets.

To quantify the adhesion between square agar gels and the bottom surface of the dish, centrifuge experiments are performed on 1.5% wt. agar-BM1 gel pellets prepared with the “*Mikado*” protocol. The centrifuge experiments are performed in a dish with a smooth bottom surface that is either made of glass or plastic (PS). Typical results are reported in Figure 2.20. The agar pellets debond gradually for gels in contact with either glass or plastic smooth surfaces. The gel first debonding occurs at centrifugal stresses σ varying between 65 Pa and 90 Pa for gel pellets in a smooth glass dish [Fig. 2.20(b)–(d)], whereas the adhesive contact between gels and the smooth plastic dish is stronger since

⁴Note that after the gel debonding, all the pellets are found in contact with the lateral wall. No residues are observed in the dish, which confirms a purely interfacial debonding scenario, as expected for a nearly elastic soft material in contact with a solid surface. Interestingly, the debonded circular agar gel pellets in contact with the lateral wall of the dish may undergo very large deformations $\delta d/d \approx 0.05 - 0.3$ without any apparent damage despite the high rotation speed of the spin coater and a centrifugal stress $\sigma = e\rho g\omega^2 R$ of several kPa acting on the gel ($R \approx 58$ mm is the distance from the center of the gel pellet in contact with the sidewall to the dish axis) [Fig. 2.18(b)]. In spite of the large centrifuge deformations of the soft material, one may also note that the peripheral region of gel pellets not in contact with the lateral wall of the dish, is almost undeformed and shows a circular shape [Fig. 2.18(c)]. Such localized deformations results from the squeezing out of water from the gel pellets and highlight the compressible and sponge-like behavior of agar gels that may lose a large amount of water by drainage through the hydrated network when the applied centrifugal volume force is high enough.

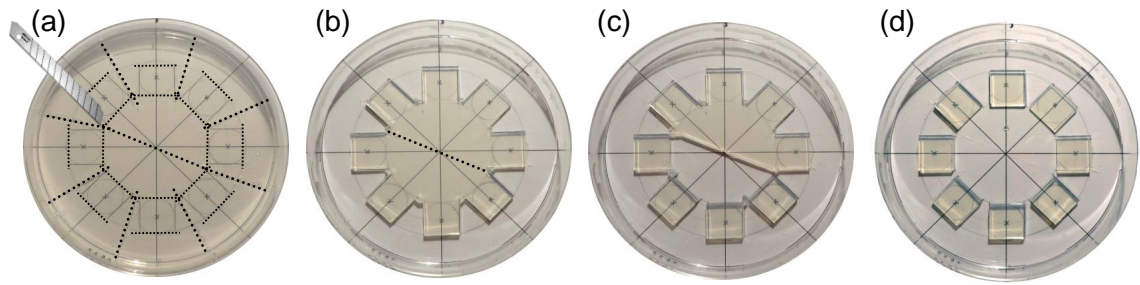


Figure 2.19: “Mikado” protocol for the preparation of square agar gel pellets by cutting a gel plate cured in a dish with a cutter blade along precise lines drawn on a template. (a)-(b) Careful removal of the peripheral parts of the gel plate followed in a second step by (c) the removal of the semi-circular half portions to obtain (d) square agar gel pellets still bound to the bottom surface of the dish.

the gel debonding requires larger shear stresses, ranging between 300 Pa and 800 Pa. From the cumulative probability $\Psi(\sigma_c)$ for gel pellet detachment in the spinning dish, one may derive the average critical shear stress $\overline{\sigma}_c$ for the agar gel first debonding [Fig. 2.20(e)]. By repeating independent centrifuge runs over more than three different dishes (24 agar gel pellets or more), the critical shear stresses reported in Figure 2.20(e) give an ensemble averaged critical shear stress [$\langle\overline{\sigma}_c\rangle=(0.08 \pm 0.01)$ kPa or (0.53 ± 0.17) kPa for the first debonding of 1.5% wt. agar-BM1 gel pellets cast in smooth glass or smooth plastic dishes, respectively, Fig. 2.20(f)]. The complete study of the shear debonding of agar gels from various types of solid surfaces is discussed in Chapter 4.

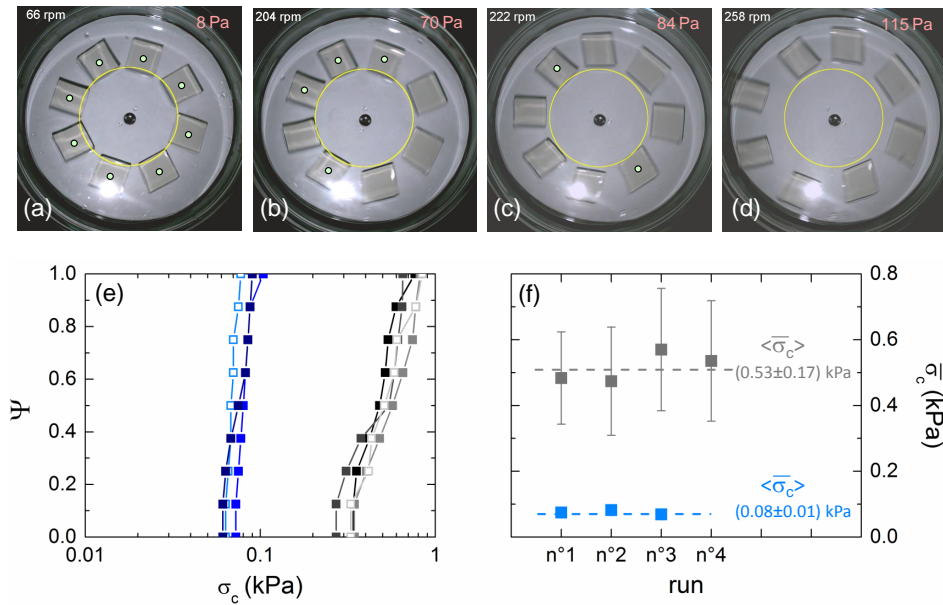


Figure 2.20: (a)–(d) Centrifuge experiment of 1.5% wt. agar-BM1 square pellets of size $d=20$ mm and thickness $e=4$ mm in frictional contact with a smooth glass surface. Views of the square agar pellets for increasing rotation speed ω and centrifugal shear stresses (a) $\sigma=8$ Pa, (b) 70 Pa, (c) 84 Pa and (d) 115 Pa. (e) Cumulative probability Ψ of the critical shear stress σ_c for the first shear debonding of 1.5% wt. agar-BM1 pellets from a smooth glass surface (blue symbols) or a smooth plastic surface (gray symbols). (f) Average critical shear stress $\overline{\sigma}_c$ derived from several independent centrifuge runs giving an ensemble averaged critical shear stress $\langle\overline{\sigma}_c\rangle=(0.08 \pm 0.01)$ kPa or $\langle\overline{\sigma}_c\rangle=(0.53 \pm 0.17)$ kPa for the first debonding of 1.5% wt. agar-BM1 gel pellets in smooth glass or smooth plastic (PS) dishes, respectively.

2.5 Gel drying

Mainly composed of water, agar gels are very sensitive to solvent-loss and drying. Two complementary techniques were used to quantify the drying of agar gels: (i) interferometry, which serves as a tool to measure the *local* thinning rate of agar gels with high accuracy, and (ii) an optical flow method based on a spatio-temporal analysis of the 2D displacement field of seed particles on the upper free surface of the gel.

2.5.1 Interferometric observations

Michelson interferometer

Interferometry is an optical technique that is commonly used for examining surface topography and for astronomy applications. Over decades, interferometric methods have been adapted to work in many wavelength ranges and various application fields such as length measurement, high-resolution spectroscopy, optical-component testing, etc. (Siesler, Ozaki, Kawata, & Heise, 2002). In the present work, a classic Michelson interferometer operated in reflection mode was used to measure the local thinning rate of gels during drying.

An agar gel cast in a plastic or glass dish is left to dry at constant temperature, $T = (25.0 \pm 0.5)^\circ\text{C}$ unless otherwise specified. The height variations of the gel during drying are monitored by means of a Michelson interferometer operated in reflection mode. The principle of a Michelson Interferometer, pictured in Figure 2.21, is to split a partially coherent incident beam (red laser diode M625L3 from Thorlabs with a wavelength $\lambda = 625\text{ nm}$ and a coherence length of about $50\ \mu\text{m}$) into two beams: a reference beam reflected by a PZT mirror and a second beam reflected by the surface of the gel. A collimating optics produces a parallel beam splitted with a semi-transparent cube. A flat field planachromat objective without immersion (Zeiss LD Epiplan 50 \times with an extra-long working distance of about 9.1 mm and a numerical aperture of 0.5) forms the image of the upper free surface of the gel in the focal plane of the camera. A second identical objective focuses the reference wave on the mirror. The mirror of the reference arm is mounted on a piezoelectric tube (Unidex 11, Aerotech) that allows to adjust the optical phase difference between the reference and the signal arms with a nanometric accuracy so that the two waves interfere

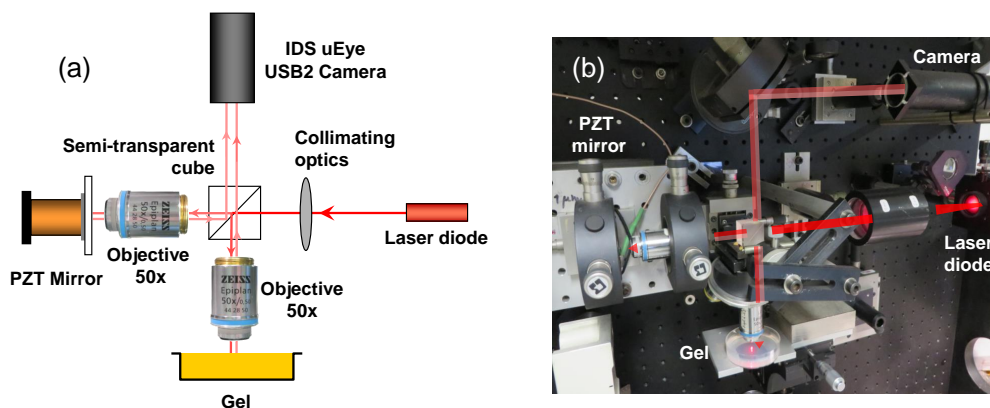


Figure 2.21: (a) Sketch of the experimental setup that consists in a Michelson Interferometer operated in reflection mode. (b) View of the corresponding experimental setup. The scale is set by the diameter of the dish of 50 mm. The experimental setup is placed in a large box that can be closed with thick curtains to limit air convection that may artificially increase the gel thinning rate.

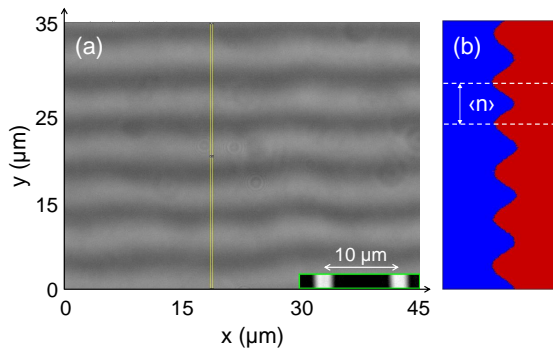


Figure 2.22: (a) Typical instantaneous interference pattern overlaid on the image of the smooth gel surface (800 pixels \times 600 pixels). Inset: image of a $10\mu\text{m}$ grid from a Leitz standard stage micrometer. (b) Spatial projection on the x -axis and along the y -axis of the gray levels of all the pixels in the thin yellow vertical rectangle selection pictured in (a). The white dashed lines highlight the distance $\langle n \rangle$ between two successive dark fringes. Experiment conducted on a 1.5% wt. agar-BM1 gel cast in a smooth plastic dish made of PS.

at the level of the sensitive surface of the camera (USB2 monochrome IDS uEye camera, UI124 \times SE-M) and produce a set of almost parallel and contrasted interference fringes overlaid on the image of the smooth gel surface. A typical image recorded at the gel surface is pictured in Figure 2.22(a).

Analysis of image sequences

The following protocol was developed to analyze the image sequence of the interference pattern [Fig. 2.22(a)] and access the average thinning rate of the gel. The mirror orientation is first adjusted so that the interference fringes are horizontal (or vertical) with about 5 to 7 fringes within the field of view ($45\mu\text{m} \times 35\mu\text{m}$). A stack of 2400 8-bit images is then recorded during ten minutes at a frequency $f = 4$ frames per second. The contrast of interference fringes remains almost unaltered during a waiting period of ten to twenty minutes since the gel thins by about $10\mu\text{m}$ to $20\mu\text{m}$, which is much less than the coherence length of the source (of about $50\mu\text{m}$). The average number $\langle n \rangle$ of pixels between two fringes, which corresponds to a half wavelength in terms of height differences that give rise to interferences, is determined through a spatial projection of the gray level of all the pixels in the thin rectangle region of interest (ROI) pictured in yellow in Figure 2.22(b).

Gel thinning leads to a phase difference between the reference and the signal waves, which results in a displacement of interference fringes in the perpendicular direction. A homemade software was developed to analyze the 8-bit image sequence and derive the average thinning rate $\langle \dot{z}(r_0, t) \rangle$ of the gel over 10 minutes (or shorter duration if need be), where r_0 denotes the distance between the center of the gel and the position where the beams impacts the gel, and t labels the time since the start of the drying experiment. The homemade software also determines the standard deviation $\delta \dot{z}(r_0, t)$ of the thinning rate representative of both temporal fluctuations in the drying dynamics and any lateral sliding motion of the gel on the bottom wall of the dish. The analysis is performed using a spatio-temporal filtering method based on the idea that detecting motion is equivalent to extracting an orientation inside a correlation image (see next Section 2.5.2). The temporal projection of the gray levels of all the pixels within the thin yellow vertical ROI pictured in Figure 2.22(a) and oriented in the exact direction of the fringe displacement produces a 8-bit spatio-temporal diagram $T(y, t)$ featuring a pattern of oblique lines [Fig. 2.23(a)]. The average tilt angle Ψ of the oblique lines with respect to the time axis is directly related to the average thinning rate of the gel at the position r_0 through the relation:

$$\langle \dot{z}(r_0, t) \rangle = \frac{\lambda}{2\langle n \rangle} f \tan(\Psi) \quad (2.4)$$

To determine the tilt angle Ψ and deduce the average thinning rate, the centered auto-correlation image $\mathcal{A}[T(y, t)]$ of the spatio-temporal diagram $T(y, t)$ is computed using a

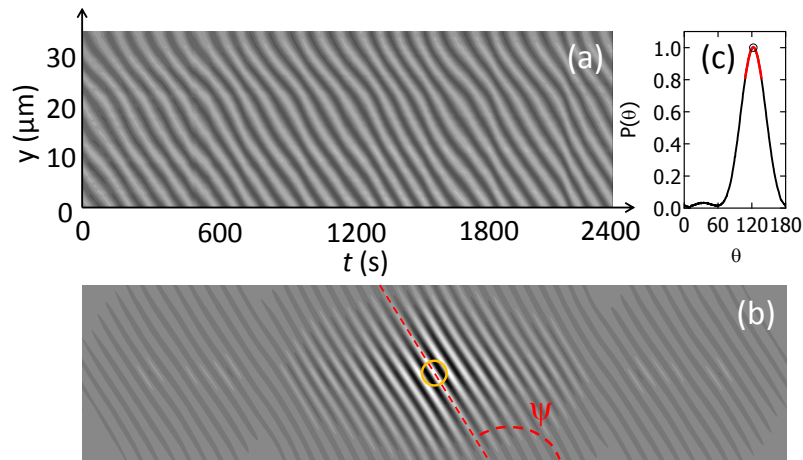


Figure 2.23: (a) 8-bit spatio-temporal diagram $T(y, t)$ that results from the temporal projection over 20 min of the gray levels of all the pixels within the thin yellow rectangle pictured in Figure 2.22(a) and oriented in the direction of the fringe displacement. (b) 16-bit centered auto-correlation image $\mathcal{A}[T(y, t)]$ of the spatio-temporal diagram $T(y, t)$ pictured in (a). (c) Angular distribution $P(\theta)$ of the 16-bit gray levels obtained from a radial integration of $\mathcal{A}[T(y, t)]$ inside a circular ROI of 50 pixels radius that is centered on the origin of the autocorrelation image [yellow circle pictured in (b)]. The fit of the angular distribution $P(\theta)$ by a Lorentzian function over an angular sector of 30° around the maximum [red curve in (c)] allows to determine the tilt angle $\Psi = 121.1^\circ$ of the ridge line [red dashed line in (b)], and to compute the gel thinning rate $v = 15.7$ nm/s averaged over 20 min. Experiment conducted at the center of a 1.5% wt. agar-BM1 gel cast in a smooth plastic dish made of PS.

Discrete Fast Hartley Transform (see next Section 2.5.2 for technical details). The 16-bit autocorrelation image shows a sharp line (or ridge line) with the same average orientation Ψ as the oblique lines in the spatio-temporal diagram $T(y, t)$ [Fig. 2.23(b)]. A radial integration of $\mathcal{A}[T(y, t)]$ inside a circular ROI centered on the origin of the autocorrelation image [yellow circle of radius $p = 50$ pixels in Fig. 2.23(b)] provides the angular distribution $P(\theta)$ of 16-bit gray levels, which is well fitted by a Lorentzian function [Fig. 2.23(c)] and gives the tilt angle Ψ of the ridge line [red dashed line in Fig. 2.23(b)]. I shall emphasize that unlike traditional PIV methods, which cross correlate two consecutive interrogation regions, the spatio-temporal analysis of a continuous space-time window provides a higher accuracy to determine the thinning rate of the gel. Finally, note that the interferometer and the gel plate are placed in a large box closed by thick curtains for the whole duration of each experiment to limit as much as possible air convection, which otherwise would affect the drying process.

2.5.2 Spatio-temporal tracking

Homemade plugins based on an optical flow method were developed to analyze the motion of seed particles on the upper free surface of an agar gel, and thus quantify the motion of the gel during drying. I will first introduce the general principle of the optical flow method that has been developed for the characterization of particle motion and fluctuations in a granular flow (Snabre, Blaj, & Pouligny, 2013, 2014).

Classical flow visualization is based on the direct observation of the 2D motion of tracer particles (Adrian, 1991; Raffel, Willert, Wereley, & Kompenhans, 2000). Digital Particle Image Velocimetry (DPIV) methods, based on the cross correlation of two distant images, give the average motion of small groups of particles contained within small regions known as interrogation regions (Prasad, 2000). However, the cross correlation of only two

images gives rise to uncertainties and false vectors may arise from the noise in the recorded images (noise error), from particle velocity gradients (gradient errors) or from random particle displacements (acceleration error) (Huang, Fiedler, & Wang, 1993; McKenna & McGillis, 2002).

Optical flow methods offer an alternative for analyzing an image sequence with a largely improved accuracy and a reduced number of false displacement vectors (Horn & Schunck, 1981; Alvarez, Weickert, & Sanchez, 1981). Optical-flow approaches consist in extracting a dense velocity field from the observed motion of photometric patterns in an image sequence. Unlike usual DPIV methods, which cross correlate two consecutive interrogation regions, the optical flow methods analyze a continuous space-time window (and not a discrete displacement), which offers a higher accuracy to determine a dense average velocity field. Despite the obvious disadvantages of DPIV methods, the mainstream of research in fluid mechanics only gradually evolves towards motion estimation in space-time windows (Heitz, Memin, & Schnorr, 2010). The term “optical flow” was first used by the psychologist James Jerome Gibson in the 1940s as part of a theory of human vision (Gibson, 1950). Low level processing in the visual cortex indeed extracts information about motion from a continuous stream of visual stimuli (Hubel & Wiesel, 1962; E. Adelson, 1991) and research in biological vision now interprets the perception of motions in the space-time domain. The optical flow methods can track not only tracer motions but also texture motions to capture clouds, sea ice or pollutant displacements from sequences of meteorological satellite images (Heitz et al., 2010). These methods are also widely used in video compression (Barron, Fleet, & Beauchemin, 1994), in computer

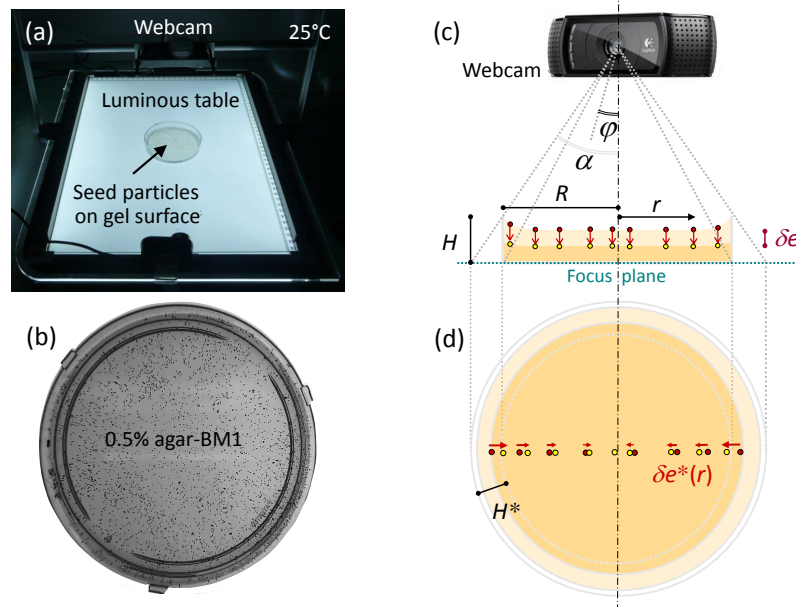


Figure 2.24: (a,b) Observation using a light table and a webcam of the motion of seed particles (diameter $200\mu\text{m}$ – $350\mu\text{m}$) on the upper free surface of a transparent gel plate of thickness $e=4\text{ mm}$ cast in a smooth plastic (PS) dish. (c) Side view of the dish and seed particle motion for a purely vertical thinning $\delta e(r)$ of the gel plate. (d) Top view of the dish and seed particle motion when focusing the webcam on the bottom surface of the dish. Light orange color and red points for the initial gel plate and particle positions, respectively. Dark orange color and yellow points for the gel plate and the new particle positions after some water evaporation, respectively. The vertical lateral wall of the dish of height H appears as concentric circles on the top view with a radius difference H^* when visualized under an angle α . Finally, $\delta e^*(r)$ is the apparent lateral displacement of the particles on the top view at a distance r from the dish center.

vision and in robotics to build a representation of the environment of a moving robot (S. Lee & Song, 2004). In this context, the optical flow algorithms proposed to measure dense displacement fields are based on either regularization methods and optimization of an objective functional (McKenna & McGillis, 2002), either spatio-temporal filtering (E. H. Adelson & Bergen, 1985) or filtered differential methods (Barron et al., 1994). Not all of these methods are well suited for particle tracking. In the following, a homemade spatio-temporal method will be presented to study the space-time dynamics of a drying agar gel cast in a dish.

An agar gel of thickness $e=4$ mm is cast in a transparent and cylindrical dish made of plastic (radius $R = 42.5$ mm) or glass ($R = 35$ mm) with some seed particles (diameter $200 \mu\text{m} - 350 \mu\text{m}$) located on the upper free surface of the gel [Fig. 2.24(b)]. The dish with the gel are then placed on a luminous table and left to dry at a temperature of $T = (25.0 \pm 0.5)^\circ\text{C}$. The gel is filmed from above with a webcam for the purpose of following the motion of the seed particles induced by the gel drying, with a spatial resolution of about $75 \mu\text{m}$ per pixel [Fig. 2.24(a)]. Because of perspective or parallax effects, the thinning of the agar gel plates induced by water evaporation results in an apparent radial displacement $\delta e^*(r, t)$ of the seed particles when observing the dish from the top. Under the assumptions of a purely vertical displacement $\delta e(r, t)$ of the seed particles, a centered visualization and a gel thickness $e=4$ mm much smaller than the distance between the camera and the dish (10 cm) [Fig. 2.24(c)], the apparent displacement $\delta e^*(r, t)$ of the particles then follows the relation:

$$\delta e^*(r, t) \approx \delta e(z, t) \tan \varphi(r) \approx \delta e(z, t) \frac{H^*}{H} \frac{r}{R} \quad (2.5)$$

where $\varphi(r)$ is the angle under which the camera detects the seed particles located at a distance r from the dish center, H is the height of the vertical lateral walls of the dish and H^* the apparent corresponding distance visualized from the top under an angle α with $\tan \varphi(r) = r \tan(\alpha)/R$ and $\tan(\alpha) = H^*/H$ [Fig. 2.24(c) and (d)].

8-bit images of the gel plate are recorded with an acquisition rate of 1 frame per minute. The spatio-temporal method used to analyze local particle motion in the n -image sequence consists in a time projection of the grey levels both along the horizontal and vertical directions within a small Region Of Interest (ROI) emphasized by a yellow square of typical size 5 mm or $m=66$ pixels in Figure 2.25(b). The small ROI yet contains enough

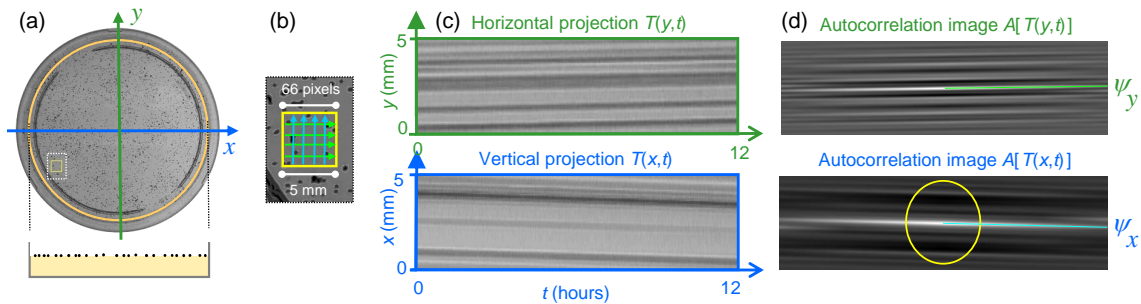


Figure 2.25: (a) Observation of the motion of surface seed particles on the upper free surface of a transparent 0.5% wt. agar-BM1 gel plate of thickness $e = 4$ mm cast in a smooth plastic (PS) dish and left to dry at $T = (25.0 \pm 0.5)^\circ\text{C}$. (b) Selection of a small square ROI of size 66 pixels emphasized by a yellow rectangle in (a). (c) Temporal projection of the gray levels along the horizontal and vertical directions within the small square ROI in (a) to produce 8-bit spatio-temporal windows $T(y, t)$ and $T(x, t)$. (d) The 16-bit autocorrelation images $A[T(y, t)]$ or $A[T(x, t)]$ display a centered bright line with the same average tilt angles Ψ_y or Ψ_x as the particle trajectories in the spatio-temporal windows. The yellow circles in (d) with a radius of 60 pixels corresponds to the region of analysis to determine the tilt angle of the ridge lines.

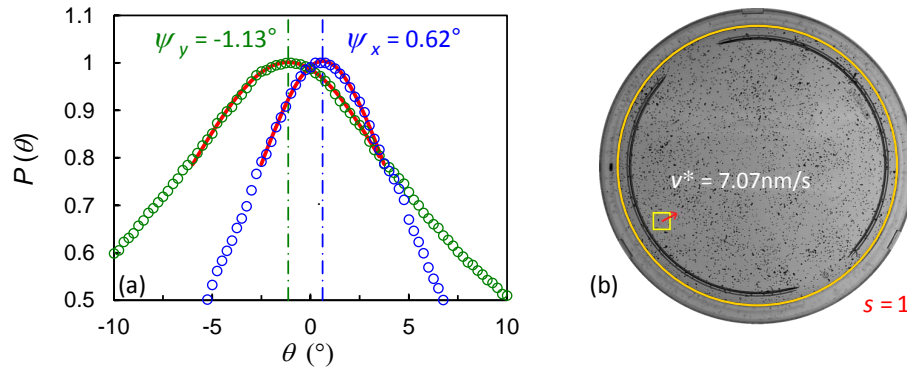


Figure 2.26: (a) Angular distributions $P(\theta)$ of the 16-bit gray levels derived from a radial integration of 16-bit autocorrelation images within a centered circular ROI of radius 60 pixels. Fitting $P(\theta)$ to a Lorentzian gives the tilt angles Ψ_y or Ψ_x of the ridge lines in the autocorrelation images and the average velocity v^* of particles in the square Region Of Interest (b). The variable $s=1$ indicates the default scale of the velocity vector in (b).

seed particles to produce a texture in the 8-bit spatio-temporal windows $T(y, t)$ and $T(x, t)$ consisting of similarly oriented particle trajectories [Fig. 2.25(c)]. The tilt angles Ψ_x and Ψ_y of the oblique lines in the spatio-temporal windows are related to the average apparent velocities v_x^* and v_y^* of particles along x and y axes, respectively, through the following relations:

$$v_x^* = \frac{f_t}{f_s} \tan \Psi_x \quad \text{and} \quad v_y^* = \frac{f_t}{f_s} \tan \Psi_y \quad (2.6)$$

where f_t in pixels per unit time and f_s in pixels per unit length are the temporal and the spatial sampling frequencies, respectively. As proposed by (E. H. Adelson & Bergen, 1985), a spectral analysis of the time-space window in the Fourier space gives a Dirac ridge whose support is orthogonal to the velocity vector. A powerful way to characterize oriented textures with a low sensitivity to noise ratio is the centered autocorrelation image that shows similarities between the source image and the shifted version. For this purpose, the 16-bit autocorrelation images of the spatio-temporal diagrams are computed using a Discrete Fast Hartley Transform, which minimizes the number of arithmetic operations compared to the traditional fast Fourier Transform (Bracewell, 1986; Bracewell, O.Buneman, H.Hao, & J.Villasenor, 1986)⁵. The autocorrelation images $\mathcal{A}[T(y, t)]$ and $\mathcal{A}[T(x, t)]$ feature a centered bright line with the same average tilt angles Ψ_y and Ψ_x as the particles trajectories in the spatio-temporal windows [Fig. 2.25(d)].

A radial integration of the 16-bit autocorrelation images gives the angular distribution $P(\theta)$ of gray levels as shown in Figure 2.26(a). The normalized angular distribution $P(\theta)$ is computed within a centered circular ROI of radius $p = 60$ pixels [yellow ROI in Fig. 2.25(c)] and discretized into 720 angular sectors (angular resolution 0.25°)⁶. Fitting $P(\theta)$ to a Lorentzian function gives the tilt angles Ψ_y and Ψ_x of the bright ridge lines with a precision

⁵A discrete 2D autocorrelation image is usually computed through the inverse Fourier transform $F^{-1}[F(T)F^*(T)]$ where $F(T)$ denotes the Fourier transform of the source image T and $*$ the complex conjugate (Wiener Kinchin theorem). Here, one uses a Discrete Fast Hartley Transform (DFHT) instead of a Discrete Fast Fourier Transform (DFFT) to reduce the required computer memory and to decrease the number of arithmetic operations (Bracewell, 1986; Bracewell et al., 1986). Prior to any discrete transform in the Hartley space, the boundaries of the spatio-temporal windows of size (n, m) are extended up to a size (N, M) such that $N = 2^i$ and $M = 2^j$. Extra pixels in the (N, M) images are padded with the averaged gray level of the (n, m) spatio-temporal windows. This procedure helps reducing high frequency noise.

⁶A nearest neighbor bicubic interpolation of 16-bit gray level pixels is further considered to significantly smooth the angular distribution function $P(\theta)$.

of about 0.02° and the average velocity $v^*(r) = (f_t/f_s)(\tan^2 \Psi_x + \tan^2 \Psi_y)^{1/2}$ of seed particles in the square region of interest [Fig. 2.26(b)].

The spatio-temporal treatment of a n image sequence can detect a local average particle displacement ranging from $1/n$ pixels per frame up to $m/4$ pixels per frame (m is the size of the square ROI). Considering $n=180$ images and a spatial resolution of $75 \mu\text{m}$ per pixel, a detectable particle displacement δe^* lies in a range of $0.5 \mu\text{m}$ to 1 mm . Therefore, equation 2.5 gives a measurable averaged vertical gel thinning velocity $(\delta e/\delta t) \approx (\delta e^*/\delta t)/\tan \alpha$ with $\tan \alpha = H^*/H \approx 0.425$ ranging from 0.1 nm/s up to 200 nm/s (three decade dynamics) for a three hours image subsequence and an acquisition rate of 1 frame per minute ($\delta t=3 \text{ hours}$ and $n=180$). Note that both block matching (DPIV) and optical flow methods rely on the assumption of almost constant brightness of the moving particles (Adrian, 1991; Barron et al., 1994), which is indeed the case for a stationary optical illumination of the gel plate in a dark room. A larger number of particles further greatly improves the statistics and the accuracy of velocity measurements but a seeding excess may lower water evaporation during gel drying.

The spatio-temporal method is thus well suited for the study of the gel drying dynamics over the whole surface of the dish. For this purpose, a homemade plugin was developed in java for use with the ImageJ image processing software (Rasband, 1997-2016). The image sequence is usually analyzed sequentially over 164 adjacent square ROIs (size $m=70$ pixels or about 5 mm) spread over the gel surface and located at a radial distance $0 < r < 0.95R$ from the dish center [Fig. 2.27(a)] to obtain the apparent 2D average velocity field $\vec{v}^*(r, t)$ during three consecutive hours [Fig. 2.27(b)]. The computing time of an image subsequence ($n=180$ frames and 164 ROIs) with a personal computer is only 1 minute. Finally, Figure 2.27(c) shows the radial dependence of the apparent velocity $v^*(r)$ averaged over the first three hours during the drying for a 0.5% wt. agar-BM1 gel plate cast in a smooth plastic dish and left to dry at a temperature $(25.0 \pm 0.5)^\circ\text{C}$. The centripetal motion of the seed particles and the linear radial variation of the apparent velocity $v^*(r)$ are representative of a purely vertical thinning of the gel, with an average rate

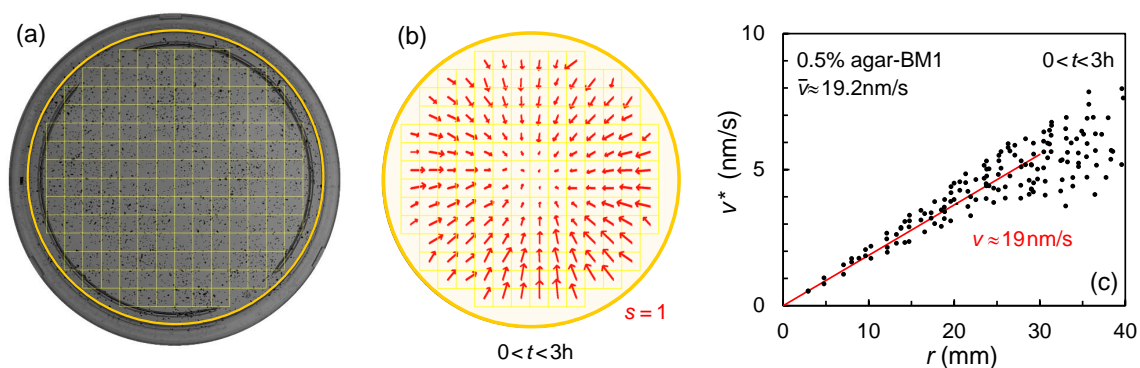


Figure 2.27: Sequential analysis of an image subsequence of duration 3 hours over 164 adjacent square ROIs (size 70 pixels, i.e. about 5 mm). (b) 2D apparent velocity field $\vec{v}^*(r, t)$ averaged over three hours and computed from the displacement of seed particles on the upper free surface of a 0.5% wt. agar-BM1 gel of thickness $e = 4 \text{ mm}$ cast in a smooth plastic (PS) dish and left to dry at $T = (25.0 \pm 0.5)^\circ\text{C}$ (scale $s = 1$ for the velocity vectors). (c) Radial dependence of the apparent averaged velocity $v^*(r)$. The best linear fit of the data over the range $0 < r < 30 \text{ mm}$ gives the average vertical thinning rate $v = 19 \text{ nm/s}$ of the gel using the following relation $v^* = vr \tan(\alpha)/R$ with $\tan(\alpha) = H^*/H = 0.425$ and $R = 42.5 \text{ mm}$. Temporal sampling frequency $f_t = 1 \text{ pixel per minute}$ and spatial sampling frequency $f_s = 1.33 \times 10^{-2} \text{ pixel}/\mu\text{m}$. Independent mass-loss measurements performed with a precision scale over the first day gives a global average thinning rate $\bar{v} \approx 19.2 \text{ nm/s}$.

$v \approx 19$ nm/s derived from the relation $v^* = vr \tan(\alpha)/R$ with $\tan(\alpha) = H^*/H = 0.425$ and $R = 42.5$ mm [Fig. 2.27(c)]. Independent mass-loss measurements performed with a precision scale over the first day gives a comparable global average thinning rate $\bar{v} \approx 19.2$ nm/s.

However, some systematic dispersion of v^* measurements is observed near the edge of the dish for large radial distances $r > 30$ mm [Fig. 2.27(c)]. Both the curvature of the meniscus over a centimetric distance and the edge effects are responsible for an accelerated water evaporation, and may significantly influence the apparent motion of the seed particles. For this reason, the analysis of the velocity fields will be later limited to the inner region of the gel plate and radial distances smaller than 30 mm. In Chapter 5, the spatio-temporal method will be used for the early detection of either the gel sliding motion on the bottom surface of the dish, or the shear deformation of the soft material near the edge of the dish. Indeed, non-vertical local motions of the gel result in a non-centripetal apparent velocity field over short drying periods long before any gel debonding from the lateral wall or any gel fracture is observed.

2.6 Properties of solid surfaces

The solid substrates and dishes used in the present work were characterized using two different techniques: 3D scanning interferometry or optical profilometry to quantify the RMS roughness of surfaces, and contact angle measurements, which provide information about the solid surface wettability.

2.6.1 3D scanning interferometry

The 3D topography map of solid surfaces was obtained with a non-contact optical interferometer (Contour Elite GT-I, Bruker). The reconstruction of the 3D surface topography map is based on the localisation of interference fringes during a vertical scan. After accurate location of the focus plane and careful adjustment of the objective axis in the direction parallel to the normal of the solid surface [Fig. 2.28(b)], a vertical scan over a distance of a few tens of micrometers provides a fast 3D reconstruction of the surface topology [Fig. 2.28(c)] with a sub nanometer vertical resolution over a large area [$100\mu\text{m} \times 128\mu\text{m}$ for an objective x50, Fig. 2.28(c)]. A statistical treatment of 3D topography maps is performed over four to five different sample areas with the software Vision64 (Bruker) to determine the surface parameters such as the average of heights \bar{R}_a , the RMS surface roughness \bar{R}_q or the fastest decay autocorrelation length \bar{R}_{al} . The RMS surface roughness

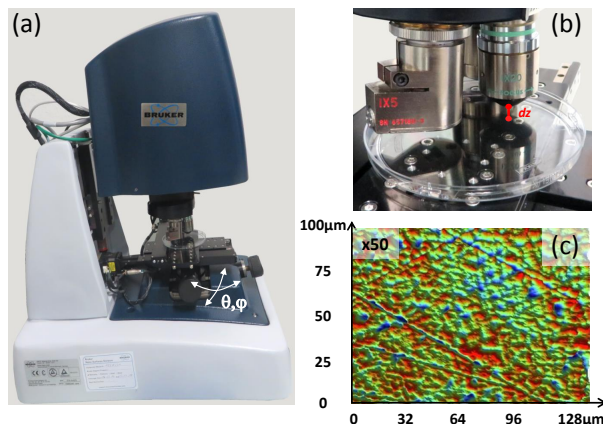


Figure 2.28: (a) View of the Contour Elite 3D optical microscope (Contour Elite GT-I, Bruker). (b) Optical analysis of a solid surface over a vertical scanning distance $dz \approx 10 \mu\text{m}$ with objectives of optical magnification x5, x20 or x50. (c) 3D color coded height map $z(x, y)$ of the bottom wall of a smooth plastic dish (objective magnification x50, average of heights $\bar{R}_a = 9.5$ nm, RMS surface roughness $\bar{R}_q = 11$ nm, fastest decay autocorrelation length $\bar{R}_{al} = 2.4$ nm).

\overline{R}_q is a much more statistically significant parameter than the average of heights \overline{R}_a and will be considered later to characterize the random texture of solid surfaces [Fig. 2.29(a-c)].

2.6.2 Water contact angle measurements

The wetting properties of solid surfaces were characterized by the measurement of the water contact angle, which reflects the relative strength of the liquid, solid, and vapor molecular interactions. For a liquid drop on a flat solid substrate, the contact angle is conventionally defined as the angle formed by liquid-solid and liquid-vapor interfaces at the ‘three phase contact line’ and further obeys the Young-Laplace equation (Young, 1805; Yuan & Lee, 2013):

$$\gamma_{lv} \cos \theta = \gamma_{sv} - \gamma_{sl} \quad (2.7)$$

where γ_{lv} , γ_{sv} and γ_{sl} represent the liquid-vapor, solid-vapor and solid-liquid surface tensions, respectively. However, in practice contact angle hysteresis is observed, ranging from the so-called advancing (maximal) contact angle to the receding (minimal) contact angle, especially for rough surfaces. The receding contact angle was considered for rough solid surfaces. Water contact angles were measured by direct optical method, using the Tracker-S tensiometer (Teclis Scientific) and the software Windrop. Experiments were performed with Milli-Q water (17 M Ω .cm at 25°C) on different flat and horizontal surfaces. All the measurements are repeated at least 3 times in different locations on the surfaces.

Water somewhat spreads on a smooth glass surface [contact angle $\theta \approx 36^\circ$, Fig. 2.29(d)]. Moreover, the large contact angle of water either on a smooth plastic surface [$\theta \approx 77^\circ$, Fig. 2.29(e)] or on a rough plastic surface [$\theta \approx 89^\circ$, Fig. 2.29(f)] indicates a low water wettability characteristic of a hydrophobic material.

The ‘‘Root-Mean-Square Roughness’’ R_q and the equilibrium water contact angle θ were determined for all the surfaces [smooth and rough solid substrates made of glass, plastic (PS or PMMA), or duralumin] used in the manuscript and the results are synthesized in table 2.2. Furthermore, the smooth surfaces made of glass and plastic were

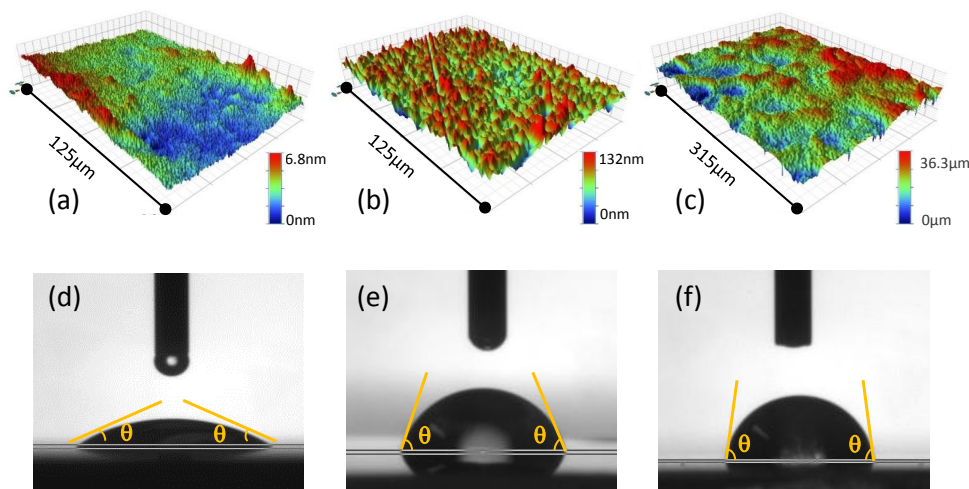


Figure 2.29: (a)–(c) 3D reconstruction of the surface topography as measured by the optical scanning profilometer for a smooth glass surface [$R_q = (0.53 \pm 0.10)$ nm] (a), a smooth plastic surface [$R_q = (12.0 \pm 3.6)$ nm] (b), and a rough plastic surface [$R_q = (1.54 \pm 0.43)$ μ m] (c). (d)–(f) Measurement of the contact angle θ of water on a smooth glass surface [$\theta = (36 \pm 2)^\circ$] (a), a smooth plastic surface [$\theta = (77 \pm 3)^\circ$] (b), and a rough plastic surface made of PS [$\theta = (89 \pm 5)^\circ$] (c).

Surface	R_q (nm)	Water contact angle θ ($^\circ$)
Smooth glass	0.53 ± 0.10	36 ± 2
Rough glass	5900 ± 2400	21 ± 2
Smooth plastic (PS)	12.0 ± 3.6	77 ± 3
Rough plastic (PS)	1540 ± 430	89 ± 5
Smooth plastic (PMMA)	1.2 ± 0.7	80 ± 2
Rough plastic (PMMA)	1000 ± 250	85 ± 3
Smooth duralumin	6.9 ± 4.4	91 ± 2
Milled duralumin	340 ± 100	–
Rough duralumin	2300 ± 300	74 ± 3
Smooth glass after UV–O ₃ treatment	0.56 ± 0.20	≈ 7
Smooth glass after silanization	1.7 ± 1.0	≈ 85
Smooth plastic after UV–O ₃ treatment	12 ± 2	≈ 10

Table 2.2: RMS surface roughness and water contact angle of solid surfaces. Note that the smooth plastic surface (PS) made of polystyrene crystal corresponds to commercial Petri dishes used by bioMérieux company for the cellular culture media.

irradiated with UV light or chemically treated to modify the wettability properties of the solid substrates without changing too much the surface roughness. UV-O₃ irradiation (UVOCS T0606B) allows to clean and produce more hydrophilic surfaces, whereas the silanization of solid substrates with OTS molecules (octadecyltrichlorosilane) provides more hydrophobic surfaces (see Section 4.3.5 for more technical details). The various solid substrates will be used in Chapter 4 to investigate the influence of both RMS surface roughness and wettability on the adhesive contact with an agar gel.

Chapter 3

Role of thermal history on agar gels

Contents

3.1 Incubation of agar solutions at 80°C	60
3.1.1 Heat-induced aging of agar sols	61
3.1.2 Impact on gelation kinetics and gel microstructure	63
3.1.3 Impact on gel adhesion and failure dynamics	65
3.1.4 Discussion and conclusion	70
3.2 Cooling kinetics of hot agar solutions	72
3.2.1 Impact of cooling rate	72
3.2.2 Impact of a temperature drop	73
3.2.3 Impact of a temperature plateau during cooling	75
3.2.4 Discussion and conclusion	76

Associated peer-reviewed articles:

▷ **Normal force controlled rheology applied to agar gelation,**

B. Mao, T. Divoux & P. Snabre,
Journal of Rheology **60**, 473–489 (2016)

▷ **Heat-induced aging of agar solutions:**

Impact on the structural and mechanical properties of agar gels,
B. Mao, A. Bentaleb, F. Louerat, T. Divoux & P. Snabre,
Food Hydrocolloids **64**, 59–69 (2017)

Agarose is not soluble in water at ambient temperature. Therefore, agar(ose) powder is traditionally introduced into boiling water and maintained at about 100°C for a few minutes to ensure a good solubilization of the polysaccharides. The latter solution is then cooled down to ambient temperature, which triggers the gelation. In this chapter, I investigate the influence of the thermal history experienced by an agar solution, on the properties of both the solution and the corresponding agar gel. We chose to work on samples with 1.5% wt. agar (i.e. 1% wt. agarose), which is the typical agarose content employed in gels used as culture medium. First, I quantify the influence of the incubation time of the agar solution at high temperature (i.e. larger than the gelation temperature) beyond a few minutes boiling. I systematically determine the structural and the mechanical properties of gels prepared after increasing incubation time of an agar sol maintained at $T=80^\circ\text{C}$ ¹ (Section 3.1). In a second part, the influence of the cooling process and thermal history of the agar solution on the gel properties are thoroughly investigated, namely the impact of the cooling rate \dot{T} , the amplitude of the temperature drop ΔT , and the effect of a pause during the cooling phase (Section 3.2). One will see that in contrast to gels with larger agarose content (Aymard et al., 2001), the viscoelastic properties of 1% wt. agarose gels are poorly sensitive to the thermal history of the cooling phase.

3.1 Incubation of agar solutions at 80°C

To assess the impact of the incubation time of agar sols at high temperature, 1.5% wt. agar-SA solutions are prepared and stored in a thermal chamber (Binder MK53) at $(80 \pm 1)^\circ\text{C}$. The moment the agar sol is placed in the chamber sets the origin of time $\mathcal{T} = 0$ and all the experiments performed later on are timestamped with respect to the initial time $\mathcal{T} = 0$. Samples are extracted every day to monitor the evolution of the sol properties, which are summarized in Section 3.1.1. Moreover, the viscoelastic properties of agar-SA gels prepared from the agar sol at regular time intervals are determined as a function of the incubation time \mathcal{T} , as detailed below in Section 3.1.2.

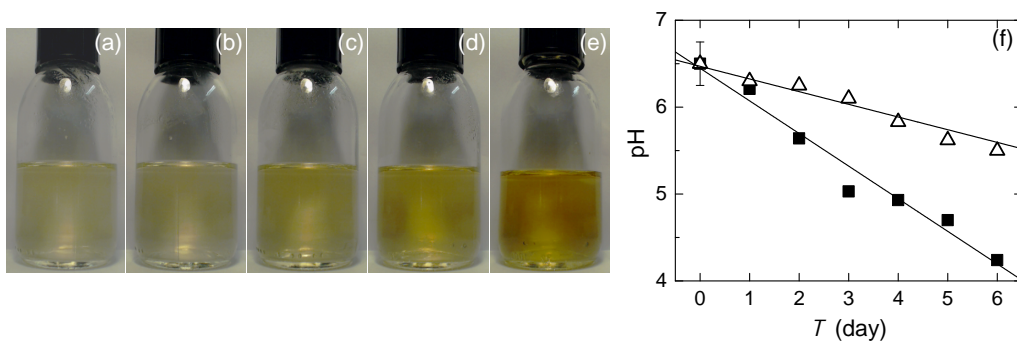


Figure 3.1: (a)–(e) Pictures of 1.5% wt. agar sol after different incubation times \mathcal{T} at $T = 80^\circ\text{C}$, respectively from left to right: $\mathcal{T} = 10$ minutes (a), 1 hour (b), 3 days (c), 6 days (d) and 12 days (e). The scale is fixed by the 4.5 cm diameter of the glass bottle. (f) Evolution of the pH measured at $T = 80^\circ\text{C}$ vs. the incubation time \mathcal{T} of the agar sol when the latter is either in contact with ambient air (■) or with a nitrogen atmosphere (△). The black lines correspond in both cases to the best linear fits of the data: $\text{pH} = 6.5 - 0.15\mathcal{T}$ and $\text{pH} = 6.4 - 0.37\mathcal{T}$ with \mathcal{T} in days.

¹An incubation temperature of 80°C is more practical than the boiling temperature of 100°C and larger than the gelation temperature.

3.1.1 Heat-induced aging of agar sols

Color change and polysaccharide oxidation.- A fresh agar sol is prepared in an Erlenmeyer flask, then sealed and stored at 80°C. The color of the solution turns from light yellow to dark yellow in a few days. This color change goes on at least over 12 days [Fig. 3.1(a)–(e)]. Samples are withdrawn every day during the first 5 days to monitor the evolution of the sol pH, which is measured at 80°C with a silver electrode (N6000 BNC, Schoot instruments) connected to a controller (C333, Consort). The pH decreases with the increasing sample age \mathcal{T} [Fig. 3.1(f)], which gives evidence of a chemical evolution of the polysaccharide molecules that is attributed to the oxidation of the hydroxyl functional group of the polymers. Indeed, when repeating the experiment on a fresh solution that is stored in contact with an atmosphere continuously enriched in nitrogen instead of ambient air, we observe that the color change and the pH decrease are both strongly reduced [Fig. 3.1(f)]. The latter experiment proves the key role of oxygen in the aging process and strongly suggests that the pH decrease can be attributed to the slow oxidation into carboxyl functions of the hydroxyl groups connected to primary carbon atoms in the agarose chains [Fig. 3.2(Right bottom)].

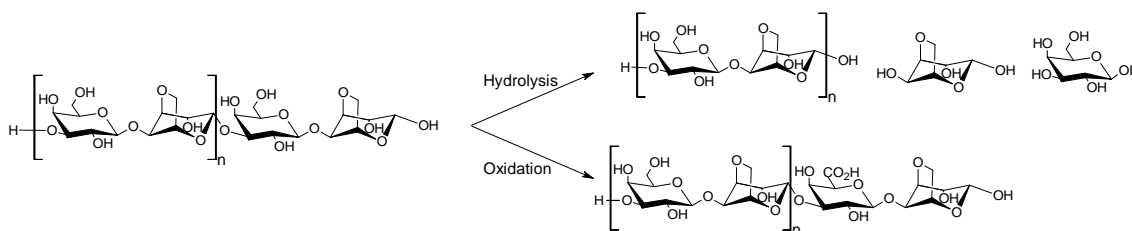


Figure 3.2: (Left) Illustration of a disaccharide unit $(AB)_n$ composing the agarose molecule. (Right) Product of the hydrolysis or oxidation of the agarose molecule as discussed in Section 3.1.1.

Viscosity change and chain hydrolysis.- Concomitantly with the pH measurements, the viscosity of the solution was determined every day through rheological experiments performed in a cone-and-plate geometry driven by a stress controlled rheometer (DHR-2, TA instruments). The cone (diameter 60 mm, angle 2°) is made of stainless steel and the bottom plate consists in a Teflon coated Peltier unit, which allows to control the sample temperature. The geometry is pre-heated before being filled by the liquid agar solution. The viscosity is determined at $T = 50^\circ\text{C}$ with a solvent trap filled with water to prevent evaporation. The shear rate is ramped down from 100 s^{-1} to 1 s^{-1} through 11 successive logarithmically spaced steps of stationary shear rate and 20 s duration each.

The polysaccharide solutions display an almost Newtonian behavior between 1 and 100 s^{-1} , from one hour after being prepared up to $\mathcal{T} = 5$ days of incubation at 80°C [Fig. 3.3(a)]. The viscosity of the 1.5% wt. agar solution decreases with increasing incubation time, which strongly suggests that the polymer chains are becoming shorter due to hydrolysis. To assess the evolution of the molecular weight of the polysaccharides, the same incubation experiment is repeated on agar solutions of different concentrations: $c = 0.05\%$ wt., 0.1% wt. and 0.2% wt.. The three solutions are stored together in the same thermal chamber to ensure a similar thermal history, and the viscosity of samples drawn at regular time intervals are determined by steady-shear experiments over the range of shear rates $1\text{ s}^{-1} \leq \dot{\gamma} \leq 100\text{ s}^{-1}$ [Fig. 3.3(b)]. For a given incubation time, a linear extrapolation of the viscosity in the limit of vanishing concentrations (i.e. intercept with the vertical

reduced viscosity axis) allows us to estimate the intrinsic viscosity of the solution defined as follows:

$$[\eta] = \lim_{c \rightarrow 0} \frac{\eta - \eta_s}{\eta_s c} \quad (3.1)$$

where η_s is the viscosity of the solvent, here $\eta_s = 0.533$ mPa.s for water at $T = 50^\circ\text{C}$. The average molecular weight \overline{M}_w of the polymer chains is further derived from the intrinsic viscosity $[\eta]$ of the solution using the Mark-Houwink equation:

$$[\eta] = K \overline{M}_w^\alpha \quad (3.2)$$

where K and α are specific of polymer solvent interactions and take the following values $K \approx 0.07$ and $\alpha \approx 0.72$ for dilute agarose solutions (Rochas & Lahaye, 1989). Both the intrinsic viscosity and the calculated average molecular weight \overline{M}_w of the polymer chains decreases linearly with the incubation time \mathcal{T} [Fig. 3.3(c)]. The average molecular weight goes from 120 kDa for a fresh agar solution down to 8 kDa after 5 days of incubation at 80°C , which confirms the progressive hydrolysis of the polysaccharides as illustrated in the right upper part of Figure 3.2.

In conclusion, the color change of the agar sol that goes with an extended heating is due to both the oxidation of the primary alcohol functions and the hydrolysis of the polymer chains. The rest of the present Section 3.1 is focused on the impact of the sol aging

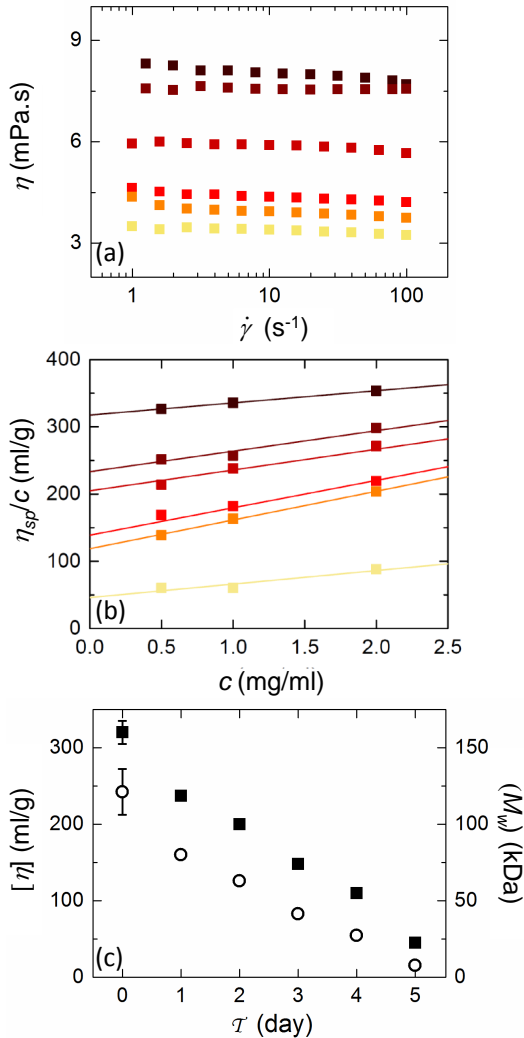


Figure 3.3: (a) Shear viscosity η of a 1.5% wt. agar solution vs. applied shear rate $\dot{\gamma}$ in a cone and plate geometry at $T = 50^\circ\text{C}$. Colors from black to yellow correspond to different incubation times of the agar solution at 80°C : $\mathcal{T} = 1$ hour, 1 day, 2, 3, 4 and 5 days. (b) Reduced viscosity $(\eta - \eta_s)/\eta_s c$ vs. the polymer concentration c , where $\eta_{sp} = (\eta - \eta_s)/\eta_s$ represents the specific viscosity of the agar sol and η_s denotes the viscosity of the solvent (water at $T = 50^\circ\text{C}$). Each point corresponds to an average over the following range of shear rates $1 \text{ s}^{-1} < \dot{\gamma} < 100 \text{ s}^{-1}$. Full lines denote the best linear fits of the data and the intercept with the vertical axis gives an estimate of the intrinsic viscosity $[\eta]$ of the agar solution as a function of the incubation time \mathcal{T} . (c) Intrinsic viscosity $[\eta]$ (■, left vertical axis) and average molecular weight \overline{M}_w (○, right vertical axis) computed from the Mark-Houwink formula vs. the incubation time \mathcal{T} of the agar solution. Error bars result from the average of viscosity data $\eta(\dot{\gamma})$ over the range $[1 \text{ s}^{-1}; 100 \text{ s}^{-1}]$ and from data extrapolation in the limit of vanishing concentrations. The typical error bar is indicated only on the first point for both $[\eta]$ and \overline{M}_w .

on the subsequent gels prepared after different incubation times of the agar solution. We will discuss the possible change in the gelation dynamics and the gel microstructure after different incubation times of the agar solution in Subsection 3.1.2. Finally, the impact of an extended incubation time of the agar sol on both the gel adhesion properties to metallic plates and the failure scenario of the gel during macro-indentation tests will be the topic of Subsection 3.1.3.

3.1.2 Impact on gelation kinetics and gel microstructure

Evolution of the gelation dynamics with the incubation time \mathcal{T} .— This section is devoted to the impact of the incubation time \mathcal{T} on the gelation dynamics. Every day, a sample withdrawn from the agar solution stored at $T = 80^\circ\text{C}$ is poured into the pre-heated gap of a parallel-plate geometry. The sample is submitted to a decreasing ramp of temperature at a constant cooling rate $\dot{T} = 1^\circ\text{C}/\text{min}$ down to 20°C to induce agar gelation, while the storage and loss moduli are measured through small strain amplitude oscillations, under controlled normal force (see Section 2.3.1 in Chapter 2 for technical details). Results obtained with a fresh solution ($\mathcal{T} = 0$) after only a few hours of incubation of the agar solution at 80°C are pictured in Figure 3.4(a)–(b). During the first half hour of cooling, the storage modulus G' remains negligible while the loss modulus G'' increases continuously. The crossing of G' and G'' provides an estimate of the gelation temperature, here referred to as T_g . Since the gelation is monitored under constant normal force ($F_N = 0.0 \pm 0.1$ N) instead of constant gap width, the decrease of the gap width (of about 1%) exactly compensates for the sample contraction associated with the sol/gel transition (Mao, Divoux, & Snabre, 2016). Finally, the storage and loss moduli both reach terminal steady-state values respectively labeled G'_0 and G''_0 after a waiting period of about 1.5 h.

The same experiment is repeated every day and the gelation kinetics of the agar sol after $\mathcal{T} = 5$ days of incubation at 80°C are reported in Figure 3.4(c)–(d). The gelation occurs later, at a lower temperature ($T_g = 32.5^\circ\text{C}$ for $\mathcal{T} \simeq 5$ days) compared with the case

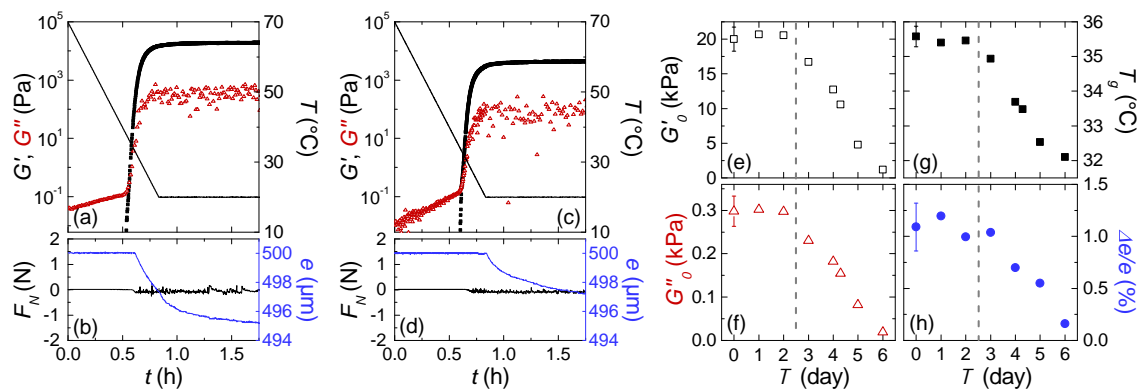


Figure 3.4: (a) Evolution of the storage (G' , \blacksquare) and loss (G'' , \triangle) moduli vs. time t during the cooling of a fresh 1.5% wt. agar sol ($\mathcal{T} \simeq 1$ hour) from $T = 70^\circ\text{C}$ down to 20°C , conducted at $\dot{T} = 1^\circ\text{C}/\text{min}$. The crossing of G' and G'' defines a gelation temperature $T_g = 35.5^\circ\text{C}$, and the viscoelastic moduli reach respective steady-state values $G'_f = 19.2$ kPa and $G''_f = 310$ Pa for $t \geq 1.75$ h. (b) Imposed normal force $F_N = (0.0 \pm 0.1)$ N and gap width e vs. time. The gap width of initial value $e_0 = 500$ μm decreases by 1% due to the sample contraction during the gelation. (c) and (d): same as in (a) and (b) for a gel prepared from an agar sol, which has been incubated $\mathcal{T} = 5$ days at 80°C . (e)–(h) Evolution of the terminal values of viscoelastic moduli G'_0 (e) and G''_0 (f), the gelation temperature T_g (g) and the relative gap decrease $\Delta e/e$ (h) vs. the incubation time \mathcal{T} of the agar sol prior to the gel preparation.

of a fresh agar sol ($T_g = 35.5^\circ\text{C}$ for $\mathcal{T} \simeq 1$ hour). Moreover, the terminal values of the storage and loss moduli of the agar gel are significantly smaller after 5 days incubation of the agar sol and the sample is further observed to contract only by $\Delta e/e \approx 0.6\%$ during the gel formation, compared to 1.1% for the sample prepared from a fresh solution. The systematic evolution of G'_0 , G''_0 , T_g and $\Delta e/e$ with the incubation time \mathcal{T} are reported in figures 3.4(e)–(h). Gels prepared from a hot agar solution younger than 3 days show the same gelation temperature and the same steady-state viscoelastic properties within error bars. However, for $\mathcal{T} \geq 3$ days, the gelation occurs later, i.e. at a lower gelation temperature, and the gel becomes weaker as \mathcal{T} increases: after 5 days of incubation at 80°C of the agar sol, the storage modulus of the agar gel decreases by 75% compared to a gel prepared from a fresh solution, which is remarkable. We emphasize that, although the aging starts from the very moment the sol is stored at 80°C in the thermal chamber as observed after one day of incubation in Figure 3.1(b), the gelation dynamics and the gel viscoelastic properties undergo no detectable change before the third day of incubation.

Evolution of the gel microstructure with the incubation time \mathcal{T} .— To provide supplemental structural information and possibly interpret the changes in the bulk mechanical properties, I have performed systematic cryo-SEM observations of gels prepared from samples extracted after different incubation times \mathcal{T} of the agar solution (see Section 2.2.1 in Chapter 2 for technical details). Cryo-SEM images are pictured in Figure 3.5(a)–(c). Gels formed from a freshly prepared solution show a fibrous-like microstructure composed of interconnected strands delimiting pores with a broad size distribution up to a few micrometers, in agreement with cryo-SEM observations reported in the literature (Charlionet et al., 1996; Rahbani et al., 2013). Gels formed from a hot solution incubated for $\mathcal{T} = 3$ days display a structurally similar network, except for thicker fibers and the presence of some foils [Fig. 3.5(b)]. Last, gels formed from hot solutions incubated for $\mathcal{T} = 5$ days show an even coarser microstructure, which now consists in foils larger than a few microns with very few fibers [Fig. 3.5(c)]. We attribute the coarsening of the gel microstructure with increasing incubation time of the agar solution to the intermolecular condensation of the polysaccharides. Indeed, the hot solution, which is transparent when fresh, becomes progressively optically diffuse with increasing incubation time, which strongly suggests the formation of micron-sized aggregates in relation with the condensation scenario sketched in Figure 3.6. The acidification of the agar solution that goes with

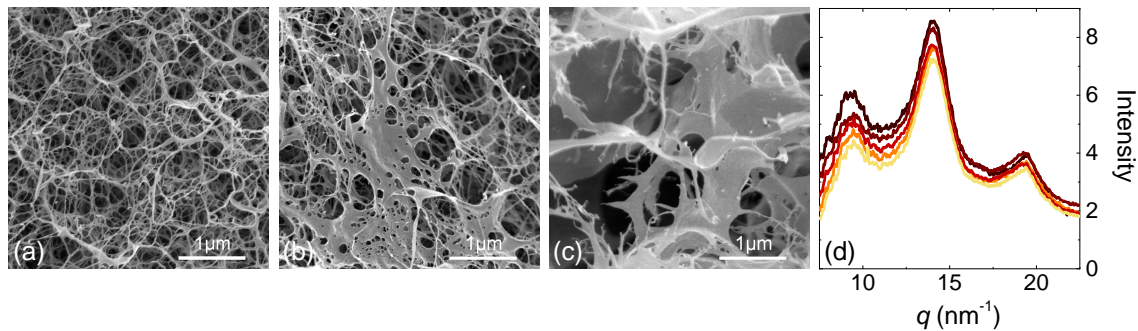


Figure 3.5: (a)–(c) Cryo-SEM images of 1.5% wt. agar gels prepared with liquid samples drawn after different incubation times $\mathcal{T} = 10$ minutes, 3 days and 5 days from a mother agar solution stored at $T = 80^\circ\text{C}$. (d) X-ray diffraction spectra $I(q)$, where q stands for the wave number. Colors from black to yellow correspond to gels prepared after different incubation times \mathcal{T} at $T = 80^\circ\text{C}$ of the same agar solution: $\mathcal{T} = 1$ hour, 1 day, 2, 4 and 5 days. X-ray diffraction experiments are performed on dried gels. See Section 2.2.2 in Chapter 2 for technical details.

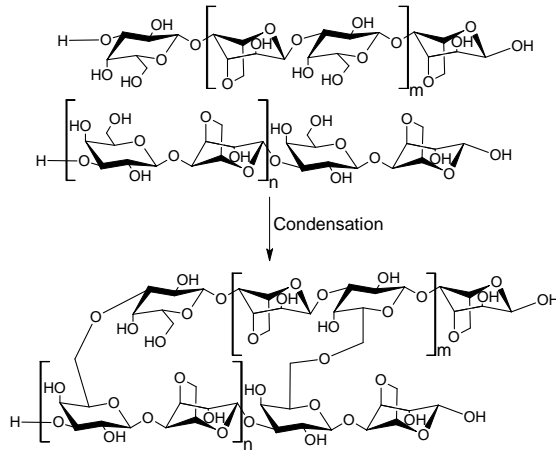


Figure 3.6: Illustration of the intermolecular condensation of the polysaccharides taking place for intermediate and large incubation times of the agar solution at 80°C. The condensation of agarose molecules leads to the formation of a foil-like microstructure pictured in Figure 3.5(b) and (c).

increasing incubation times \mathcal{T} [Fig. 3.1(f)] indeed favors the intermolecular condensation of agarose molecules.

To probe smaller scales, and determine whether or not the fibrous and foil-like microstructures are made from the same elementary components, I performed X-ray diffraction experiments on samples prepared after different incubation times \mathcal{T} of the agar sol (see Section 2.2.2 in Chapter 2 for technical details). X-ray experiments are performed on dried gels to remove as much as possible the diffraction spectra associated with water. Results are reported in Figure 3.5(d). The X-ray diffraction spectrum of a dried gel obtained from a fresh solution (\mathcal{T} of a few hours) shows 3 maxima at the following wavenumbers: $q_1 = 9.45 \text{ nm}^{-1}$, $q_2 = 13.86 \text{ nm}^{-1}$ and $q_3 = 19.3 \text{ nm}^{-1}$, which correspond respectively to the following characteristic lengths: $d_1 \equiv 2\pi/q_1 = 0.66 \text{ nm}$, $d_2 = 0.45 \text{ nm}$ and $d_3 = 0.32 \text{ nm}$. Such a result is in quantitative agreement with the seminal work of Foord and Atkins (Foord & Atkins, 1989). The agarose chains are associated into 3-fold double helices in the gel, and q_1 and q_3 correspond respectively to the distance between two different and two identical saccharides, while q_2 stands for the helix diameter. For increasing incubation time \mathcal{T} , the shape of the diffraction spectra and the positions of the maxima remain identical, which proves that the building blocks of the gel are the same despite the heat-induced aging of the agar sol. The decay of the maxima amplitude for increasing incubation time \mathcal{T} further indicates that an increasing fraction of polymer chains is not involved in the double helix formation during the gelation process, which is compatible with an increasing amount of intermolecular condensation.

3.1.3 Impact on gel adhesion and failure dynamics

This last section is dedicated to the impact of the incubation time \mathcal{T} of agar sol on the non-linear rheological properties and the yielding scenario of agar gels. First, the evolution of the gel adhesion properties to the metallic plates is quantified by performing strain sweep experiments. Second, the spatially-resolved scenario of the gel failure is investigated benchmark macro-indentation experiments after different incubation time \mathcal{T} of the agar sol at $T = 80^\circ\text{C}$.

Gel shear-induced debonding.- The gelation experiments reported in Figure 3.4 and conducted in a parallel-plate geometry under controlled zero normal force, end after two hours when both the gel storage modulus G' and the gel thickness e reach steady-state values. The rheometer is then switched from controlled normal force to constant

gap width, maintaining the latest value of e , and a strain sweep experiment is performed to quantify the adhesion of the agar gel to the metallic plates. Controlled oscillations of frequency 1 Hz and increasing strain amplitude from $\gamma = 0.01\%$ up to 100% are imposed to the agar gel over a duration of 2160 s. Gels prepared after different incubation times display a similar response as shown in Figure 3.7(a): the storage modulus remains constant in the low strain regime, and increases at larger strain amplitudes to reach a maximum value G'_m at $\gamma = \gamma_c$ markedly depending on the previous incubation time of the agar sol. Finally, the storage modulus G' sharply decreases above the critical strain amplitude γ_c . The increase of G' under external stress corresponds to the strain hardening of the agar gel, classically observed for biopolymer gels (Groot, Bot, & Agterof, 1996; Storm et al., 2005; Pouzot et al., 2006; J. Zhang, Daubert, & Foegeding, 2007; Brenner, Nicolai, & Johannsson, 2009; Carrillo et al., 2013; Broedersz & MacKintosh, 2014) including agar(ose) gels (Barrangou et al., 2006; Nakauma et al., 2014). The subsequent and abrupt decay of the storage modulus G' for strain amplitudes larger than γ_c can be interpreted as the interfacial debonding of the gel from the upper plate. The latter conclusion is supported by the fact that the gel remains intact and shows no macroscopic crack nor residues on the solid surfaces when raising the upper plate after the strain sweep test.

Therefore γ_c provides an estimate of the critical strain above which the gel debonds from the metallic plates of the shear cell as a result of interfacial debonding and water release, although we cannot rule out the presence of microscopic failure inside the gel. Furthermore, the strain responses $G'(\gamma)$ of gels prepared after various incubation times of the agar solution can be superimposed by plotting $(G' - G'_*)/(G'_m - G'_*)$ vs. γ/γ_c , where G'_* denotes the steady-state storage modulus determined in the linear regime [Fig. 3.7(b)]. Such a rescaling suggests that the same debonding scenario is at stake for all the strain sweep experiments. As the critical strain γ_c increases linearly with the incubation time \mathcal{T} [inset in Fig. 3.7(b)], one can conclude that softer gels prepared from sol heated over

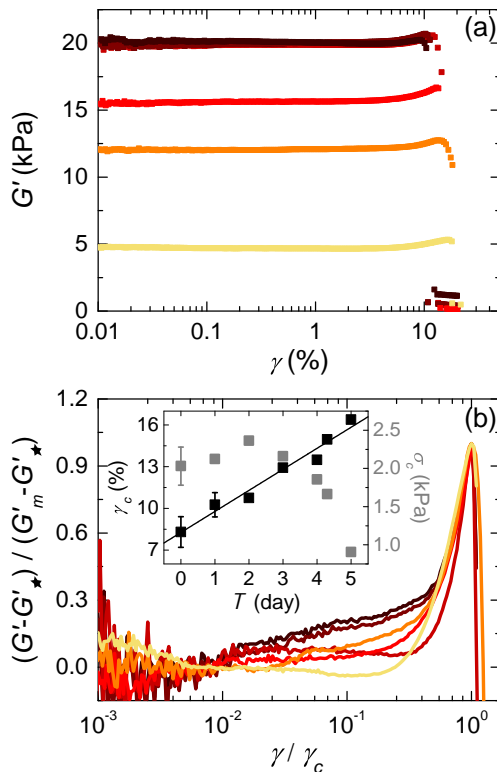


Figure 3.7: (a) Storage modulus G' vs. strain amplitude γ monitored during a strain sweep experiment performed at $f = 1$ Hz. The strain amplitude increases logarithmically from $\gamma = 0.01\%$ to 100% over a duration of 2160 s (9 s/point). Colors from black to yellow correspond to 1.5% wt. agar gels obtained after different incubation times of the same agar solution at 80°C : $\mathcal{T} = 1$ hour, 1 day, 2, 3, 4 and 5 days. (b) Normalized storage modulus $(G' - G'_*)/(G'_m - G'_*)$ where $G'_* = G'(\gamma = 0.1\%) \simeq G'_0$ vs. normalized strain amplitude γ/γ_c , where γ_c denotes the critical strain amplitude at which G' is maximum. Inset: Evolution of γ_c (■) and $\sigma_c = \sigma(\gamma_c)$ (■) vs. the incubation time \mathcal{T} of the agar sol. The black line corresponds to the best linear fit of data: $\gamma_c = 7.8 + 1.7\mathcal{T}$ with \mathcal{T} in days. Error bars were determined by repeating the experiments on three different samples.

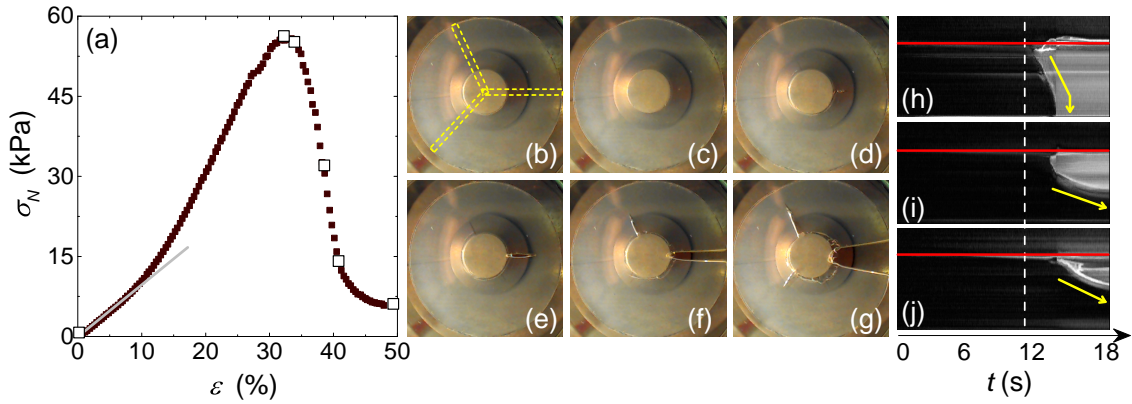


Figure 3.8: (a) Normal stress σ_N vs. compressive strain ϵ during the indentation run with a flat-ended cylinder, of an agar gel disk of thickness 3.9 mm, prepared from a fresh solution ($\mathcal{T} \simeq 1$ hour). (b)–(g) Images taken during the indentation of the disk at $\epsilon = 0\%$, 32.7% (stress maximum), 34.2% (nucleation of the first macroscopic crack), 39.1%, 41.9% (the first crack reaches the outer edge of the agar disk) and 48%. The corresponding strain deformations are emphasized by open squares in (a). The spatial scale is set by the gel diameter of 34 mm, and the circle visible at the center of each picture is the bottom surface of the indenter (diameter 10 mm) moving down at a constant speed of $100 \mu\text{m/s}$. (h)–(j) Spatio-temporal diagrams obtained from the orthoradial projection of the gray levels within the three radial sections that encompass the fractures, and which are pictured as yellow rectangles in (b) – respectively horizontal (0°), 120° and 240° . For all the diagrams, the first image is subtracted from the image sequence to improve the contrast and better visualize the crack propagation. The upper and lower limits of each diagram correspond respectively to the center and the peripheral region of the gel disk, so that the height of each diagram represents the gel disk radius of 17 mm. The horizontal red line refers to the outer region of the indenter. The white vertical dashed line in (h)–(j) marks the time for which the stress reaches the maximum value observed on the mechanical response reported in (a). The slope of the yellow arrows in (h)–(j) further gives an estimate of the crack front velocity.

longer durations release water less easily under shear. In other words, the transition from static friction to hydrodynamic lubrication under shear occurs at a larger critical strain for softer gels obtained after a prolonged incubation of the agar solution. Nonetheless, we shall emphasize that γ_c is characteristic of the boundary conditions, and that the use of other materials for the upper and lower plates would lead to different values and/or dependence of γ_c with the incubation time \mathcal{T} . Note that the adhesion properties of agar gels on various solid surfaces will be discussed in more details in Section 4.2.4 and Section 4.3.5 in Chapter 4.

Finally, the critical debonding stress defined as $\sigma_c = \sigma(\gamma_c)$ also bears a signature of the aging of the agar sol and markedly drops after an extensive incubation of the agar sol at 80°C, in a similar way as the gel viscoelastic moduli does [Fig. 3.4(e)–(f)]. Indeed, the debonding shear stress is roughly constant for incubation times \mathcal{T} shorter than 3 days and decreases for gels prepared from a solution incubated over a longer period [inset Fig. 3.7(b)].

Macro-indentation experiments.– The bulk mechanical properties of agar gels in the non-linear regime were investigated using macro-indentation tests. Circular agar gel pellets (diameter of about 34 mm and thickness of about 4 mm) are prepared after different incubation times \mathcal{T} of the same agar solution and indented with a flat-ended cylinder of diameter 10 mm. The deformation and the damage of the gel disk are monitored from below through a transparent bottom plate by means of a high resolution webcam, while the normal force sensor of the rheometer (DHR-2, TA instrument) is used to record the stress-strain curve $\sigma(\epsilon)$ (see Section 2.3.2 in Chapter 2 for technical details).

Indentation results for a gel prepared from a fresh solution ($\mathcal{T} \simeq 1$ h) are reported in Figure 3.8. The stress increases linearly with the strain up to a few percents, followed by a faster than linear increase associated with the strain hardening of the gel, up to a maximum value $\sigma_N^{(m)}$ at $\epsilon = \epsilon^{(m)}$. Meanwhile, the agar gel shows no visible damage by the naked eye neither in the linear regime, nor in the strain hardening regime [Fig. 3.8(b)] and remains intact up to the stress maximum [Fig. 3.8(c)]. The first fracture becomes visible right after the stress maximum, and nucleates at a finite distance from the indenter [Fig. 3.8(d)]. As the compressive strain increases beyond $\epsilon^{(m)}$, the stress rapidly decays towards a lower plateau value, while two other fractures nucleate at an angle of about 120° of the first fracture [Fig. 3.8(e) and (f)]. The three fractures grow along the disk radius and propagate towards the edge of the gel [Fig. 3.8(g)]. A spatio-temporal plot consisting in an orthoradial projection of the gray levels within a thin radial section of the gel disk pictured in yellow in Figure 3.8(b), confirms that the first fracture indeed nucleates at a finite distance from the indenter [Fig. 3.8(h)]. Furthermore, the former representation shows that the tip of the first fracture grows at a constant speed $u_1 = (4.7 \pm 0.4)$ mm/s up to about 3 mm from the edge of the disk, where the fracture opening suddenly accelerates. The second and third fractures grow with a lower velocity, which also decreases as the crack propagates towards the edge of the disk [Fig. 3.8(i) and (j)].

Building upon this first test, the exact same indentation runs were repeated on agar gels prepared after different incubation times \mathcal{T} of the agar solution. Strain-stress curves $\sigma_N(\epsilon)$ reported in Figure 3.9(a) indicates a similar mechanical behavior to the one discussed above for $\mathcal{T} = 1$ hour: the compressive stress first increases linearly in the small strain regime ($\epsilon \leq 5\%$), then the soft material shows some strain hardening under stress before reaching a rupture point which coordinates $(\epsilon^{(m)}, \sigma_N^{(m)})$ strongly depends on the incubation time. Beyond the maximum stress, a first fracture nucleates in the vicinity of the indenter, and the stress shows a rapid decay towards a plateau value concomitantly to the nucleation and growth from the intender of two or three supplemental radial fractures. The Young's modulus E of agar gels can be estimated from the initial slope of the stress-strain curves (see Section 2.3.2 in Chapter 2 for more technical details). Figure 3.9(b)–(d) report the evolution of the Young's modulus E as well as the rupture parameters $\sigma_N^{(m)}$ and $\epsilon^{(m)}$ with the incubation time \mathcal{T} of the agar sol. For $\mathcal{T} \leq 2$ days, the three parameters show consistent values within error bars, illustrating that the Young's modulus and the rupture point remain the same despite some chemical degradation of the polysaccharides is already present (Fig. 3.1). For $\mathcal{T} \geq 3$ days, the Young's modulus E decreases linearly to

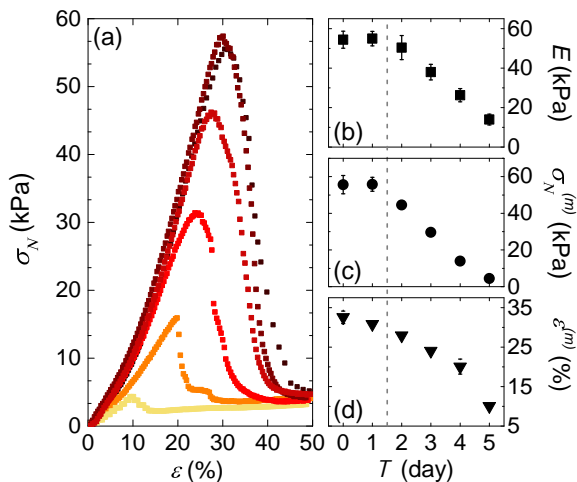


Figure 3.9: (a) Normal stress σ_N vs. compressive strain ϵ monitored during macro-indentation experiments of 1.5% wt. agar-SA gels. Colors from black to yellow stand for 1.5% wt. agar gels prepared from the same hot solution, which is left at $T = 80^\circ\text{C}$ for different incubation times: $\mathcal{T} = 1$ hour, 1 day, 2, 3, 4 and 5 days. (b) Young's modulus E of the gel vs. the incubation time \mathcal{T} of the agar sol when considering a Poisson coefficient of $\nu = 0.3$. (c) Stress maximum $\sigma_N^{(m)}$ reached during the indentation vs. the incubation time \mathcal{T} . (d) Compressive strain $\epsilon^{(m)}$ associated with the stress maximum vs. the incubation time \mathcal{T} . Error bars were determined by repeating the experiments on three different samples.

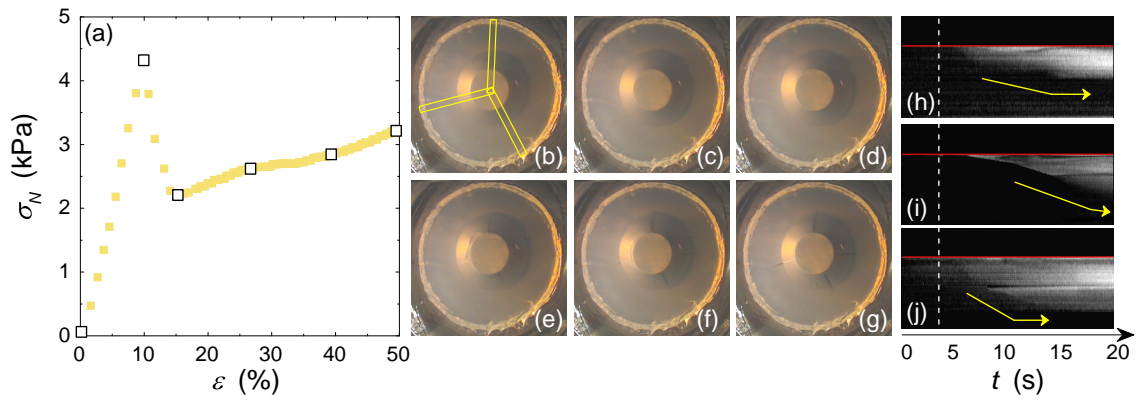


Figure 3.10: Normal stress σ_N vs. compressive strain ϵ during the macro-indentation experiment of a 1.5% wt. agar-SA gel disk prepared from a hot solution incubated during $\mathcal{T} = 5$ days. (b)–(g) Images taken during the indentation of the disk at respectively $\epsilon = 0$, $\epsilon = 9.8\%$ (stress maximum), $\epsilon = 15.1\%$, 26.2% , 39.1% and 48.6% . The corresponding strain deformations are emphasized by open squares in (a). The spatial scale is set by the gel diameter of 34 mm, and the circle visible at the center of each picture is the surface of the indenter (diameter 10 mm) moving down at a constant speed of $100 \mu\text{m/s}$. (h)–(j) Spatio-temporal diagrams obtained from the orthoradial projection of the gray levels within the three radial sections that encompass the first three fractures growing during the test, and which are pictured as yellow rectangles in (b), respectively upper, lower and almost horizontal rectangle. For all the diagrams, the first image is subtracted from the image sequence to improve the contrast and better visualize the crack propagation. The upper and lower limits of each diagram correspond respectively to the center and the peripheral region of the gel disk, so that the height of each diagram represents the gel disk radius of 17 mm. The horizontal red line refers to the outer edge of the indenter. The white vertical dashed line in (h)–(j) marks the time at which the stress reaches the maximum value observed on the mechanical response reported in (a). The slope of the yellow arrows in (h)–(j) further gives estimate of the crack front velocity.

reach one tenth of the initial value for a gel prepared from a sol incubated for $\mathcal{T} = 5$ days. Furthermore, the gel failure occurs at a lower compressive strain with increasing incubation time \mathcal{T} of agar sol: from $\epsilon^{(m)} \simeq 30\%$ for $\mathcal{T} = 1$ day, down to $\epsilon^{(m)} \simeq 10\%$ for $\mathcal{T} = 5$ days [Fig. 3.10(a)]. The failure scenario of a gel prepared from an incubated agar solution shows quantitative differences with that reported for a fresh gel [Fig. 3.8 and Fig. 3.10]. Indeed, for a gel prepared after $\mathcal{T} = 5$ days of incubation of the agar sol at 80°C , the stress maximum is associated with the formation of a plastic region in the vicinity of the indenter [see the left side of the indenter in Figure 3.10(d)], and fractures only grow at much larger strain values $\epsilon^{(m)}$ [Fig. 3.10(e)–(g)].

As a possible observable representative of the difference in the rupture process of gels prepared after different incubation times \mathcal{T} , one considers the nucleation time τ of the first fracture that is visible by naked eye. The first fracture appears at a lower compressive strain when increasing the incubation time of the agar sol, as clearly observed in the spatio-temporal diagrams of the gel radial section which encompass the first fracture for gels prepared after an incubation time $\mathcal{T} = 1, 3$ and 5 days [Fig. 3.11(a)–(c)]. More quantitatively, the nucleation time of the first fracture starts decreasing for $\mathcal{T} \geq 2$ days [Fig. 3.11(d)], in a similar fashion to the behavior of the compressive strain $\epsilon^{(m)}$ associated with the stress maximum, which also decreases after two days of incubation, as discussed above [Fig. 3.9(d)]. Furthermore, although the first fracture appears sooner with increasing incubation time, fractures become less visible and propagate more slowly as illustrated by the slope of the yellow arrows in Figure 3.11(a)–(c). Finally, the crack propagation becomes much more localized in the radial direction, for gels prepared from a solution incubated at 80°C for more than two days [Fig. 3.10(b)–(g)]. Indeed, for increasing incubation time

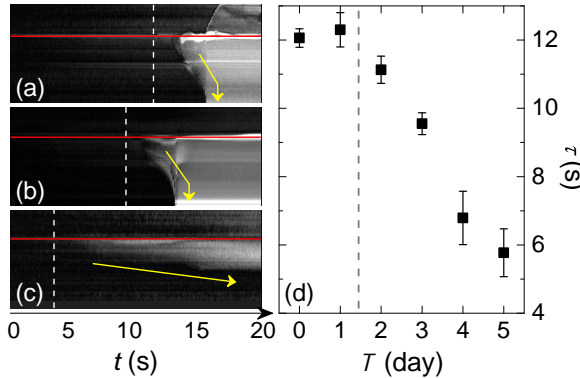


Figure 3.11: (a)–(c) Spatio-temporal diagrams of the radial section of 1.5% wt. agar gel disks that encompass the first fracture, for gels prepared at different incubation times. From top to bottom: $\mathcal{T} = 1, 3$ and 5 days. For each diagram, the first image is subtracted from the image sequence for a better contrast. The horizontal red line refers to the outer edge of the indenter while the height of each diagram represents the gel disk radius of 17 mm. The white vertical dashed lines mark the time at which the compressive stress reaches the maximum observed in Figure 3.9(a). The slope of the yellow arrows in (a)–(c) illustrate the velocity of the crack front. (d) Nucleation time τ of the first fracture observed during macro-indentation experiments of gels prepared after different incubation times \mathcal{T} of the same agar solution at $T = 80^\circ\text{C}$.

\mathcal{T} , agar gels exhibit a more ductile behavior compared to the brittle-like rupture scenario reported in Figure 3.8 for gels prepared from a fresh agar sol. Such a brittle to ductile transition is clearly visible in the post-mortem images of the gel disks [compare Fig. 3.8(g) and Fig. 3.10(g)]. In brief, a prolonged incubation of the agar solution produces weaker gels through which fractures propagate more slowly because of the gel ductile behavior. Such a ductile behavior is also responsible for the increase of the critical shear strain γ_c above which the gel debonds from the plates under shear, as reported above in Figure 3.7(b).

3.1.4 Discussion and conclusion

We can conclude from Section 3.1.1 that the agarose molecules of an agar solution stored at $T = 80^\circ\text{C}$ experience hydrolysis and intramolecular oxidation less than a day after starting the incubation. Yet, the impact on the gelation dynamics of the solution aging is only visible after three days of incubation, at $\text{pH} \simeq 5$. Indeed, the intermolecular oxidation of the agarose molecules, which is responsible for a change in structural and mechanical properties of the agar gels only occurs after three days of incubation. I shall emphasize that the exact value of three days depends on the temperature at which the agar solution is stored, and also on the agar composition, which may affect the evolution of the pH. Indeed, I have repeated the same test as the one reported in Figure 3.4 on a different agar brand (BioMérieux instead of Sigma-Aldrich). In the latter case, the shear elastic modulus starts decreasing after an incubation time longer than five days (Fig. 3.12) instead of three (Fig. 3.4). Therefore, any estimate of the critical duration \mathcal{T}_c below which the incubation period of an agar sol has no effect on the agar gels properties should be determined anew for every agar-based sample of interest, especially if that sample contains additional components, which may impact the pH and thus the oxidation and the hydrolysis of the agarose molecules.

For long incubation times $\mathcal{T} > \mathcal{T}_c$ of the solution, the agar gel microstructure becomes coarser as the result of intermolecular condensation of the agarose molecules. The growth of micron-sized foils during the gelation creates larger pores in the microstructure of the agar gel leading to both weaker shear and compression elastic modulus. A few days of incubation of the agar sol above the gelation temperature lower the storage modulus of the agar gel by 80%, which illustrates how the incubation time may affect and could be

used to modify the agar gel mechanical properties. Concomitantly with the weakening of the elastic properties, gels made from overcooked agar sol exhibit smaller yield strains $\epsilon^{(m)}$ in compression and a more ductile behavior as fractures created during macro-indentation tests remain localized close to the indenter. I shall emphasize that one cannot relate directly the decrease of $\epsilon^{(m)}$ to the change of molecular weight of the agarose molecules. Indeed, increasing the incubation time of the agar sol leads both to a condensation of the polysaccharides and an oxidation, i.e. chain breakage, which makes it difficult to compare the present results with data from previous rheological studies performed on agarose gels of different molecular weight (Watase & Nishinari, 1983). Finally, a prolonged heating of the agar sol also results in an increase of the critical shear strain γ_c above which the gel debonds from the plate-plate geometry during oscillatory shear experiments of increasing strain amplitude.

Beyond macro-indentation and oscillatory shear tests, we have shown that a 1.5% wt. agar gel prepared from a fresh agar solution exhibits a Poisson coefficient such as $0.1 \leq \nu \leq 0.3$. Such values are quantitatively smaller than the value of 0.5 commonly admitted in the literature (Chen, Liao, Boger, & Dunstan, 2001; Scandiucci de Freitas et al., 2006; Norziah, Foo, & Karim, 2006) and shows that 1.5% wt. agar gels are somewhat compressible. Experimentally, the main uncertainty on the Poisson coefficient ν comes from the determination of the storage modulus G' . Only the zero normal force protocol used here allows to compensate for the gel contraction that otherwise strongly affects the terminal value of the elastic shear modulus G' determined with a constant gap width geometry (Mao et al., 2016). Indeed, the storage modulus of agar gels reported in (Norziah et al., 2006) and measured at constant gap width, shows either a drift associated with a strain hardening behavior or an abrupt drop during the gelation, both effects resulting from the contraction of the sample during gel formation that may lead to a systematic error on G' .

To conclude, the present study quantitatively extends the pioneering observations of (Whyte, Englar, & Hosford, 1984) on heat-induced aging of agar solutions and provides a quantitative estimate for the critical duration below which an agar solution can be stored at high temperature without affecting the properties of the subsequent gels. As such, our results should serve in the future as a guideline for the design of efficient manufacturing processes of agar-based materials.

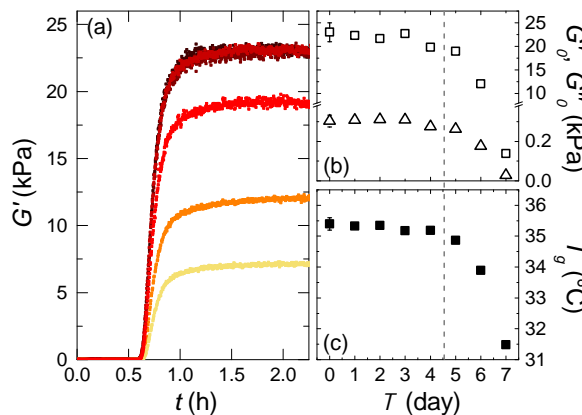


Figure 3.12: Gelation experiments performed on 1.5% wt. agar-BM1 gels. (a) Storage modulus G' vs time t during the cooling from $T = 70^\circ\text{C}$ down to 20°C , at $\dot{T} = 1^\circ\text{C}/\text{min}$ of various samples extracted from the same agar sol after various incubation times $\mathcal{T} = 1$ hour, 2 days, 4, 6 and 7 days coded in color from black to yellow. (b) Steady-state values of storage (G' , \square) and loss (G'' , \triangle) moduli reached at the end of the gelation process vs. the incubation time \mathcal{T} of agar solution. (c) Gelation temperature T_g defined as the crossing temperature of G' and G'' , vs. the incubation time \mathcal{T} . Error bars in (b) and (c) are only indicated on the first point and were determined by repeating the experiment with three different agar solutions.

3.2 Cooling kinetics of hot agar solutions

Section 3.1 was focused on the impact of the incubation time of the agar sol at 80°C, on the gel structural and mechanical properties. In this section, I will discuss the influence of thermal history during the agar gel preparation, in relation with the cooling of the hot agar sol. All the agar gels involved in this section are prepared with samples extracted from a fresh solution ($\mathcal{T} = 0$) containing 1.5% wt. of agar (Sigma Aldrich, ref. A5306 – see Section 2.1 in Chapter 1). I study here the impact of the cooling rate \dot{T} of the agar sol on the gel elastic properties, as well as the role of the amplitude of the temperature drop and the impact of a pause at constant temperature during the cooling process. The agar gelation is monitored in a parallel-plate geometry with mixed boundary conditions: a rough and passivated upper duralumin plate, and a smooth and Teflon coated bottom Peltier plate. The agar gel sample, sandwiched between the two plates is surrounded with an oil layer to prevent water evaporation. Finally, all the rheological experiments reported in this section are conducted using the zero normal force protocol described in Section 2.3.1, in Chapter 2.

3.2.1 Impact of cooling rate

A series of gelation experiments were performed on 1.5% wt. agar solution at different cooling rates ranging from 0.1 to 10°C/min to analyze the impact of the cooling rate \dot{T} on the gel elastic properties. For each experiment, the temperature is decreased from 70°C down to $T_f = 20^\circ\text{C}$. The zero normal force protocol is applied to monitor the gelation, and the amplitude of the oscillating strain is further adapted to the value of the storage modulus, to properly determine the intersection of G' and G'' (see Section 2.3.1 for technical details).

Results are displayed in Figure 3.13. The formation dynamics of the gel strongly depends on the cooling rate \dot{T} : a rapid cooling results in an earlier gelation [Fig. 3.13(a)]. More quantitatively, the gelation time t_g , defined here as the time at which $G'(t_g) = G''(t_g)$ is inversely proportional to the cooling rate \dot{T} and allows us to rescale the temporal evolution of the storage modulus into a single master curve [Fig. 3.13(b)]. Such a rescaling hints at a unique gelation scenario that is independent of the cooling rate. The gelation temperature, defined as $T_g = T(t_g)$ decreases with the cooling rate [Fig. 3.13(d)]. Indeed, the gelation occurs at $T = 37^\circ\text{C}$ at $\dot{T} = 0.1^\circ\text{C}/\text{min}$, while the agar sol remains liquid down to 31°C for a rapid cooling rate of $10^\circ\text{C}/\text{min}$ [Fig. 3.13(d)]. Interestingly, the gelation temperature has no influence upon the steady-state viscoelastic properties of the gel at $T = 20^\circ\text{C}$ since the terminal values $\bar{G}'_f = (24.2 \pm 0.6)$ kPa and $\bar{G}''_f = (340 \pm 10)$ Pa are independent of the cooling rate \dot{T} in the range of $0.1^\circ\text{C}/\text{min}$ to $10^\circ\text{C}/\text{min}$, within error bars as shown in Figure 3.13(c). Such a result strongly suggests that the gel should present the same microstructure, which is confirmed by scanning cryoelectron microscopy (cryo-SEM) observations on agar gel samples prepared at different cooling rates: $\dot{T} = 0.2^\circ\text{C}/\text{min}$, $1^\circ\text{C}/\text{min}$, and $10^\circ\text{C}/\text{min}$. As shown in Figure 3.14, the gel microstructure is qualitatively the same, which supports the idea that lower cooling rates only delay the gelation, without affecting the terminal viscoelastic properties of a 1.5% wt. agar gel. Finally, the sample contraction, which is robustly observed during agar gelation between parallel plates, becomes more important for increasing cooling rates, independently of the presence of an oil rim [Fig. 3.13(e)]. The relative sample contraction increases from about 1% for $\dot{T} \leq 1^\circ\text{C}/\text{min}$, up to 5%, at $\dot{T} = 10^\circ\text{C}/\text{min}$. This last point will be further discussed in Section 3.2.4.

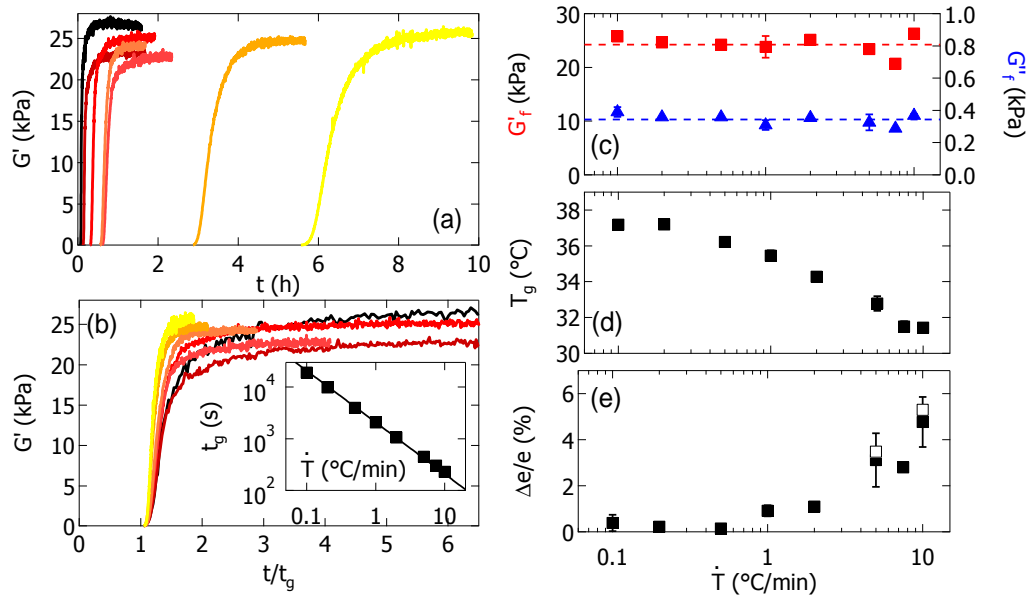


Figure 3.13: (a) Evolution of the storage modulus G' vs. time t when decreasing more or less rapidly the temperature of a 1.5% wt. agar solution from 70°C to 20°C. Colors from black to yellow encode different cooling rates: $\dot{T} = 10, 5, 2, 1, 0.5, 0.2, 0.1^\circ\text{C}/\text{min}$. (b) Same data set plotted vs. the normalized time t/t_g , where t_g is the gelation time defined by the intersection of G' and G'' . Inset: gelation time t_g vs. the cooling rate \dot{T} . The black line corresponds to the best linear fit of the data in logarithmic scale, which equation is: $t_g \dot{T} = 34.9^\circ\text{C}$. (c) Terminal values G'_f (■) and G''_f (▲) of the storage and loss moduli respectively vs. the cooling rate \dot{T} . The horizontal dashed lines stand for the mean values of the gel viscoelastic moduli: $\bar{G}'_f = (24.2 \pm 0.6)$ kPa and $\bar{G}''_f = (340 \pm 10)$ Pa. (d) Gelation temperature T_g vs. the cooling rate \dot{T} . (e) Relative variation of the gap width e vs. the cooling rate \dot{T} . Each experiment is performed with an initial gap width $e_0 = 500 \mu\text{m}$ and with a thin layer of oil surrounding the sample. Open squares (□) denote experiments performed with water in the solvent trap and no surrounding oil layer.

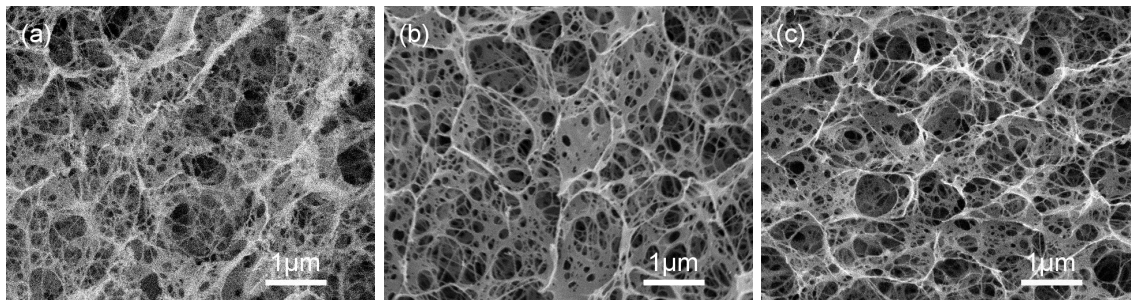


Figure 3.14: Cryo-SEM images of 1.5% wt. agar gels prepared at different cooling rates: (a) $\dot{T} = 0.2^\circ\text{C}/\text{min}$, (b) $\dot{T} = 1^\circ\text{C}/\text{min}$, and (c) $\dot{T} = 10^\circ\text{C}/\text{min}$. (see Section 2.2.1 in Chapter 2 for technical details).

3.2.2 Impact of a temperature drop

Here, one considers a fixed cooling rate $\dot{T} = 1^\circ\text{C}/\text{min}$ and a variable final temperature T_f at the end of the cooling ramp to assess the impact of the amplitude of the temperature drop on the gel mechanical properties. The sample is loaded as a liquid into the preheated gap of the rheometer, and the temperature is swept from 70°C down to T_f , where the terminal temperature T_f is chosen between 20°C and 38°C.

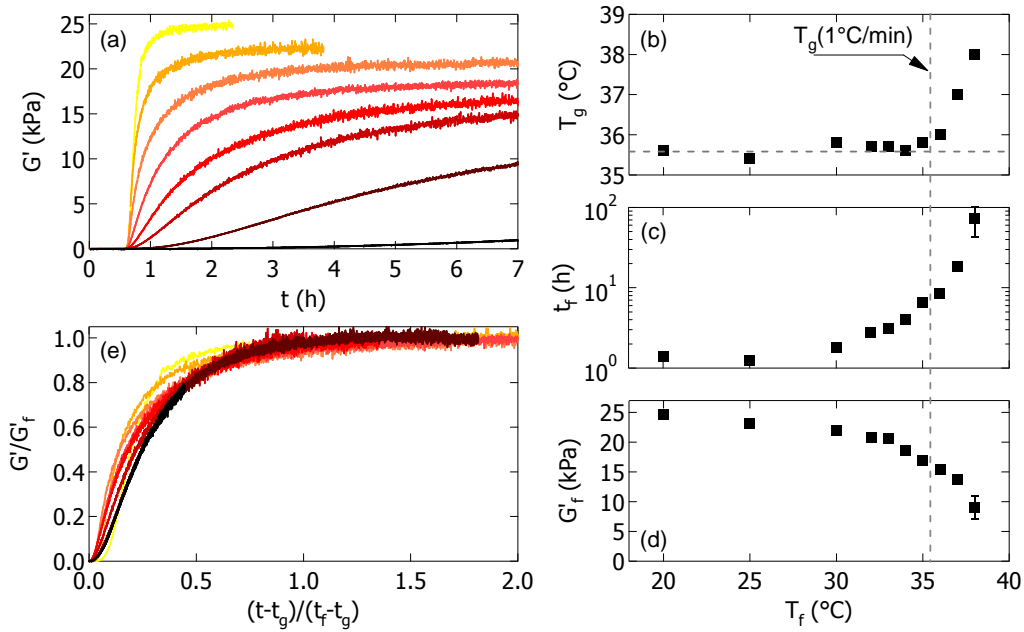


Figure 3.15: (a) Evolution of the storage modulus G' vs. time t while cooling a 1.5% wt. agar-SA solution at a constant rate of $\dot{T} = 1^\circ\text{C}/\text{min}$ from $T = 70^\circ\text{C}$ down to T_f . Colors from yellow to black stand for different end-of-ramp temperatures: $T_f = 20, 30, 32, 34, 35, 36, 37$ and 38°C . (b) Gelation temperature T_g as determined by the intersection of G' and G'' vs. the terminal temperature T_f . (c) Time t_f for the storage modulus to reach a steady-state value vs. the terminal temperature T_f in semi-logarithmic scale. (d) Steady-state value of the storage modulus G'_f vs. the terminal temperature T_f . (e) Normalized storage modulus G'/G'_f vs. reduced time $(t-t_g)/(t_f-t_g)$, where G'_f stands for the steady-state value of G' . All experiments are performed with a thin layer of oil surrounding the sample.

As illustrated in Figure 3.15(a), the terminal temperature T_f impacts both the gelation dynamics and the steady-state value of the storage modulus. Imposing a cooling rate $\dot{T} = 1^\circ\text{C}/\text{min}$, fixes the gelation temperature to $T_g \simeq 35.5^\circ\text{C}$ [Fig. 3.13(d)]. I will therefore discuss the gelation dynamics whether T_f is larger or smaller than 35.5°C . For $T_f \leq 35.5^\circ\text{C}$, the gelation always starts at $T_g = 35.5^\circ\text{C}$ confirming that the intersection of G' and G'' is a robust observable mainly depending on the cooling rate [Fig. 3.15(b)]. Moreover, the time t_f for the storage modulus to reach a steady-state value (within 5%) increases with the final temperature T_f , which accounts for an increasing duration of the gelation process as the terminal temperature is increased [Fig. 3.15(c)]. Surprisingly, the gelation dynamics becomes slower for $T_f \geq 35.5^\circ\text{C}$, but the gelation is still observed, at least up to $T = 38^\circ\text{C}$. Within this temperature range, the slowing down of the dynamics now results from the increase of both the gelation time t_g and the time t_f to reach the steady-state, i.e. for increasing values of T_f , the intersection of G' and G'' occurs later and once the gel is forming ($G' > G''$) more time is required for the storage modulus G' to reach the terminal value G'_f [Fig. 3.15(b) and (c)]. Finally, one observes the formation of softer gels with a lower storage modulus G'_f for increasing terminal temperatures T_f [Fig. 3.15(d)]. Such a behavior is observed whether T_f is smaller or larger than $T_g(1^\circ\text{C}/\text{min}) \simeq 35.5^\circ\text{C}$, which suggests that the gel formation scenario is likely to be the same on both sides of $T_g(1^\circ\text{C}/\text{min})$ despite the dynamics is strongly slowed down for $T_f > T_g(1^\circ\text{C}/\text{min})$.

Indeed, here again the gelation curves $G'(t)$ obtained for different terminal temperature T_f can be rescaled into a single master curve by plotting G'/G'_f versus $(t-t_g)/(t_f-t_g)$ [Fig. 3.15(e)]. The latter function provides the best rescaling among other temporal func-

tions such as t/t_f , t/t_g , etc., which demonstrates that the duration $t_f - t_g$ between the gelation start and the steady-state is the relevant unit of time associated with the gelation of 1.5% wt. agar gels. Furthermore, the existence of a master curve confirms the existence of a single gelation scenario, which is supposedly the same as the one evidenced by the experiments performed at different cooling rates (Section 3.2.1). This result also indicates that the gel storage modulus is mostly a function of the terminal temperature T_f reached at the end of the temperature ramp, and that the functional $G'_f(T_f)$ reflects the temperature dependence of a gel with a single microstructure, whether it has been formed above or below 35.5°C. This point is discussed in more detail in the following paragraph.

3.2.3 Impact of a temperature plateau during cooling

A last series of experiments was performed to determine whether the agar gels obtained at 20°C after cooling and waiting at different intermediate temperatures close to $T_g(1^\circ\text{C}/\text{min}) \simeq 35.5^\circ\text{C}$ display similar mechanical properties. Gelation experiments of 1.5% wt. agar solutions similar to the ones reported in Section 3.2.2 are performed by decreasing the temperature at $1^\circ\text{C}/\text{min}$ from 70°C down to a plateau temperature T_p , chosen between 20°C and 38°C and maintained for 8 h before resuming the cooling down to $T_f = 20^\circ\text{C}$. Figure 3.16(a) shows the gelation kinetics for a temperature stop at $T_p = 33^\circ\text{C}$ during 8 hours. The storage modulus reaches a constant value while $T = T_p$ in agreement with data reported in Figure 3.15. The subsequent drop of temperature down to $T_f = 20^\circ\text{C}$ leads to a new increase of the storage modulus G' which terminal value, G'_f , is compatible with the value measured by direct cooling from 70°C to 20°C , i.e. without any plateau temperature. The experiments repeated at different values of the plateau temperature T_p further support the following conclusion: the terminal values G' and G'' of the agar gel

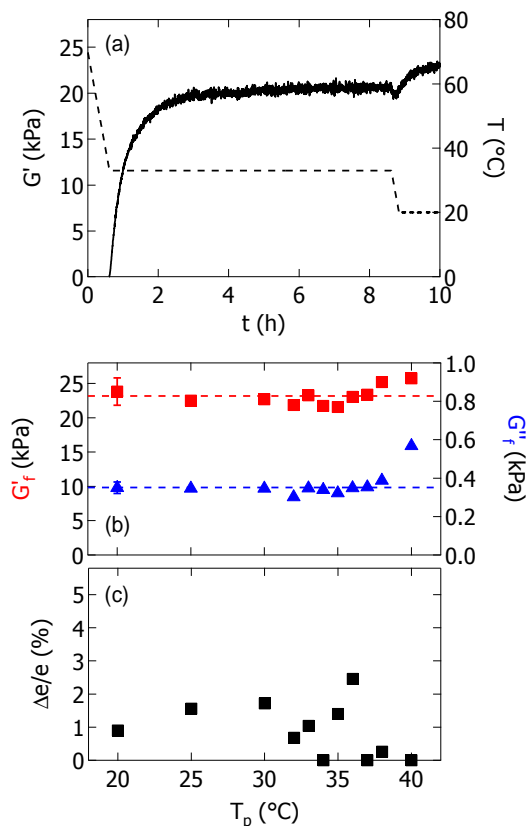


Figure 3.16: (a) Evolution of the storage modulus G' (solid line, left axis) and temperature T (dashed line, right axis) versus time t . The temperature is decreased at a cooling rate $\dot{T} = 1^\circ\text{C}/\text{min}$, from $T = 70^\circ\text{C}$ down to $T = T_p = 33^\circ\text{C}$. The latter temperature is maintained for 8 h before resuming the cooling down to $T_f = 20^\circ\text{C}$ at $\dot{T} = 1^\circ\text{C}/\text{min}$. (b) Terminal values G'_f (■) and G''_f (▲) of the storage and loss moduli vs. the plateau temperature T_p . The horizontal dashed lines stand for the mean values of the gel viscoelastic moduli: $\bar{G}'_f = (23.2 \pm 0.5)$ kPa and $\bar{G}''_f = (0.35 \pm 0.01)$ kPa. For the sake of clarity, the typical error bar determined by repeating the experiment is indicated only on one data point. (c) Relative variation of the gap width e vs. the plateau temperature T_p . All experiments are performed with a thin layer of oil surrounding the sample.

viscoelastic moduli are independent of any plateau temperature T_p [Fig. 3.16(b)], whether the temperature stop occurs above or below the gelation temperature $T_f = 35.5^\circ\text{C}$ selected by the cooling rate. In the case of a temperature plateau and final cooling at 20°C , the terminal values of G'_f and G''_f are once again compatible within error bars with the ones reported in Figure 3.13(c) for different cooling rates. Such a robust result could indicate that the gelation of a 1.5% wt. agar solution is mainly controlled by spinodal demixing phenomena expected to take place over timescales much shorter than the timescale associated with the cooling process (i.e. 50 min). As a result, the storage and loss moduli of the agar gel formed upon cooling are fixed by the terminal temperature T_f while the thermal history poorly impacts the gel linear properties. Finally, the gel contraction slightly varies from one experiment to the next, ranging between 0 and 2%, with a mean value $\Delta e/e \simeq 1\%$ [Fig. 3.16(c)], but does not show any significant trend with the plateau temperature T_p . Note that such a non-zero value justifies the use of the zero normal force protocol instead of a constant gap width to determine the gel viscoelastic properties.

3.2.4 Discussion and conclusion

The present study proves that the cooling rate \dot{T} affects neither the terminal elastic properties nor the microstructure of agar gels. This observation strikingly contrasts with results from the literature where agarose gels prepared at constant gap width appear stronger for lower cooling rates (Medin, 1995; Mohammed et al., 1998). Such a discrepancy may be related to the sample contraction during the gelation and associated with a partial loss of contact between the gel and the solid plates in previous studies, as already discussed in Chapter 2 [see Fig. 2.2(a) and (d)]. Indeed, a sample contraction is robustly observed during the gel formation, and further increases with the cooling rate [Fig. 3.13(d)] ($\Delta e/e \approx 5\%$, at $\dot{T} = 10^\circ\text{C}/\text{min}$). A rapid cooling freezes the microstructure far from its minimum energy state and the subsequent relaxation of internal elastic stresses then favors the contraction of the network². For a fixed gap width, the sample contraction is enough to trigger a partial loss of contact between the gel and the plates leading to an underestimation of the storage modulus. Besides, the present results demonstrate that larger cooling rates lead to larger gel contractions, which is compatible with the apparent decrease of the gel storage modulus reported in the literature when investigating the rheological properties of gels under rapid cooling and constant gap width. Hence the relevance of the zero normal force protocol, especially for large cooling rates where the gel contraction becomes non-negligible.

Moreover, one should keep in mind that the cooling rate \dot{T} selects the gelation temperature T_g , estimated from the intersection of viscoelastic moduli of G' and G'' . However, the cooling rate has no detectable influence upon the linear viscoelastic properties of agar gels determined at 20°C , at least over two decades of cooling rates from $0.1^\circ\text{C}/\text{min}$ to $10^\circ\text{C}/\text{min}$. The sample contraction depending on the cooling rate and the weak dependence of agar gel rheology upon the thermal history are not incompatible. Indeed, the storage modulus of the agar gel scales as a power-law of the agarose concentration, with an exponent close to 2.2 (Normand, Lootens, et al., 2000). Therefore a 5% increase in the

²Surprisingly, the rapid cooling of liquid cocoa butter or chocolate results in a similar relative contraction during the liquid–solid transition [of about 5% for cocoa butter cooled from 50°C down to 20°C at a rate of $5^\circ\text{C}/\text{min}$ (Habouzit & Snabre, 2010)] that greatly helps the release of the fully crystallized material from a mold. Furthermore, a cooling rate smaller than $1^\circ\text{C}/\text{min}$ (under-tempered conditions in chocolate production) promotes both the small-scale rearrangements of triglycerides and the growth of more stable polymorphs structures well before complete cocoa butter crystallization thus preventing a macroscopic contraction and the demolding of the solid material.

agar concentration due to the gap width decrease during a rapid cooling results in a 12% increase in the storage modulus G' , at best. The uncertainty in the measurement of the storage modulus G' is of the same order of magnitude as emphasized in Section 2.3.1, in Chapter 2, which may explain why the reported viscoelastic properties of agar gels appear as weakly influenced by the cooling rate and the thermal history of the sample.

Finally, the gel viscoelastic properties are mostly controlled by the terminal temperature at the end of the cooling process. Such a simple and striking result strongly suggests that the local gelation scenario is mainly controlled by the rapid spinodal demixing of the agar solution (Manno et al., 1999). More concentrated samples, such as 2% wt. agarose gel, display properties that are more sensitive to the thermal history (Aymard et al., 2001), which is probably linked to the fact that the gelation scenario then involves a competition between spinodal demixing and direct gelation (Manno et al., 1999; San Biagio et al., 1996). These results provide a strong guideline for the manufacturing of culture media in Petri dishes. Indeed, the agar-based sol is poured hot in the Petri dishes, that are cooled down at about 5°C/min by crossing a tunnel on a conveyor belt inside which both temperature and humidity are controlled. Such a cooling rate is an upper limit, as larger cooling rates might lead to a larger contraction of agar gel which promotes the long-term detachment of the gel from the lateral wall of the dish (see Section 5.2 in Chapter 5), and rendering the culture media unusable.

Chapter 4

Adhesion and debonding of agar gels from solid surfaces

Contents

4.1	Adhesion of hydrogels on solid surfaces: a short review of the literature	80
4.2	Gel adhesive properties determined by shear rheology	85
4.2.1	Influence of gel thickness (gap width)	85
4.2.2	Influence of the strain sweep-rate	86
4.2.3	Influence of agar concentration	87
4.2.4	Influence of the solid surface properties	88
4.3	Gel adhesion properties determined with a spinning centrifuge	89
4.3.1	Impact of contact duration between the gel and the plate	90
4.3.2	Impact of gel thickness	92
4.3.3	Impact of the rate of increase of the spinner rotation speed	93
4.3.4	Impact of agar concentration	94
4.3.5	Impact of the solid surface properties	95
4.4	Discussion and conclusion	98

4.1 Adhesion of hydrogels on solid surfaces: a short review of the literature

Improving the adhesion properties of agar gels on the bottom wall of Petri dishes requires to understand the mechanisms of bond formation and debonding of a soft hydrogel from a solid surface. An empirical criterion for a polymeric material to form a good adhesive contact with a solid surface, known as the Dahlquist criterion, is for the gel to show an elastic modulus G' smaller than 100 kPa (Dahlquist, 1969; Creton & Leibler, 1996; Gay, 2002). Indeed, if the gel is highly deformable, a “good contact” with a solid surface may be achieved with no need for applied pressure, even for a rough surface (Gay, 2002). Conversely, materials with an elastic modulus G' exceeding 100 kPa hardly deform, and do not make a “good contact” with a solid surface, even under reasonable pressure. In that case, a relatively low surface roughness of the substrate can partially prevent the adhesion between macroscopic solids (adhesion paradox) (Fuller & Tabor, 1975; Persson, Albohr, Tartaglino, Volokitin, & Tosatti, 2005; Martina, Creton, Dammam, Jeusette, & Lindner, 2012).

The relative importance of adhesive stresses and bulk elasticity is a matter of length scale. The elasto-adhesive length, $h_0 = |S|/E$ defined as the ratio of the Dupré interfacial work of adhesion $|S|$ (or spreading parameter) and the Young’s modulus E of the soft material, defines the length scale below which surface energies become dominant and induce large elastic deformations (Persson et al., 2005; Creton & Ciccotti, 2016). In short, elasticity prevents the gel deformation at large length scales $L > h_0$, whereas surface stresses flatten the surface at smaller scales. Weak attractions, such as Van der Waals interactions, may induce large enough elastic deformations of a soft material under moderate applied load, which results in a partial adhesive contact between the gel and the solid substrate. Moreover, the contact area between the gel and the substrate is not constant but increases with both the contact time and the squeezing force by deformation of the soft material and/or liquid dewetting of the surface (Fuller & Tabor, 1975; Tokita, 2016).

The separation speed and the energy dissipated during the debonding process further determine the adhesive performance. As a matter of fact, the failure energy for surface separation may be several orders of magnitude larger than the thermodynamic work of adhesion $|S|$ in the typical range from 1 mN/m – 100 mN/m (Israelachvili, 1992). Indeed, the viscoelastic properties of a soft material may greatly enhance the force needed to break the adhesive bonds between the gel and the substrate, leading to important bulk deformations with cavity nucleation and fibril formation. Such a *cohesive failure* of the gel leaves gel residues on the substrate at the end of the debonding process (Crosby, Shull, Lakrout, & Creton, 2000; Creton, Hooker, & Shull, 2001; Grillet, Wyatt, & Gloe, 2012). In the case of weakly viscoelastic soft materials characterized by a damping coefficient $\tan \delta = G''/G' < 0.01$, the propagation of an interfacial fracture induces a fast debonding process –or *adhesive failure*– for relatively small material deformations (strain $\epsilon < 1$). Weak adhesion and negligible visco-elastic effects favor interfacial crack propagation. The interfacial debonding mode of nearly elastic soft materials dramatically reduces the failure energy (Nase, Ramos, Creton, & Linder, 2013) and further preserves the solid substrate from material residues.

One should keep in mind that soft hydrogels are essentially composed of water, which also plays a key role in the adhesive properties of the gel with a solid substrate. Indeed, when a polymer gel is in contact with a solid surface, the presence of a thin water film at the gel/substrate interface weakens the adhesive contact, and the water expelled from the bulk of the gel promotes the lubrication of the surface. Therefore, the fact that a

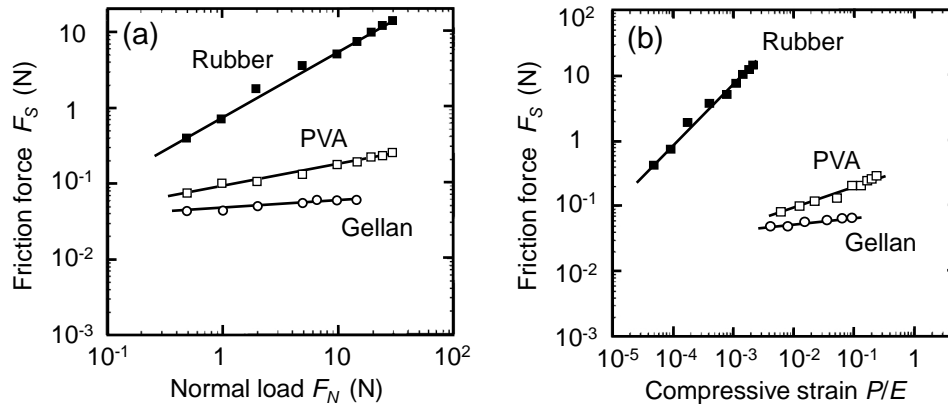


Figure 4.1: (a) Friction force F_S versus normal load F_N and (b) Friction force F_S versus compressive strain P/E for rubber ($E \approx 7.5$ MPa), PVA ($E \approx 14$ kPa) and gellan ($E \approx 60$ kPa) sliding in air on a smooth glass surface (sliding velocity $v = 7$ mm/min, material thickness 5 mm, surface area $A = 9$ cm² and contact pressure 10 kPa $< P = F_S/A < 0.2$ kPa). Reprinted from (Gong et al., 1999).

poroelastic hydrogel combines solid-like and liquid-like properties in contact with a solid surface makes both the adhesion and the friction properties challenging to understand.

Motivated by understanding the friction between articular cartilages, numerous studies have focused on the tribological behavior of soft elastic materials under large normal loads for which the liquid plays the key role (McCutchen, 1962). Indeed, the low friction between cartilage surfaces under compression arises from the fact that the pressurized interstitial fluid supports most of the normal load transmitted across the porous matrices (Ateshian, 2009). In comparison, the friction properties of hydrogels that weakly adhere to solid surfaces have revealed more complex features that strongly depend upon the mesh size of the network, the applied load as well as the wettability and the roughness of the substrate (Gong, Higa, Iwasaki, Katsuyame, & Osada, 1997; Gong et al., 1999; Gong, Iwasaki, & Osada, 2000). Frictional properties of hydrogels have been studied over the last 20 years by using a tribometer and a parallel-plate rheometer. The soft material is compressed under a known normal stress against a surface, which is then set into motion. The rotation speed of the substrate is increased by step, while the torque response is recorded (Gong, 2006). Gong et al. found that the sliding friction of soft hydrogels in air on a glass surface does not obey the empirical Amontons–Coulomb’s law, which reads $F_S = \mu_d F_N$, where F_S and F_N denote respectively the friction force and the normal load, and μ_d is the dynamic friction coefficient that is characteristic of the material properties (hardness and surface topography) (Gong et al., 1999). Unlike solid-like material such as rubber, non-ionic soft hydrogels such as PVA or gellan display a friction force F_S that is almost independent of the normal load F_N [Fig. 4.1(a)] and further decreases with increasing sliding velocity (Gong et al., 1997, 1999).

Deviation from the Amontons–Coulomb behavior has been also reported for a 1% wt. agarose gel sliding on a glass substrate, during which the friction stress $\sigma_S = F_s/A$ remains constant when the normal pressure $P = F_s/A$ is varied between 1 kPa and 20 kPa [Fig. 4.2(a)] (Gong et al., 2000). In comparison, the friction stress of a 2% wt. agarose gel increases with the normal load and becomes nearly constant only above a critical pressure $P_c = 5$ kPa that corresponds to a 5% relative amount of water wept from the soft gel [Fig. 4.2(b)]. For the 1% wt. agarose gel, the water is expelled from the gel bulk at a lower normal pressure $P > P_c \approx 1$ kPa, accounting for the earliest saturation of the friction force and the decrease of the dynamic friction coefficient $\mu_d = \sigma_S/P$ when increasing the

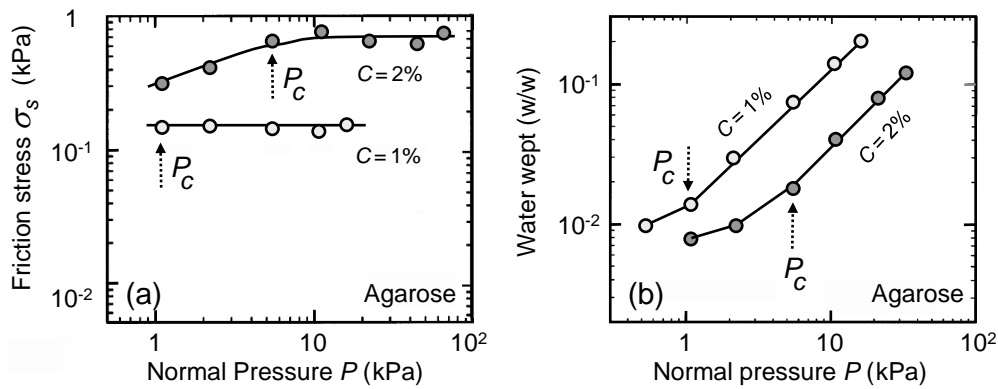


Figure 4.2: (a) Friction stress σ_s and (b) relative amount of water wept versus the normal pressure P applied either on a 1% wt. agarose gel (\circ) or a 2% wt. agarose gel (\bullet) sliding in air on a smooth glass surface ($E \approx 26$ kPa for $C_{\text{agarose}} = 1\%$ wt., $E \approx 140$ kPa for $C_{\text{agarose}} = 2\%$ wt., sliding velocity $v = 3$ mm/s, thickness 5 mm, surface area $A = 9$ cm²). The arrows indicate the critical pressure P_c above which the relative amount of water swept from the gel exceeds 5%. Reprinted from (Gong et al., 2000).

normal load (Fig. 4.2). Therefore, the non-classical sliding behavior of hydrogels is apparently associated with the presence of water-film located at the gel/solid interface, and wept from the gel above a critical deformation.

For solid materials, the linear dependence of the friction force with the load arises both from the elasto-plastic yielding deformation of transient micro-contacts, and from the linear increase with the applied load of the real contact area between the two rough surfaces (Fuller & Tabor, 1975). One may expect such a scenario to remain valid for hydrogels at rest, and subject to a normal load large enough to ensure a good adhesive contact between the gel and the surface, as confirmed by (Nitta, Kato, Haga, Nemoto, & Kawabata, 2005) for a 2% wt. agar gel ($E \approx 100$ kPa) and the following range of normal pressure 0.1 kPa $< P < 1$ kPa. The gel sliding contributes to weaken the adhesive contact with the substrate and leads to a mixed lubrication or elasto-hydrodynamic transition where the liquid film only partially supports the applied load. The transition from a boundary lubricated regime dominated by contact asperities to a mixed lubrication regime was first introduced by Stribeck in 1902 to describe the reduced friction of a solid material on a wet interface (Stribeck, 1902; Jacobson, 2003; Persson & Scaraggi, 2011).

More recently, the macroscopic contact between a non-ionic hydrogel and a glass substrate was successfully observed at rest, and during the sliding motion of the gel on the surface, while measuring the friction stress $\sigma_S(v)$ in a compressive strain-controlled mode (Yamamoto et al., 2014). Despite the weak difference in refractive index between the water and the hydrogel, reliable observations at the critical angle of refraction have provided images of the thin liquid film thicker than a few tens of nanometer, which is sandwiched between the glass and the gel (Yamamoto et al., 2014). In situ observations reveal that the water film trapped at the interface prior to the sliding of a neutral hydrogel on the smooth glass, is actually macroscopic (Fig. 4.3). The sprawl of the water trapped at the interface and the decrease of the contact area between the gel and the substrate results in a drop of the friction, which is representative of the transition towards the elasto-hydrodynamic regime [Fig. 4.3(b)]. More generally, the low friction coefficient of hydrogels and other soft materials is attributed to the high water-content and the formation of a water film at the sliding interface (Dunn, Sawyer, & Angelini, 2014).

The partial adhesive contact and the drop in friction observed for increasing velocity are especially prominent in the case of low normal pressure and smooth surfaces. A

4.1 Adhesion of hydrogels on solid surfaces: a short review of the literature 83

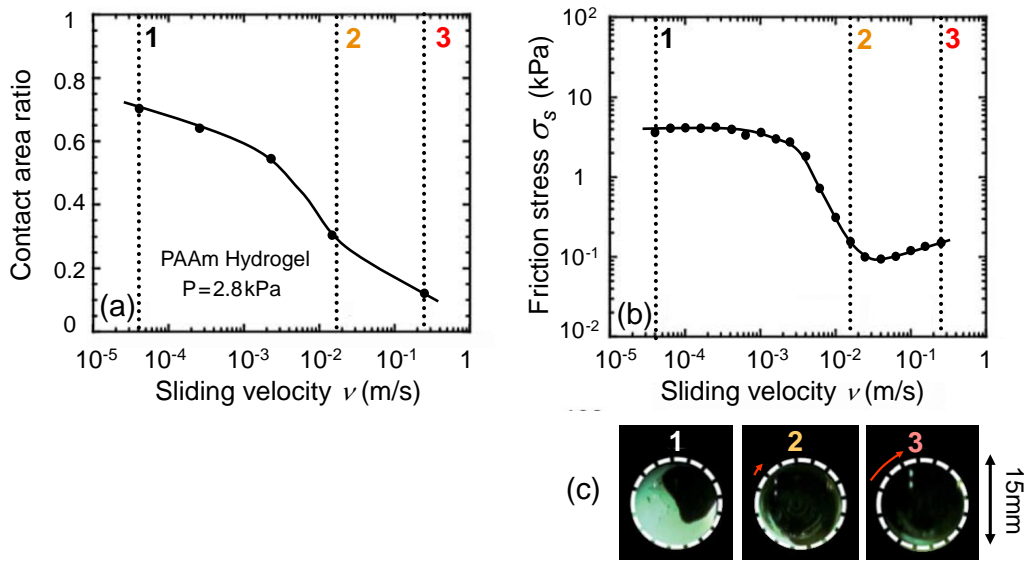


Figure 4.3: (a) Contact area ratio defined as the ratio of the contact area to the whole disk area, and (b) friction stress σ_s versus the sliding velocity v of a 10% polyacrylamide hydrogel on a smooth glass surface under a normal pressure $P = 2.8$ kPa ($E \approx 41$ kPa, gel thickness 2.6 mm, surface area $A = 1.8$ cm²). (c) Images of the initial gel-glass contact (1) and water wetting in the mixed lubrication regime (2-3). Reprinted from (Yamamoto et al., 2014).

stable and higher level of friction much less sensitive to the sliding velocity is observed when increasing the normal load P (Fig. 4.4) or the hydrogel surface roughness (Fig. 4.5) (Ahmed et al., 2014; Yashima, Takase, Kurokawa, & Gong, 2014). According to (Yashima et al., 2014), a rough gel with an average surface roughness $R_a > 1$ μ m displays channels that drain water on a smooth glass surface, whereas flat and smooth gels trap water, which leads to a weakly-controlled low friction. Note furthermore that friction experiments with hydrogels are often characterized by poor reproducibility due to the random nature of the initial adhesive contact, and the macroscopic size of water films trapped at the gel/substrate interface (Yamamoto et al., 2014).

In the present chapter, I report on the static friction of an agar gel with a substrate

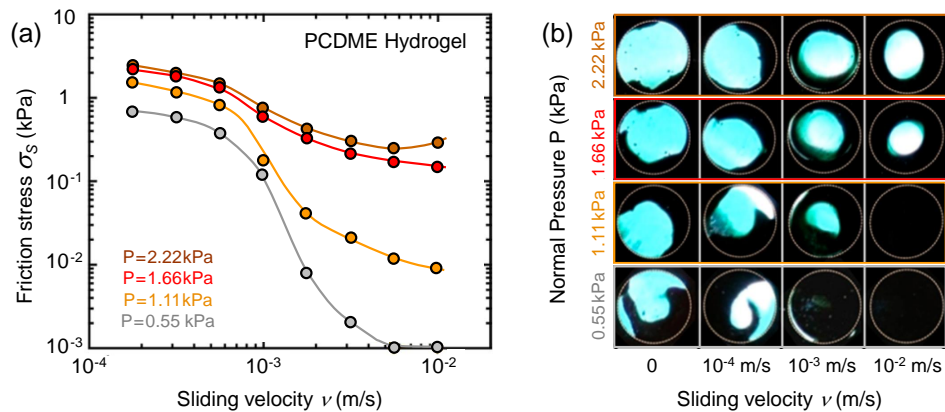


Figure 4.4: (a) Friction stress σ_s versus sliding velocity v of a zwitterionic PCDME hydrogel on a smooth glass surface under different normal pressure, ranging from 0.55 kPa to 2.22 kPa ($E \approx 120$ kPa, gel thickness 3.1 mm, surface area $A = 1.8$ cm² and pH=6.8). (b) Images of the gel-glass contact interface for different normal loads and sliding velocities. Reprinted from (Ahmed et al., 2014).

of well-controlled surface roughness and wettability. The goal is to quantify the critical shear stress beyond which the gel detaches from the substrate. Traditional experimental methods for testing the adhesive performance of soft solids consist in bringing a probe in contact with the material and measure the tensile force or the shear force required for surface separation until failure (Fig. 4.6). Peeling techniques have been employed to test the adhesion of tapes and pressure sensitive adhesives (Urahama, 1989), while tensile tests have been used to study soft viscoelastic adhesives and cohesive failure (Leger & Creton, 2008). Unfortunately, these methods are unadapted for studying millimeter-thick agar gels in Petri dishes. Indeed, in such conditions, the normal pressure acting on the gel only arises from gravity forces and is about a few tens of Pascal ($20 \text{ Pa} < P = e\rho g < 80 \text{ Pa}$ for a gel thickness $2 \text{ mm} < e < 8 \text{ mm}$, a gel density $\rho \approx 10^3 \text{ kg/m}^3$ and $g \approx 9.81 \text{ m/s}^2$), which is much less than usual compressive stresses reported in the literature. As a consequence, one may expect a partial and weak adhesive contact of a neutral agar gel on a smooth surface as some water films may remain trapped at the hydrogel/substrate interface. We have chosen to use shear tests so as to quantify the weak adhesion of agar gel pellets in contact with various well-controlled substrates. The gel is always cured directly in contact with the substrate of interest, and left untouched until the detachment –or *first debonding*– takes place. Following that first step, the gel can be carefully placed back in contact with the substrate and left to rest for a given duration, before the detachment –or *second debonding*– is measured.

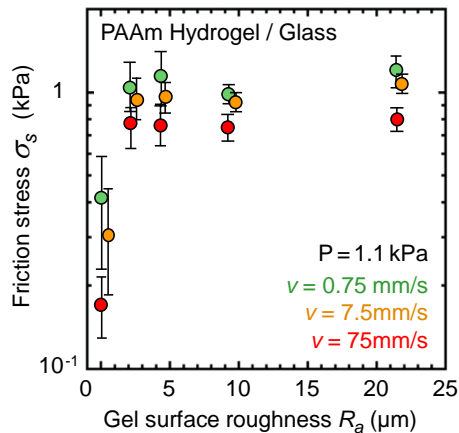


Figure 4.5: Friction stress σ_s vs. the average surface roughness R_a of a neutral polyacrylamide hydrogel sliding on a smooth glass surface (normal pressure $P = 1.1 \text{ kPa}$, $E \approx 130 \text{ kPa}$, gel thickness 2.4 mm , surface area $A = 1.8 \text{ cm}^2$). Reprinted from (Yashima et al., 2014).

The first section reports the results of strain sweep experiments conducted with a commercial rheometer. Oscillations of increasing strain amplitude are applied to the gel in a plate-plate geometry until the gel detaches from the plates. The second section introduces an original centrifuge method using a modified spin-coater to test the stress-induced detachment of several agar gel pellets adhering to a dish¹. The centrifuge method appears as an efficient and reproducible way to explore the shear-induced debonding of agar gels for a wide variety of experimental conditions, as the centrifuge runs allow us to perform a statistical analysis and to achieve high accuracy in the determination of both the first and second debonding stresses.

¹The use of a centrifuge technique to determine the adhesive properties of soft materials is quite original as, to our knowledge, only entomologists have used such a method to study the attachment forces of insects on various surfaces (Federle, Rohseitz, & Hölldobler, 2000; Federle, Baumgartner, & Hölldobler, 2004).

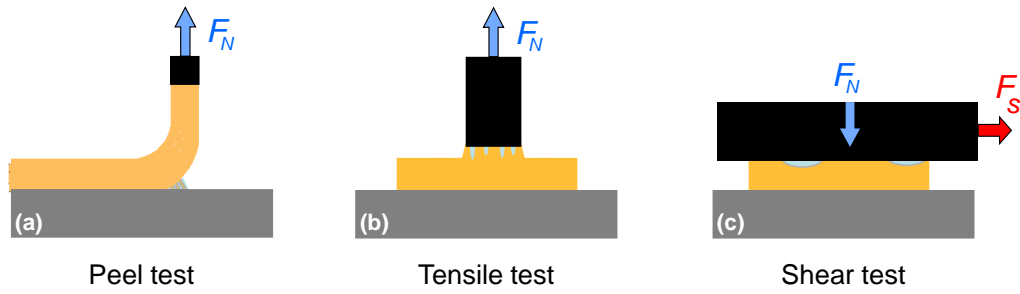


Figure 4.6: Schematic representation of the classical techniques used to determine the adhesive properties of a soft material on a solid substrate. (a) Peel test (b) Tensile test (probe-tack, point contact method) with a flat cylindrical probe and (c) shear test in a rheometer.

4.2 Gel adhesive properties determined by shear rheology

Large Amplitude Oscillatory Shear (LAOS) experiments provide a way to study quantitatively the loss of adhesion (or debonding) between a gel and a solid surface by applying oscillations of increasing stress or strain amplitude. In this section, I will first discuss the influence of the gel thickness (i.e. gap width) and the rate at which the strain is increased, on the measurements of the adhesive properties. Second, I will present the influence of agar concentration and the properties of the substrate (i.e. the surface roughness and the wettability) on the shear stress for first gel debonding. Note that before each LAOS test, an agar gel is prepared anew in the parallel-plate geometry by cooling down a hot agar solution at $1^\circ\text{C}/\text{min}$ from 50°C down to 20°C . The gelation is monitored with both the zero normal force protocol and the strain adapted protocol to prevent any premature debonding of the gel from the plates (see Section 2.3.1 and Section 2.4.1 in Chapter 2 for technical details). We use smooth plastic (PS) plates glued on both the upper and the bottom plates of the geometry for most of the LAOS tests, except in Section 4.2.1 where we use a smooth PMMA upper plate and a smooth (Teflon coated) bottom plate. Section 4.2.4 summarizes the influence of the surface properties on the first debonding of agar gels cast in a parallel-plate geometry.

4.2.1 Influence of gel thickness (gap width)

Let us start by illustrating the influence of the agar gel thickness (or gap width) on the LAOS measurements. A 1.5% wt. agar-BM1 gel is prepared in a parallel-plate geometry by setting the initial gap width to different values varying from $200\ \mu\text{m}$ to $1000\ \mu\text{m}$. The upper rotating plate is made of PMMA and displays a smooth surface (RMS surface roughness $R_q = (29 \pm 7)\ \text{nm}$ as determined by 3D scanning interferometry), while the bottom surface consists in a smooth and Teflon coated Peltier plate. For each experiment, the hot agar solution is introduced in the gap and the temperature is decreased from 50°C to 20°C with a cooling rate $1^\circ\text{C}/\text{min}^2$. The zero normal force protocol is applied to monitor the gelation, and the strain amplitude is further adapted to the value of the gel elastic modulus as described in Section 2.3.1, for the purpose of measuring accurately

²Since the glue used to fix the plastic (PS) plates on both the rotor and the stator is sensitive to high temperatures, the cooling protocol is modified to start from 50°C instead of 70°C and therefore slightly differs from the other gelation experiments reported in Chapter 3. Note that an initial temperature of 50°C remains higher than the gelation temperature of the agar solution, which is $T_g \approx 35^\circ\text{C}$ and that such an initial temperature has no influence on the mechanical and structural terminal properties of the agar gel (see Section 3.2.2 and Section 3.2.3 in Chapter 3).

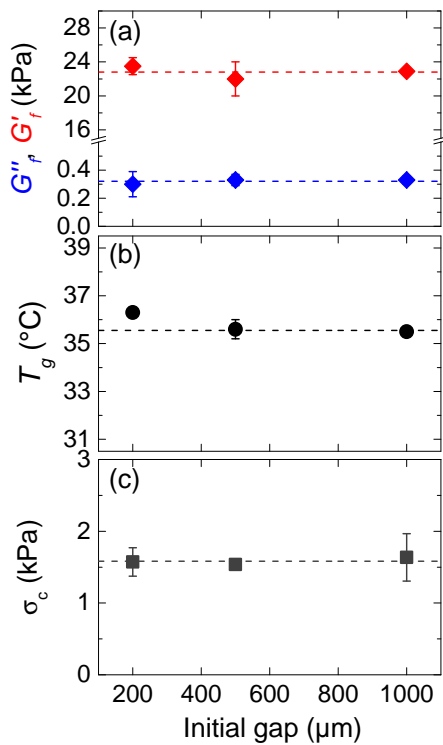


Figure 4.7: (a) Terminal values G'_f and G''_f of the elastic shear and loss moduli of 1.5% wt. agar-BM1 gels vs. the initial gap width. The horizontal dashed lines stand for the mean values of the gel viscoelastic moduli: $\bar{G}'_f = (22.8 \pm 0.4)$ kPa and $\bar{G}''_f = (320 \pm 43)$ Pa. (b) Gelation temperature T_g vs. the initial gap width. The horizontal dashed line stands for the mean value of T_g : $\bar{T}_g = (35.6 \pm 0.2)^{\circ}\text{C}$. (c) Critical shear stress σ_c vs. the initial gap width. The horizontal dashed line is the mean value of σ_c : $\bar{\sigma}_c = (1.58 \pm 0.10)$ kPa. Error bars correspond to the dispersion of data obtained by repeating the experiment on 3 to 5 independent samples.

the gelation temperature T_g defined as the intersection of G' and G'' , and also to prevent the debonding of the agar gel during the gelation. After 90 minutes, the gel elastic shear (resp. loss) modulus G' (resp. G'') and the gel thickness e reach steady-state values. The rheometer is then switched to a constant gap mode, i.e. the gap width is fixed to the latest value, and an oscillatory strain experiment is performed at a frequency of 1 Hz. The oscillating strain amplitude is ramped up from $\gamma = 0.01\%$ to 100%, within 2160 s and the critical oscillating stress σ_c beyond which the gel detaches from the plates is measured.

The results displayed in Figure 4.7(a) and (b) clearly demonstrate that the gelation temperature T_g and the gel terminal viscoelastic moduli G'_f and G''_f are independent of the initial width of the gap. Furthermore, the critical shear stress σ_c beyond which the gel detaches from the upper plate is also independent from the gel thickness, within error bars [Fig. 4.7(c)]. The latter result nicely coincides with that obtained with the centrifuge method that will be discussed later in Section 4.3.2, and shows that the gel thickness can be fixed once and for all for the rest of the study. Therefore, the initial gap width is fixed to 500 μm in the next sections, so as to investigate the influence of both the rate at which the strain is increased, and the agar concentration upon the first debonding stress σ_c of agar gel cast in the parallel-plate geometry.

4.2.2 Influence of the strain sweep-rate

To quantify the influence of the rate at which the oscillating strain amplitude γ is increased, upon the critical stress associated with the gel debonding from the PS plates, we have repeated the strain sweep experiments over different durations ranging from 100 s to 12960 s (3.6 hours). Each experiment is performed on a 1.5% wt. agar-BM1 gel prepared anew, following the same protocol discussed in the previous paragraph. The evolution of the elastic shear modulus G' as the strain amplitude is increased from $\gamma = 0.01\%$ up to 100% is reported in Figure 4.8(a). For the sake of clarity, the storage modulus G' is

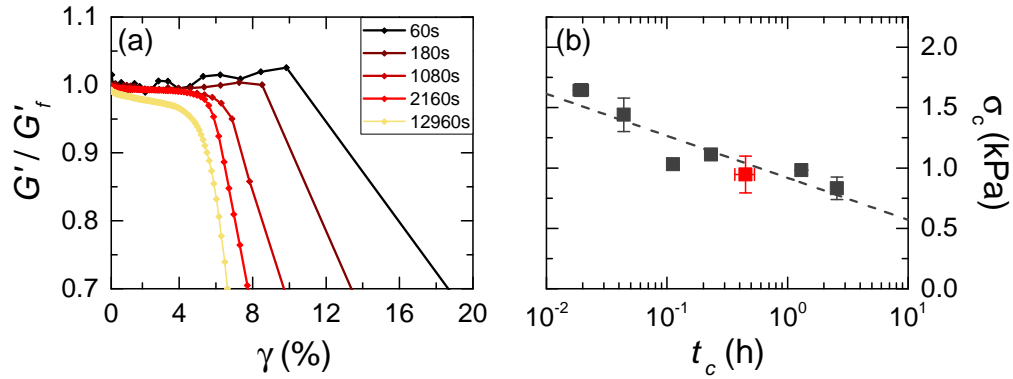


Figure 4.8: Normalized elastic modulus G'/G'_f vs. oscillating strain amplitude γ for strain sweep experiments performed at a frequency of 1 Hz. The strain amplitude is increased logarithmically from $\gamma = 0.01\%$ to 100% over a duration varying from 60 s to 12960 s (colors from black to yellow). (b) Critical shear stress σ_c vs. critical time t_c for gel debonding. The red square (■) denotes the strain sweep run performed in 2160 s, which corresponds to the default condition considered for strain sweep experiments in the next sections. The dashed line, of equation $\sigma_c = (0.90 \pm 0.07) - (0.35 \pm 0.07) \log(t_c)$ in kPa and with t_c in hours, is the best fit of the data in semi-logarithmic scale. Error bars correspond to the dispersion of the results obtained by repeating the experiment on 3 to 5 independent samples.

normalized by the terminal value G'_f defined earlier and measured prior to the start of the strain sweep. For all the strain sweeps, the gel displays a similar response: G'/G'_f is constant at low strain amplitude and decreases sharply above a critical shear strain of amplitude γ_c to which corresponds a critical shear stress σ_c , when the gel debonds from the plates. Both the critical strain and stress are decreasing functions of the sweep rate. Lower sweep rate leads to the fatigue (or slow deterioration) of the adhesive bond between the gel and the plates, which results in the gel debonding at lower strain values. We further define the critical time t_c as the duration elapsed between the start of the strain sweep experiment and the debonding of the gel from the PS plates. The critical shear stress σ_c decreases logarithmically with the experiment time t_c [Fig. 4.8(b)], which confirms the idea of the slow aging of the adhesive bond between the gel and the plates. These results will be further discussed in Section 4.3.3, in light of the experiments performed with the spinner.

4.2.3 Influence of agar concentration

To examine the influence of agar concentration on the adhesion properties of agar gels to a smooth plastic surface, a series of agar-BM1 gels of different concentrations was prepared in the parallel-plate geometry, with an initial gap of about $500 \mu\text{m}$ and following the same protocol as previously described. For each gel, the critical shear strain γ_c and the critical shear stress σ_c associated with the first gel debonding are measured through strain sweep experiments performed at 1 Hz, with a strain amplitude increasing logarithmically from 0.01% to 100% in 2160 s. The results pictured in figure 4.9 demonstrate that both the critical strain γ_c and the critical stress σ_c strongly depend on agar concentration. The critical strain γ_c decreases as a power law of the agar concentration with an exponent close to 1.2 [Fig. 4.9(a)], while the critical stress σ_c shows a non-linear and non-trivial increase with the agar concentration. The latter dependence is in good agreement with the results obtained with the spinning centrifuge reported in Section 4.3.4, and will be discussed later in Section 4.4.

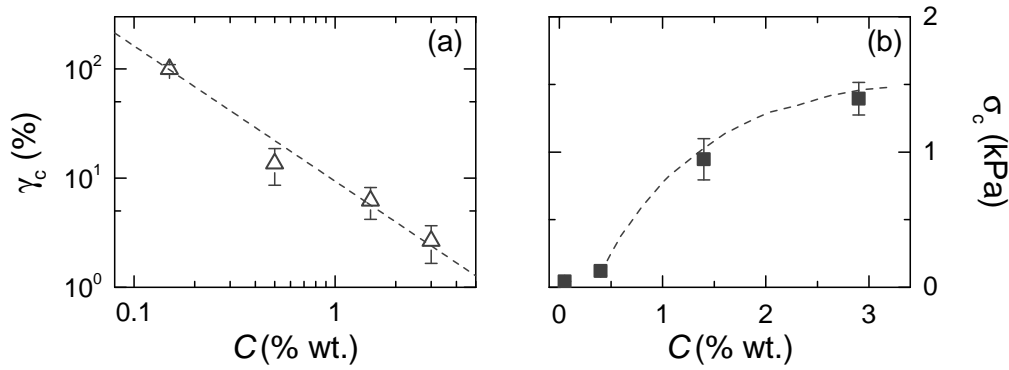


Figure 4.9: (a) Critical shear strain γ_c and (b) critical shear stress σ_c vs. the agar-BM1 concentration C . The dashed line in (a) is the best power-law fit of the data, which equation in logarithmic scale reads: $\log(\gamma_c) = (1.0 \pm 0.1) - (1.2 \pm 0.1) \log C$ with γ_c in % and C in % wt.. The dashed line in (b) is a guide for the eye. Error bars correspond to the dispersion of the results obtained by repeating the experiment on 3 to 5 independent samples.

4.2.4 Influence of the solid surface properties

The present section concerns the impact of the surface properties, especially the roughness and the wettability, on the adhesion properties of agar gels. We have prepared different types of surfaces that can be glued to the parallel-plate geometry, both to the upper and lower plate so as to tune the boundary conditions symmetrically. The surfaces are as follows: glass, plastic (PS) and polymethyl-methacrylate (PMMA). Moreover, a set of these smooth surfaces are sandblasted to turn them into rough boundary conditions. We have also used duralumin rotors that are either polished with a suspension of ultra-fine aluminium oxide particles to produce a smooth mirror-like surface, or sandblasted to be turned into a rough surface. The average RMS roughness of all these surfaces is systematically determined using a 3D scanning optical microscope (Bruker Contour GT-I) and the wettability of the solid surfaces is quantified by measuring the contact angle of water drops (see Section 2.6 in Chapter 2 for more technical details).

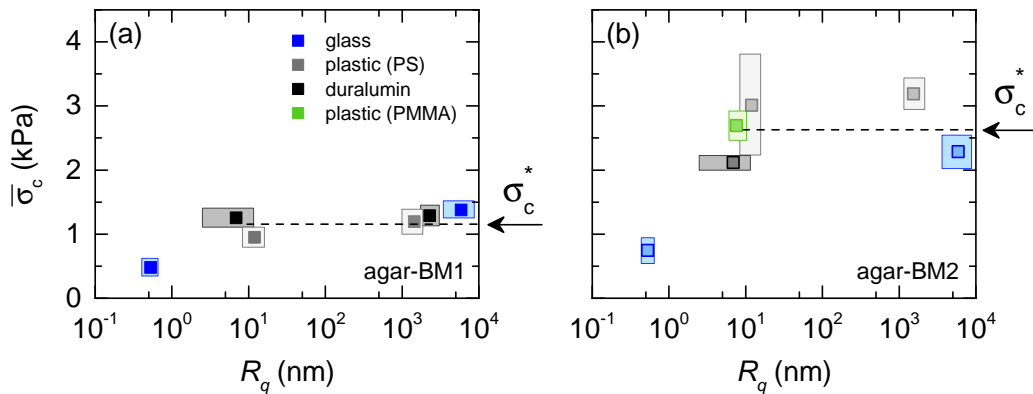


Figure 4.10: Average critical shear stress σ_c of 1.5% wt. agar-BM1 (a) and agar-BM2 (b) gels vs. the average RMS roughness R_q for smooth or rough solid surfaces made of glass (blue symbols), plastic PS (gray symbols), plastic PMMA (green symbols) and duralumin (black symbols). The horizontal dashed lines highlight the mean value of the average critical shear stress for R_q in the range of 10 nm to 10 μm : $\sigma_c^* = (1.2 \pm 0.2)$ kPa and $\sigma_c^* = (2.6 \pm 0.5)$ kPa for agar-BM1 gels and agar-BM2 gels respectively. Error bars correspond to the dispersion of the results obtained by repeating the experiments on 3 to 5 independent samples.

An extensive series of strain sweep experiments was performed with both agar-BM1 and agar-BM2 gels³, and prepared in the parallel-plate geometry with the solid surfaces presented above. Figure 4.10(a) and (b) show the average critical stress σ_c for 1.5% wt. agar gels respectively made with agar-BM1 and agar-BM2, as a function of the average RMS roughness R_q of the solid surfaces. Both batches of agar gels show similar behavior of σ_c vs. R_q : the critical shear stress increases with the surface roughness up to $R_q \simeq 10$ nm. For $R_q > 10$ nm, the average critical shear stress σ_c is independent of the plate surface roughness. The latter plateau value, noted σ_c^* , depends on the agar batch: agar gels prepared with agar-BM2 show a larger debonding stress ($\sigma_c^* \approx 2.6$ kPa) than gels prepared with the agar-BM1 ($\sigma_c^* \approx 1.2$ kPa). In fact, if agar-BM1 and agar-BM2 present a close polymer composition (70% agarose and 30% agarpectin) and similar mechanical properties once gelified, they show different ionic composition, which may influence the adhesion properties of the corresponding gels, as will be further discussed in Chapter 6, Section 6.2. Finally, the same data sets of critical shear stresses are plotted in Figure 4.11 as a function of the surface contact angle θ of water, which is representative of the solid surface wettability. Surprisingly, the results show no obvious influence of the water contact angle θ upon the average critical stress σ_c . The role of both the plates surface roughness and wettability has been confirmed using the centrifuge method, which gives results more statistically significant based on 30 to 40 independent measurements compared to the 3 to 5 strain sweep rheology experiments reported here. The results obtained with the centrifuge method will be discussed in Section 4.4.

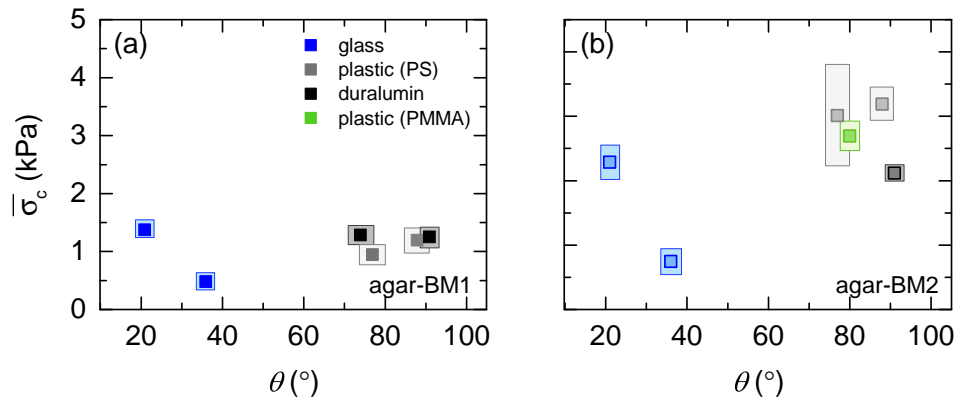


Figure 4.11: Average critical shear stress σ_c of 1.5% wt. agar-BM1 (a) and 1.5% wt. agar-BM2 (b) gels vs. the water contact angle θ for smooth and rough solid surfaces made of glass (blue symbols), PS plastic (gray symbols), PMMA plastic (green symbols) and duralumin (black symbols). Error bars correspond to the dispersion of the results obtained by repeating the experiments on 3 to 5 independent samples.

4.3 Gel adhesion properties determined with a spinning centrifuge

In addition to the strain sweep experiments presented above, the adhesion between an agar gel and a solid surface can be further quantified by using a ‘spinner centrifuge’, which has been introduced in Chapter 2. The centrifuge method allows us to characterize both the first and second gel debonding of an agar gel pellet on a solid surface. The *first*

³More information about the composition of the two different agar batches BM1 and BM2 provided by the bioMérieux company are listed in Section 2.1, Chapter 2.

debonding refers to the loss of contact between the gel and the solid plate, for a gel sample that has been formed directly in contact with the plate. The first debonding is therefore identical to that determined with the rheological experiments and discussed in the previous section. Once the first centrifuge run is completed, one may replace the agar gel pellets to their initial position, wait for a certain duration and start a new centrifuge run. The gel detachment during that second run is referred to as the *second debonding*. In the present section, we first discuss the influence of (i) the waiting time prior to the centrifuge run, (ii) the gel thickness, and (iii) the rate of increase of the rotation speed on both the first and second gel debonding. Second, we discuss the impact of agar concentration and the surface properties of the solid substrate (roughness and wettability) on the critical shear stress associated with the shear-induced debonding of gel samples.

4.3.1 Impact of contact duration between the gel and the plate

The static friction coefficient μ_s between two solid materials increases with the period of time τ during which the two materials have been in contact. Such aging behavior of μ_s corresponds to an increase in the real contact area through asperity creep, and results from a glassy-like relaxation process or molecular rearrangements in the nanometer-thick interfacial region of contact between the two solids (Berthoud, Baumberger, G'Sell, & Hiver, 1999; Persson, 1999). In practice, the slow increase of μ_s is usually well described over several decades of time by a logarithmic increase that reads $\mu_s = \alpha_s + \beta_s \log(\tau)$, where $\beta_s \approx 0.01 - 0.1$ is a positive slope (Berthoud et al., 1999; Bureau, Baumberger, & Caroli, 2006)⁴. In recent years, some experimental studies have investigated the aging of the static contact between hydrogels and smooth solid surfaces (Nitta et al., 2005; Maeda, Chen, Tirrell, & Israelachvili, 2002; Baumberger, Caroli, & Ronsin, 2003; A. Suzuki, Ishii, Yamakami, & Nakano, 2011). Nitta *et al.* reported that the static friction $\mu_s(\tau)$ of a 2% wt. agar gel immersed in water and weakly adhering on a smooth glass substrate under a normal pressure $P \approx 0.5$ kPa increases logarithmically with the duration τ of contact prior to sliding, with a slope $\beta_s \approx 0.510$. The slow drainage of the water layer at the gel/glass interface and the formation of an heterogeneous adhesive contact as revealed by optical reflectance microscopy may account for the aging of the agar gel static friction. For gelatin gels on a smooth glass surface, the static friction threshold σ_c also increases logarithmically with the time τ elapsed between the first contact and the sliding: $\sigma_c \approx \alpha_c + \beta_c \log(\tau/\tau_0)$ with τ in seconds and $\tau_0 = 1$ s, a time introduced to express β_c in kPa unit. The slope β_c depends on the gelatin concentration⁵ suggesting that the contact aging results from the slow relaxation of the polymer chains dangling from the network and free to bond with the glass substrate (Baumberger et al., 2003).

To study the aging of an agar gel in contact with a solid substrate, we have prepared 1.5% wt. agar-BM1 gels that are cured in smooth plastic dishes (gel thickness $e = 4$ mm) and stored in the fridge at 5°C with a lid to minimize water evaporation. After a waiting time T in the fridge, gel pellets are prepared using the '*mikado*' protocol introduced in Chapter 2 and centrifuge experiments are performed on 8 pellets, with a rate of increase of the rotation speed of $d\omega/dt = 3.33$ rpm/s, so as to determine the critical shear stress σ_c , beyond which the gel pellets debond. For $T = 25$ min, σ_c ranges between 0.35 kPa and 0.6 kPa, and repeating the experiment for various waiting times T , one observes that σ_c increases with T [Fig. 4.12(a)]. Despite some data dispersion likely due to the

⁴Note that the choice of the time unit affects the α_s value but not the slope β_s .

⁵ $\alpha_c(\tau = 1 \text{ s}) \approx 0.35$ kPa and $\beta_c \approx 0.15$ kPa for $c = 5\%$, and $\alpha_c(\tau = 1 \text{ s}) \approx 2.6$ kPa and $\beta_c \approx 0.35$ kPa for $c = 10\%$.

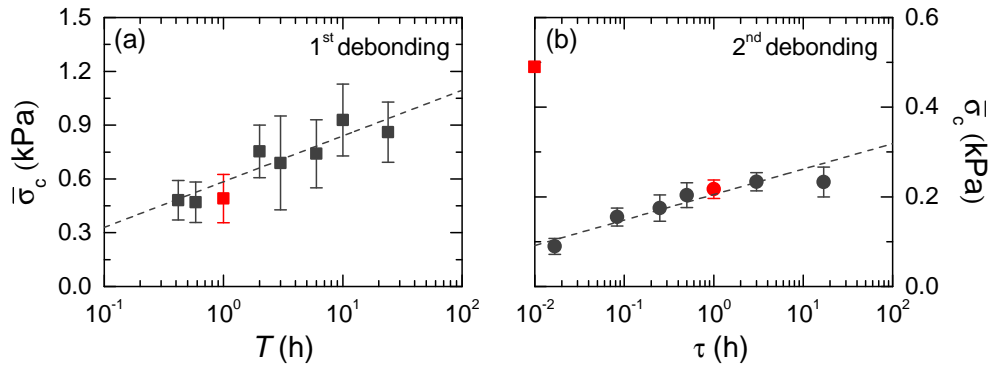


Figure 4.12: (a) Average critical shear stress $\bar{\sigma}_c$ vs. the waiting time T for gel first debonding. (b) Average critical shear stress $\bar{\sigma}_c$ vs. the waiting time τ for gel second debonding with $T = 1$ h. The red square (■) and the red disk (●) denote the centrifuge run performed with $T = 1$ h for the first debonding and $T = 1$ h, $\tau = 1$ h for the second debonding respectively, which are typical waiting times used for other experiments in the rest of the section. The gray dashed lines are the best linear fit of the data in semi-logarithmic scale, which equations are $\bar{\sigma}_c(T) \approx 0.6 + 0.25 \log(T/T_0)$ and $\bar{\sigma}_c(\tau) \approx 0.2 + 0.05 \log(\tau/\tau_0)$ for gel first and second debonding respectively, with $T_0 = \tau_0 = 1$ hour. Centrifuge experiments are performed on 1.5% wt. agar-BM1 gel pellets in smooth plastic dishes with a rate of increase of the rotation speed $d\omega/dt = 3.33$ rpm/s. Error bars correspond to the standard deviation of the ensemble averaged critical shear stress for 3 to 5 centrifuge runs that is $3 \times 8 = 24$ up to $5 \times 8 = 40$ gel pellets.

heterogeneous properties of the adhesive contacts, one can see clearly that the average critical shear stress $\bar{\sigma}_c(T)$ logarithmically increases with T , with a slope $\beta_c \approx 0.25$ kPa [$\bar{\sigma}_c \approx 0.6 + 0.25 \log(T/T_0)$ with σ_c in kPa, T in hours and $T_0 = 1$ h, a time introduced to express β_c in kPa unit]. Such an increase is significant and cannot be attributed to any bulk phenomena such as water evaporation from the gel while the latter is stored in the fridge. Indeed, after a day in the fridge the mass loss of gels is smaller than 0.5%. Therefore the logarithmic increase of σ_c is due to the aging of the adhesive contact between the gel and the substrate.

We now turn to the second debonding. After a fridge storage time of $T = 1$ h and a first debonding, the agar gel pellets are carefully replaced to their initial positions (thanks to a homemade template) by slowly sliding the pellets on the plastic dish. The plate is then stored again in the fridge at 5°C with a cover lid for another waiting period τ ranging from 2 minutes to 24 hours. A second centrifuge run is then performed with a rate of increase of the rotation speed of $d\omega/dt = 3.33$ rpm/s to measure the critical shear stress for the second shear-induced debonding of gel samples [Fig. 4.12(b)]. We observe a similar logarithmic increase of the average critical shear stress with the waiting time τ ,

	1 st debonding $\bar{\sigma}_c(T = 1\text{ h})$ (kPa)	2 nd debonding $\alpha_c(T, \tau = 1\text{ h})$ (kPa)	2 nd debonding $\beta_c(T, \tau = 1\text{ h})$ (kPa)
Smooth glass [$R_q = (0.52 \pm 0.09)$ nm]	0.072	0.045	0.01
Smooth plastic [$R_q = (11.8 \pm 3.6)$ nm]	0.49	0.2	0.05
Rough glass [$R_q = (5.9 \pm 2.4)$ μm]	0.94	0.45	0.12
Rough plastic [$R_q = (1.54 \pm 0.43)$ μm]	1.77	0.45	0.13

Table 4.1: Average critical shear stress $\bar{\sigma}_c(T = 1$ h) for the first gel debonding of 1.5% wt. agar-BM1 gel pellets on smooth or rough dishes made of glass or plastic (PS); and α_c , β_c values characterizing the time evolution of the average critical stress for the second debonding after the gel has been replaced to its initial position with $T_0 = \tau_0 = 1$ hour. See Table 2.2 for the RMS surface roughness and water wettability of the different surfaces.

that reads $\bar{\sigma}_c \approx 0.2 + \beta_c \log(\tau/\tau_0)$ with $\beta_c \approx 0.05$ kPa, τ in hours and $\tau_0 = 1$ h. Moreover, for a given waiting time, the adhesion of the gel to the plate is weaker in comparison with the gel first debonding, showing that placing back the gel pellets to their initial positions does not rebuild the bond that was formed during the agar gelation.

Measurements of the first debonding (for $T = 1$ h) and of the second debonding after different waiting times τ were also performed on 1.5% wt. agar-BM1 gels in smooth or rough dishes made of glass or plastic. The adhesive contact displays similar features to that described above with a quasi-instantaneous adhesion of the gel when replaced to its original position, and a logarithmic increase of the average debonding shear stress with the waiting time τ . The gels in contact with rough solid surfaces show more pronounced aging effects with larger values of β_c (Table 4.1) since rough surfaces likely provide larger channels for water drainage from the gel/plate interface. Water drainage at the gel/plate interface after the gel is replaced at its initial position and aging effects will be discussed in more details in Section 4.4.

4.3.2 Impact of gel thickness

For a contact between two solid materials that obeys the laws of Amontons–Coulomb, the critical shear stress necessary for the failure of the multicontact interface (MCI) scales linearly with the normal pressure. In the case of a hydrogel in contact with a solid substrate, the water release from the gel may influence the failure of the adhesive contact and the critical shear stress associated with the gel debonding. To study the influence of normal pressure on gel debonding, we have prepared 1.5% wt. agar-BM1 gels of different thicknesses $e = 2, 4$ and 8 mm in smooth plastic dishes (PS). The first debonding of the corresponding agar gel pellets is measured with a rate of increase of the rotation speed of $d\omega/dt = 3.33$ rpm/s after a waiting time $T = 1$ h. After the first centrifuge run, agar gel pellets are carefully replaced by gentle sliding to their initial positions and stored in the fridge with a cover lid. After a new waiting time of 1 hour at 25°C, a second centrifuge run is performed with a rate of increase of the rotation speed of $d\omega/dt = 3.33$ rpm/s.

Interestingly, the average critical shear stress $\bar{\sigma}_c$ is independent of the gel thickness e , for both the first and second debonding (Fig. 4.13). Such results confirm the previous ones

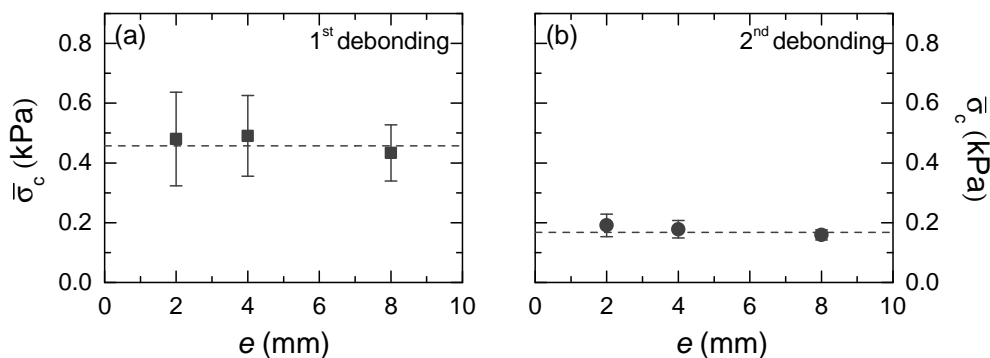


Figure 4.13: Average critical shear stress $\bar{\sigma}_c$ for the first gel debonding ($T = 1$ h) (a) and the second gel debonding ($T = 1$ h, $\tau = 1$ h) (b) vs. the gel thickness e . The horizontal dashed lines stand for the mean values of the average critical shear stress $\bar{\sigma}_c$, with $\bar{\sigma}_c = (0.46 \pm 0.02)$ kPa and $\bar{\sigma}_c = (0.17 \pm 0.02)$ kPa for the first and second debonding, respectively. Centrifuge experiments are performed with 1.5% wt. agar-BM1 gel pellets on a smooth plastic dish with a rate of increase of the rotation speed $d\omega/dt = 3.33$ rpm/s. Error bars correspond to the standard deviation of the ensemble averaged critical shear stress for 3 to 5 centrifuge runs that is $3 \times 8 = 24$ up to $5 \times 8 = 40$ gel pellets.

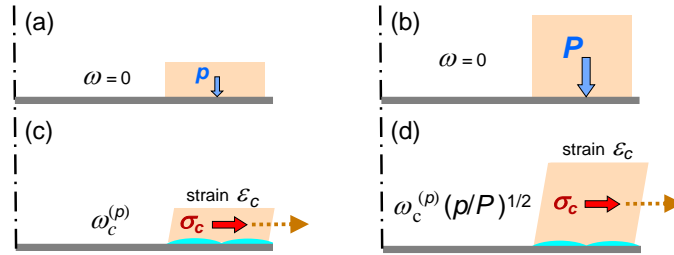


Figure 4.14: Schematic representation of hydrogels in the centrifuge at rest (a) and (b), or at the critical rotation speed $\omega_c^{(p)}$ (c) or $\omega_c^{(P)} = \omega_c^{(p)}(p/P)^{1/2}$ (d) depending on the thickness and the gravity pressure (p, P) acting on the gel pellets. In the limit of small normal pressure and vanishing compressive strain, water invasion of the adhesive contact and gel debonding occur for an identical critical shear strain ϵ_c independently of the gel thickness.

obtained with the rheological LAOS experiments reported in Section 4.2.1, i.e. the fact that the gel first debonding is independent of the initial gap width (Fig. 4.7). Furthermore, the average critical shear stress $\bar{\sigma}_c$ for the second shear-induced debonding after a waiting time $\tau = 1$ hour is about 50% lower than the stress $\bar{\sigma}_c$ measured for the first debonding, which indicates a weakening of the adhesive contact after replacing the gel, in agreement with the data reported in Figure 4.12.

As prescribed by the law of Amontons–Coulomb’s law, one could have expected a linear increase of the critical shear stress $\sigma_c = e\rho\omega_c^2 r$ with the normal pressure $P = e\rho g$ and the thickness e of the soft adhesive material. However, in the limit of vanishing compressive strain P/E , the centrifuge experiments show that the gel debonding is controlled by the shear deformation of the soft material leading to an inverse square root dependence of the critical rotation speed ω_c with the gravity pressure $P = e\rho g$ and the gel thickness e (Fig. 4.14). Such a behavior strongly suggests a sponge-like behavior of the soft hydrogel and the stress-induced invasion of the gel/substrate contact interface by water, prior to the gel debonding. A critical stress $\bar{\sigma}_c \approx 0.5$ kPa and a critical strain $\epsilon_c \approx \bar{\sigma}_c/G'$ of a few percent (with an elastic shear modulus $G' \approx 20$ kPa for 1.5% wt. agar-BM1 gels) are large enough for water to be squeezed out from the bulk of the hydrogel and lubricate the gel/substrate interface. Indeed, the critical shear strain γ_c for the debonding of 1.5% wt. agar gel from the plates under oscillatory shear ranges between 3% and 9% [Fig. 4.9(a)]. Furthermore, the observation of the solid/gel interface in a homemade shear cell shows the formation of dark spots that could indicate the stress-induced formation of interfacial water films [Fig. A.3(d) in Appendix A] and a progressive debonding of the 1.5% wt. agar-BM2 gel when increasing the shear strain from a few percent to 14% [see Fig. A.3(f) in Appendix A]. In conclusion, the average critical shear stress $\bar{\sigma}_c$ is representative of the strength of the adhesive contact between the gel and the plate independently of the gel thickness, because of the high water-content of hydrogels and the stress-induced lubrication of the interface.

4.3.3 Impact of the rate of increase of the spinner rotation speed

We now examine the impact of the rate of increase of the spinner rotation speed on the debonding of agar gels. For this purpose, independent centrifuge runs are performed with different rates of increase of the rotation speed: $d\omega/dt = 3.33$ rpm/s, 10 rpm/s or 36 rpm/s. Depending on the rate of increase of the rotation speed $d\omega/dt$, the characteristic residence time $\bar{\omega}_c/(d\omega/dt)$ of gel pellets in the centrifuge, expressed as a function of the average critical rotation speed $\bar{\omega}_c$ for gel debonding, ranges from some tens of sec-

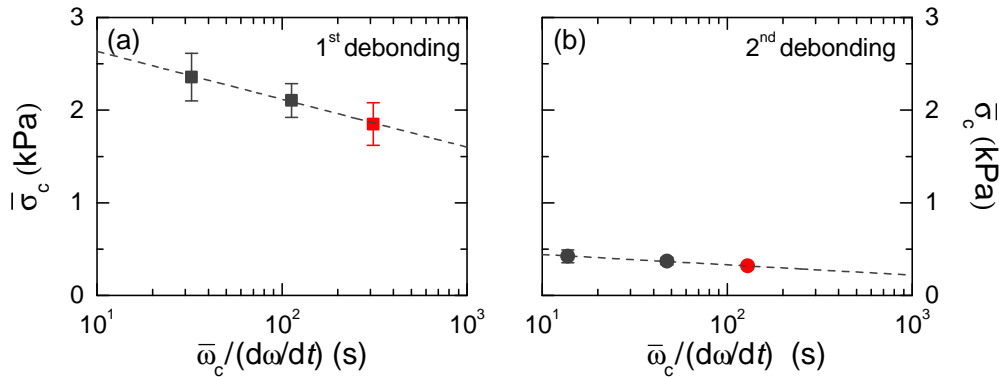


Figure 4.15: Average critical shear stress $\bar{\sigma}_c$ vs. the average residence time $\bar{\omega}_c/(d\omega/dt)$ of gel pellets for (a) the first debonding ($T = 1$ hour) and (b) the second debonding ($T = 1$ hour, $\tau = 1$ hour) where $\bar{\omega}_c$ represents the average rotation speed necessary for the detachment of the agar gel pellets. The red square (■) and the red disk (●) highlight the centrifuge runs performed at a rate of increase of the rotation speed of $d\omega/dt = 3.33$ rpm/s, which corresponds to the rate used in the experiments reported in the next sections. The gray dashed lines are the best linear fit of the data in semi-logarithmic scale with $\bar{\sigma}_c \approx 3.2 - 0.5 \log[\bar{\omega}_c/(d\omega/dt)]$ and $\bar{\sigma}_c \approx 0.08 - 0.04 \log[\bar{\omega}_c/(d\omega/dt)]$ for the first and second gel debonding, respectively. Centrifuge experiments are performed on 1.5% wt. agar-BM2 gel pellets on a smooth plastic dish with $e = 4$ mm. Error bars correspond to the standard deviation of the ensemble averaged critical stress for 3 to 5 centrifuge runs that is $3 \times 8 = 24$ up to $5 \times 8 = 40$ gel pellets.

onds for $d\omega/dt = 3.33$ rpm/s, up to a few minutes for $d\omega/dt = 36$ rpm/s. The average critical shear stress $\bar{\sigma}_c$ associated with the first debonding of the 1.5% wt. agar-BM2 pellets increases when centrifuge runs take place over shorter timescales [Fig. 4.15(a)]. Note that such time-dependent effects are even more pronounced for softer gels pellets made of 0.5% wt. agar-BM2, which indicates an influence of the gel deformability and viscous dissipation phenomena on the debonding dynamics. Moreover, the second debonding of the agar gel pellets is less sensitive to the rate of increase of the rotation speed $d\omega/dt$ [Fig. 4.15(b)], likely as a result of the smaller critical shear stress $\bar{\sigma}_c$ and lower gel deformation at debonding. In the next section, we choose to perform centrifuge runs with the minimum rate of increase of the rotation speed that is accessible with the spinner, i.e. $d\omega/dt = 3.33$ rpm/s to reduce as much as possible the viscous dissipation phenomena that may contribute to overestimate the critical stress for gel debonding.

4.3.4 Impact of agar concentration

The influence of agar concentration on the gel adhesion properties were also investigated with the centrifuge method. Agar-BM1 and agar-BM2 gel pellets with polymer concentrations ranging from 0.5% wt. to 3% wt. were prepared in smooth plastic dishes using the “*mikado*” protocol before performing two centrifuge runs. The results pictured in Figure 4.16 show the average critical shear stress $\bar{\sigma}_c$ for the first gel debonding ($T = 1$ hour) and the second gel debonding ($T = 1$ hour, $\tau = 1$ hour) vs the agar concentration. The average critical stress $\bar{\sigma}_c$ increases with the agar concentration, for both the first and second gel debonding. First, the gels prepared with agar-BM2 display a greater adhesion to smooth plastic dish than that prepared with agar-BM1. Such a result, likely due to the differences in ionic composition between the two types of agar, is more pronounced for the first debonding. The centrifuge runs further show a non-linear dependence with the agar concentration of the critical shear stress associated with the first debonding [Fig. 4.16(a)], in good agreement with the LAOS experiments discussed in the previous section [see

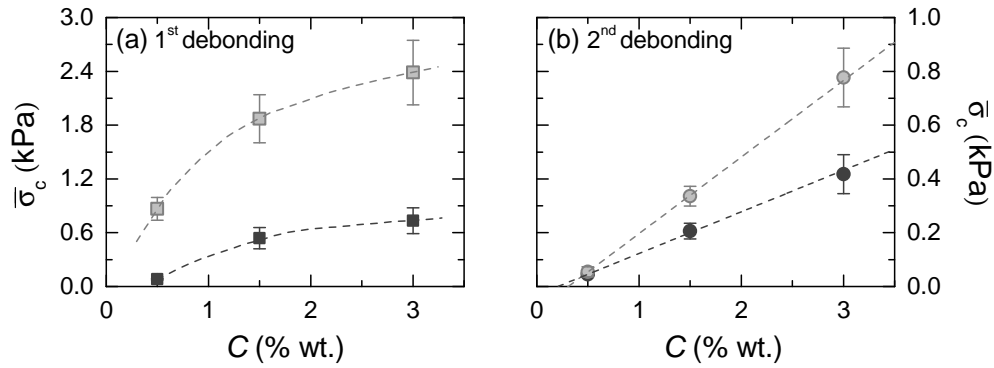


Figure 4.16: Average critical shear stress $\bar{\sigma}_c$ vs. the agar concentration C for agar-BM1 (dark gray) and agar-BM2 (light gray) gel pellets for (a) the first debonding ($T = 1$ h) and (b) the second debonding of the gel ($T = 1$ h, $\tau = 1$ h) in contact with a smooth plastic dish. Dashed lines are guides for the eye. The centrifuge experiments are performed with gel pellets of thickness $e = 4$ mm. The rate of increase of the rotation speed is $d\omega/dt = 3.33$ rpm/s. Error bars correspond to the standard deviation of the ensemble averaged critical stress for 3 to 5 centrifuge runs, that is $3 \times 8 = 24$ up to $5 \times 8 = 40$ gel pellets.

Fig. 4.9(b)]. Moreover, the critical shear stress measured for the second debonding of the gel increases linearly with the the agar concentration [Fig. 4.16(b)]. Such significant differences between the agar concentration dependence of the critical shear stress for the first and second debonding strongly suggest the presence of trapped liquid films at the gel/solid interface before the first debonding. Furthermore, the weaker critical shear stress (and the linear concentration dependence) for the second debonding of gels placed back to their original position is most likely due to the mismatch between the roughness of the gel bottom surface and that of the plastic dish, as later discussed in Section 4.4.

4.3.5 Impact of the solid surface properties

Solid surface roughness and gel debonding

The present section concerns the influence of the surface roughness of the solid substrate on the critical shear stress associated with the first and the second debonding of the gel. For this purpose, glass and plastic (PS) dishes were sandblasted and circular smooth, or sandblasted, duralumin plates, or polymethyl-methacrylate (PMMA) plates, were glued to the bottom wall of large smooth plastic dishes. Some duralumin circular plates were also polished with a suspension of ultra-fine aluminium oxide particles to produce smooth mirror-like surfaces (see Section 2.6 in Chapter 2 for more details).

The first debonding of 1.5% wt. agar-BM1 gel pellets in contact with various solid surfaces was investigated for different agar concentrations at 25°C, after a storage time in the fridge of $T = 1$ h [Fig 4.17(a)–(c)]. For all the concentrations, the same trend is observed: the average critical stress $\bar{\sigma}_c$ associated with the first debonding increases as a power law of the average RMS roughness \bar{R}_q of the solid surface, up to a threshold \bar{R}_q^* beyond which $\bar{\sigma}_c$ is roughly constant, independent of the RMS roughness of the substrate over almost two decades. For $\bar{R}_q < \bar{R}_q^*$, a single power-law $\bar{\sigma}_c \propto \bar{R}_q^\chi$ with the exponent $\chi = 2/3$ independent of the agar concentration is found to describe the data, whereas for $\bar{R}_q > \bar{R}_q^*$ the shear stress plateau noted $\bar{\sigma}_c^*$ increases with the agar concentration: $\bar{\sigma}_c^* = 0.15$ kPa, 0.8 kPa and 1.4 kPa for agar concentrations $C = 0.5\%$ wt., 1.5% wt. and 3% wt., respectively. The value of the surface roughness threshold $\bar{R}_q^*(C)$, as determined by the intersection of the two regimes, slowly increases from 20 nm to 28 nm when increasing

the agar-BM1 concentration from 0.5% wt. to 3% wt..

After the first centrifuge run, the gel pellets are placed back to their original position and allowed to rest for $\tau = 1$ h before starting a second centrifuge run to determine the critical shear stress for the second debonding. The results of experiments performed for different smooth and rough solid surfaces are summarized in Figure 4.17(d)–(f). The critical shear stress associated with the second debonding shows the same dependence with the RMS surface roughness of the solid substrate as that discussed above for the first debonding. Yet, the second debonding appears as more reproducible than the first one, and measurements of the average critical shear stress $\bar{\sigma}_c$ show a better precision. Once more, the values of the critical shear stress are smaller than that determined for the first debonding. For substrates of low surface roughness, i.e. $\bar{R}_q < \bar{R}_q^*$, a power law $\bar{\sigma}_c \propto \bar{R}_q^\chi$ with an exponent $\chi \approx 1/2$, slightly lower than the value associated with the first debonding, best describes the experimental data. For $\bar{R}_q > \bar{R}_q^*$, the stress plateau $\bar{\sigma}_c^*$, increases with the agar concentration, and the surface roughness threshold $R_q^*(C)$ that separates the two regimes increases from 18 nm to 28 nm with the agar-BM1 concentration.

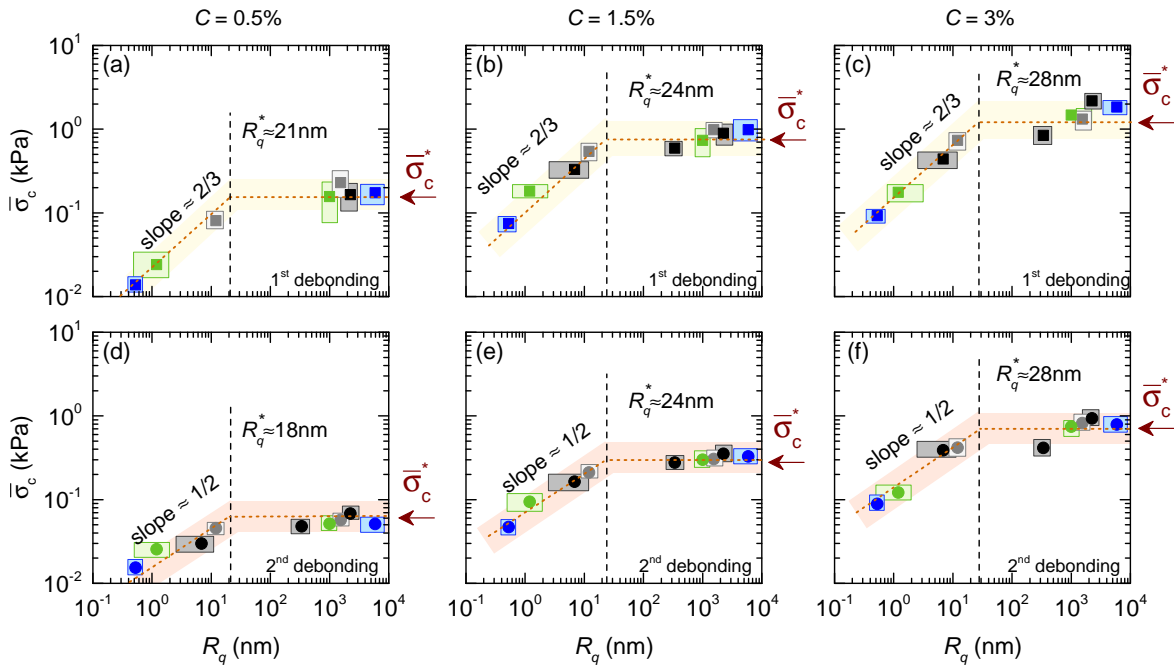


Figure 4.17: (a)–(c) Average critical shear stress $\bar{\sigma}_c$ associated with the first debonding of the gel vs. the average RMS roughness \bar{R}_q of the solid surfaces. Data obtained with agar-BM1 gel pellets for different agar concentrations $C=0.5\%$ wt. (a), 1.5% wt. (b) and 3% wt. (c), after a storage time in the fridge of $T = 1$ h. (c)–(e) Average critical shear stress $\bar{\sigma}_c$ associated with the second debonding vs. the average RMS roughness \bar{R}_q of solid surfaces. Data obtained with agar-BM1 gel pellets for different agar concentrations $C=0.5\%$ wt. (a), 1.5% wt. (b) and 3% wt. (c) for $T = 1$ h and $\tau = 1$ h. The RMS surface roughness threshold \bar{R}_q^* delimits a weak adhesive regime where the critical stress $\bar{\sigma}_c$ follows a power-law scaling with the surface roughness, from a stronger adhesive regime where the critical stress, noted $\bar{\sigma}_c^*$, weakly depends on the surface roughness. For $\bar{R}_q < \bar{R}_q^*$, the power-law exponent is $2/3$ for the first debonding and $1/2$ for the second debonding. Experiments performed at 25°C with gels in glass dishes (square blue symbols), PS plastic dishes (square gray symbols), duralumin surfaces (square black symbols) and PMMA plastic surfaces (square green symbols) with a rate of increase of the rotation speed $d\omega/dt = 3.33$ rpm/s. Error bars (i.e. colored rectangles) correspond to the standard deviation of the ensemble averaged critical stress for 3 to 5 centrifuge experiments, that is $3 \times 8 = 24$ up to $5 \times 8 = 40$ gel pellets.

Solid surface wettability and agar debonding

The last experimental section deals with the influence of wettability upon the adhesion of an agar gel on a solid surface. On the one hand, smooth glass and plastic dishes were exposed for 30 minutes to UV-O₃ in an ultraviolet ozone cleaning system (UVOCS T0606B) to produce hydrophilic surfaces. UV-O₃ removes organic contaminants, which are converted into volatile substances. As a result, the wettability of both smooth glass and smooth (PS) plastic surfaces is increased (water contact angle of about $\theta \approx (7 \pm 2)^\circ$ and $\theta \approx 10^\circ$, respectively). Moreover, optical observations with a 3D scanning interferometer of solid surfaces exposed to UV-O₃ during 1 hour shows no significant change in the average RMS surface roughness ($R_q \approx 0.5 - 0.6$ nm and $R_q \approx 10 - 14$ nm for UV-O₃ treated smooth glass and plastic surfaces, respectively). On the other hand, glass dishes were silanized with molecules of octadecyltrichlorosilane (OTS). The C17 aliphatic chains self-assemble to form a layer that increases the hydrophobicity of the glass (Silberzan, Leger, Ausserre, & Benattar, 1991; Brzoska, Azouz, & Rondelez, 1994; Watson, Nie, Wang, & Stokes, 2015). Glass silanization requires OH-terminated sites on the surface of interest and therefore extensive cleaning of the dish prior to any surface treatment. Glass dishes are first hydroxylated in a piranha solution of concentrated sulphuric acid and hydrogen peroxide at a ratio 3:1 during 20 minutes⁶, before being rinsed with double distilled water and dried with nitrogen. Direct OTS functionalization was then performed by immersing the glass dishes during two hours in a glass beaker containing a 2% wt. OTS solution in anhydrous toluene (Silberzan et al., 1991; Brzoska et al., 1994). The glass dishes were finally rinsed with toluene and dried with nitrogen before annealing for a few hours at 95°C. The measurement of the water contact angle of about 85° confirms the hydrophobicity of OTS functionalized smooth glass surfaces. Moreover, 3D scanning microscopic observations and AFM views of OTS functionalized smooth glass surfaces further show a polymer brush like texture with an average surface roughness $R_q \approx (1.7 \pm 1.0)$ nm three to four times larger than the average RMS roughness of smooth glass surfaces, i.e. $R_q \approx (0.53 \pm 0.10)$ nm. OTS molecules are likely in a nearly upright configuration on the smooth glass surface since the thickness of an ideal OTS monolayer ranges from 2 nm to 3 nm under various conditions of sample preparation (Watson et al., 2015).

Centrifuge runs performed 1 hour after the gelation of 1.5% wt. agar-BM1 show no significant impact of the solid surface wettability upon the critical shear stress for the first debonding of agar gels, neither with the UV-O₃ exposure nor with the OTS treatment of the solid substrate [Fig. 4.18(a)]. The uncertainty in the measurements of the critical shear stress might hide a subtle effect of the surface treatment, but the centrifuge runs performed with a wide variety of smooth or rough materials (glass, PS plastic, PMMA, duralumin) do not show any marked influence of the solid surface wettability. In a similar fashion, the critical shear stress associated with the second debonding remains almost unchanged after the UV-O₃ exposure of the smooth glass and plastic dishes [Fig. 4.18(b)]. Yet, the OTS functionalization of smooth glass dishes leads to a slightly more adhesive contact [see the square blue symbols with a red color outline in Fig. 4.18(b)]. Note that the roughness increase of the silanized smooth glass surface is taken into account in Figure 4.18(b). The data points for OTS functionalized surfaces remain nonetheless outside of the colored region representative of the adhesive behavior determined for the untreated surfaces.

⁶The preparation of the piranha solution is known to be dangerous when adding hydrogen peroxide to sulfuric acid, never the other way around.

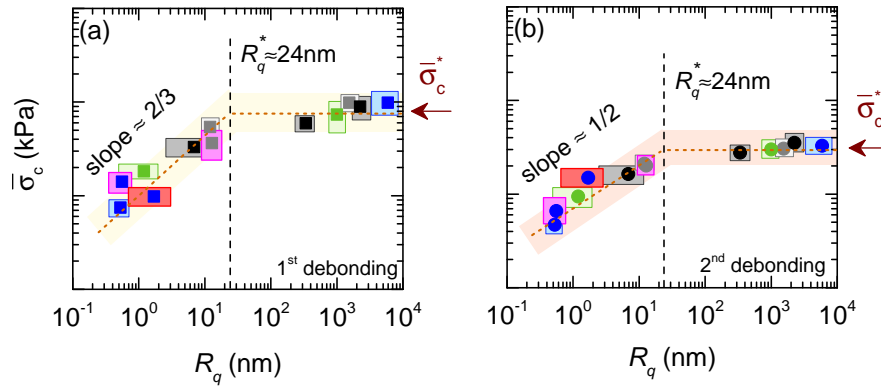


Figure 4.18: Average critical shear stress $\bar{\sigma}_c$ of 1.5% wt. agar-BM1 gel vs. the average RMS roughness \bar{R}_q of solid surfaces for (a) the first debonding with $T = 1$ h and (b) the second debonding with $\tau = 1$ h. The data displayed in (a) and (b) are the same as that displayed in Figure 4.17(b) and (e), with supplementary data corresponding to UV- O_3 exposed smooth glass dishes (square blue symbols in pink color rectangles), UV- O_3 exposed smooth plastic dishes (square gray symbols in pink color rectangles) and OTS functionalized smooth glass dishes (square blue symbols in red color rectangles). Other symbols correspond to untreated glass, plastic (PS or PMMA) or duralumin surfaces [see Fig. 4.17(b) and (e) for more details]. Experiments performed at 25°C with a rate of increase of the rotation speed $d\omega/dt = 3.33$ rpm/s. Error bars (i.e. colored rectangles) correspond to the standard deviation of the ensemble averaged critical stress for 3 to 5 centrifuge runs, that is $3 \times 8 = 24$ to $5 \times 8 = 40$ gel pellets.

4.4 Discussion and conclusion

In this chapter, the adhesion between agar gels and solid surfaces has been studied using two different methods: oscillatory shear rheology and a modified spinner centrifuge. Shear rheology allows us to form the gel in a parallel-plate geometry, taking into account the sample contraction during the gelation. The rheometer leads to a precise measurement of both the critical shear stress and the critical strain associated with the first debonding of the gel sample from the parallel plates. However, each measurement requires a time consuming preparation of a new gel, making it difficult to gather the large number of measurements that is necessary to reduce the data dispersion associated with the heterogeneous properties of the solid/gel contact. In comparison, the spinner centrifuge allows us to test the debonding of 8 gel pellets in a single experiment leading quickly to better statistics. Moreover, the centrifuge offers the possibility to replace the agar gel pellets to their initial positions in the dish, and to perform a second run to measure the second debonding of the gel. Using these two methods, the first and second debonding of agar gels were thoroughly investigated, exploring the role of the gel thickness, the time elapsed between the start of the experiment and the gel debonding ($30 \text{ s} < t_c < 3 \text{ h}$), the agar concentration ($0.5\% \text{ wt.} < C < 3\% \text{ wt.}$) and the solid surface properties (roughness and wettability). Both rheological and centrifuge experiments lead to comparable results with a critical shear stress that is independent of the gel thickness. The deviation from the Amontons–Coulomb behavior was shown to be representative of a stress-induced lubrication of the adhesive contact between the gel and the substrate, and the interfacial debonding of the agar gel occurs for a critical shear strain that is larger than a few percent.

We now provide a rationale for the main results of the present chapter, presented in Figure 4.17. One first considers the shear-induced debonding of agar gels from rough solid surfaces with an average RMS surface roughness $R_q > R_q^*$. In that case, the critical shear stress $\bar{\sigma}_c$ for agar gel debonding was shown to take a constant value $\bar{\sigma}_c^*$ that weakly depends upon the texture of the solid surface. The plateau values of the critical shear

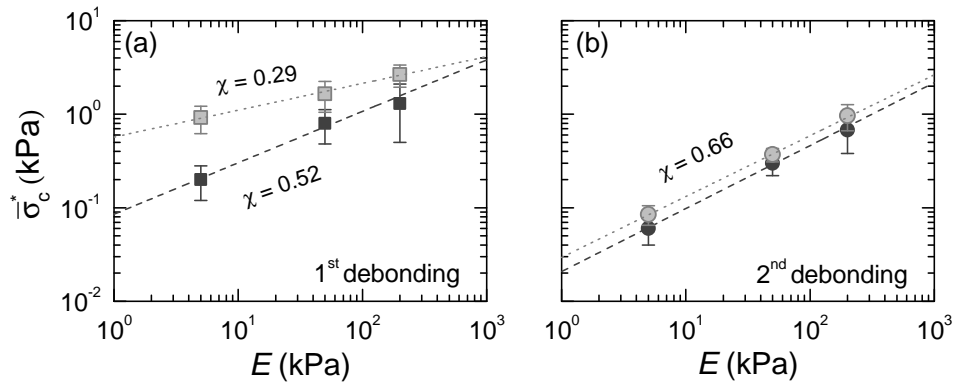


Figure 4.19: Average plateau value $\bar{\sigma}_c^*$ of the critical stress for (a) the first and (b) the second debonding of agar-BM1 and agar-BM2 gels vs. the gel elastic modulus E . The plateau value $\bar{\sigma}_c^*$ corresponds to solid surfaces with an average roughness $\bar{R}_q > \bar{R}_q^*$. The dashed lines are the best fits of the data in logarithmic scale for the first gel debonding ($\bar{\sigma}_c^* \propto E^{0.52}$ for agar-BM1 and $\bar{\sigma}_c^* \propto E^{0.29}$ for agar-BM2) and the second gel debonding ($\bar{\sigma}_c^* \propto E^{0.66}$ for both agar BM1 and agar BM2).

stress $\bar{\sigma}_c^*$ extracted from Figure 4.17 for both the first and second debonding are plotted in Figure 4.19 as a function of the gel elastic Young's modulus E , otherwise determined through macro-indentation experiments (see Section 2.3.2 for technical details). As a striking result, the critical shear stress $\bar{\sigma}_c^*$ associated with the first debonding scales as a power law of E , with an exponent $\chi \approx 0.52$ for agar-BM1 gels and $\chi \approx 0.29$ for agar-BM2 gels [Fig. 4.19(a)]. Besides, the critical shear stress for the second debonding of both agar-BM1 and agar-BM2 gels also shows a power-law scaling $\bar{\sigma}_c \propto \bar{R}_q^\chi$, but with the same exponent $\chi \approx 0.66$ [Fig. 4.19(b)].

We start by describing the second debonding, which appears simpler than the first one. To account for the power-law dependence, we describe the gel network as a collection of adjacent blobs with a size ξ that controls the gel elasticity (De Gennes, 1979; Stauffer, Coniglio, & Adam, 1982). The scaling theory from de Gennes and Stauffer *et al.* relates the elastic modulus $E(C)$ of a polymer material, which is function of the polymer concentration C , to the blob size through the relation: $E \approx 3kT/[\xi(C)]^n$, where n is a critical exponent worth $n \approx 3$ for stiff chains, and kT represents the thermal energy. If we assume that the adhesive contact between the gel and the substrate does not involve any intercalated liquid film, the critical shear stress $\sigma_c(C)$ associated with the debonding of the gel from the substrate is expected to obey an inverse square dependence with the mesh size $\xi(C)$, insofar as each blob of the gel may establish a bond with the solid surface. Within such a framework, the critical shear stress should scale with the Young's modulus as follows: $\sigma_c(C) \propto \xi^{-2} \propto E^{2/3}$, which is indeed in excellent agreement with the scaling observed for the second debonding of both agar-BM1 and agar-BM2 gels [Fig. 4.19(b)]. This result confirms that the characteristics of the second debonding do not depend on the details of the gel ionic composition. Moreover, we have seen that the elastic modulus E of agar gels plotted as a function of the agarose concentration obeys a power law, which reads $E(C) \approx (C - C_g)^p$, where $C_g \approx 0.1\%$ denotes the agarose percolation threshold and the exponent $p \approx 1.6 - 1.8$ [see Fig. 1.6(d) in Chapter 1]. From this scaling and the scaling between E and ξ discussed above, one may derive a scaling law for the mesh size as a function of the polymer concentration: $\xi(C) \approx (C - C_g)^{-m}$, with $m = p/n \approx 0.5 - 0.6$. As a consequence, the same assumption of an heterogeneous adhesive contact between the gel and the substrate, without any intercalated liquid films, leads to the following scaling for the debonding stress: $\sigma_c(C) \propto \xi^{-2} \propto (C - C_g)^{2p/n} \approx (C - C_g)^{1-1.2}$. Such

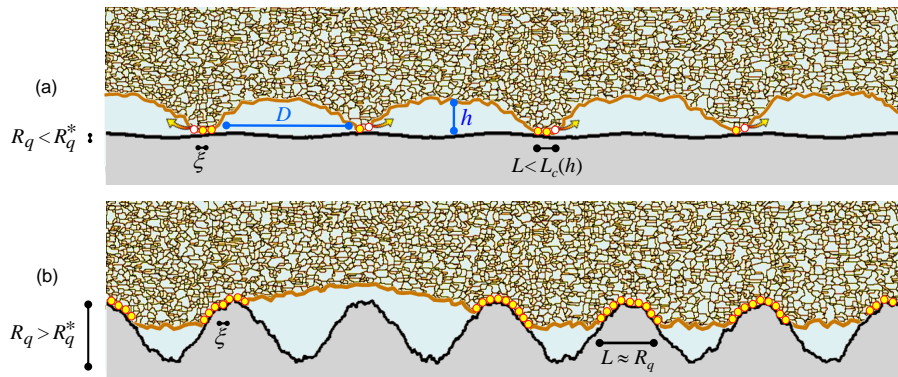


Figure 4.20: Schematic representation of the adhesive contact after agar gelation (before a first debonding) on (a) a smooth solid surface with RMS roughness $R_q < R_q^*$ or (b) a rough solid surface with RMS roughness $R_q > R_q^*$. The polymer network (dark orange color) soaked with water (blue color) interacts with the solid surface (gray color) at the scale of the mesh size ξ through weak energy bonds represented as yellow disks. The white disks and arrows represent unstable links with the smooth solid surface and which are breaking up.

a result is in agreement with the quasi-linear agar(ose) concentration dependence of the critical shear stress σ_c reported for the second gel debonding of both agar-BM1 or agar-BM2 gels [see Fig. 4.16(b)]. The latter result further supports the idea that prior to the second debonding, the adhesive contact between the agar gel and the solid substrate is heterogeneous and does not involve any liquid films at the interface.

We now turn to the first debonding. The adhesive contact between the gel and the substrate, right after the gelation and prior to the first debonding appears as peculiar and much more sensitive to the agar batch. Moreover, the critical shear stress displays a non-linear increase with the agar concentration [Fig. 4.9(b) and Fig. 4.16(a)] and show a power-law increase with the gel elastic modulus, $\sigma_c \propto E^\chi$, with an exponent $\chi \approx 0.52$ for agar-BM1 and $\chi \approx 0.29$ for agar-BM2. In both cases, the exponent is smaller than the value of $2/3$ derived above [Fig. 4.19(a)]. We propose that the peculiar behavior of the adhesive contact between the gel and the substrate, after gelation and prior to the first debonding likely results from the presence of water films at the gel/substrate interface.

A condition for the adhesion of a soft material on a solid substrate is the dewetting of the water films located at the interface (Martin & Brochard-Wyart, 1998). The stability of trapped films depends on the sign of the spreading parameter $S = \gamma_{sg} - (\gamma_{sl} + \gamma_{lg})$, which compares the surface energies γ_{sg} and $\gamma_{sl} + \gamma_{lg}$ of an adhesive contact and a lubricated contact, respectively (De Gennes, Brochard-Wyart, & Quéré, 2005). For $S < 0$, the contact gains in surface energy by excluding the liquid film, whereas wetting and lubrication of the substrate occurs for $S > 0$. For weak physical interactions such as hydrogen bonds, the spreading parameter can be expressed as⁷ $S \approx -kT/\xi^2$, which leads to the following expression for the elasto-adhesive length $h_0 \approx |S|/E \approx \xi$ with $E \approx kT/\xi^3$. Surface energies induce elastic deformation of the gel at length scales smaller than the elasto-adhesive length $h_0 \approx \xi$ (Persson et al., 2005; Creton & Ciccotti, 2016). One now considers an adhesive bridge of size L between a soft material and a smooth solid surface with a surrounding intercalated liquid film of thickness h [Fig. 4.20(a)]. A water film at the interface between

⁷The relation $S \approx -kT/\xi^2$ neglects the solid/liquid and liquid/gel surface tensions. The high water content of agar gels makes negligible the surface energy γ_{lg} of the water/gel contact but the hydrophilic/hydrophobic properties of the solid surface may somewhat influence the spreading parameter $|S|$ and the solid/gel contact. Agar gel adhesion on hydrophilic (following exposure to UV-O₃) or hydrophobic silanized surfaces will be considered in the last part of the discussion.

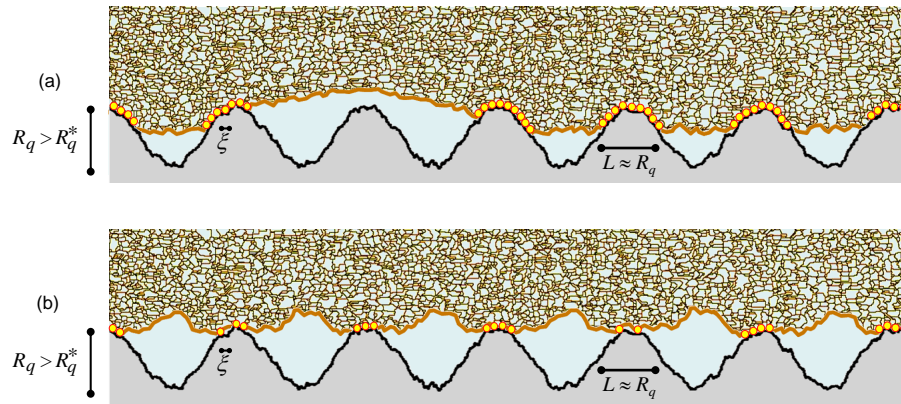


Figure 4.21: Schematic representation of the adhesive contact on a rough solid surface with RMS roughness $R_q > R_q^*$ (a) after agar gelation (prior to the first debonding) and (b) after the gel has been positioned back on the substrate following the first debonding (and prior to the second debonding). The polymer network (dark orange color) soaked with water (blue color) interacts with the solid surface (gray color) at the scale of the mesh size ξ through weak energy bonds represented as yellow disks.

a solid surface and a soft material behaves as a metastable flat ellipsoid with a diameter $D \approx h^2/h_0$ of micrometric extent for a film thickness $h \approx 100$ nm and an elasto-adhesive length $h_0 \approx \xi \approx 10$ nm (Martin, Silberzan, & Brochard-Wyart, 1997). The stability of the gel/solid contact of size L can be further described by the balance between the adhesive energy SL^2 and the stored elastic energy $E\varepsilon^2L^3$, where $\varepsilon = h/L$ is the elastic strain of the deformed gel of volume L^3 (Persson & Mugele, 2004; Martin et al., 1997). Minimizing the balance energy with respect to L gives the critical size $L_c \approx h^2/2h_0$ for the nucleation and the growth of adhesive bridges on a smooth surface. Therefore, in the sub-critical regime, the weak adhesive contact of a soft material on a smooth solid surface may be viewed as a series of small adhesive bridges of size $L < L_c$ separated by metastable intercalated liquid films of thickness $h \gg \xi$ [Fig. 4.20(a)].

Moreover, surface imperfections may induce the dewetting of the liquid films and the growth of the adhesive bridges (Martin, Buguin, & Brochard-Wyart, 2001). Assuming a dewetting of the liquid film of thickness h for asperities of RMS surface roughness $R_q \approx h$, adhesive bridges may grow and reach a stable size $L \approx R_q$ when the condition $R_q > L_c \approx R_q^2/2h_0$ is fulfilled. The latter condition gives a critical RMS roughness $R_q^* \approx 2h_0 \approx 2\xi$, where R_q^* should scale as $\xi(C)$, and therefore should decrease with the agar concentration. However, the critical RMS roughness R_q^* measured experimentally increases with the agar concentration C : $R_q^* \approx 21$ nm, 24 nm, 28 nm for $C = 0.5\%$ wt., 1.5% wt. and 3% wt. agar-BM1 gels, respectively [Fig. 4.17(a)–(c)].

Actually, liquid dewetting at soft interfaces may only partially control the adhesion of agar gels on solid surfaces, since the adhesive gel/solid contact forms during the gelation. Indeed, agar gelation goes with a contraction in bulk of the sample (see Section 2.3.1 in Chapter 2) and as a result, the water moving from the bulk to the gel/solid interface may promote the formation of water films. Since the gel contraction increases with the agar concentration [see Fig. 6.1(c) in Chapter 6], one may expect thicker water films and a higher critical roughness R_q^* for gels of higher agar concentrations. The increase of the thickness h of the water film with the agar concentration weakens the adhesive contact between the gel and the substrate, and results in the non-linear concentration dependence of the critical shear stress associated with the first debonding, as observed experimentally [Fig. 4.9(b), Fig. 4.16(a)]. Under such conditions, one may expect a higher

adhesive contact of the gel on the apex of asperities on a rough solid substrate with a RMS surface roughness R_q larger than the thickness h of the intercalated water films formed during gelation [Fig. 4.20(b)]. In that framework, the critical surface roughness $R_q^* \approx h$ is representative of the characteristic thickness h of intercalated water layers on a smooth surface. Therefore, for smooth surfaces, i.e. $R_q < R_q^*$, the critical shear stress increases as a power law of the surface roughness of the solid substrate: $\sigma_c \approx R_q^{2/3}$ [Fig. 4.17(a)–(c)] since surface imperfections of growing height favor water dewetting from the apex of the asperity. In the case of rough surfaces, i.e. $R_q > R_q^*$, the liquid is likely located in the valleys formed by the surface asperities, and the adhesive bridges of size $L \approx R_q$ are located on the apex of the asperities [Fig. 4.20(b)], without any significant deformation of the polymer network because adhesive bonds are formed early during the gelation. As a consequence, the surface roughness of the substrate weakly influences the gel contact area with a rough solid surface, and the critical shear stress for the first debonding $\bar{\sigma}_c^*$ is constant for $R_q > R_q^*$. Following the same reasoning, one can understand that the gel contraction during gelation and the lower contact area between the gel and the substrate when increasing the agar concentration, influence the E -dependence of the critical shear stress. On a rough surface, the latter scaling reads $\bar{\sigma}_c^*(E) \approx E^\chi$, with an exponent $\chi \approx 0.3$ for agar-BM1 gels and $\chi \approx 0.5$ for agar-BM2 gels [Fig. 4.19(a)]. The presence of additives and the ion composition of agar may strongly influence the gelation dynamics and the gel contraction near the solid surface asperities, which results in significant changes in the adhesive contact and exponent value $\chi \approx 0.3 - 0.5$ smaller than $2/3$. Nonetheless, the liquid dewetting from the apex of asperities remains likely incomplete even on rough surfaces [Fig. 4.20(b)]. Indeed, water cannot be squeezed out from the interface after the gelation, and the liquid drainage is limited by the diffusion of water in the gel network. Pockets of liquid are trapped as soon as the contact area ratio (contact area/whole area) between randomly rough surfaces is larger than 0.4, because of the percolation of the elastic contacts (Dapp, Lucke, Persson, & Muser, 2012).

During the first debonding, the sliding motion of agar gel pellets inside the dish appears as a very efficient way to remove the liquid films formed during agar gelation [Fig. 4.21(a)]. The effect could be explained by a very recent paper from Hutt and Persson (Hutt & Persson, 2016) that introduces a “scraping mechanism” for the rapid removal of the lubrication layer when a soft material slides onto a rough solid surface. Under an external shear force, the liquid pressure builds up on the rear side of the lubricated contact (because of the increasing distance between the surfaces) and decreases on the inlet side [Fig. 4.22(b)], which deforms the soft sliding material as indicated in Figure 4.22(c). Such a mechanism favors the output of the liquid film until the motion of the gel stops

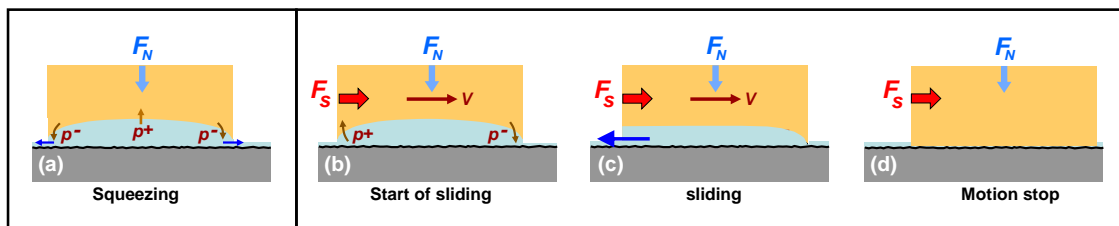


Figure 4.22: Schematic representation of liquid drainage from the interface between a soft material and a rough solid surface during (a) stationary contact or (b-d) sliding. The sliding motion induces (b) a transient asymmetric hydrodynamic deformation of the soft material and (c) a rapid thinning of the lubrication layer until (d) close contact with the solid surface and motion stop. Reprinted from (Hutt & Persson, 2016).

[Fig. 4.22(d)]. Indeed, the observation of agar gel pellets slowly sliding on a dry surface shows the continuous release of tiny water drops leaving a wet trail in the wake of the soft material. Therefore, a scraping mechanism as the gel slides on the surface could account for the release of the intercalated water films from the interface, and explain why the contact between the gel and the rough solid surface turns into a heterogeneous adhesive contact with no liquid film. Finally, despite the removal of the water films after the first debonding, the shear stress required for the second gel debonding on rough surfaces is always smaller than that required for the first debonding, whatever the agar concentration. The reason is the following: when the gel cast in a dish is replaced on the solid surface after the first debonding, the gel asperities do not coincide any more with the complex topography of the solid substrate, which results in a lower adhesion of the gel to the substrate [Fig. 4.20(b)].

Another key result of the present study is that the debonding experiments (LAOS and centrifuge runs) performed with various surfaces (glass, plastic, PPMA, duralumin) indicate no significant influence of the surface wettability upon the adhesive contact. Only a few papers in the literature deal with the role of surface wettability on the frictional behavior of neutral hydrogels. The work by (Tominaga et al., 2008) deals with the velocity dependence of sliding friction under relatively high normal pressure ≈ 14 kPa. It shows that the hydrophobicity of the substrate changes the adhesion strength of polyvinyl alcohol (PVA) hydrogels and also reduces the friction in the lubricated hydrodynamic regime. A possible explanation given by the authors is the formation of gas bubbles on the hydrophobic surface. Usually, a hydrophobic interface increases the sliding friction when the asperity contact regions are separated by a thin fluid film at the nanometer scale. The sliding of the contact regions may indeed promote the formation of dry surface areas, where the friction is higher than for lubricated surfaces (Lorenz, Rodriguez, Mangiagalli, & Persson, 2014). For hydrophilic interfaces, the surface separation between sliding surfaces may even increase due to the build up of fluid pressure. Comparatively, agar gels cured in dishes behave quite differently from lubricated soft solid materials. Since the adhesive contact between the gel and the substrate forms during gelation, one indeed expects a prime influence of the surface roughness of the substrate, and a negligible (or second order) impact of the wettability of the substrate upon the critical stress for first gel debonding, as observed experimentally [Fig. 4.18(a)]. Nevertheless, hydrophobic substrates may increase the sliding friction of agar gels after the first shear-induced debonding and speed up the removal of intercalated water films resulting in a strengthening of the adhesive contact in line with the experimental observations for smooth silanized glass surfaces [Fig. 4.18(b)].

Finally, we can explain within this framework the slow increase with the waiting time T , of the critical shear stress $\bar{\sigma}_c$ associated with the first gel debonding [Fig. 4.12(a)]. The liquid entrapment after gelation is followed by the slow diffusion of water through the polymer network, which is responsible for an increase in the gel adhesion to the solid surface. Moreover, the liquid drainage from a rough interface may speed up the increase of the critical stress $\bar{\sigma}_c$ associated with the second debonding of agar gels on rough surfaces, once the gel has been replaced to its initial position on the substrate [Fig. 4.15(b), Table 4.1]. On longer time scales, water films may be drained through the polymer network, leading to the swelling of the gel and/or compensating for the water lost by evaporation. The swelling of hydrogels is mainly governed by the osmotic and frictional properties of the network through the collective diffusion coefficient $D_c \approx M/f$ where $M = E(1 - \nu)/[(1 + \nu)(1 - 2\nu)]$ is the osmotic bulk modulus, ν the Poisson coefficient and $f \approx \eta/\xi^2$ the friction between the polymer network and the liquid (Lorenz et al., 2014; Tanaka & Fillmore, 1979; Y. Y. Suzuki, Tokita, & Mukai, 2009; Tokita, 2016). The expression of the collective diffusion coefficient $D_c \approx E\xi^2/\eta \approx kT/(\eta\xi)$ highlights the

importance of the network fluctuations at the scale of the mesh size ξ , for the transport properties of gels. The swelling of agar gel pellets of thickness $e = 4$ mm thus occurs in a characteristic time $T_c = e^2/D_c \approx \eta e^2 \xi / kT$ of a few hours. Therefore, the slow diffusion of interfacial water films through the poroelastic gel network may reasonably account for the aging of the adhesive contact when waiting a few hours after agar gelation [Fig. 4.12(a)] or after the gel has been replaced to its initial position on the substrate [Fig. 4.12(b)].

Appendix A

Observations of agar gels under compression or shear

The present appendix concerns two kinds of observations performed with a homemade cell designed to visualize (i) the water released from a gel under compression, at the air/gel interface, and (ii) the shear-induced debonding of an agar gel from a solid surface. In the first series of experiments, a square piece of gel is submitted to an uniaxial compression, whereas in the second series of experiments we focus on the debonding of an agar gel from a transparent plastic plate induced by shear. We determine both the critical compressive strain ε_c for the water to be squeezed-out from the agar gel under compression, and the critical shear strain γ_c for the debonding of the gel under shear. Experiments are performed for agar-BM2 gels of different agar concentrations. The results are compatible with that obtained in both the LAOS and the centrifuge experiments reported in Chapter 4, and support a debonding scenario based on a stress-induced lubrication of the solid/gel interface.

A.1 Water release at the air/gel interface of a gel under compression

A homemade cell, using a manual linear stage, was specifically developed to control the uniaxial compression of a block of agar gel cast in a rectangular tank (dimensions: width 40 mm, length $L \approx 38.5$ mm and height $e \approx 5$ mm). The bottom wall of the cell is made of PMMA, whereas the lateral walls are made of smooth plastic (PVC). The cell is filled with the hot agar solution, which is left to gel at ambient temperature. The gel and the cell are then stored in the fridge at 5°C for one hour, and covered with a lid to minimize water evaporation. Compression experiments are further performed at 25°C by turning the plastic knob attached to a manual linear stage, which moves the left wall of the cell [Fig. A.1(a)]. The compression is made by step of $\delta l \approx 100 \mu\text{m}$, with a precision of about 10 μm , over a distance $l_{max} \approx 8$ mm, which corresponds to a total compressive strain $\varepsilon_{max} \approx l_{max}/L \approx 20\%$. The gel compression is performed either in 80 s (rapid compression) or in 15 minutes (slow compression) and after each compression step δl , an image of the air/gel interface is recorded with a webcam (Logitech HD c920) in automatic snapshot mode at 1 s/frame (resp. 10 s/frame) for rapid (resp. slow) compressions.

The compression of a 1.5% wt. agar-BM2 gel leads to the formation of water droplets

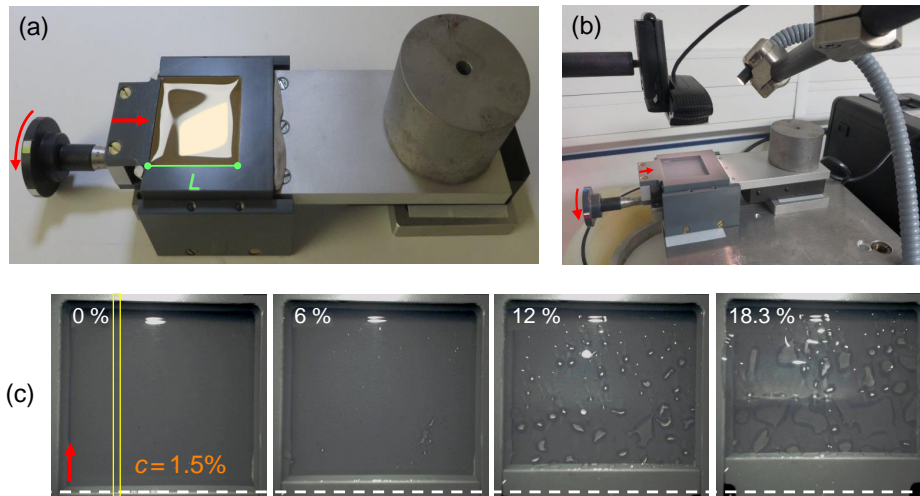


Figure A.1: (a) Experimental setup: a block of agar gel cast in a homemade rectangular cell (width 40 mm, longitudinal size $L \approx 38.5$ mm, and thickness $e \approx 5$ mm) is compressed through the step by step rotation of a plastic knob attached to a manual linear stage. One full revolution of the plastic knob corresponds to a displacement of $500 \mu\text{m}$ of the left vertical wall of the cell. The knob has 5 marks, which allows us to perform compressions by steps of $100 \mu\text{m}$ with a precision of about $10 \mu\text{m}$. (b) Observation of the air/gel interface with a webcam (Logitech HD c920) during the gradual compression of the gel block (c) Images of the gel block at different stages of a *slow* compression: $\varepsilon \approx 0, 6\%, 12\%$, and 18% . The red arrow in (c) indicates the compression direction (y axis).

at the air/gel interface for a compressive strain $\varepsilon = l/L$ larger than a few percents¹ [Fig. A.1(c)]. The temporal projection of the gray levels of all the pixels within the thin yellow vertical Region Of Interest (ROI) pictured in Fig. A.1(c) and oriented in the compression direction y allows us to build a spatio-temporal diagram $ST[\varepsilon(t), y]$ in which the formation of water droplets at the air/gel interface are clearly visible [Fig. A.2(a) and (b)]. Therefore, we introduce the critical compressive strain ε_c as the strain beyond which the first water drop is visible at the air/gel interface. For instance, we find $\varepsilon_c \approx 10\%$ for a 0.5% wt. agar-BM2 gel under *slow* compression [see the left column in Fig. A.2(a)].

A series of *slow* and *rapid* compression experiments performed on agar-BM2 gels of different concentrations show that the critical strain ε_c decreases for increasing agar concentrations, and that for a given agar concentration, the critical strain is always larger for *rapid* compressions [Fig. A.2(c)]. In brief, water is most likely expelled from a gel of large agar concentration during a *rapid* compression. These results are in agreement with that obtained with the LAOS experiments performed in a parallel plate. Indeed, the critical shear strain γ_c for gel debonding also decreases for increasing agar concentration [see Fig. 4.9(a) in Section 4.2.3]. However, a more quantitative comparison is delicate since LAOS (and centrifuge) experiments concern a shear deformation and not a compression. Yet, the relative agreement between the experimental values of ε_c (compression) and γ_c (shear) suggests that the liquid pressure inside the gel is isotropic and builds up uniformly under stress.

¹The gel plate weakly adheres to the smooth PMMA bottom wall and the smooth vertical plastic (PVC) walls of the cell. One assumes here that gel debonding from the walls during the compression experiment weakly influences the sweeping out of water from the air/gel interface indeed mainly controlled by the build up of the liquid pressure in the bulk gel under compression insofar as the gel plate remains flat without any significant bending.

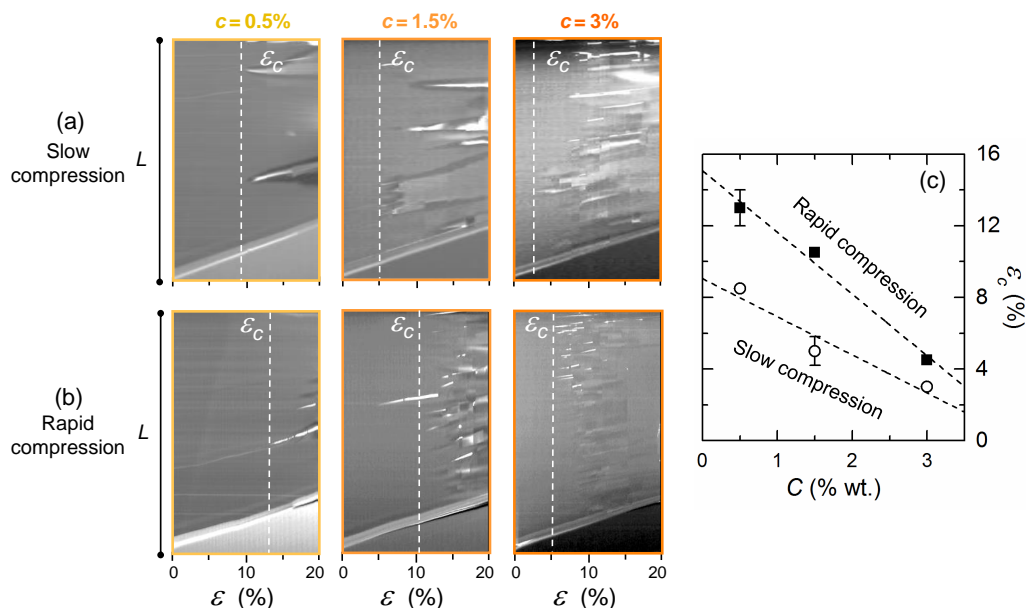


Figure A.2: Spatio-temporal diagrams $ST[\varepsilon(t), y]$ obtained from the projection of the gray levels of all the pixels within the thin yellow rectangle pictured in Fig. A.1(c) for (a) a *rapid*, or (b) a *slow* compression experiments of agar-BM2 gels of various concentrations: 0.5% wt. (left column), 1.5% wt. (center column) and 3% wt. (right column). The vertical white dotted lines indicate the critical compressive strain ε_c for the formation of water droplets at the air/gel interface. (c) Critical compressive strain ε_c vs the agar concentration C for rapid (full squares) and slow (open circles) compression experiments. Error bars in (c) correspond to the standard deviation of the data for 2 compression runs.

A.2 Shear-induced debonding of the gel from a solid surface

As a complement to the LAOS and centrifuge experiments, the homemade cell was adapted to shear a gel plate in contact with a moving solid surface. First, the agar gel is cast in a square volume (size 26 mm, and thickness $e = 5$ mm) bounded by a solid frame [Fig. A.3(a)]. After storing the cell in the fridge for one hour and removing the square frame, a plastic PMMA plate of rectangular shape (width 26 mm, length 75 mm and thickness 2 mm) is put in contact with the upper surface of the gel plate, and fixed with screws on the left mobile part of the cell [Fig. A.3(b)]. The step by step rotation of the manual linear stage ensures a uniaxial motion of the transparent PMMA plate and a shear deformation of the adhesive contact between the moving plastic plate and the gel [Fig. A.3(c)]. After each step $\delta l \approx 50 \mu\text{m}$ of the plastic plate, an image of the solid/gel adhesive contact is recorded with a webcam (Logitech HD c920). Moreover, the use of a sandblasted plastic plate and a direct illumination of the surface with a white beam source inclined at about 45° makes it possible to visualize the adhesive contact between the gel and the solid transparent surface [Fig. A.3(d)]. Images recorded during the shear experiment of a 0.5% wt. agar-BM2 gel show a progressive debonding of the gel, which takes place at the edge of the gel/plate contact region and becomes complete when the shear strain reaches 30% [Fig. A.3(d)]². A zoom on the adhesive region further reveals that beyond $\gamma \approx 5\%$, dark spots of about $50 \mu\text{m}$ size appears. These spots could correspond to stress-induced water films formed at the gel/plate interface.

²Note that the adhesion area between the gel and the solid plate covers only partially the surface of the gel square at the start of the shear experiment [left image of Fig. A.3(d)]. This is most likely due to some water evaporation during the storage of the gel in the fridge and some weak bending of the thin plastic plate (thickness 2 mm) in contact with the gel plate.

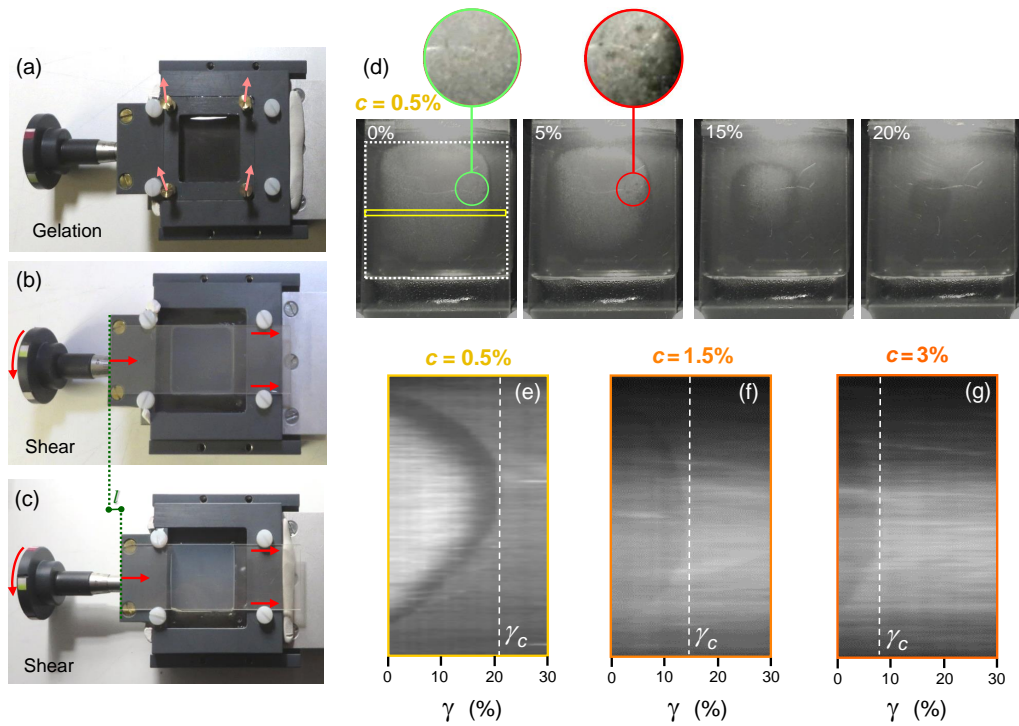


Figure A.3: (a) Agar gel plate cast in a square volume (size 26 mm and thickness $e = 5$ mm). (b) After storage of the homemade cell in the fridge for one hour and removal of the square solid frame, a rectangular transparent rough plastic plate is put in contact with the gel and fixed with screws on the left mobile part of the cell. (c) The step by step rotation of the plastic knob attached to the manual linear stage ensures the uniaxial motion of the transparent plastic plate and the shear deformation of the adhesive contact between the gel and the moving plastic plate. (d) Shear experiment of a 0.5% wt. agar-BM2 gel and views of the adhesion area for increasing shear strain $\gamma = 0\%$, 5% , 15% and 20% . The dotted white square in the left image emphasizes the contours of the square gel plate and the magnified images enclosed in a green (or red) circle show the apparition of dark spots for a shear strain $\gamma \approx 5\%$. (e)–(g) Spatio-temporal diagrams $ST[\gamma(t), x]$ obtained from the projection of the gray level values of all the pixels within the thin yellow rectangle pictured in the left view of (d) during the shear experiments of 0.5% wt. (e), 1.5% wt. (f) and 3% wt. (g) agar-BM2 gel plates. The vertical white dotted lines indicate the critical shear strain γ_c beyond which the failure of the adhesive contact is complete.

The temporal projection of the gray levels of all the pixels within the thin yellow horizontal ROI pictured in Fig. A.3(d) produces a spatio-temporal diagram $ST[\varepsilon(t), x]$ in which the shear-induced debonding of the gel from the plate is clearly visible [Fig. A.3(e)]. The experiment is repeated at two other concentrations [Fig. A.3(f)–(g)], and the spatio-temporal diagrams show a decrease of the debonding shear strain γ_c for increasing agar concentrations: from $\gamma_c \approx 20\%$ at 0.5% wt. to $\gamma_c \approx 8\%$ at 3% wt. in good agreement with the results of the LAOS experiments performed with a rheometer [see Fig. 4.9(a) in Section 4.2.3]. This observation strongly supports the idea that the shear-induced debonding of agar gel involves the expulsion of water from the bulk of the gel, and the lubrication of the adhesive contact. As a consequence, the departure from Amontons–Coulomb’s friction behavior of agar gels and the weak dependence of the debonding shear stress σ_c with the thickness of the gel (see Fig. 4.13 in Section 4.3.2) is most likely related to the stress-induced lubrication of the adhesive contact.

Chapter 5

Drying of agar gels

Contents

5.1	Drying of gels	110
5.2	Gel drying dynamics studied by tracking experiments	112
5.2.1	Drying of agar gel plates cast in a dish	113
5.2.2	Influence of agar concentration	116
5.2.3	Influence of solid surface properties	118
5.3	Gel local thinning-rate measured by interferometry	121
5.3.1	Influence of dish material and wall roughness	121
5.3.2	Drying of a thin agar gel cast in a glass dish	122
5.3.3	Influence of dish geometry	124
5.4	Mechanical and structural properties of agar gels during drying	126
5.5	Discussion and conclusion	128

Associated peer-reviewed article:

▷ **Impact of saccharides on the drying kinetics of agarose gels measured by *in-situ* interferometry,**

B. Mao, T. Divoux & P. Snabre,
***Scientific Reports* **7**, 41185 (2017)**

5.1 Drying of gels

Hydrogels, including agar gels are mainly composed of water and contain only a few percent in mass of natural or synthetic polymers that are linked together either by covalent bonds, or by physical interactions. Therefore, hydrogels are highly sensitive to water loss through evaporation and stress-induced solvent release (Brown, Litvinov, Discher, Purohit, & Weise, 2009), which can further induce a mechanical and structural evolution of the gel. The role of the present chapter is to shed some light on the link between the water-loss and the mechanical properties of agar gels.

The drying of polymer gels –and especially agar gels– has been quantified by different techniques such as macroscopic observations (Zrinyi, Rosta, & Horskay, 1993), weighing (Iglesias, Garcia, Roques, & Bueno, 1993), and more local investigation techniques such as small angle neutron scattering (Bastide, Duplessix, Picot, & Candau, 1984), fluorescence spectroscopy (Tari & Pekcan, 2008), and interferometry (Wu & Yan, 1994; Zhou & Wu, 1996). The seminal work of (Scherer, 1992a) has shown that the shrinkage of organometallic gels is controlled by the rate of liquid transport through the solid phase under the action of the osmotic pressure, which drives the liquid from the inner wet region of the gel to the dry external region. Moreover, the internal pressure gradient may further cause the warping and cracking of the gel network left to dry (Scherer, 1992b). The growth of poorly controlled surface pattern and the propagation of cracks in soft materials has motivated a large research effort that is still ongoing (Bertrand, Peixinho, Mukhopadhyay, & MacMinn, 2016), and for which edge effects and boundary conditions, occupy a special place.

Edge effects are commonly observed during the drying of sessile colloidal or sol-gel drops (Deegan, 2000; Pauchard & Allain, 2003; Loussert, Bouchaudy, & Salmon, 2016). The physics of three-phase contact line motion, flow fields, and mass transportation play

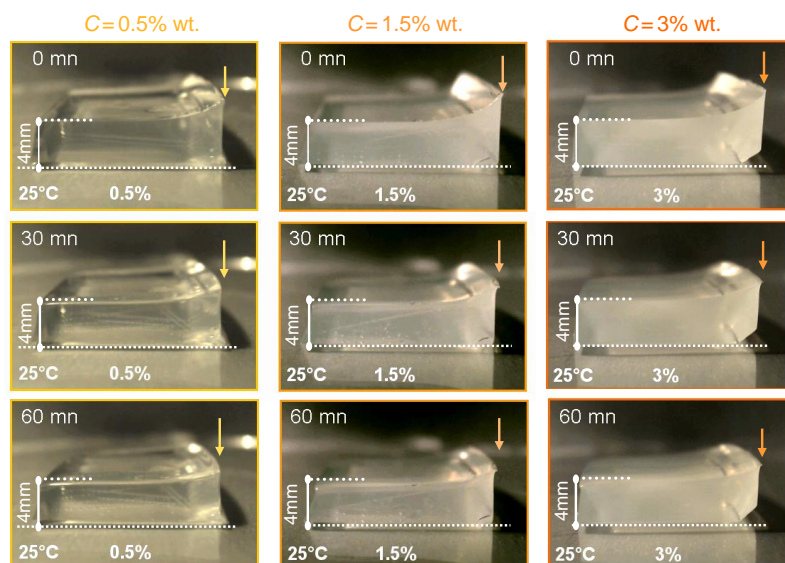


Figure 5.1: Observations of the drying of a square pieces of 0.5% wt. (left column), 1.5% wt. (middle column) and 3% wt. (right column) agar gels (length of about 2 cm, thickness 4 mm) extracted with a cutter from the peripheral region of a gel plate cast in a smooth plastic dish (diameter 90 mm) and carefully placed on a flat plastic surface. The vertical arrows highlight the fast thinning of the gel at the edge of the meniscus, while the decrease of the gel thickness in the flat region is much slower. Observations performed at $T = 25^{\circ}\text{C}$.

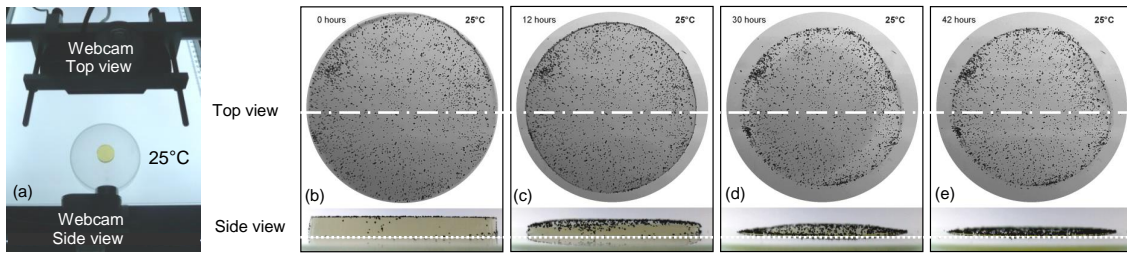


Figure 5.2: (a) View of the experimental setup that allows to image from the top and the side, a 1.5% wt. agar-BM1 gel cylinder (diameter 50 mm, thickness 4 mm) that is left to dry on a semi-infinite smooth plastic (PS) surface. Images at time $t = 0$ (b), $t = 12$ hours (c), $t = 30$ hours (d) and $t = 42$ hours (e). Observations are performed at $T = (25.0 \pm 0.5)^\circ\text{C}$. The black dots on (b)–(e) are seed particles (diameter $200\ \mu\text{m}$ – $350\ \mu\text{m}$) located on the upper free surface of the gel to determine the local displacement field. The mirror line on top views highlights the nearly symmetric shape of the gel during drying, and the dotted line on side views shows the horizontal solid/gel interface.

an important role in the drying of complex fluid droplets. As a compelling example, the “coffee stain” effect is a well-known phenomenon that occurs when fine coffee granules initially dispersed in water aggregate along the periphery of a drying drop and form a circular ring (Deegan et al., 1997; Kajjya, Kaneko, & Doi, 2008). Edge effects lead to the divergence of the flux of the water vapor near the contact line, and convection currents in the fluid, induced by water evaporation from the hemispherical surface of the drop, indeed result in the formation of ring stains during the drying of coffee drops. Alternative examples of edge effects can be found in other domains of physics. For instance, the increased dehydration of baked potato wedges near their extremities is responsible for the darker color of the edges, and their crunchy taste (Bocquet, 2007).

Edge effects are also involved in the drying of agar gels. As a first example, Figure 5.1 shows the drying dynamics of a square piece of agar gel placed on a smooth plastic surface, after being extracted with a cutter from the peripheral region of a cylindrical agar gel cast in a Petri dish. The experiment is repeated with three gels of different agar concentrations $C = 0.5\%$, 1.5% and 3% wt.. In the three experiments, we observe that the thinning of the flat region of the gel is slow compared to the collapse of the gel meniscus, which always occurs in about 1 hour, most likely due to edge effects. As a second example, we monitor the drying of agar gel cylinders of thickness 4 mm and diameter 50 mm placed on a solid surface [Fig. 5.2(a)]. Drying results in both the vertical thinning and radial shrinking of the gel without any apparent formation of surface patterns or cracks¹ as shown in Figure 5.2(c)–(e). The motion analysis of passive seed particles located on the upper free surface of the agar gel confirms the presence of edge effects, as the thinning rate of the gel peripheral region is much faster than that of the center part of the gel cylinder (see Appendix 5.5).

In practice, the drying of commercial gels cast in Petri dishes is more complex since the boundary conditions and especially the gel adhesion on the sidewall of a circular dish may influence the gel drying dynamics. The present chapter concerns the drying dynamics of agar gel cast in circular dishes and left to dry at constant temperature. In Section 5.2, we apply an innovative spatio-temporal method to monitor the 2D deformation field of the upper free surface of an agar gel cast in a dish and left to dry at 25.0°C . We examine the role of the boundary conditions (smooth vs rough) for cylindrical dishes made of glass or plastic, and discuss the gel sliding and/or gel fracture at the wall. Section 5.3 is dedicated

¹Only a delamination of the gel turned into a nearly transparent film may occur at long time, when drying is nearly complete.

to measuring the gel thinning rate using a method based on reflection interferometry. We also examine the influence of the dish geometry and the boundary conditions on the gel vertical thinning rate. We unravel the key role of the height of the side wall of the dish relative to the gel thickness and provide a robust observable representative of the gel drying dynamics. The interferometric method will be further used in Chapter 6 to study the influence of additives (salts, polymers, surfactants, etc.) upon the gel thinning rate and the drying scenario.

5.2 Gel drying dynamics studied by tracking experiments

The spatio-temporal method used to determine the 2D velocity field of the gel free surface during the drying process was already presented in Section 2.5.2, Chapter 2. In brief, a camera is used to record the motion of seed particles located on the upper free surface of the agar gel, and an image sequence is processed with an optical flow method. This particle tracking allows us to investigate the influence of the Petri dish properties (nature of the dish material and surface roughness) and the influence of agar concentration on the 2D deformation field of the gel free surface during drying. On the basis of experimental observations, a strong correlation is established between a short term sliding of the gel on the bottom wall of dish and the subsequent long term detachment or fracture of the gel during the drying process. An interpretation is further proposed for a possible occurrence of gel detachment (or fracture) based on the gel adhesiveness on the solid walls and the surface roughness of the dish.

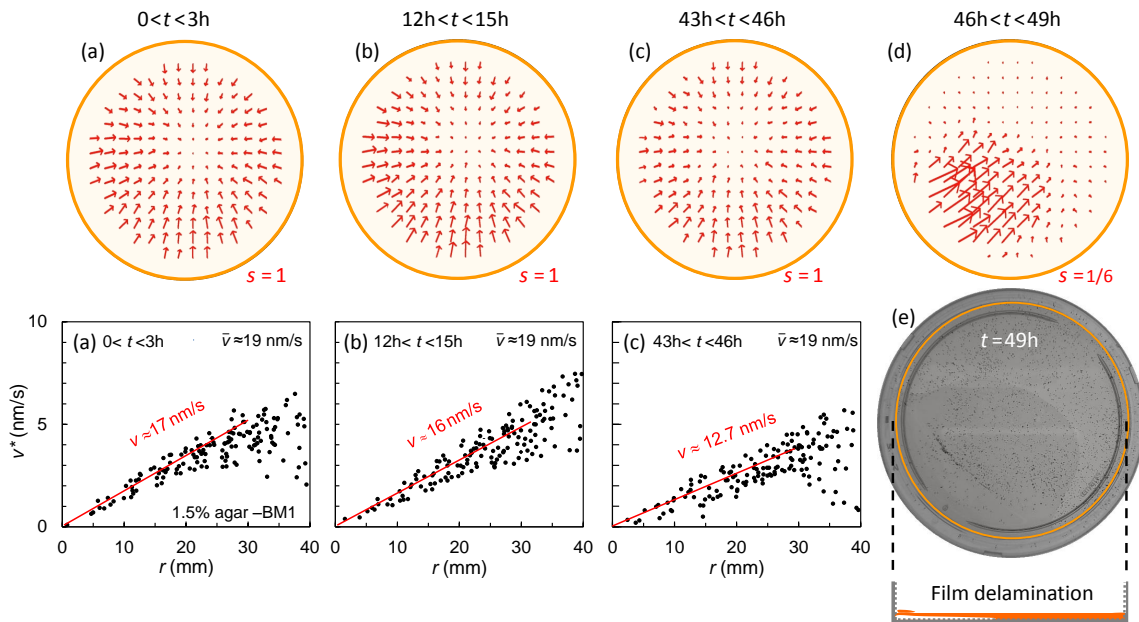


Figure 5.3: (a)–(e) Apparent 2D velocity field $\bar{v}^*(r, t)$ computed from the motion of seed particles located on the upper free surface of a 1.5% wt. agar-BM1 gel of thickness $e = 4$ mm cast in a smooth plastic (PS) dish. The delamination of the almost dried gel in a smooth plastic dish is observed at $t \approx 45$ h in (d) and (e). Plots below (a)–(c) show the radial dependence of the apparent averaged velocity $v^*(r)$ and the red lines correspond to the best linear fit of the data for $0 < r < 30$ mm. The average vertical thinning rate v is derived from the following equation $v^* = vr \tan(\alpha)/R$ with $\tan(\alpha) = H^*/H = 0.425$ and $R = 45$ mm. Temporal sampling frequency $f_t = 1$ pixel per minute and spatial sampling frequency $f_s = 1.33 \times 10^{-2}$ pixel/ μm . The variable $s = 1$ indicates the default scale of the velocity vectors. Experiments performed at a temperature $T = (25.0 \pm 0.5)^\circ\text{C}$.

5.2.1 Drying of agar gel plates cast in a dish

Let us first consider a 1.5% wt. agar-BM1 gel (thickness $e = 4$ mm) cast in a smooth plastic dish made of PS [RMS surface roughness $R_q = (12.0 \pm 3.6)$ nm] and left to dry at a constant temperature $T = (25.0 \pm 0.5)^\circ\text{C}$ over a duration of 49 hours. The spatio-temporal analysis of the motion of seed particles located on the upper free surface of the gel shows an apparent centripetal 2D velocity field $\vec{v}^*(r, t)$ and a purely vertical gel thinning over the whole drying process [Fig. 5.3(a)–(c)]. It is only once the drying process reaches an end after two days, that a gel delamination is observed at the edge of the dish [Fig. 5.3(d) and (e) for $46 \text{ h} < t < 49 \text{ h}$] which is likely due to large in plane residual stresses (Vella, Bico, Boudaoud, Roman, & Reis, 2009). During the first 12 h, the average vertical thinning rate v derived from the radial velocity $v^*(r)$ takes a somewhat constant value $v \approx 17$ nm/s, before decreasing after 24 hours. Moreover, independent mass-loss measurements performed on the same gel with a precision scale over 24 hours gives a global average thinning rate $\bar{v} \approx 19$ nm/s, in good agreement with the average vertical thinning rate v derived from the spatio-temporal analysis of the particles motion. The purely vertical thinning of the gel suggests that there is no sliding of the gel on the bottom wall of the smooth plastic dish.

To confirm that result, dense metallic spheres (diameter $500 \mu\text{m}$) were added to a hot 0.5% wt. agar-BM1 solution, which is then cast in the same dish as described above. Being denser than the agar sol, the metallic spheres settle on the bottom wall of the dish prior to the gelation [Fig. 5.4(a)]. As a result, the spheres are close to the focus plane and the apparent velocity v^* measured experimentally coincides with the real velocity v of particles. The spatio-temporal analysis of a 3 hour recording during the drying of the 0.5% wt. agar-BM1 gel shows again a centripetal 2D velocity field [Fig. 5.3(b) and (c)]. Furthermore, the

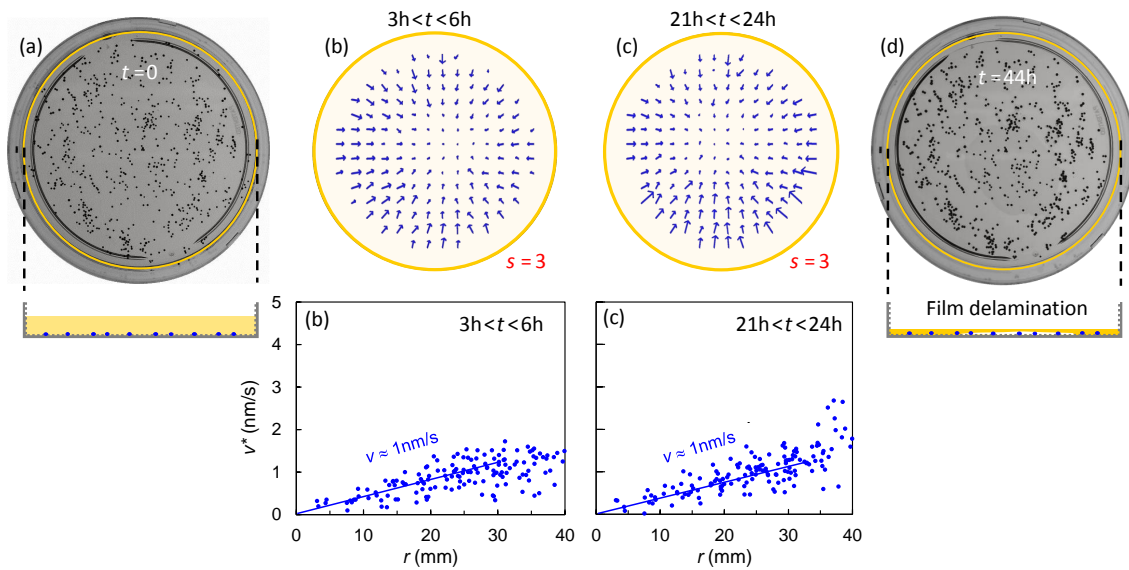


Figure 5.4: (a) Metallic spheres (diameter $500 \mu\text{m}$) embedded in a 0.5% wt. agar-BM1 gel cast in a smooth plastic (PS) dish (thickness $e = 4$ mm). The spheres are located randomly on the bottom wall of the dish. (b)–(c) Apparent 2D velocity field $\vec{v}^*(r, t)$ and radial dependence of the average apparent velocity $v^*(r)$ of the metallic spheres during the gel drying. The blue lines are the best linear fits of data for $0 < r < 30$ mm. Temporal sampling frequency $f_t = 1$ pixel per minute and spatial sampling frequency $f_s = 1.33 \times 10^{-2}$ pixel/ μm . The variable s indicates the scale of the velocity vectors. (d) The delamination of the almost dried gel from the edge of the dish is observed for $t \approx 42$ h. Experiments performed at a temperature $T = (25.0 \pm 0.5)^\circ\text{C}$.

average velocity of the metallic particles is less than 1 nm/s, which indicates a radial elastic deformation of the soft agar gel and the absence of any macroscopic sliding of the gel on the bottom wall of the dish. Indeed, the corresponding shear strain $\gamma \approx vt/e$ of about 4% wt. after 48 hours of drying (with $v \approx 1$ nm/s and $e \approx 4$ mm) remains smaller than the critical strain $\gamma_c \approx 15\%$ necessary for the debonding of the soft 0.5% wt. agar-BM1 gel in contact with a smooth plastic surface [see Fig. 4.9(d) in Chapter 4 for independent measurements]. Finally, the delamination of the dry agar gel is observed again after 42 hours [Fig. 5.4(d)].

We now turn to the drying of a 1.5% wt. agar-BM1 gel into a smooth dish made of glass [RMS surface roughness $R_q = (0.52 \pm 0.10)$ nm]. Interestingly, the drying dynamics, which is reported in Figure 5.5, is radically different from that observed in a smooth plastic dish. The apparent 2D velocity field at the gel free surface is no longer centripetal but rather displays centrifugal features, i.e. velocity vectors pointing towards the edge of the dish [Fig. 5.5(a)]. Furthermore, the particles velocity field exhibits a radial asymmetry and clearly shows convective motions after a few hours drying [Fig. 5.5(b)] well before the gel detaches from the lateral wall of the dish, which occurs suddenly at $t_d \approx 12.5$ hours [Fig. 5.5(c) and (d)]. We interpret the centrifugal velocity field as the early signature of the long term detachment of the agar gel from the lateral wall of dish. Moreover, considering a constant vertical thinning rate $v(z)$ of the gel, one could extract the horizontal 2D velocity field $\bar{w}^*(r, t) = \bar{v}^*(r, t) - \bar{v}^*(z)$ of the seed particles. However, such an analysis does not provide any additional information about the gel drying dynamics and falls outside the scope of the present work. Instead, we report in Figure 5.5(a)–(c) as red lines the apparent velocity $v^* = vr \tan(\alpha)/R$ that is expected for a purely vertical motion of the gel free surface and a thinning rate $v \approx 20$ nm/s. The latter value has been determined over 12 hours in the same experimental conditions by independent mass-loss measurements

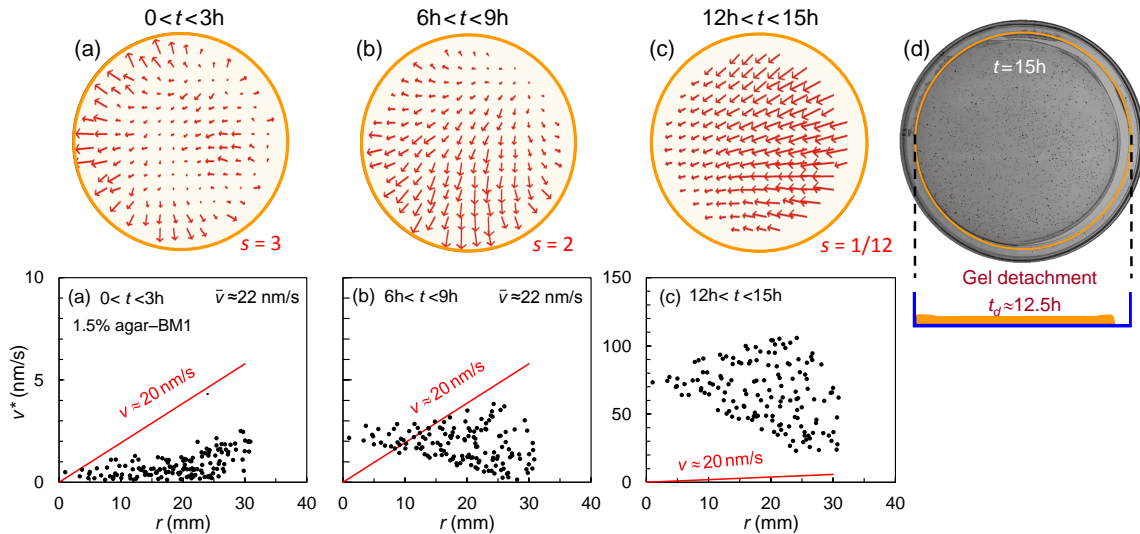


Figure 5.5: (a)–(c) Apparent velocity field $\bar{v}^*(r, t)$ and radial dependence of the average apparent velocity $v^*(r)$ of seed particles located at the free surface of a drying 1.5% wt. agar-BM1 gel of thickness $e = 4$ mm, cast in a smooth glass dish. The red lines show the expected apparent velocity $v^*(r)$ for a purely vertical motion of the gel free surface with a vertical thinning rate $v = 20$ nm/s and obey the equation $v^* = vr \tan(\alpha)/R$, with $\tan(\alpha) = H^*/H = 0.425$ and $R = 35$ mm. Temporal sampling frequency $f_t = 1$ pixel per minute and spatial sampling frequency $f_s = 1.33 \times 10^{-2}$ pixel/ μm . The variable s indicates the scale of the velocity vectors. (d) The detachment of the gel from the lateral wall of the smooth glass dish is observed at $t_d \approx 12.5$ h. Experiments performed at a temperature $T = (25.0 \pm 0.5)^\circ\text{C}$.

with a precision scale. The mismatch between the red lines in Figure 5.5(a)–(c) and the experimental data $v^*(r)$ confirms a significant horizontal displacement of the seed particles.

To determine whether the centrifugal velocity field of the particles located at the gel free surface is related to the sliding of the gel on the bottom wall of the glass dish, some metallic spheres were added in a hot 0.5% wt. agar-BM1 solution before being cast in a glass dish. We monitor simultaneously the motion of both the metallic spheres embedded in the gel and located on the bottom wall of the dish, and that of seed particles located on the upper free surface of the gel left to dry (Fig. 5.6). Once more, the apparent 2D velocity field of the particles at the gel free surface displays somewhat centrifugal features during the first hours of drying, followed by convective motions after a few hours, before the gel finally detaches at $t_d \approx 17.5$ h–19 h, as determined by two independent tracking experiments. Moreover, the analysis of individual particle trajectories gives almost identical velocity vectors for couples of particles consisting of one metallic sphere and a nearby seed particle on the gel free surface² [Fig. 5.6(b) and (d)]. As a consequence, the drying of agar gels in a smooth dish made of glass involves an early sliding of gel on the bottom wall of the dish and a subsequent long term gel debonding from the lateral wall. Therefore, the non-centripetal velocity field early observed in the first hours can then be considered as a robust observable to predict the later gel detachment.

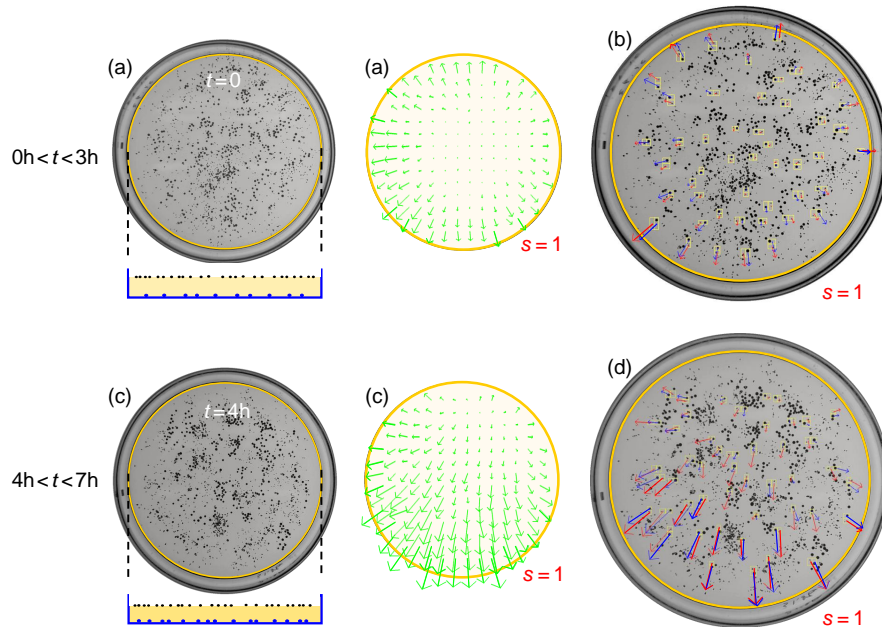


Figure 5.6: (a)–(c) Tracking of both metallic spheres (diameter $500 \mu\text{m}$) embedded inside the gel and located randomly on the bottom wall of the dish, and seed particles (diameter $200 \mu\text{m}$ – $350 \mu\text{m}$) located on the upper free surface of a 0.5% wt. agar-BM1 gel plate cast in a smooth glass dish. The apparent 2D velocity field $\vec{v}^*(r, t)$ of both metallic and seed particles is pictured as green vectors for two independent tracking experiments, one pictured for $0 < t < 3$ h (a) and the other one for $4 \text{ h} < t < 7$ h (c). (b) and (d) Apparent velocity vectors $\vec{v}^*(r, t)$ for about 100 couples of particles consisting of a single metallic sphere (red vectors) located on the bottom wall and a nearby single seed particle (blue vectors) located on the gel free surface. The gel detachment from the sidewall of the dish respectively occurs at $t_d \approx 17.5$ h and $t_d \approx 19$ h for the two independent tracking experiments. Temporal sampling frequency $f_t = 1$ pixel/min and spatial sampling frequency $f_s = 1.33 \times 10^{-2}$ pixel/ μm . The variable $s = 1$ indicates the default scale of the velocity vectors. Experiments performed at a temperature $T = (25.0 \pm 0.5)^\circ\text{C}$.

²The careful analysis of the individual motion of couples of single metallic sphere and nearby seed particle was performed over more than 100 couples of particles. Such a meticulous task required a few days work just for making the images (b) and (d) in Figure 5.6!

5.2.2 Influence of agar concentration

In this section, one considers the influence of agar concentration upon the drying dynamics of agar gels cast in a smooth dish made of plastic or glass. Apparent 2D velocity fields $\vec{v}^*(r, t)$ for particles at the free surface of gels of different concentrations and cast in **smooth plastic dishes** are reported in Figure 5.7. All the velocity fields show centripetal features during the entire drying experiments [Fig. 5.7(a)–(c)], without any long term detachment of the agar gel from the sidewall of the dish [Fig. 5.7(d)–(f)]. The adhesive contact between the gel and the walls of the plastic dish appears strong enough to resist the build up of internal stresses during the gel drying, preventing the gel detachment until the complete drying of the gel.

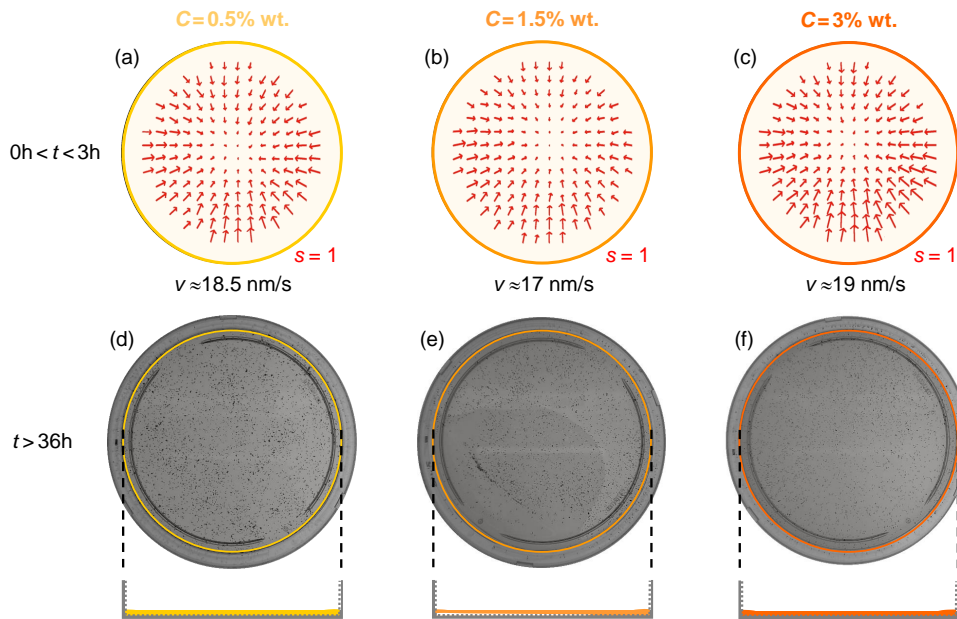


Figure 5.7: Apparent 2D velocity field $\vec{v}^*(r, t)$ during the first three hours of the drying of a 0.5% wt. (a), 1.5% wt. (b) and 3% wt. (c) agar-BM1 gels cast in a **smooth plastic (PS) dish**. (d)–(f) No detachment of the gel from the lateral wall of the dish was observed, even after 36 hours of drying. The average vertical thinning rate v of the gel that is derived from tracking experiments is indicated below the 2D apparent velocity field. Temporal sampling frequency $f_t = 1\text{ pixel/min}$ and spatial sampling frequency $f_s = 1.33 \times 10^{-2}\text{ pixel}/\mu\text{m}$. The variable s indicates the scale of the velocity vectors. Independent mass-loss measurements performed with a precision scale over 24 hours on 0.5%, 1.5%, and 3% wt. agar-BM1 gels give a global average thinning rate $\bar{v} \approx 19, 19, \text{ and } 21\text{ nm/s}$, respectively. Experiments performed at a temperature $T = (25.0 \pm 0.5)^\circ\text{C}$.

As for the case of agar gels cast in **smooth glass dishes**, the weak adhesion of the gel on a smooth glass surface results in an early sliding of the gel on the bottom wall of the dish, which is detectable during the first hour of the drying experiment [Fig. 5.8(a)–(c)] and leads to a subsequent detachment of the gel from the lateral wall of the dish. The phenomenon is robust for all the agar concentrations explored, and the detachment times t_d decreases for increasing concentrations in agar ($t_d \approx 14\text{ h}, 12\text{ h}$ and 8 h for agar concentrations $C = 0.5\% \text{ wt.}, 1.5\% \text{ wt.}$ and $3\% \text{ wt.}$, respectively). Such a result can be interpreted by the fact that a lower gel deformability promotes a faster build up of the internal stresses during gel drying, which favors an earlier detachment of the gel. These findings clearly show that a weak adhesion of an agar gel to the dish can cause the gel detachment from the sidewall of the dish before complete drying. Finally, we emphasize that the water evaporation rate v from an agar gel cast in a smooth dish weakly depends

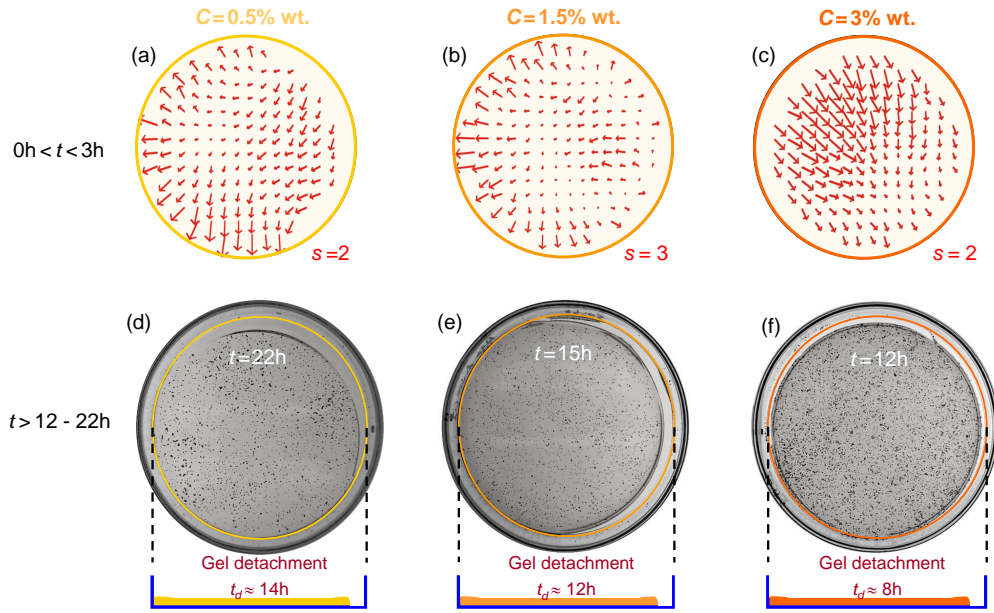


Figure 5.8: Apparent 2D velocity field $\vec{v}^*(r, t)$ during the first three hours of the drying of a 0.5% wt. (a), 1.5% wt. (b) and 3% wt. (c) agar-BM1 gels cast in a **smooth glass dish**. Gel detachment from the lateral wall of the dish is observed at $t_d \approx 14$ h, 12 h, and 8 h for gels of agar concentration 0.5%, 1.5% and 3% wt., respectively. Temporal sampling frequency $f_t = 1$ pixel/min and spatial sampling frequency $f_s = 1.33 \times 10^{-2}$ pixel/ μm . The variable s indicates the scale of the velocity vectors. Independent mass-loss measurements performed with a precision scale over 24 hours on 0.5%, 1.5%, and 3% wt. agar-BM1 gels give a global average thinning rate $\bar{v} \approx 24, 22, 19.5$ nm/s, respectively. Experiments performed at a temperature $T = (25.0 \pm 0.5)^\circ\text{C}$.

upon the agar concentration in the range of 0.5% wt. to 3% wt., which is in good agreement with the interferometric observations that will be discussed in the next chapter (see Fig. 6.3 in Chapter 6).

At this point, one could be tempted to conclude that a smooth dish made of plastic is sufficient to prevent any long term detachment of the gel from the sidewall of the dish. Unfortunately, this is not true as evidenced in Figure 5.9 for a commercial gel cast in a smooth plastic dish. As will be shown in Chapter 6, Section 6.4, the presence of additives in the gel and especially surfactant molecules may considerably lower the adhesion between the gel and the plate, even for a smooth plastic surface and thus promote both the sliding of the gel on the bottom wall of the dish and the detachment of the gel from the sidewall



Figure 5.9: View of a commercial Petri dish (hot agar solution loaded with different additives and cast in a smooth plastic dish) after gel detachment from the lateral wall of dish at $t_d \approx 5.4$ h.

of the dish after a relatively short drying period ($t_d \approx 5.4$ h for a 43811-BM commercial gel plate).

5.2.3 Influence of solid surface properties

In Chapter 4, Section 4.3.5, we have seen that the adhesion between an agar gel and a solid surface is considerably strengthened for increasing values of the surface roughness. Therefore, increasing the surface roughness of the walls of the Petri dish could prevent a priori the sliding of the gel on the bottom wall, and the long term detachment of the agar gel from the sidewall of the dish. To check such an assumption, we have monitored the drying dynamics of a 1.5% wt. agar-BM1 gel cast in a rough glass dish of RMS surface roughness $R_q = (5.9 \pm 2.4) \mu\text{m}$ [Fig. 5.10 (left)]. Contrary to what was expected, the apparent 2D velocity field $\vec{v}^*(r, t)$ of the seed particles located at the free surface of the gel exhibits non-centripetal features and some radial asymmetry even during the first hours of drying, which is representative of either the sliding of the gel on the dish bottom surface or some pronounced deformation of the gel [Fig. 5.11(a)]. Moreover, we observe the propagation of an internal crack and the formation of a circular fracture along the edge of the dish after a relatively short drying period $t_f \approx 8$ h [Fig. 5.11(d)].

Complementary tracking experiments performed during the drying of 0.5% wt. and 3% wt. agar-BM1 gels cast in rough glass dishes show a similar phenomenology. The apparent 2D velocity field of particles located on the free surface of the gel displays non-centripetal features and we see the formation of a circular fracture along the edge of the gel plate systematically after a drying period that depends on the gel agar concentration: 33 hours (0.5% wt. agar-BM1), 8 hours (1.5% wt. agar-BM1) and 5 hours (3% wt. agar-BM1). A softer gel of 0.5% wt. agar-BM1 exhibits a higher mechanical resistance to crack propagation since the critical shear strain for gel damage is much higher than that of a more concentrated and less deformable gel of 3% wt. agar-BM1. Note that the drying of a 3% wt. agar-BM1 gel cast in a rough plastic dish [with a somewhat lower RMS surface roughness $R_q = (1.54 \pm 0.43) \mu\text{m}$] leads to identical features with the formation of a circular fracture along the edge of the dish after about 5 hours.

We now examine the case of a drying experiment performed in a dish that is only partially sandblasted. We have prepared two glass dishes for which either the bottom wall only [Fig. 5.10 (center)] or the sidewall only [Fig. 5.10 (right)] have been sandblasted. In the case of a smooth sidewall and a rough bottom, the radial symmetry of the apparent 2D velocity field $\vec{v}^*(r, t)$ associated with the motion of the gel free surface is preserved at least in the first hours of drying [Fig. 5.11(b)] and the gel fracture takes place much

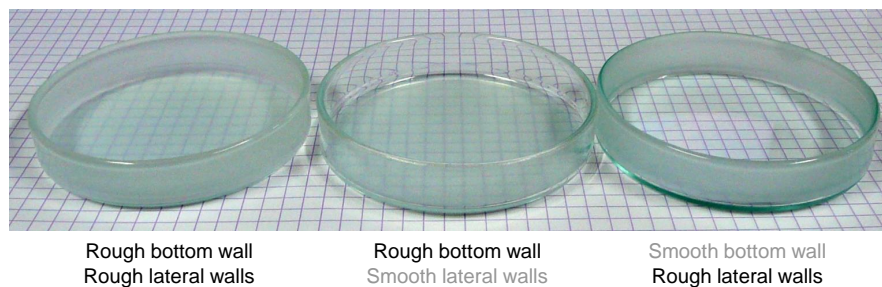


Figure 5.10: Pictures of three glass dishes: (left) rough glass dish which has been sandblasted [RMS surface roughness $\bar{R}_q = (5.9 \pm 2.4) \mu\text{m}$]; (center) glass dish which shows a smooth sidewall [$\bar{R}_q = (0.52 \pm 0.09) \text{nm}$] and a sandblasted bottom wall; (right) glass dish with a smooth bottom wall and a sandblasted sidewall.

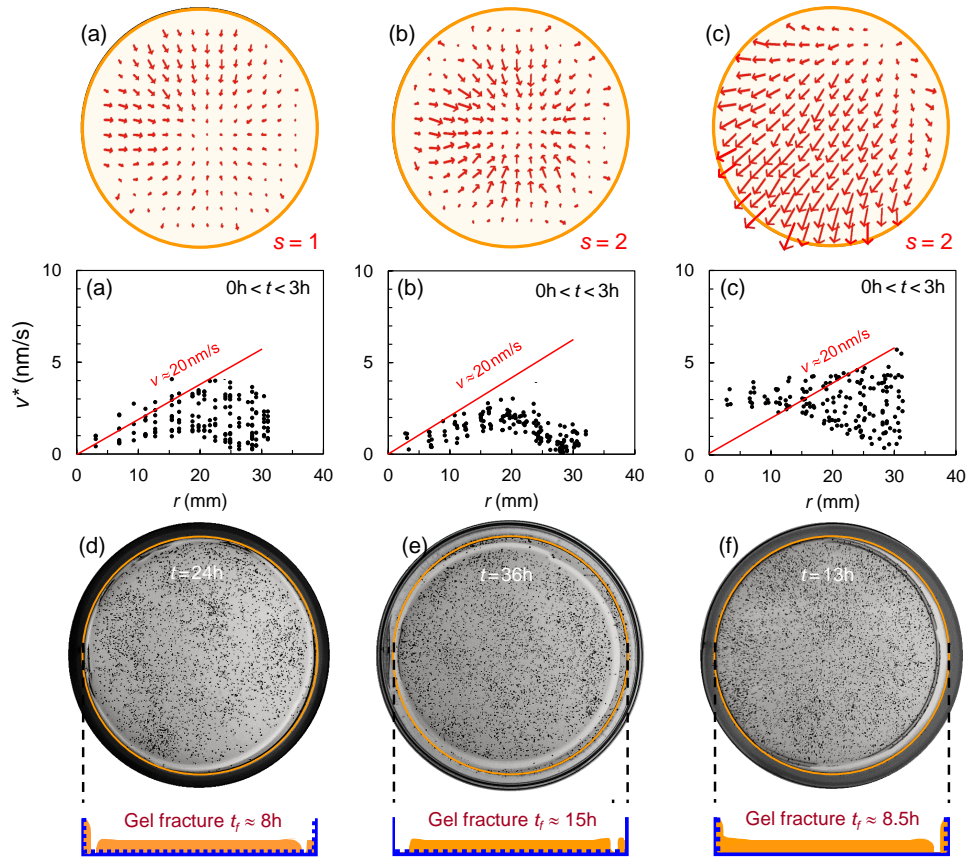


Figure 5.11: Apparent 2D velocity field $\vec{v}^*(r, t)$ and radial dependence of the apparent velocity $v^*(r)$ during the first three hours of the drying of 1.5% wt. agar-BM1 gels cast in (a) a glass dish with rough bottom wall and rough sidewall, (b) a rough bottom wall and smooth sidewall, (c) a smooth bottom wall and a rough sidewall at $T = (25.0 \pm 0.5)^\circ\text{C}$. The red lines in (a)–(c) show the expected apparent velocity $v^*(r)$ for a purely vertical motion of the gel free surface with a vertical thinning rate $v = 20$ nm/s that obeys the equation $v^* = vr \tan(\alpha)/R$ with $\tan(\alpha) = H^*/H = 0.425$ and $R = 35$ mm. The formation of a circular fracture along the edge of the gel plate is observed at $t_f = 8$ h (a), $t_f = 15$ h (b), and $t_f = 8.5$ h (c). Temporal sampling frequency $f_t = 1$ pixel/min and spatial sampling frequency $f_s = 1.33 \times 10^{-2}$ pixel/ μm . The variable s indicates the scale of the velocity vectors. Independent mass-loss measurements performed with a precision scale over 24 hours gives a global average thinning rate $\bar{v} \approx 20, 19.5$ and 19.5 nm/s for the agar-BM1 gel represented in (a), (b) and (c) respectively.

later at 15h instead of 8h for the fully sandblasted dish³ [Fig. 5.11(e)]. Finally, the drying dynamics of a 1.5% wt. agar-BM1 gel plate cast in the dish with a sandblasted sidewall and a smooth bottom [Fig. 5.11(c)] shows a more pronounced horizontal motion of the seed particle located at the free surface of the gel. Such a non centripetal 2D velocity field results from gel deformation since a gel fracture occurs at the same time along the edge of the dish [Fig. 5.11(f)] as in the case of a fully sandblasted dish [Fig. 5.11(d)].

From all these experiments we can conclude that the walls of the dish play a crucial role in the gel drying and the growth of fracture. In a glass dish with smooth walls of nanometric surface roughness, the weak adhesion of the agar gel to the dish promotes the sliding of the gel both on the bottom wall and along the sidewall, resulting in the delayed detachment of the gel from the dish before the drying of the gel is complete. The edge of the fully dried gel then systematically appears as smooth and uniform, which is

³Note that only a retraction of the gel plate without any gel fracture is observed when both the lateral wall and a 1 mm width region of the circular edge corner of the dish are preserved from sand blasting.

representative of a homogeneous slip of the gel along the vertical lateral wall of the dish [Fig. 5.12(a)]. For a plastic dish that shows intermediate surface roughness ($R_q \approx 10$ nm), the gel adhesion to the wall is more important, which may prevent both the sliding of the gel on the bottom wall and the gel detachment from the sidewall during the whole drying process. However, the presence of additives such as surfactants (e.g. in commercial gels), may lower the adhesion between the gel and the smooth plastic dish and promote a long term gel detachment. Moreover, the roughness of the sidewall may cause a non-uniform slipping of the gel [Fig. 5.12(b)]. In the case of a plastic dish with intermediate level of surface roughness ($R_q \approx 10$ nm), both the wall asperities and the presence of the edge corner at the bottom of the dish result in a stick-slip motion of the gel close to the sidewall as evidenced by the presence of parallel stripes visible on the fully dried film [Fig. 5.12(b)]. Finally, a strong adhesive contact between the agar gel and the walls of a sandblasted dish ($R_q \approx 1$ μm) prevents the sliding of the gel on the bottom wall. However, the high surface roughness inhibits at the same time any vertical slipping of the gel along the sidewall, which inevitably leads to large in-plane shear deformations and a long-term fracture since the internal stresses in the gel near the dish edge corner cannot be relaxed [Fig. 5.12(c)]. Note that in general, the slip of the gel at the sidewall allows for the relaxation of internal stresses in the gel near the edge of the dish, delaying and/or preventing the fracture of the gel.

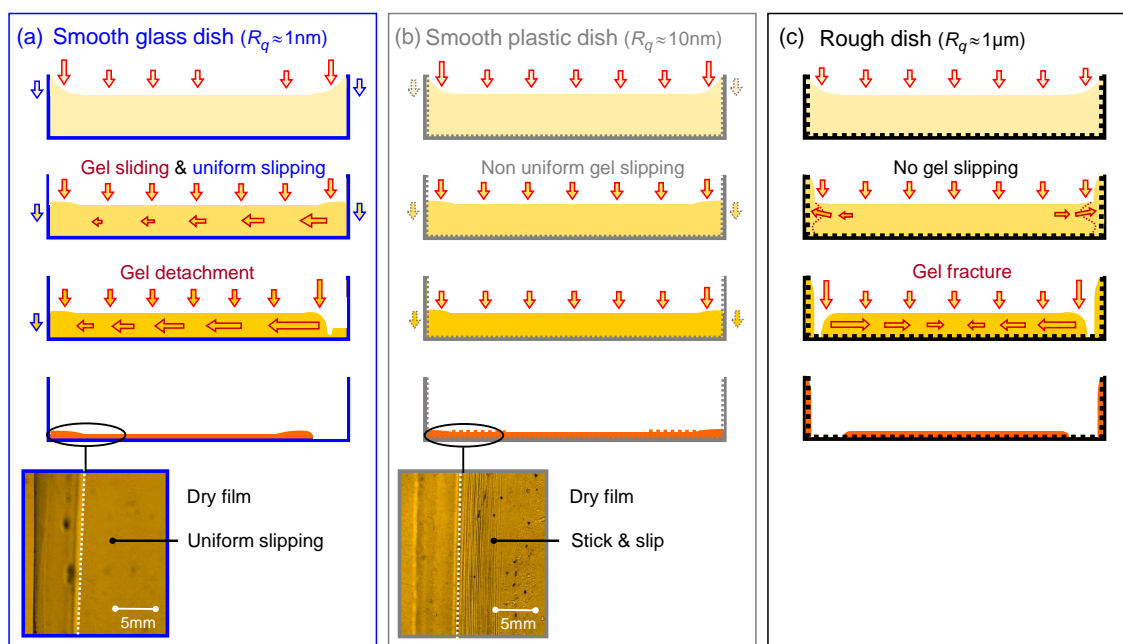


Figure 5.12: Schematic representations of the drying dynamics of an agar gel cast in (a) a smooth glass dish (RMS surface roughness $R_q \approx 1$ nm), (b) a smooth plastic dish (RMS surface roughness $R_q \approx 10$ nm) and (c) a rough dish (RMS surface roughness $R_q \approx 1$ μm). A smooth glass dish allows the sliding of the gel on the bottom wall and a uniform slip of the gel along the sidewall that results in a long-term detachment of the agar gel from the sidewall, which later turns into a uniform dry agar film (a). An increase in the wall roughness (10 nm for a smooth plastic dish or 1 μm for a sandblasted dish) strengthens the gel adhesion to the wall and may prevent the long term detachment of the gel from the sidewall (b) and (c). An intermediate surface roughness of the walls may further cause a stick-slip motion of the agar gel in the vicinity of the sidewall, leading to the formation of parallel stripes clearly visible on the dry agar film (b). Finally, a larger adhesion of the gel on sandblasted surfaces of micrometric roughness inhibits any wall slip along the sidewall and inevitably leads to the formation of a circular inner crack that propagates along the edge of the dish (c).

5.3 Gel local thinning-rate measured by interferometry

Agar plates used as growth culture media are very sensitive to water loss, which may lead to the gel detachment from the sidewall of the dish, or the fracture of the gel as reported in the previous section. Here we aim at measuring with a high accuracy the local thinning-rate of agar gel in the early stage of the drying process, well before the gel detaches or fractures. We use *in-situ* interferometric observations to measure the vertical thinning-rate of agar gels cast in circular dishes and left to dry at constant temperature $T = (25.0 \pm 0.5)^\circ\text{C}$, or $T = (20 \pm 1)^\circ\text{C}$.

The thinning-rate of an agar gel is determined by monitoring the dynamics of an interference pattern that is analyzed with a homemade spatio-temporal method already described in Section 2.5.1 in Chapter 2. In what follows, the first subsection concerns the influence of the dish compliance and the wall surface roughness on the drying dynamics. We seek the optimal conditions to monitor the vertical thinning rate of agar gels without any artifacts, and show that a small dish with smooth walls meets this criterion. The second subsection deals with the spatially-resolved drying scenario of a thin agar gel (initial thickness $e_0 = 1$ mm) cast in a smooth glass dish. This section will lead us to focus on the thinning rate of the gel at the center of the dish, whose dependence to the dish geometry will be finally examined in the last subsection.

5.3.1 Influence of dish material and wall roughness

We first discuss the compliance of the Petri dish on the dynamics of the interference pattern. For this purpose, we have performed a series of experiments on empty dishes placed in the arm of the interferometer in the absence of any gel. The temporal dynamics of the interference fringes is shown in Figure 5.13 for semi-flexible plastic dishes made of polystyrene (PS) and of diameter 90 mm and 50 mm, and a rigid glass dish of diameter 50 mm. Thermally-induced deformations of the large plastic dish of diameter 90 mm give rise to large amplitude fluctuations of the interference pattern [Fig. 5.13(a)], whereas the fluctuations of the interference pattern are of much smaller amplitude for a less deformable 50 mm diameter dish made of plastic [Fig. 5.13(b)] and a rigid 50 mm diameter glass dish [Fig. 5.13(c)]. Therefore, plastic or glass dishes of diameter 50 mm will be now considered to minimize the contribution of the dish compliance to the fluctuations of the interference pattern.

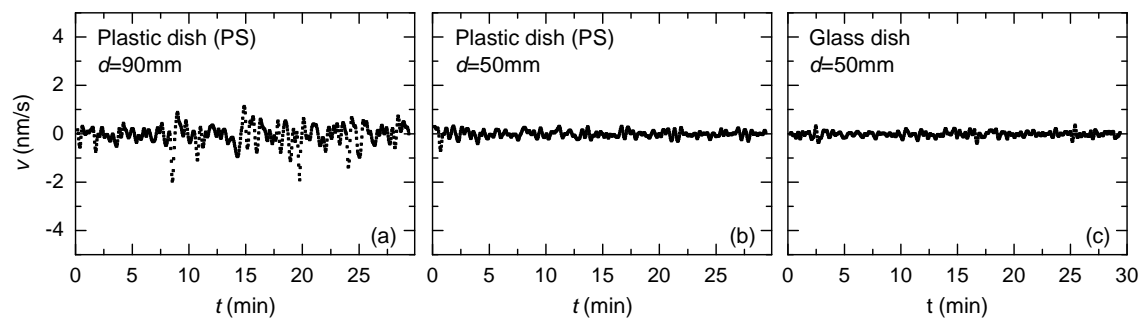


Figure 5.13: Time evolution of the scrolling velocities of the interference fringes for an empty and smooth plastic dish (PS) of diameter 90 mm (a) and 50 mm (b), and an empty smooth glass dish of diameter 50 mm (c) placed in the arm of the interferometer. Measurements are performed at the center of the dish. The root mean square value of the velocity fluctuations in (a), (b) and (c) is respectively $\delta v = 0.5$ nm/s, 0.15 nm/s and 0.1 nm/s, respectively.

We now turn to the impact of the surface roughness of the dish on the drying dynamics of the gel. For this purpose, we consider a 1.5% wt. agar-BM1 gels cast either in a smooth plastic dish [RMS surface roughness $R_q = (11.8 \pm 3.6)$ nm] or in a rough plastic dish with sandblasted walls [RMS roughness $R_q = (1.54 \pm 0.43)$ μm]. As shown in Figure 5.14(a) and (c), the average thinning rate v of the agar gel remains constant over a drying period of 3 hours, and is identical within error bars for both smooth and rough plastic dishes [$\langle v_{smooth} \rangle = (14.8 \pm 2.1)$ nm/s and $\langle v_{rough} \rangle = (14.3 \pm 4.4)$ nm/s]. Nonetheless, the thinning rate of an agar gel cast in a rough plastic (PS) dish shows much larger temporal fluctuations than that of a gel cast in a smooth plastic dish [Fig. 5.14(d) to be compared with Fig. 5.14(b)]. The latter result can be associated with the complex dynamics of the contact line between the gel and the rough sidewall of the sandblasted plastic dish. Indeed, the contact line may be trapped and released suddenly during the drying of the gel, which generates a stick-slip like motion of the gel as discussed in Section 5.2.3, impacting the dynamics of the interference fringes. In the next sections, one only considers smooth dishes made of plastic or glass with a small enough diameter (50 mm) to minimize the short-time fluctuations of the interference pattern during the drying of the agar gel.

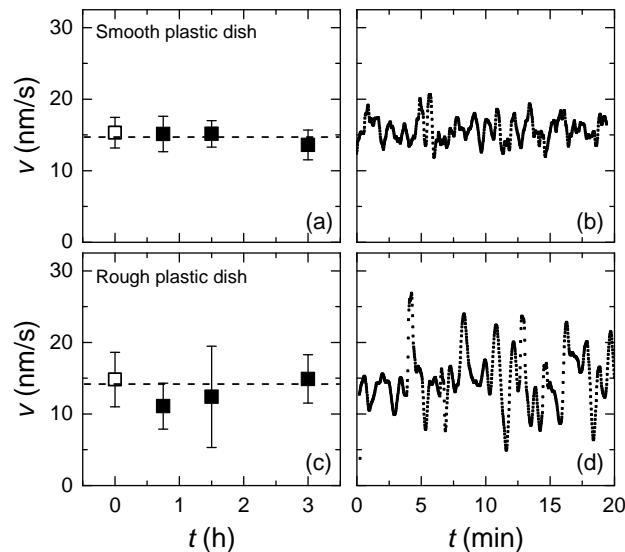


Figure 5.14: Average thinning rate v of 1.5% wt. agar-BM1 gels cast in (a) a smooth plastic dish and (c) in a rough plastic dish, and determined at different times during a drying experiment of duration 3 hours. Each point corresponds to an average over 20 min. Error bars stand for the standard deviation of the average thinning rate computed over 20 min. Horizontal dashed lines in (a) and (c) highlight the average data value. (b) [resp. (d)] shows the time-resolved evolution of the gel thinning rate $v(t)$ for the data associated with the first point pictured as \square in (a) [resp. (c)]. Experiments conducted at $T = (25.0 \pm 0.5)^\circ\text{C}$ in dishes of diameter 50 mm.

5.3.2 Drying of a thin agar gel cast in a glass dish

We now examine the spatially-resolved drying scenario of a 1.5% wt. agar-BM1 gel of thickness 1 mm cast in a smooth glass dish (diameter 50 mm, vertical wall of height $H = 12$ mm). The drying process is monitored by *in-situ* interferometry at different locations on the gel free surface and by independent mass-loss global measurements at a temperature of $T = (21.0 \pm 0.5)^\circ\text{C}$.

The thinning-rate averaged periodically over a duration of 10 min is first measured as a function of time at the center of the dish, and at three other locations r along the dish

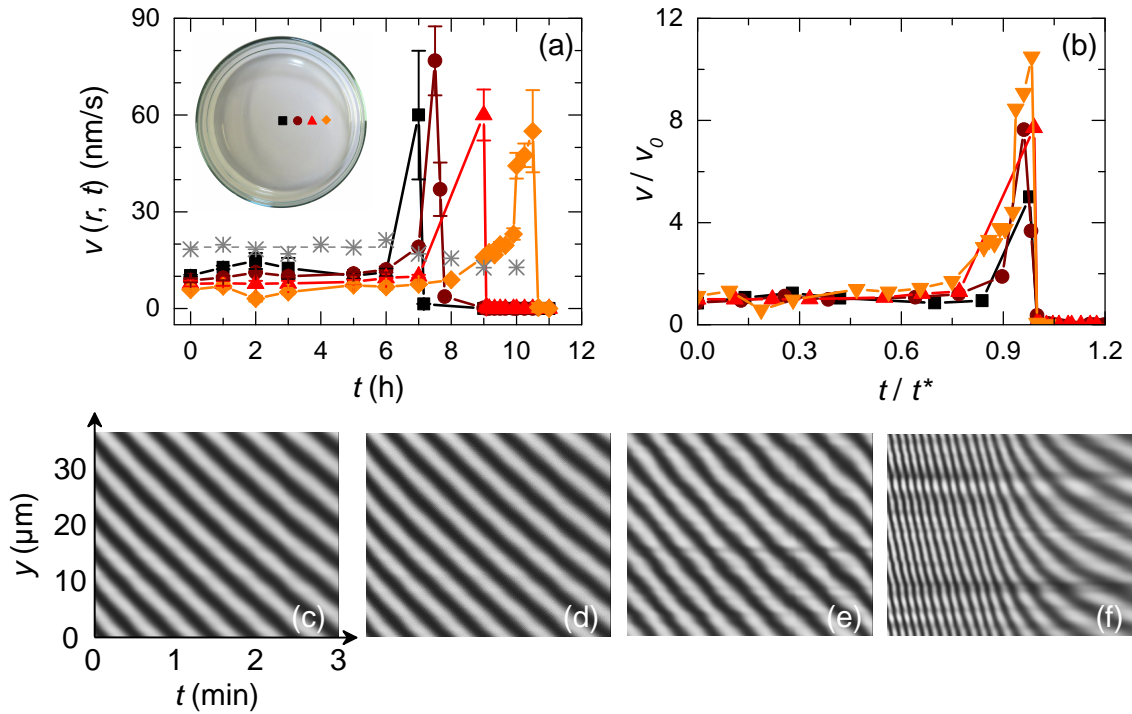


Figure 5.15: (a) Local thinning rate $v(r, t)$ vs time t for a 1.5% wt. agar-BM1 gel cast in a smooth glass dish of diameter $2R = 50$ mm ($e_0 = 1$ mm, $H = 12$ mm) at different locations r from the center of the plate with $r/R = 0$ (■), 0.2 (●), 0.4 (▲) and 0.6 (◆). The stars (*) stand for independent mass-loss measurements performed with a precision scale indicating an average global thinning rate of 19.1 ± 0.5 nm/s over the first 6 hours (horizontal dashed line). (b) Same data as in (a) where the local thinning rate for each data set has been normalized by the value averaged over the first 6 hours and the time t has been normalized by the time $t^*(r)$ associated with the largest thinning rate reached at a radial position r during the drying process. (c)–(f) Spatio-temporal diagrams of the fringe displacement recorded over a period of 10 min during the drying process at the center of the agar gel and at different times $t = 0, 3, 6$ and 7 h. The autocorrelation images of each of these patterns provides the average thinning rates $v = (10.2 \pm 0.8)$ nm/s (c), $v = (12.5 \pm 1.0)$ nm/s (d), $v = (11.3 \pm 0.9)$ nm/s (e) and $v = (58 \pm 20)$ nm/s (f). The latter are used for the data pictured as (■) in (a). Experiment conducted at $T = (21.0 \pm 0.5)^\circ\text{C}$.

radius [$r/R = 0, 0.2, 0.4$, and 0.6 in Fig. 5.15(a)]. During the first 6 hours, the gel thins at constant speed at the center of the dish. For $t \geq 6$ h, the thinning-rate increases abruptly, goes through a maximum and stops as the drying process ends. A similar scenario is observed at the 3 other locations but shifted in time, which gives evidence of a spatially heterogeneous drying process: the gel thins slightly faster at the center of the dish. Indeed, the center region of the gel becomes dry first, which is supported by direct observations (see Fig. 5.16 for pictures of the gel)⁴. Despite such an inhomogeneous drying process, the evolution of $v(r, t)$ is robust for different radial positions r along the gel radius, as confirmed by the rescaling of the data on a single mastercurve [Fig. 5.15(b)].

Interestingly, the local average thinning rates measured by interferometric observation during the first 6 hours are almost twice smaller than the global thinning rate determined by independent mass-loss measurements [(*) in Fig. 5.15(a)]. Both local and global measurements are performed in the exact same conditions, which suggests that the water loss

⁴The faster thinning of the center region of the agar gel is related to the large height $H - e_0 = 11$ mm of the sidewall with respect to the gel thickness, and the small dish diameter of 50 mm. In the case of both a smaller height $H - e_0$ (i.e. larger gel thickness) and a larger dish diameter, the effect is less pronounced and the circular edge of the gel plate usually dries in about the same time as the central region of the plate.

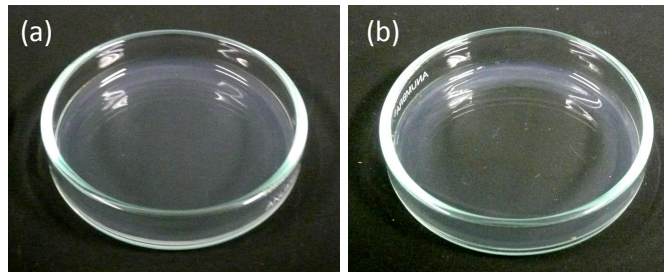


Figure 5.16: Pictures of an agar gel cast in a dish of 50 mm diameter made of glass: (a) prior to the drying experiment, and (b) 8 hours after the start of the drying experiment at $T = (21.0 \pm 0.5)^\circ\text{C}$. The complete drying occurs first at the center of the dish, suggesting a slightly larger thinning rate of the gel at the center of the dish, as quantified in Figure 5.15(a).

is more important than expected from the sole local measurements, which are limited to $r/R \leq 0.6$. Unfortunately, due to the lateral wall of the dish, one cannot approach the objective near the edge region of the sample and focus on the gel close from the wall. Direct observations of the dish from the side shows that the gel exhibits a curved meniscus of a few millimeter height in the vicinity of the wall (see Fig. 5.1 in Section 5.1). Water evaporates faster through the meniscus due to edge effects, which accounts for the apparent discrepancy between local and global measurements. Furthermore, the maximum thinning rate of about 60 nm/s reported in Figure 5.15(a) corresponds to the passage under the observation region (at a distance r from the dish center) of the triple line that marks the frontier between the dry gel, the humid gel and air. The triple line moves outwards, towards the lateral wall of the dish and water evaporation is most likely enhanced at that very location which also accounts for the discrepancy between the local and global measurements. Note that similar velocities of about 50 nm/s to 100 nm/s are also observed near the edge of a gel cylinder when drying on a semi-infinite smooth plastic surface (see Fig. B.1 and B.2 in Appendix 5.5).

In conclusion, the interferometric observations allow to monitor with a high accuracy both the gel thinning rate averaged over short periods of time (typically 10 min) at various locations on the gel free surface. The thinning rate of the gel determined at the center of the dish remains constant over the first hours of the drying process, and we now study the dependence of such a robust observable to the dish geometry.

5.3.3 Influence of dish geometry

The present subsection concerns the impact of the dish geometry on the average thinning rate v measured at the center of the dish. One first explores the effect of the height $(H - e_0)$ of the sidewall relative to the gel thickness, where e_0 is the gel thickness prior to any drying and H the height of the sidewall [see the sketch in Figure 5.17(a)]. For this purpose, the average thinning rate v of 1.5% wt. agar-BM1 gels cast in smooth plastic dishes (diameter of 50 mm and fixed height $H = 12$ mm) is measured for different initial gel thickness e_0 , ranging from 2 mm to 10 mm. Measurements performed at the center of the dish show that the gel thinning rate v decreases for increasing values of $(H - e_0)$, as reported in Figure 5.17(a). A higher lateral wall relative to the gel thickness delays water evaporation by limiting the diffusion of the water vapor standing above the gel free surface, creating a humid area that leads to lower thinning rates. Furthermore, a complementary set of experiments with 1.5% wt. agar-BM1 gels cast in plastic dishes of various heights H was performed, while keeping constant the height $(H - e_0) = 4$ mm of the sidewall relative

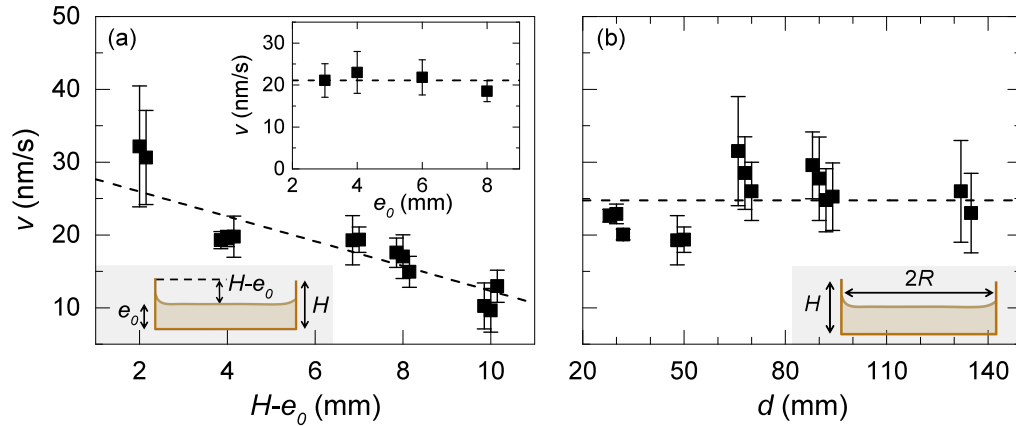


Figure 5.17: (a) Average thinning rate v of 1.5% wt. agar-BM1 gels, measured at the center of a smooth dish vs. the height $H - e_0$ of the lateral sidewall relative to the gel thickness, where H and e_0 stand respectively for the height of the sidewall of the dish and the initial thickness of the gel (see the sketch in the lower inset). The dish height is kept constant ($H = 12$ mm) and the thickness of the gel is varied from $e_0 = 2$ mm to 10 mm, such that $H - e_0$ varies from 2 mm to 10 mm. For each value of $H - e_0$, three independent experiments were performed on gels prepared anew. Each point corresponds to an average over 10 minutes and the error bars represent the standard deviation computed over the same duration. The dashed line is the best linear fit of the data: $v = (29.3 \pm 2.3) - (1.7 \pm 0.3)(H - e_0)$ in nm/s with $(H - e_0)$ in mm. All the experiments are performed at $T = (25.0 \pm 0.5)^\circ\text{C}$ in a smooth plastic dish made of PS, except for the experiments at $H - e_0 = 7$ mm in a smooth glass dish. Inset: average thinning rate v of 1.5% wt. agar-BM1 gels measured at the center of the dish vs. the gel initial thickness e_0 with $H - e_0 = 4$ mm (the initial relative height $H - e_0$ is kept constant for all the experiments). The dashed line stands for the average value: $v = (21.0 \pm 0.5)$ nm/s. (b) Average thinning rate v of 1.5% wt. agar-BM1 gels measured at the center of the dish and averaged over 10 minutes vs. the dish diameter $d = 2R$. The relative height $H - e_0 = 7$ mm of the lateral wall is kept constant for all the experiments. For each value of the dish diameter $2R$, we perform two to four independent experiments on gels prepared anew. Error bars correspond to the standard deviation of the thinning rate over 10 minutes. The horizontal dashed line stands for the average value: $\langle v \rangle = 24.7$ nm/s. Experiments conducted at $T = (25.0 \pm 0.5)^\circ\text{C}$ in smooth glass dishes.

to the gel thickness. The average thinning rate v of the gel is constant and independent of the initial thickness of the gel, from $e_0 = 3$ mm to $e_0 = 8$ mm [inset in Figure 5.17(a)], showing that for a constant value of $(H - e_0)$, the initial gel thickness e_0 has no significant influence upon water loss. The gel thinning rate at the center of the dish is thus mainly controlled by the water vapor environment located above the gel free surface through the experimental parameter $(H - e_0)$.

Measurements of the gel thinning rate in the center region of smooth glass dishes of different diameters were finally performed, every other parameters being kept constant ($H - e_0 = 7$ mm and $H = 12$ mm). Data reported in Figure 5.17(b) appear as independent of the dish diameter for $30 \leq 2R \leq 135$ mm, which confirms that the average thinning rate v measured at the center of the dish is a robust and pertinent observable to characterize the short-time drying dynamics of agar gels. In Chapter 6, the thinning rate v measured at the center of the dish will be used as a key observable to compare the drying of agarose and agar gels, and more generally investigate the influence of various additives on the drying kinetics of agar(ose) gels (see Section 6.2 in Chapter 6).

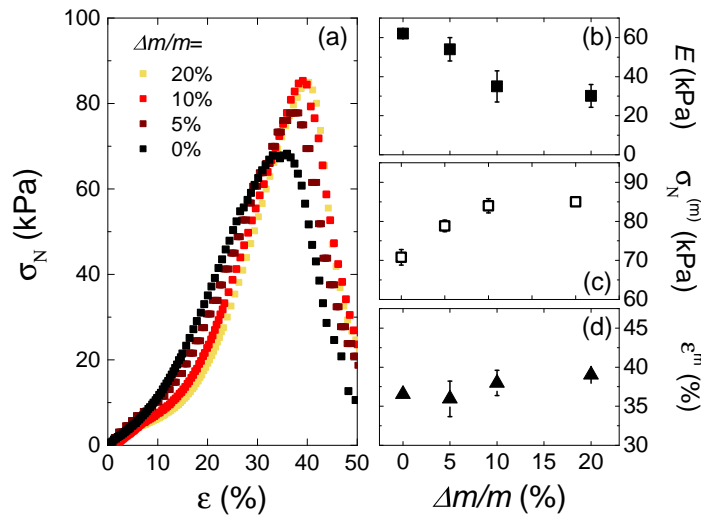


Figure 5.18: Normal stress σ_N vs. compressive strain ϵ monitored during macro-indentation experiments of agar gels cylinders. Colors from black to yellow stand for the relative water loss $\Delta m/m_0$ of 1.5% wt. agar BM-1 gels left to dry at ambient temperature. (b) Young's modulus E of the gel vs. the relative water loss $\Delta m/m_0$ when considering a Poisson coefficient $\nu = 0.3$. (c) Stress maximum $\sigma_N^{(m)}$ reached during the indentation run vs. $\Delta m/m_0$. (d) Compressive strain $\epsilon^{(m)}$ associated with the stress maximum vs. $\Delta m/m_0$. Error bars are determined by repeating the experiments on three different samples.

5.4 Mechanical and structural properties of agar gels during drying

The influence of water evaporation upon the bulk mechanical properties of agar gels was investigated using macro-indentation tests. Agar gels of initial thickness $e_0 \approx 4$ mm are prepared in smooth plastic dishes and left to dry at ambient temperature until the water loss ranges between 5% and 20% wt.. The gels are then extracted by stamping the center of the gel with a circular punch tool to obtain gel disks of diameter $2R = 34$ mm diameter, which are then indented with a flat-ended cylinder of diameter 10 mm. During the indentation experiments, the normal force sensor of the rheometer (DHR-2, TA instrument) is used to record the stress-strain $\sigma(\epsilon)$ response of the gel (see Section 2.3.2 in Chapter 2 for technical details).

Results of indentation runs on 1.5% wt. agar-BM1 gels are reported in Figure 5.18 for different relative water loss $\Delta m/m_0$. Strain-stress curves $\sigma_N(\epsilon)$ indicate a similar mechanical behavior whatever the water loss, with first a linear increase of the stress for small applied strains ($\epsilon \leq 5\%$), followed by some strain hardening before reaching a maximum stress ($\epsilon^{(m)}$, $\sigma_N^{(m)}$), beyond which point, the stress decreases abruptly ($\epsilon > 40\%$) [Fig. 5.18(a)]. The Young's modulus E of the gel is estimated from the initial slope of the stress-strain curves (see Chapter 2, Section 2.3.2 for more details)⁵. The evolution of the Young's modulus E as well as the stress $\sigma_N^{(m)}$ and strain $\epsilon^{(m)}$ at failure are reported in Figure 5.18(b)–(d) as a function of the relative water loss $\Delta m/m_0$. Both the Young's modulus E and the critical stress $\sigma_N^{(m)}$ for gel failure appear as very sensitive to water loss. The Young's modulus E decreases for a moderate water loss, and is divided by a factor 2 for a relative water loss larger than 10% [Fig. 5.18(b)]. The critical stress $\sigma_N^{(m)}$ increases for increasing water loss, showing that the agar gel becomes more resistant to

⁵We consider in a first approximation that whatever the relative water loss, the gel is characterized by a Poisson coefficient of $\nu = 0.3$.

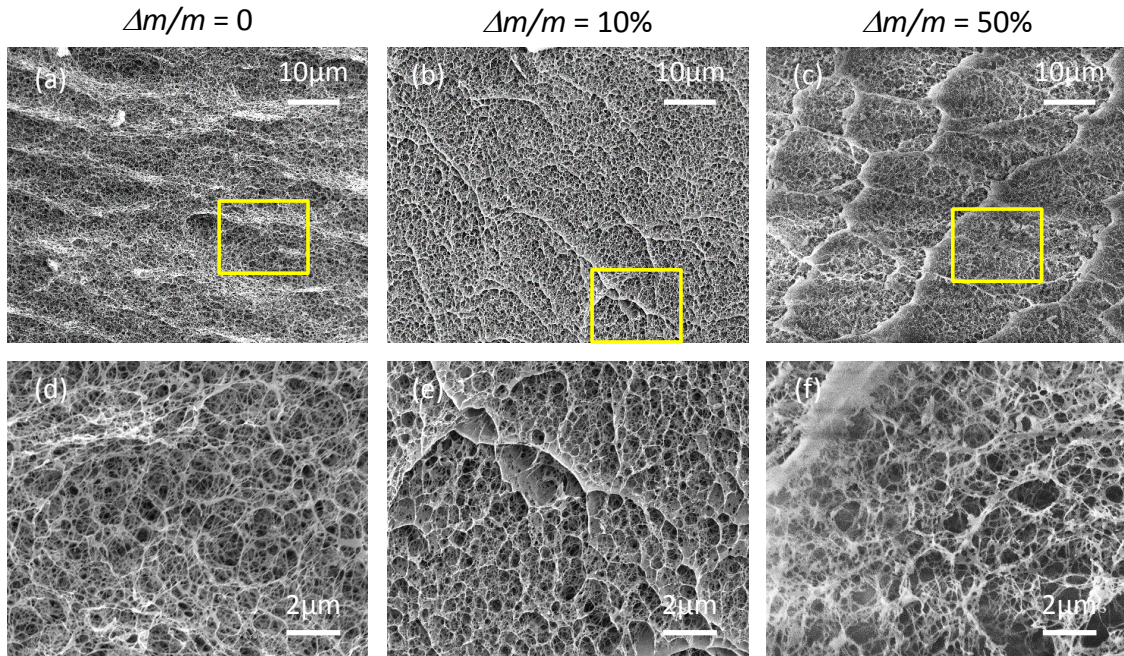


Figure 5.19: Cryo-SEM images of 1.5% wt. agar-BM1 gels after a relative water loss of $\Delta m/m = 0\%$ (a) and (d), $\Delta m/m = 10\%$ (b) and (e), and $\Delta m/m = 50\%$ (c) and (f). In each case, a gel sample is mounted on a pin stub and immersed in liquid nitrogen for about 5 min, before being placed in the low vacuum preparation chamber of a scanning electron microscope (JEOL 6700F). The chamber is cooled down to $T = -90^\circ\text{C}$ and the sample cut in situ with a scalpel. The temperature is then increased at a rate of $5^\circ\text{C}/\text{min}$ up to $T = -50^\circ\text{C}$ and maintained constant for about 5 min to sublime the water frozen inside the gel. The temperature is then decreased back to $T = -85^\circ\text{C}$. The sample is coated with a nanolayer of gold-palladium, before being cooled down to $T = -160^\circ\text{C}$ and finally introduced in the observation chamber of the microscope. Samples are imaged in SEI mode, at 5 kV.

failure [Fig. 5.18(c)]⁶. Finally, the water loss has no significant influence upon the critical strain $\epsilon^{(m)}$ for gel failure [Fig. 5.18(d)].

To further investigate the impact of the water loss on agar gels, the microstructure of 1.5% wt. agar-BM1 gels left to dry at ambient temperature is further observed using cryo-SEM observations (see Section 2.2.1 in Chapter 2 for technical details). Agar gels without any water loss shows a fibrous-like microstructure composed of interconnected strands delimiting pores with a broad size distribution up to a few micrometers [Fig. 5.19(a) and (d)], in agreement with cryo-SEM observations reported in the literature (Charlionet et al., 1996; Rahbani et al., 2013). Moreover, a relative water loss of 10% or 50% wt. induces a collapse of the small scale pores together with the formation of lamellar and cellular-like structures at the micron scale [Fig. 5.19(b) and (e), (c) and (f)]. The growth of such a larger scale microstructure is most likely responsible for the decrease of the compression modulus in agar gels left to dry.

⁶A change in the mechanical properties of agar gels left to dry was also observed in a compression cell. Experiments performed with agar plates kept at the ambient temperature during a few hours no longer show the formation of water droplets at their free surface, under external compression but only a plastic buckling. Moreover, continuous rheology experiments performed during the slow drying of agar gels also show a drop of the storage modulus G' as soon as the water loss exceeds 5% (Mao, Bouchaudy, Salmon, Divoux, & Snabre, 2017).

5.5 Discussion and conclusion

In the present chapter, I have shown that the drying of agar gels in Petri dishes is strongly influenced by the nature of the dish. The gel thins at a typical velocity of 15 nm/s at a temperature of 25°C, while the friction of the gel on either the bottom wall or the lateral wall of dish dictates whether the gel will detach from the wall, or fracture. A weak adhesion of the gel to the dish, as for a smooth glass dish, promotes wall slip and the gel detachment as water evaporates, whereas a strong adhesion as for a sandblasted dish, leads to the growth of a circular fracture along the edge of the dish. The plastic material used by bioMérieux company for the commercial Petri dishes displays a moderate roughness of about 10 nm, which allows the agar gel to slip along the sidewall, while suppressing gel sliding on the bottom wall of the dish, and preventing a long term detachment of the gel. However, the detachment of the gel is still widely observed in some types of commercial plates, which is most likely due to the presence of additives in the commercial culture media, such as surfactant. Interferometry will be further used in Chapter 6 to quantify the influence of several additives commonly used in culture media on the thinning rate of agar gels. Last but not least, I have shown that both the mechanical properties and the microstructure of agar gels are strongly sensitive to water evaporation. A relative water loss of only 10% induces a collapse of the small scale pores and the formation of larger structures at the micron scale, which results in the decrease in the gel Young's modulus and a higher mechanical resistance to failure.

Indeed, complementary observations of the compression of agar gel plates after 12 hours drying at 25°C (with water loss of about 25%) show no more the nucleation of droplets at the free surface but only a plastic buckling (Fig. 5.20). Moreover, the time evolution of the agar gel mechanical properties can be further “in-situ” monitored in the rheometer during the drying process through the use of the normal force controlled protocol (Mao, Bouchaudy, Salmon, Divoux, & Snabre, 2017). The upper plate of a parallel-plate geometry is topped with a doughnut-like lid to ensure a slow and uniform drying of the agar gel along the radial direction. As the water evaporates, the gap width slowly decreases and unexpectedly the storage modulus G' of the agar gel also decreases as a likely result of the collapse of the microstructure (see more details in Chapter 7: Conclusion).

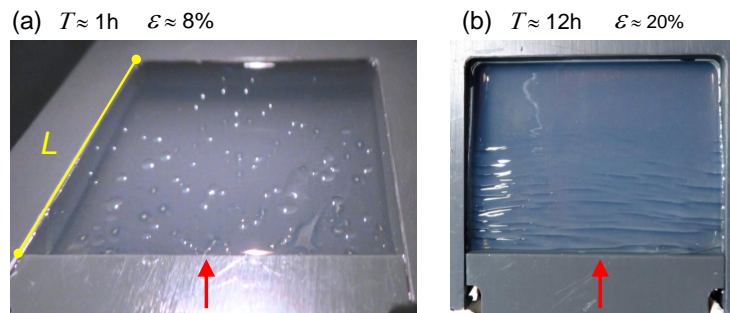


Figure 5.20: Views of a 1.5% wt. agar-BM2 gel plate (size $L \approx 40$ mm and thickness $e \approx 5$ mm) compressed in a homemade cell for a water loss less than 0.5% wt. (a) or about 25% wt. (b). The compressive strain $\varepsilon = l/L$ of the gel plate is $\varepsilon = 8\%$ (a) or $\varepsilon = 20\%$ (b). Experiments conducted at $(25 \pm 1)^\circ\text{C}$ when waiting either 1 hour (a) or 12 hours (b) after gel gelation. The red arrows indicate the compression direction.

Appendix B

Observations during the drying of a non-constrained agar gel

The present supplement concerns the drying dynamics of an agar gel disk (diameter 50 mm and thickness $e = 4$ mm) left to dry at controlled temperature $T = (25.0 \pm 0.5)^\circ\text{C}$ on a semi-infinite smooth plastic (PS) surface [Fig. B.1(a)]. The gel disk was stamped with a circular punch tool of diameter 50 mm from a gel cast in a smooth plastic dish.

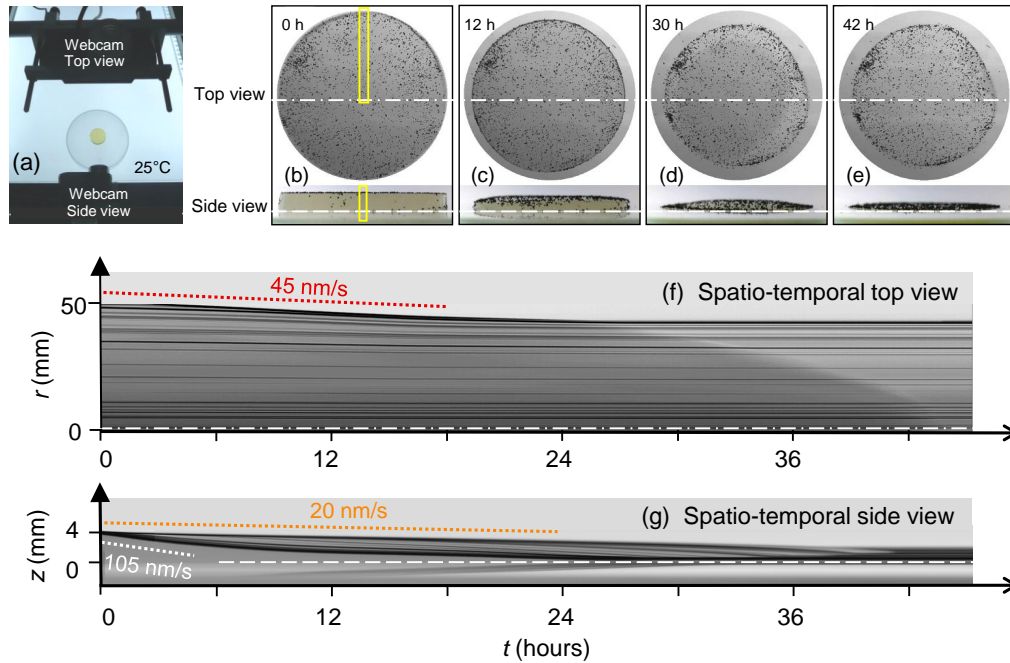


Figure B.1: (a) Experimental setup, which allows us to image the top and side views of a circular 1.5% wt. agar gel disk (diameter 50 mm, thickness 4 mm) left to dry at $T = (25.0 \pm 0.5)^\circ\text{C}$ on a semi-infinite smooth plastic (PS) surface. Images taken at (b) $t = 0$, (c) 12 h, (d) 30 h and (e) 42 h. The motion of the seed particles (diameter $200\mu\text{m}$ – $350\mu\text{m}$) located on the upper free surface of the gel disk allows for a spatio-temporal analysis of the gel drying dynamics. Spatio-temporal diagram (f) $T[r, t]$ from the top view and (g) $T[z, t]$ from the side view obtained from the time projection of all the pixels within the yellow vertical ROIs pictured in (b). The red, orange and white dotted lines highlight respectively the radial retraction velocity $v_r(0 < t < 12 \text{ h}) \approx 45 \text{ nm/s}$ of the circular gel disk, and the thinning rates $v_z(R, 0 < t < 3 \text{ h}) \approx 105 \text{ nm/s}$ and $v_z(r = 0, t) \approx 20 \text{ nm/s}$ of both the edge and the center region of the agar gel disk. The white horizontal line in the spatio-temporal diagram $T[z, t]$ pictured in (g) highlights the horizontal solid/gel interface.

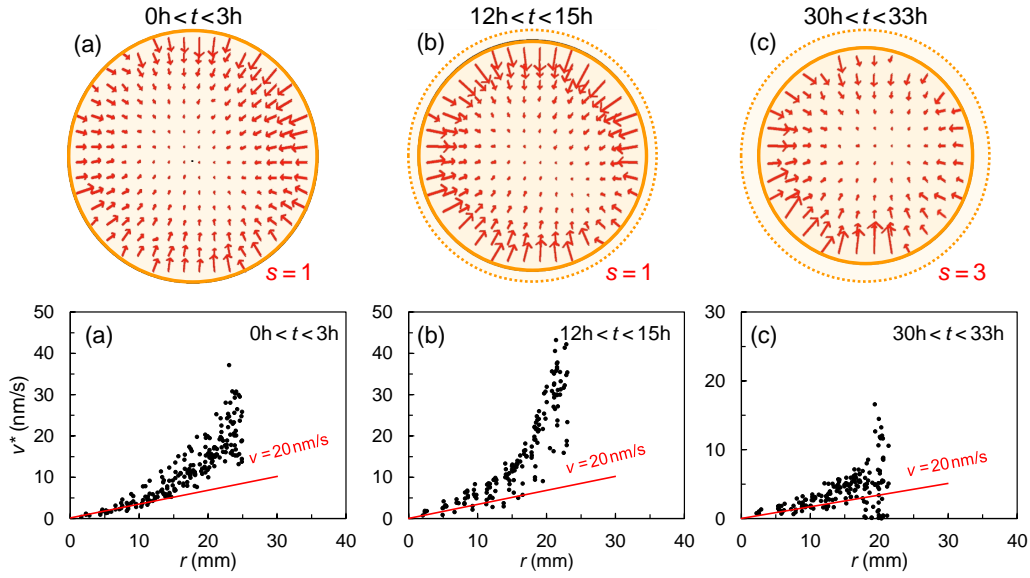


Figure B.2: Apparent 2D velocity field $\vec{v}^*(r, t)$ and radial dependence of the apparent velocity $v^*(r)$ of the gel free surface during the drying of a circular 1.5% wt. agar gel disk (diameter 50 mm, thickness 4 mm) on a semi-infinite smooth plastic (PS) surface for (a) $0 < t < 3$ h, (b) $12 \text{ h} < t < 15$ h and (c) $30 \text{ h} < t < 33$ h at $T = (25.0 \pm 0.5)^\circ\text{C}$. The red lines in (a)–(c) show the expected apparent velocity $v^*(r)$ for a purely vertical motion of the gel free surface with a vertical thinning rate $v = 20$ nm/s that obeys the following equation $v^* = vr \tan(\alpha)/R$, with $\tan(\alpha) = H^*/H = 0.425$ and $R = 25$ mm. Temporal sampling frequency $f_t = 1$ pixel/min and spatial sampling frequency $f_s = 1.7 \times 10^{-3}$ pixel/ μm . The variable s indicates the scale of the velocity vectors.

The vertical thinning and the radial shrinking of the gel disk are simultaneously monitored using two webcams (Logitech HD c920) located either on the top or on the side of the disk. The temporal projection of the gray levels of all the pixels within the thin yellow vertical ROIs pictured in Figure B.1(b) produces two spatio-temporal diagrams $T[r, t]$ and $T[z, t]$ featuring the shrinking and the thinning dynamics of the circular gel disk during the drying process [Fig. B.1(b)–(e)].

The spatio-temporal diagram from the top view $T[r, t]$ in Figure B.1(f) shows the radial shrinkage of the agar gel during the first twenty hours with a radial velocity $v_r \approx 45$ nm/s of the edge of the gel disk. After a drying period of about twenty hours, the gel disk looks like a flattened drop with almost dry edges, beyond which the water evaporation does not induce any radial retraction but only a thinning of the center part of the gel pellet until complete drying [Fig. B.1(d)–(e)]. The spatio-temporal diagram from the side view $T[z, t]$ in Figure B.1(g) shows the existence of edge effects during the first hours of the gel drying, with an accelerated thinning of the gel edge [velocity $v_z(r, t) \approx 105$ nm/s for $r \approx R = 25$ mm and $0 < t < 3$ h] compared to the thinning rate $v = v_z(r = 0, t) \approx 20$ nm/s of the center region of the gel during most of the drying process at $T = (25.0 \pm 0.5)^\circ\text{C}$.

Finally, the apparent 2D velocity fields $\vec{v}^*(r, t)$ of the seed particles located on the gel free surface are derived from a spatio-temporal analysis of the image sequences recorded with the webcam located above the circular gel disk [Fig. B.2(a)–(c)]. The velocity fields in Figure B.2 nicely confirm the heterogeneous drying dynamics of the gel disk with an accelerated water evaporation and gel retraction of the edge region of the disk ($20 \text{ mm} < r < 25$ mm) during the first 20 hours, and a slower vertical thinning of the center region of the gel ($0 \text{ mm} < r < 10$ mm) over the whole drying process.

Chapter 6

Role of additives on agar(ose) gel properties

Contents

6.1	Role of agaropectin on agarose gels	132
6.1.1	Impact on gelation and agarose gel debonding	133
6.1.2	Impact on the microstructure of agarose gels	135
6.1.3	Impact on agarose gel drying kinetics	135
6.2	Role of ionic species on agar gels	136
6.2.1	Anions: impact on gelation and gel debonding	137
6.2.2	Cations: impact on gelation and gel debonding	140
6.2.3	Impact of anions and cations on the drying kinetics of agar gels .	141
6.3	Effect of saccharides on agarose gels	141
6.3.1	Impact on gelation and gel debonding	143
6.3.2	Impact on the drying kinetics of agarose gels	144
6.3.3	Impact on agarose gel microstructure	145
6.4	Effect of surfactants on gel debonding	146
6.5	Discussion and conclusion	148

Associated peer-reviewed article:

▷ **Impact of saccharides on the drying kinetics of agarose gels measured by *in-situ* interferometry,**

B. Mao, T. Divoux & P. Snabre,
Scientific Reports **7**, 41185 (2017)

Depending on their applications, commercial agar plates used for the detection of microorganisms contain numerous additional components on top of agarose, such as blood, soy, ionic species, non-gelling saccharides, proteins, surfactants, etc. This long list of additives affects the gelation of the culture media, as well as the viscoelastic properties, the adhesive properties and the drying kinetics of agar-based gels. If it is clearly out of the scope of my PhD to study the influence of all these components on the behavior of agar-based culture media, we can still rationalize the impact of the most common ones using the techniques introduced in Chapter 2 and the know-how gained in the previous chapters.

In the first section of the present chapter, I will report a comparative study between gels made of pure agarose and gels made of agar, i.e. agarose and agaropectin. Indeed, as a non-gelling polysaccharide, agaropectin can be considered as the first key additive to agarose gels and we will determine its role on the properties of agar gels. In the second section, we examine the impact of three different classes of additives commonly used in commercial culture media, namely 7 ionic species (sulfate, chloride, iodide, potassium, lithium and sodium), 4 (poly)saccharides of different molecular weights (dextran, glucose, guar gum and xanthan gum), and 2 types of surfactants: an ionic and a non-ionic one (Lecithin and Tween 80). In practice, the additives are added at the early stage of the gel preparation, i.e. in a hot agarose (or agar) solution.

We then perform systematically the following series of tests: the gelation process is monitored in a parallel-plate geometry using the zero normal force and the strain-adapted protocols to determine the gelation temperature T_g , the relative contraction $\Delta e/e$ of the sample during the gelation, and the steady-state values of the storage and loss moduli, G'_f and G''_f of the gel (see Section 2.3.1 in Chapter 2 for technical details). Once gelified, the sample microstructure is visualized by cryo-SEM microscopy (see Section 2.2.1 in Chapter 2). We also characterize the adhesive properties of these agar-based gels on smooth plastic (PS) surfaces, which is the material commercial Petri dishes are made of. Oscillatory strain sweep experiments are used to determine the critical shear strain and stress associated with the first debonding of the gel (see Section 2.4.1 in Chapter 2 for more details). Finally, the impact of each additive on the water-holding capacity of a gel cast in a Petri dish and left to dry at a constant temperature of 25°C is quantified by interferometric observations (see Section 2.5.1 in Chapter 2 for details on the method). For these experiments, gels are cast in smooth plastic dishes of diameter 50 mm, smaller than that of the commercial dishes. These smaller dishes are much less sensitive to thermally induced deformations and the gels cast in such dishes experience a shrinkage only in the vertical direction, which makes the interferometric experiments much easier to interpret (see Fig. 5.12 in Section 5.3, Chapter 5 for more explanations).

6.1 Role of agaropectin on agarose gels

As discussed in Chapter 1, agarose is a neutral polysaccharide with remarkable gelling capacity and therefore widely used as a gelling component in various commercial products, including culture media. However, both the low production yield and the high cost of agarose¹ force companies to use powder of lower grades composed of both agarose and agaropectin². Agaropectin, which is a charged polysaccharide structurally similar to

¹The cost of pure agarose ranges currently between 2€ and 8€ per gram depending on the product quality, whereas agar costs only about 0.2€–0.3€ per gram.

²Note that the ratio agarose/agaropectin depends on the agar quality and varies from one producer to another (Marx, 2013; Matsushashi, 1990).

agarose, shows a higher sulfate content and does not gel (Duckworth, Hong, & Yaphe, 1971). Therefore, a better understanding of the properties and performance of agarose gels containing agarpectin is of practical importance.

6.1.1 Impact on gelation and agarose gel debonding

To compare the formation of agarose gel with and without agarpectin, I have prepared two types of solutions at various concentrations: the first one contains only agarose and the second one is made with agar-BM1, which contains about 70% wt. of agarose and 30% wt. agarpectin (see Table 2.1 in Chapter 2). Gelation experiments are performed as follows: a sample is loaded in a parallel-plate geometry coated with smooth plastic (PS) plates and connected to a stress-controlled rheometer. The gelation is triggered by decreasing the temperature from 50°C to 20°C with a cooling rate 1°C/min. Following the zero normal force and strain-adapted protocols, we determine the gelation temperature T_g as the intersection of the storage and loss moduli, the relative sample contraction $\Delta e/e$ during the sol-gel transition and the terminal values of the viscoelastic moduli: G'_f and G''_f . The results, pictured in Figure 6.1(a)–(c) clearly demonstrate that the gelation process of agarose gels is mainly controlled by the agarose concentration. Indeed, agar and

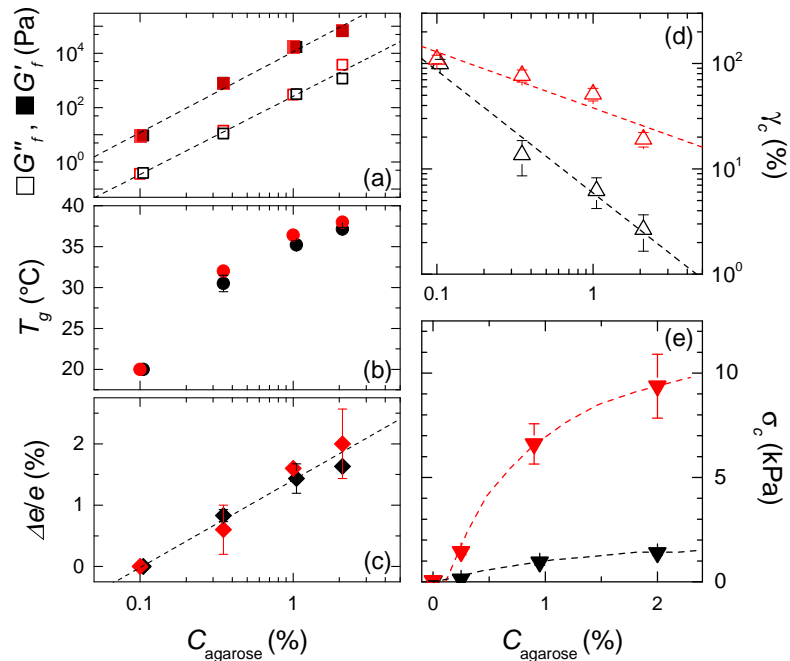


Figure 6.1: Gelation and first debonding properties of pure agarose gels (red symbols) and agar-BM1 gels (content: about 70% wt. agarose and 30% wt. agarpectin) (black symbols) for different agarose concentrations. (a) Terminal storage modulus (G'_f , ■) and loss modulus (G''_f , □) vs. agarose concentration. Black dashed lines in (a) correspond to the best power-law fit of the data, with equations $G'_f \propto (C_{\text{agarose}})^{2.78 \pm 0.14}$ and $G''_f \propto (C_{\text{agarose}})^{2.73 \pm 0.11}$. (b) Gelation temperature T_g vs. agarose concentration. (c) Relative variation of the gap width $\Delta e/e$ vs. agarose concentration. The black dashed line in (c) is the best linear fit of the data in semi-logarithmic scale, with $\Delta e/e = 1.5 + (1.43 \pm 0.11) \log(C_{\text{agarose}})$. (d) Critical shear strain γ_c for the gel first debonding from smooth plastic plates vs. agarose concentration. The dashed lines are the best linear fit of the data in logarithmic scale, with equations $\log(\gamma_c) = (1.6 \pm 0.1) - (0.5 \pm 0.1) \log(C_{\text{agarose}})$ for agarose gels and $\log(\gamma_c) = (0.8 \pm 0.1) - (1.2 \pm 0.1) \log(C_{\text{agarose}})$ for agar-BM1 gels, respectively. (e) Critical shear stress σ_c for the gel first debonding from smooth plastic plates vs. the agarose concentration. The dashed curves are only guides for the eye. Error bars correspond to the dispersion of the results obtained by repeating the experiments on 3 to 5 different samples.

agarose samples prepared with the same agarose concentration display a similar gelation temperature T_g [Fig. 6.1(b)] and compatible viscoelastic moduli within error bars over more than a decade in agarose concentration. Both moduli scale as a power law of the agarose concentration (below 2% wt.) with a scaling exponent close to 2.7 [Fig. 6.1(a)]. Furthermore, both types of samples show, within error bars, compatible relative contractions during the sol/gel transition. In both cases the contraction displays a logarithmic increase with the agarose concentration [Fig. 6.1(c)].

Once the sample jelled, the adhesion between agar(ose) gels and a smooth plastic (PS) surface is quantified by a strain sweep experiment. A ramp of strain oscillating at 1 Hz and of amplitude increasing from $\gamma = 0.01\%$ to 100% is imposed to each sample in 2160 s to measure the critical shear strain γ_c and the critical shear stress σ_c associated with the first debonding of the gel [Fig. 6.1(d) and (e)]. For both types of gel, one observes that the adhesive properties decrease for increasing agarose concentration. Nevertheless, the agarose concentration is not the only parameter that controls the gel debonding, as for a given agarose concentration, pure agarose gels show a much better adhesion to the plastic plates than agar gels. The lower values of γ_c and σ_c for agar gels most likely result from the presence of agaropectin molecules and/or other additives in the agar-BM1 powder (see Table 2.1 in Chapter 2). It is worth noting that a similar decrease of agarose adhesive properties to plastic surfaces is observed when loading agarose gels with other non-gelling polysaccharides than agaropetin, such as xanthan gum and guar gum as discussed later on in Section 6.3. Such a result strongly suggests that the agaropetin is indeed responsible for the lower adhesive properties of agar gels. Finally, the debonding stress σ_c increases non-linearly with the agarose concentration for both types of samples [Fig. 6.1(e)]. This observation was previously related to the sample contraction that occurs during the gelation, and which leads to the formation of intercalated liquid films at the gel/substrate interface (Section 4.4, Chapter 4). Within that framework, increasing the agarose concentration promotes both the gel contraction [Fig. 6.1(c)] and the wetting of the contact area between the gel and the substrate, leading in turn to a somewhat lower adhesion of the agar(ose) gel on the plastic surface.

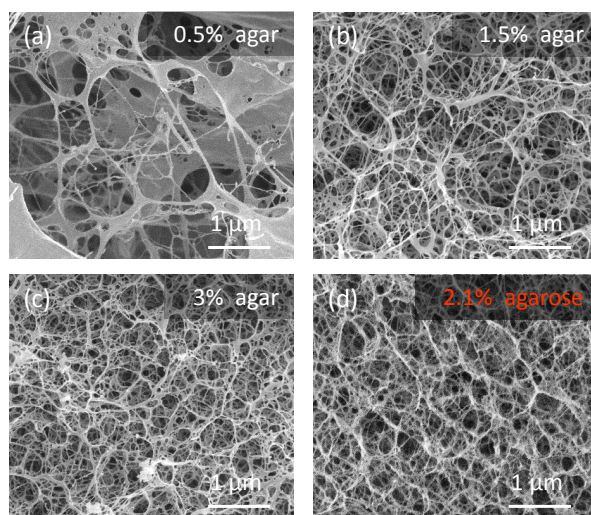


Figure 6.2: Cryo-SEM images of agar-BM1 gels at different agar concentrations $C = 0.5\%$ wt. (a), 1.5% wt. (b) and 3% wt. (c) corresponding to agarose concentrations $C_{agarose} = 0.35\%$ wt., 1.05% wt. and 2.1% wt., respectively. (d) Cryo-SEM image of a pure agarose gel with $C_{agarose} = 2.1\%$ wt.. See Section 2.2.1 in Chapter 2 for the technical details concerning the sample preparation for SEM.

6.1.2 Impact on the microstructure of agarose gels

Cryo-SEM observations were systematically performed on agar and agarose gels at different concentrations to visualize the microstructure (see Section 2.2.1 for technical details). Results for agar gels of different agar concentrations 0.5% wt., 1.5% wt. and 3% wt., which correspond to agarose concentrations of about 0.35% wt., 1.05% wt. and 2.1% wt., respectively are pictured in Figure 6.2(a)–(c). Agar gels display a fibrous-like microstructure composed of interconnected strands delimiting pores, in agreement with other cryo-SEM data reported in the literature (Charlionet et al., 1996; Rahbani et al., 2013). The network becomes denser and the mesh size smaller for increasing agarose concentration, which is to be related with the increase of the elastic shear modulus with agarose concentration [Fig. 6.1(a)]. Moreover, a pure agarose gel prepared with 2.1% wt. of agarose displays a similar microstructure to that of a 3% wt. agar gel of equivalent agarose concentration $C_{\text{agarose}} = 2.1\%$ wt. [compare Fig. 6.2(c) and (d)], which supports the fact that only agarose molecules are involved in the network formation of agar gels (Araki, 1956). Agaropeptin molecules act as passive molecules embedded in the pores network.

6.1.3 Impact on agarose gel drying kinetics

We now compare the drying kinetics of agarose and agar gels by using interferometric observations to measure the thinning rate of gels cast in smooth plastic dishes of diameter 50 mm (see Section 2.5.1 in Chapter 2 for more technical details). Experiments on pure agarose gels left to dry at $T = (25.0 \pm 0.5)^\circ\text{C}$ reveal that the average thinning rate v is about 25 nm/s, and independently of the agarose concentration within 0.125% and 3% wt. [Fig. 6.3(a), ■]. Interestingly, the thinning rate of agarose gels is comparable to that of a water pool with the same initial volume as that of the gel [blue star symbol (★) in Fig. 6.3(a)], which suggests that agarose gels present few water-binding components, and behave as passive sponges from which water evaporates freely. Independent compression experiments performed on gellan gels (Nakamura, Shinoda, & Tokita, 2001) and quantitative NMR study of agarose gels (Woessner et al., 1970; Andrasko, 1975; Davies et al., 2010) indeed show that most of the water molecules within the agar gels are not bounded to the network but freely diffuse.

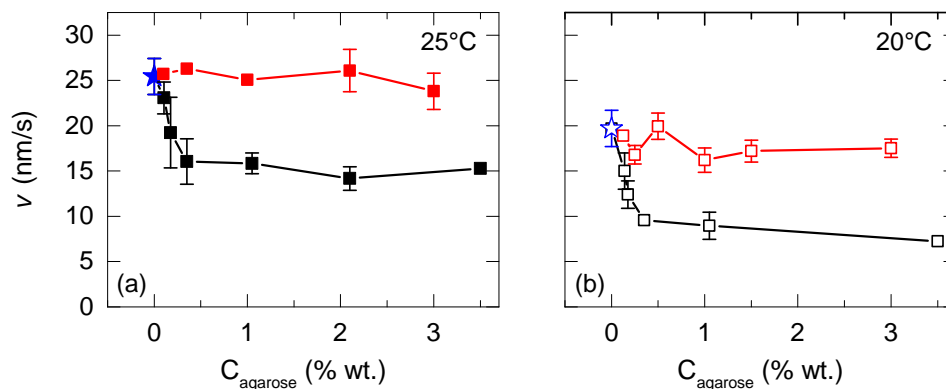


Figure 6.3: Average thinning rate v of agarose gels (■, □) and agar-BM1 gels (content: 70% wt. agarose and 30% wt. agaropeptin, ■, □), measured at the center of the gel plate cast in a smooth plastic (PS) dish, vs. the agarose concentration. Experiments performed at 25°C (a) and 20°C (b). The blue star symbol ★ denotes the thinning rate of a water pool with the same volume as the agar(ose) gels and monitored in the exact same experimental conditions. Error bars correspond to average standard deviation associated with 3 independent measurements conducted over 10 minutes each.

The average thinning-rate v of agar-BM1 gels prepared at various concentrations was further determined and reported in Figure 6.3(a) as (■). Over the whole range of agarose concentrations explored, agar gels exhibit a smaller thinning rate than a gel with the same agarose content but without any agarose molecules. The thinning rate of agar gels abruptly decreases for increasing agarose concentrations, for $C_{\text{agarose}} \leq 0.4\%$ wt. and takes a constant value of about 15 nm/s for $C_{\text{agarose}} > 0.4\%$ wt.. Such observations strongly suggest that agarose molecules act as water-binding components, which actively slow down the water evaporation and therefore reduce the gel thinning-rate. This point will be further discussed in Section 6.3, where we study in more details the drying kinetics of agarose gels loaded with polysaccharides of different molecular weights. Finally, repeating the same series of experiments at a lower temperature of $T = (20.0 \pm 0.5)^\circ\text{C}$ leads to the same results, confirming the larger thinning rate of agarose gels compared to agar gels prepared with a similar agarose content [Fig. 6.3(b)].

6.2 Role of ionic species on agar gels

The addition of salt to polymer gels often has dramatic effects on both the gelation dynamics and the melting temperature of hydrogels. The impact of ions on the gelation kinetics of gels made of anionic polysaccharides such as carrageenans, gellans, alginates or pectins has been particularly well studied (Payens & Snoeren, 1972; Rinaudo, Karimian, & Mallas, 1979; V. J. Morris & Chilvers, 1983; Hermansson et al., 1991; Liu, Huang, & Li, 2016). Cations have been reported to affect the gelation temperature and the melting temperature of carrageenan gels due to the formation of charged tertiary structures. However, the effects of anions on the gelling process of anionic polysaccharides is still unclear and the nature of anions is reported to have only a weak influence on the gelation of carrageenans except for iodide ions (Rochas & Rinaudo, 1980; Piculell & Nilsson, 1989; Watase, Nishinari, Williams, & Phillips, 1990).

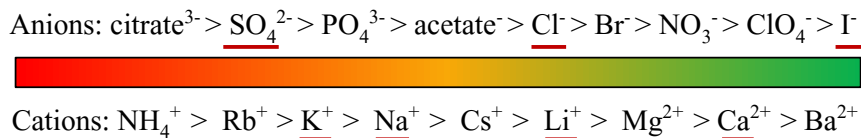


Figure 6.4: Some examples of anionic and cationic species ordered in the Hofmeister series. Reprinted from (Kunz, 2010; Rossetto et al., 2008). The ions underlined in red are the ones considered in the present work.

The situation is even less clear for neutral polysaccharides such as agarose, which yet displays a repeating disaccharide structure quite similar to its anionic equivalent, i.e. carrageenan. Anion-specific effects have been reported on both the conformational transition and the association of the agarose molecules, and interpreted in terms of weak anion binding to agarose molecules (Piculell & Nilsson, 1989). Furthermore, the addition of either K₂SO₄ or NaCl to a 0.5% wt. agar hot solution was shown to shorten the gelation time (Iwase, 1938), while many other ions have been reported to either speed up³ or slow down the agar gelation (Matsushashi, 1990). Such effects are generally more pronounced for anions than for cations and may correspond to a reoccurring trend first noticed by Franz Hofmeister in 1888 while he was studying the effect of cations and anions on the solubility of proteins (Hofmeister, 1888). Today, the “salting-out” effects are commonly exploited

³K⁺ > Na⁺ for cations; and SO₄²⁻ > CH₃COO⁻ > C₄H₄O₆²⁻ > Br⁻ for anions. This order strongly recall that of the Hofmeister series (Fig. 6.4).

in protein purification through the use of “*Ammonium sulfate precipitation method*”. The Hofmeister series or *lyotropic series* order either the anions or cations with decreasing salting out efficiency from left to right (Fig. 6.4). On the one hand, the ions at the left of the series such as SO_4^{2-} usually strengthen the hydrophobic interaction, increase the solvent surface tension and decrease the water solubility of solutes (one talks about “salting-out” effect or “Kosmotropic” ions). On the other hand, the ions located to the right of the Hofmeister series weaken the hydrophobic effect and can increase the water solubility of macromolecules (one talks about “salting-in” effects or “Chaotropic” ions) (Chaplin, 2014). A molecular understanding of the Hofmeister series is still under debate and it remains unclear whether the ions affect the bulk water properties or directly interact with the macromolecules (Kunz, 2010; Xie & Gao, 2013). However, dynamic measurements of the correlation time of water molecules in aqueous salt solutions clearly demonstrate that anions have no influence on the dynamics of bulk water, even at very high concentrations of both kosmotropic and chaotropic ions (Omta, Kropman, Bakker, & Bakker, 2003), which strongly suggests that ion-related effects most likely involve ion/polymer interactions (Y. Zhang & Cremer, 2006).

During my PhD, I chose to investigate the anions and cations underlined in red in Figure 6.4, which cover the Hofmeister series and can be added to a hot agar solution without affecting its neutral pH. The three anions selected are sulfate SO_4^{2-} , chloride Cl^- and iodide I^- , all considered with the same counter ion: Na^+ . The four cations selected are: potassium K^+ , sodium Na^+ , lithium Li^+ and calcium Ca^{2+} , all considered with the same counter ion: Cl^- . Salt concentrations are chosen depending on the valence of the ionic species, in such a way that the amount of counter ion is the same for all agar gels (Table. 6.1). The amount of salt added in solution is also chosen low enough to remain below the solubility limit, and large enough compared to the amount of ionic species already present in the agar powder.

		Molar mass (g/mol)	ion valence	% wt.	mol/L
Anions	Na_2SO_4	142.04	2	1.94	0.14
	NaCl	58.44	1	1.50	0.27
	NaI	149.54	1	4.10	0.27
Cations	KCl	74.55	1	2.04	0.27
	LiCl	42.39	1	1.16	0.27
	NaCl	58.44	1	1.50	0.27
	CaCl_2	110.98	2	1.52	0.14

Table 6.1: Salts concentrations considered in the next sections to investigate anion and cation effects with either the same sodium (Na^+) or chloride (Cl^-) counter ion concentration.

We first report on the effect of anions (SO_4^{2-} , Cl^- and I^-) on the properties of a 1.5% wt. agar gel, and determine the impact of the anion concentration by preparing gels with different amounts of chloride (Cl^-) in the range of 0.5% wt. to 6% wt.. Second, I will report on the effects of cations (K^+ , Na^+ , Li^+ and Ca^{2+}) on agar gels, before comparing the thinning rate of agar gels loaded with either anions or cations.

6.2.1 Anions: impact on gelation and gel debonding

To determine the salting effects of anions, four different agar solutions were prepared: a reference 1.5% wt. agar-BM1 solution without any additional salt, and three other 1.5% wt. agar-BM1 solutions each loaded with sodium salts of different anions (SO_4^{2-}

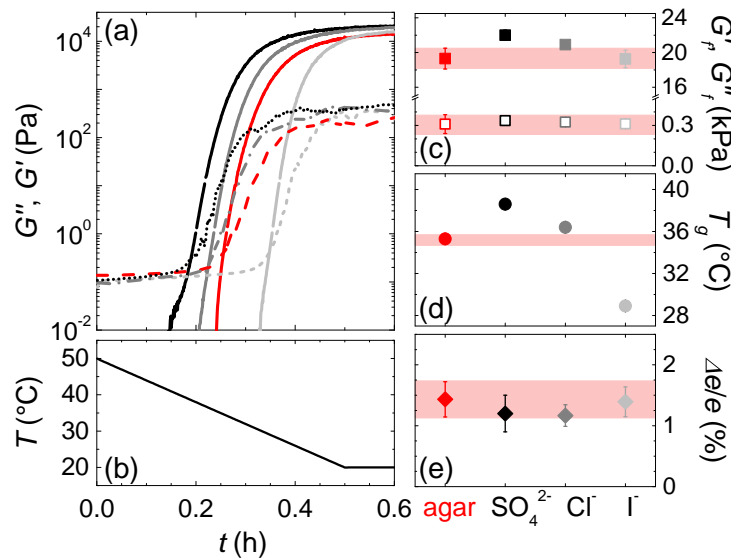


Figure 6.5: (a) Temporal evolution of the viscoelastic moduli G' (solid lines) and G'' (dotted lines) determined through SAOS experiments during the gelation of four different 1.5% wt. agar-BM1 solutions: a reference sample without additional salt (red lines) and three samples loaded respectively with 0.14 mol/L SO_4^{2-} (black lines), 0.27 mol/L Cl^- (dark gray lines) and 0.27 mol/L I^- (light gray lines). Concentrations are chosen so as the amount of sodium counter ion is the same in all the gels. (b) Profile of temperature during the gelation process. (c) Terminal viscoelastic moduli G'_f and G''_f , (d) Gelation temperature T_g defined by the crossover of the storage and loss moduli, and (e) Relative contraction $\Delta e/e$ of the samples during the gelation. Data reported for the reference agar solution (red color) and agar solutions loaded with 3 different anions ordered along the Hofmeister series (Fig. 6.4). Error bars correspond to the dispersion of the results obtained by repeating the experiments on 3 to 5 different samples. The red stripes highlight the errors bars for the reference sample.

at 0.14 mol/L, Cl^- at 0.27 mol/L and I^- at 0.27 mol/L). The gelation is monitored in a parallel-plate geometry connected to a stress-controlled rheometer, following the zero normal force protocol (see Section 2.3.1 in Chapter 2). The gel adhesion properties are quantified through strain sweep experiments once the agar gel has been cured for 1.5 h.

The formation of the 1.5% wt. agar gel is affected by the presence of the anions [Fig. 6.5(a)]. The gelation occurs sooner, i.e. at a higher temperature in the presence of sulfate ($T_g \approx 38.6^\circ\text{C}$) or chloride ($T_g \approx 36.3^\circ\text{C}$) compared to the reference agar gel ($T_g = 35.5 \pm 0.3^\circ\text{C}$), whereas the gelation occurs later in the presence of iodide, i.e. at lower temperature ($T_g \approx 29^\circ\text{C}$) [Fig. 6.5 (d)]. Moreover, the gelation temperature of the sample decreases along the Hofmeister series with a difference of about 10°C between the first and the last anion in the series. However, the addition of anions has no significant influence upon the terminal viscoelastic properties G'_f , G''_f of agar gels [Fig. 6.5(c)], nor on the sample contraction $\Delta e/e$ during the gelation [Fig. 6.5(c)].

To determine the effect of the anions on the microstructure of the 1.5% wt. agar-BM1 gels, cryo-SEM observations were performed on the various samples (Fig. 6.6). In comparison with the fibrous-like nanometric microstructure of the reference agar gel without any additive [Fig. 6.6(a)], one can see larger pores with a size of several microns and the presence of aggregated fibers in the presence of “Kosmotropic” anions such as sulfate or chloride species [Fig. 6.6(b) and (c)]. Surprisingly, the addition of “Chaotropic” iodide anions leads to the formation of an even bigger cellular-like microstructure and the absence of any fibrous structure [Fig. 6.6(d)]. The mechanism underlying the formation of such microstructure is still unclear.

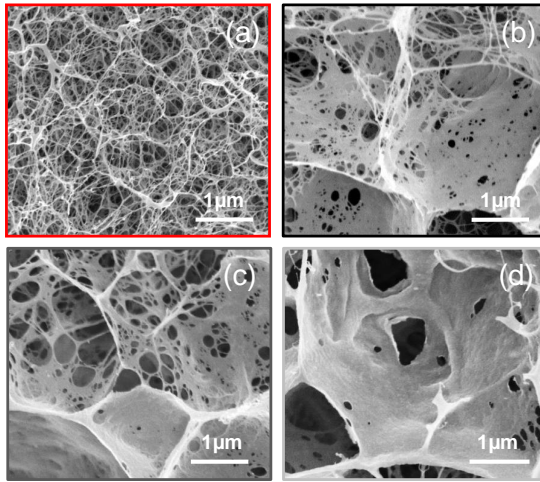


Figure 6.6: Cryo-scan electron micrographs of the reference 1.5% wt. agar-BM1 gel (a) and three different agar gels loaded with various anions: (b) 0.14 mol/L SO_4^{2-} , (c) 0.27 mol/L Cl^- and (d) 0.27 mol/L I^- . Concentrations are chosen so as the amount of counter ion (sodium Na^+) is the same in all the gels. Each micrograph is framed with the same color code as that used in Figure 6.5. See Section 2.2.1 in Chapter 2 for the technical details concerning the sample preparation for SEM.

Finally, the adhesion properties of the anion-loaded gels in contact with smooth plastic (PS) plates were determined using strain sweep experiments with a progressive increase of the oscillatory shear strain amplitude from $\gamma=0.01\%$ to 100% in 2160 s. A similar shear-induced debonding scenario is observed for both the reference gel and the anion-loaded gels, as shown in Figure 6.7(a): the storage modulus is constant in the low shear strain regime, and sharply decreases above a critical shear strain amplitude γ_c , which corresponds to a maximum shear stress σ_c . The presence of anions in the gel results in an increase of the debonding stress σ_c from smooth plastic plates [Fig. 6.7(b)]. The effect of the anions decreases along the Hofmeister series, and the “Kosmotropic” anions better improve the gel adhesive properties with the plastic plate.

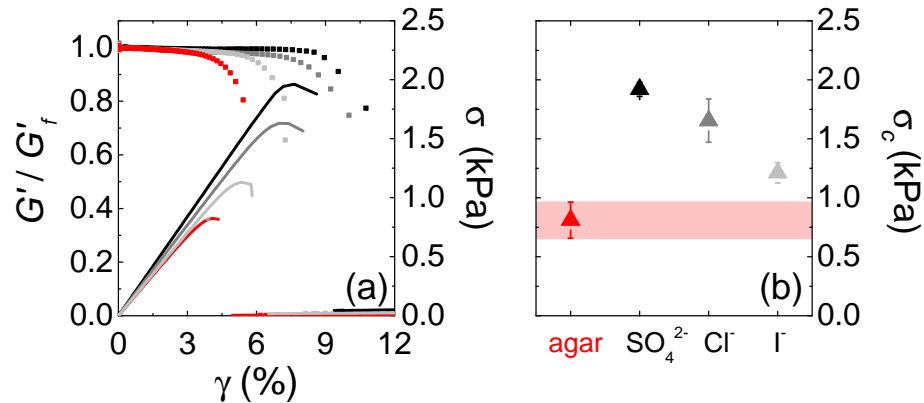


Figure 6.7: (a) Left axis: Normalized storage modulus G'/G'_f vs. shear strain amplitude γ during a strain sweep experiment, where G'_f stands for the terminal value of the storage modulus in the linear regime. Right axis: shear stress σ vs. shear strain amplitude γ during the strain sweep experiments (oscillation frequency: 1 Hz - total duration of the sweep: 2160 s). (b) Critical shear stress σ_c for the gel debonding from smooth plastic plates, defined as the stress maximum visible in (a). Data reported for 1.5% wt. agar-BM1 gels: red stands for the reference, and the gray scale stands for the gels loaded with anions: 0.14 mol/L SO_4^{2-} , 0.27 mol/L Cl^- and 0.27 mol/L I^- from dark to light gray following the Hofmeister series in Figure 6.4. The color code is the same as that used in Figure 6.5 and Figure 6.6. Error bars correspond to the dispersion of the results obtained by repeating the experiments on 3 to 5 different samples. The red stripe highlights the errors bars for the reference sample.

To further quantify the impact of the anion concentration on the gelation kinetics, the microstructure and the adhesive properties of agar gels, I have prepared solutions of

1.5% wt. agar-BM1 loaded with various concentrations of sodium chloride (NaCl) ranging from 0.5% wt. to 6% wt. (i.e. molar concentration from 0.09 mol/L to 1.08 mol/L). The results are summarized in Figure 6.8. First, the presence of NaCl has no significant influence on the terminal viscoelastic moduli G'_f , G''_f of the gel over the range of salt concentrations explored [Fig. 6.8(a)], in agreement with previous results. However, gels containing NaCl show a coarser microstructure composed of cellular structures, which size increases regularly with the salt concentration [Fig. 6.8(d)–(g)]. Furthermore, the gelation temperature T_g increases with the salt concentration, by up to 4°C for an addition of 6% wt. of NaCl [Fig. 6.8(b)]. Finally, the gel adhesion to smooth plastic (PS) plates is markedly reinforced for increasing salt concentrations, and the critical shear stress σ_c saturates above 1.5% wt. NaCl.

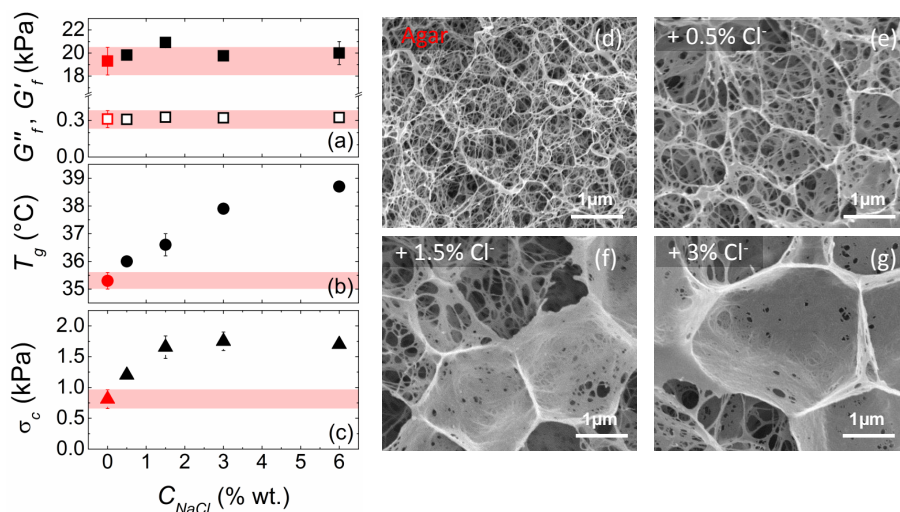


Figure 6.8: (a) Terminal viscoelastic moduli G'_f and G''_f , (b) Gelation temperature T_g and (c) Critical shear stress σ_c for the debonding of 1.5% wt. agar-BM1 gels from a plastic (PS) surface vs. the NaCl concentration added to the agar solution. The red stripes highlight the errors bars for the reference sample prepared without any additional NaCl. Error bars correspond to the dispersion of the results obtained by repeating the experiments on 3 to 5 different samples. (d)–(g) Scanning electron micrographs of the reference sample 1.5% wt. agar-BM1 gel (d) and the gels loaded with increasing amount of sodium chloride: 0.5% wt. (e), 1.5% wt (f), and 3% wt (g), which correspond to the molar concentrations of 0.09 mol/L, 0.27 mol/L and 0.54 mol/L. See Section 2.2.1 in Chapter 2 for the details of the sample preparation.

6.2.2 Cations: impact on gelation and gel debonding

The effect of cations on the properties of agar gels are studied in a very similar fashion as that described for the anions. I have prepared a series of 1.5 % wt. agar-BM1 solutions loaded with four different chloride salts of different cation species: potassium K^+ (0.27 mol/L), sodium Na^+ (0.27 mol/L), lithium Li^+ (0.27 mol/L) and calcium Ca^{2+} (0.14 mol/L) as listed in Table 6.1. Concentrations are chosen such that the amount of counter ion (Cl^-) is the same for all the gels. The gelation and the adhesive properties are studied through rheological experiments, and the results are summarized in Fig. 6.9. The gelation scenario is insensitive to the presence of cations: the gelation temperature T_g , the gel contraction $\Delta e/e$ during the gelation and the terminal viscoelastic moduli G'_f , G''_f of the gel remain unchanged in the presence of the cationic species [Fig. 6.9(a)–(c)]. However, the addition of salt increases the adhesion of the gel to the plastic plate as evidenced by the larger values of σ_c [Fig. 6.9(d)]. The values of σ_c are yet compatible within error bars

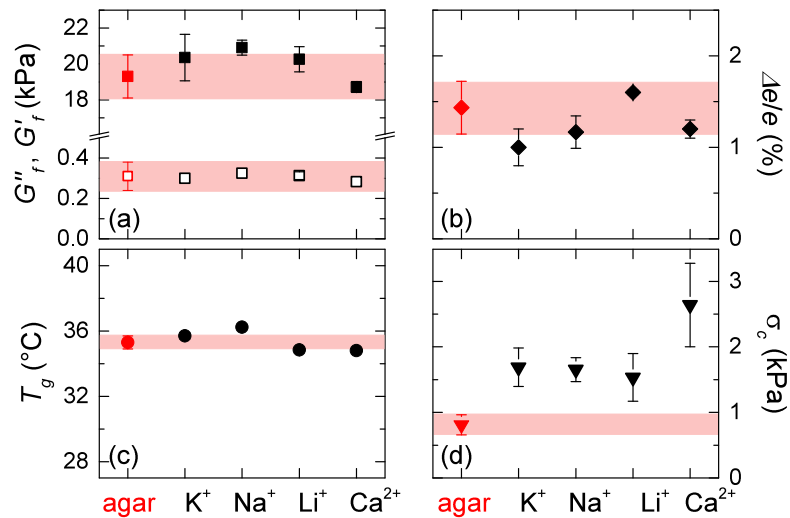


Figure 6.9: (a) Terminal viscoelastic moduli G'_f, G''_f , (b) Relative contraction $\Delta e/e$ of the sample during gelation, (c) Gelation temperature T_g , and (d) Critical shear stress σ_c for the debonding of 1.5% wt. agar-BM1 gels. The red symbol corresponds to the reference gel, and the black ones stand for gels prepared with different cations: 0.27 mol/L K^+ , 0.27 mol/L Na^+ , 0.27 mol/L Li^+ and 0.14 mol/L Ca^{2+} . Concentrations are chosen so as the amount of counter ion (Cl^-) is the same for all the gels. The ions are ordered following the Hofmeister series (Fig. 6.4). Error bars correspond to the dispersion of the results obtained by repeating the experiments on 3 to 5 different samples. The red stripes highlight the errors bars for the reference sample without any additive.

with that reported in Figure 6.7(b) and Figure 6.8(c) in the anionic study when adding Cl^- (0.27 mol/L, 1.5% wt.) - at least for KCl, NaCl and LiCl. Therefore, the improved adhesive properties of cation-loaded agar gels are most likely due to the presence of the chloride counter ion. The only remarkable increase in the critical shear stress that might be due to the cation is observed for gels prepared with calcium cation Ca^{2+} .

6.2.3 Impact of anions and cations on the drying kinetics of agar gels

The drying kinetics of agar gels loaded with the same anionic and cationic salts as discussed in the last two subsections was monitored through interferometric observations. The thinning rate v of ions-loaded agar gels cast in smooth plastic (PS) dishes and left to dry at temperature $T = (25.0 \pm 0.5)^\circ C$ is measured at the center of the dish and averaged over 10 minutes (Fig. 6.10). Neither the anions, nor the cations have any significant influence on the drying kinetics of agar gels.

6.3 Effect of saccharides on agarose gels

We now turn to the effect of saccharides, which are commonly added in minute amounts ($< 2\%$ wt.) into agar-based culture media. Non-gelling saccharides such as sucrose, glucose, maltose, xanthan gum, etc. have been shown to impact the formation of agarose gels (Watase, Kohyama, & Nishinari, 1992; Nishinari et al., 1992; Russ et al., 2013) and their mechanical properties (Watase et al., 1990; Nagasaka & Taneya, 2000; Normand et al., 2003) when introduced in large amounts (5% wt. or higher). An excess mass of non-gelling saccharides indeed results in (i) a larger gel storage modulus, (ii) larger strain and stress at failure and (iii) lower water release under external load (Nishinari & Fang, 2016b). However, the impact of non-gelling saccharides loaded in minute amounts in agar

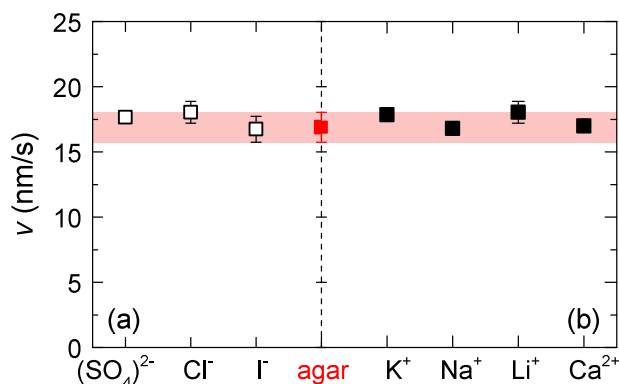


Figure 6.10: Vertical thinning rate v of agar gels cast in smooth plastic (PS) dishes and left to dry at $T = (25.0 \pm 0.5)^\circ\text{C}$. Data reported for a reference 1.5% wt. agar-BM1 gel without any additive (red symbol) and gels of identical agar concentration loaded with different (a) anions: SO_4^{2-} (0.14 mol/l), Cl^- (0.27 mol/L) and I^- (0.27 mol/L), and (b) cations: K^+ (0.27 mol/L), Na^+ (0.27 mol/L), Li^+ (0.27 mol/L), and Ca^{2+} (0.14 mol/L). The ions are ordered following the Hofmeister series (Fig. 6.4). Concentrations are chosen so as the amount of counter ion is the same in all the gels. Error bars correspond to the average standard deviation associated with 3 independent measurements conducted over 10 minutes each. The red stripe highlights the errors bars for the reference sample.

gels is still unknown. Therefore, I have studied the impact of polysaccharides on both the mechanical/structural properties and the drying kinetics of agarose gels, at a much lower amount than previously reported in the literature (0.5% wt. or lower).

We consider the addition of the following (poly)saccharides: glucose (CAS 50-99-7, Roquette), dextran from *Leuconostoc mesenteroides* (CAS 9004-54-0, Sigma Aldrich), guar gum (CAS 9000-30-0, ref. G4129 Sigma-Aldrich), and xanthan gum (CAS 11138-66-2, ref. G1253 Sigma-Aldrich), which properties are summarized in Table 6.2. Agarose gels with minute amounts of additives are prepared as follows: hot solutions are prepared by mixing 1% wt. agarose powder (or 1.5% wt. agar-BM1 for the agarose gel with agaropectin) with milli-Q water (17 M Ω .cm at 25 $^\circ\text{C}$) brought to a boil, before adding the saccharides. The temperature is maintained constant at 100 $^\circ\text{C}$ for about 10 mins (20 mins or more for hot agar solutions loaded with guar or xanthan gum of lower solubility in water) then decreased to 80 $^\circ\text{C}$. The agar(ose)-based solution is prepared anew for each series of experiment to prevent any oxidation of the agarose molecules (Whyte et al., 1984; Mao et al., 2016).

Additives	Formula	Average M_w (kDa)
Glucose	$\text{C}_6\text{H}_{12}\text{O}_6$	0.18
Dextran	$\text{H}(\text{C}_6\text{H}_{10}\text{O}_5)_x\text{OH}$	40
<i>Agaropectin</i>	-	120 ± 30
Guar Gum (polydisperse)	-	~ 220
Xanthan Gum	-	> 1000

Table 6.2: Properties of the saccharides loaded in agarose gels. Note that agaropectin is naturally present in the agar powder (with a mass fraction of about 30%). To determine its average molecular weight, the agaropectin molecules were first separated from the agarose ones following the method described in ref (Hjerten, 1962) and a diluted agaropectin solution was further analyzed using size exclusion chromatography (Mitsuiki et al., 1999).

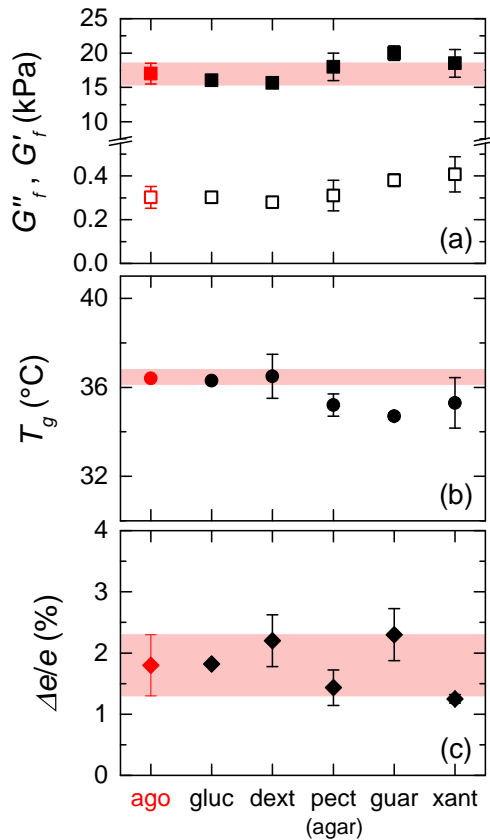


Figure 6.11: (a) Terminal viscoelastic moduli G'_r, G''_r (b) Gelation temperature T_g as determined by the crossover of G' and G'' during the sol/gel transition and (c) Relative contraction $\Delta e/e$ of the sample during the sol/gel transition for various 1 % wt. agarose gels: the red symbol stands for the reference agarose gel without any additive (“ago”) and the black symbols for agarose gels loaded with 0.43% wt. of various non-gelling saccharides: glucose (“gluc”), dextran (“dext”), agaropectin (“pect”), guar gum (“guar”) and xanthan gum (“xant”). Error bars correspond to the dispersion of the results obtained by repeating the experiments on 3 to 5 different samples. The red stripe highlights the errors bars for the reference sample without any additive.

6.3.1 Impact on gelation and gel debonding

The linear viscoelastic properties of 1% wt. agarose gels loaded with 0.43% wt. of the various saccharides listed above are determined by rheology. A typical experiment goes as follows: the agarose solution is loaded in a parallel-plate geometry coated with smooth plastic (PS) surfaces (initial gap width $e_0 = 500 \mu\text{m}$). The gelation is triggered by decreasing the temperature from 50°C down to 20°C with a cooling rate of $1^\circ\text{C}/\text{min}$ and monitored by SAOS using the zero normal force and the strain-adapted protocols (see Section 2.3.1 and Section 2.4.1 in Chapter 2 for more technical details). The results are summarized in Figure 6.11. The addition of saccharides weakly influences the viscoelastic properties of the 1% wt. agarose gel [Fig. 6.11(a)] and both the gelation temperature T_g and the sample contraction associated with the sol/gel transition are insensitive to the presence of the non-gelling (poly)saccharides [Fig. 6.11(b) and (c)]. Such results clearly demonstrate that the addition of (poly)saccharides in that low concentration range ($< 0.5\%$ wt.) does not modify the linear mechanical properties of a 1% wt. agarose gel.

Strain sweep experiments were further performed to quantify the influence of non-gelling saccharides on the adhesion properties of the 1% wt. agarose gel to the smooth plastic (PS) plates. Shear strain oscillations (1 Hz) of increasing amplitude from $\gamma = 0.01\%$ to 100% are imposed to the gels with additives to measure the critical shear stress σ_c associated with the gel debonding from the plastic plate. The results pictured in Figure 6.12 show that the addition of non-gelling saccharides of small or intermediate molecular weights such as glucose ($M_w = 0.18 \text{ kDa}$) and dextran ($\overline{M}_w = 40 \text{ kDa}$) has no effect on the adhesive properties of the agarose gel in contact with a smooth plastic (PS) plate. However, the 1 % wt. agarose gels loaded with non-gelling saccharides of larger molecular weight such as agaropectin, guar or xanthan gum ($\overline{M}_w > 100 \text{ kDa}$) show a much

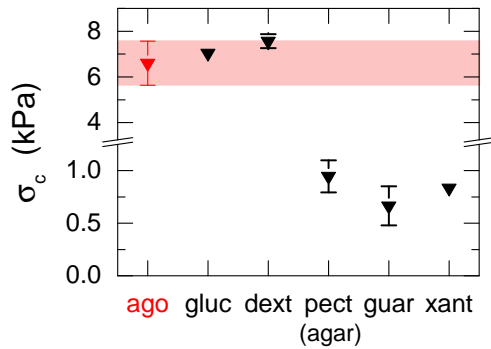


Figure 6.12: Critical shear stress σ_c for the debonding of a 1% wt. agarose gel from a plastic (PS) surface. The red symbol stands for the reference agarose gel without any additive (“ago”) and the black symbols for agarose gels loaded with 0.43% wt. of various non-gelling saccharides: glucose (“gluc”), dextran (“dext”), agaropectin (“pect”), guar gum (“guar”) and xanthan gum (“xant”). Error bars correspond to the dispersion of the results obtained by repeating the experiments on 3 to 5 different samples. The red stripe highlights the errors bars for the reference sample without any additive.

lower debonding stress. The latter result is consistent with that reported earlier in the manuscript on a 1.5% wt. agar-BM1 gel, which shows lower values for the critical shear stain γ_c and stress σ_c compared to a 1% wt. agarose gel (Fig. 6.1 in Section 6.1).

6.3.2 Impact on the drying kinetics of agarose gels

To push further the study of the impact of non-gelling saccharides on the water-holding capacity of agarose gels, I have repeated the same drying experiments as reported in Figure 6.3(a) in Section 6.1, on agarose gels of various concentrations and loaded with 0.43% wt. of glucose. The value of 0.43% wt. is chosen such that the ratio saccharide/agarose is identical to the ratio agaropectin/agarose of about 3/7 in agar-BM1

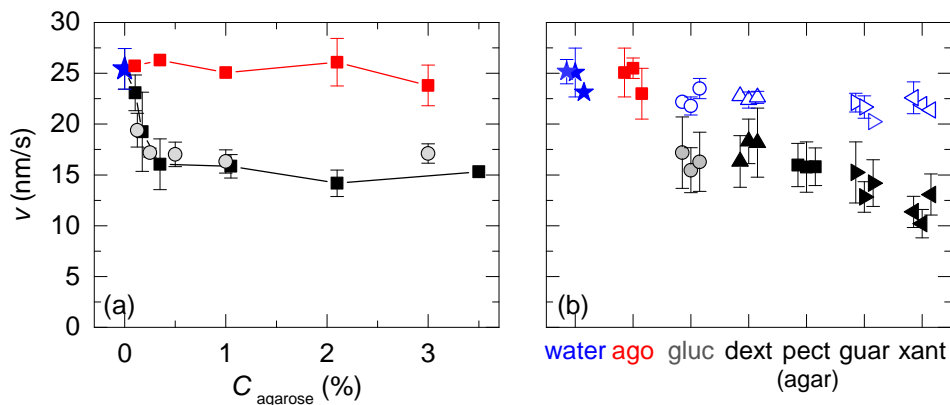


Figure 6.13: (a) Thinning rate v determined at the center of plastic (PS) dishes for agarose gels (■), agar-BM1 gels (■) and agarose gels loaded with 0.43% wt. glucose (●), vs. the gel concentration in agarose. The amount of loaded saccharides (0.43% wt.) is chosen so that the saccharide/agarose ratio in all samples is identical to the agaropectin/agarose ratio of about 3/7 in the agar-BM1 sample. The blue star (★) denotes the thinning rate of a water pool with the same volume as the agar(ose) gels and monitored in the exact same experimental condition. (b) Average thinning rate v of a reference 1% wt. agarose gel (“ago” ■) and 1% wt. agarose gels loaded with 0.43% wt. of one of the following non-gelling saccharides: glucose (“gluc”, ●), dextran (“dext”, ▲), agaropectin (“pect”, ■), guar gum (“guar”, ►) or xanthan gum (“xant”, ◄). Note that the agaropectin-loaded gel was prepared with agar-BM1 without mixing agaropectin and agarose. Finally, the blue open symbols (○, △, ▽, ◁) stand for measurements performed on the aqueous solution of the corresponding saccharide, at the same concentration and without any agarose. Data are missing for agaropectin, which is not commercially available as a pure product. Three independent experiments were performed on gels prepared anew. Error bars correspond to the standard deviation of the average thinning rate over the duration of the experiment (10 minutes). Experiments conducted at $T = (25.0 \pm 0.5)^\circ\text{C}$ in smooth plastic (PS) dishes.

samples. The results pictured in Figure 6.13 show that the agarose gels loaded with glucose (●) display the same thinning rates as that loaded with agaropectin (■). Such a nice observation proves that the water-holding capacity of agarose gels loaded with non-gelling saccharides is not sensitive to the molecular weight of the saccharide, but only depends on the amount of saccharides added to the agarose sample.

Fixing the agarose concentration to 1% wt., I have quantified the thinning rate of agarose gels loaded with 0.43% wt. glucose, dextran, guar gum or xanthan gum [Fig. 6.13(b)]. Interestingly, the presence of non-gelling saccharides systematically lowers the thinning rate of the 1% wt. agarose gel, and the drop is poorly sensitive to the molecular weight of the non-gelling additive. This result shows that, even in minute amounts, non-gelling saccharides act as water-binding sites that efficiently slow down water evaporation and delay the shrinkage of agarose gels submitted to drying. Finally, as a last experimental confirmation I have performed a series of drying experiments on aqueous solutions of the same non-gelling saccharides, i.e. without any agarose, and at the same concentration (0.43% wt.). Data reported as blue open symbols in Figure 6.13 show that the saccharides in solution slightly decrease the thinning rate of water [(★) in Fig. 6.13], but far less than when the saccharides are embedded (at the same concentration) in an agarose gel [filled symbols in fig. 6.13(b)]. Therefore the water-holding capacity of non-gelling saccharides is strongly enhanced when embedded in an agarose gel matrix displaying an arrested dynamics.

6.3.3 Impact on agarose gel microstructure

The microstructure of 1% wt. agarose gels loaded with different non-gelling saccharides was characterized through Cryo-SEM observations (see Section 2.2.1 in Chapter 2 for technical details). Representative results are pictured in Fig. 6.14. Agarose gels loaded with glucose, dextran and guar gum display a coarser microstructure than that of the 1% wt. agarose gels and the 1.5% agar-BM1 gels (equivalent to 1% agarose content). Such

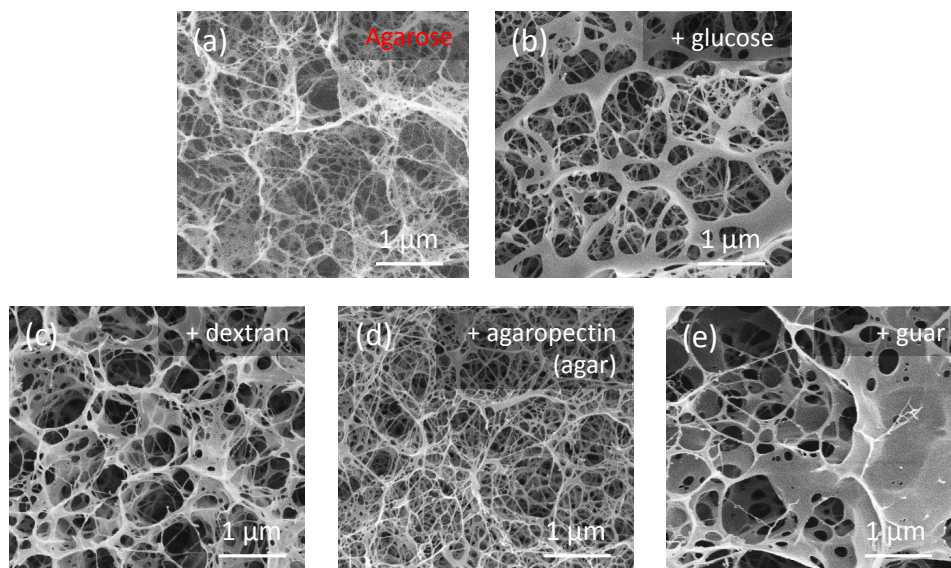


Figure 6.14: Cryo-SEM images of 1% wt. agarose gels: pure agarose (a) or loaded with non-gelling saccharides of different molecular weights: Glucose – $M_w = 0.18$ kDa (b), Dextran – $\overline{M_w} = 40$ kDa (c), Agaropectin (agar) – $\overline{M_w} \approx 120$ kDa (d) and Guar – $\overline{M_w} \approx 220$ kDa (e). See Section 2.2.1 in Chapter 2 for the technical details concerning the sample preparation for SEM.

structural differences do not appear significant enough to affect the linear elastic properties of the gels, which are compatible within error bars [see Fig. 6.11(a)]

6.4 Effect of surfactants on gel debonding

The final section of the present chapter is dedicated to surfactants, another class of additives commonly encountered in culture media to adjust the gel performance. Two different surfactants have been studied: Tween 80 (CAS 9005-65-6, Sigma Aldrich), which is a non-ionic surfactant and lecithin (CAS 8002-43-5, Sigma Aldrich), which is an ionic surfactant. The critical micellar concentration (CMC) of Tween 80 in water is about 1.3% wt.–1.5% wt. (Harris & Angal, 1989) while lecithin is insoluble in water and can be only dispersed at very small concentrations because of a strong liability for self-assembling into aggregates (Shchipunov, 2002).

Both surfactants are found in minute amounts in commercial culture media with a usual quantity of about 0.5% wt. for Tween 80 and 0.01% wt. for Lecithin. To investigate their impact on the properties of agar gels, hot agar solutions are prepared by mixing agar-BM1 powder with milli-Q water (17 M Ω .cm at 25°C) brought to a boil for 10 min before adding the surfactant. Aside the aging of agar solutions (Whyte et al., 1984; Mao, Bentaleb, Louerat, Divoux, & Snabre, 2017), high temperatures also promote an auto-oxidative degradation of Tween 80. Moreover, lecithin molecules can interact with agar polymers and precipitate within a few hours. Therefore, agar solutions loaded with surfactants cannot be kept for long and are prepared anew prior to each experiment.

Additives	Class	Name	Formula	HLB
Tween 80	non-ionic	Polysorbate 80	C ₆₄ H ₁₂₄ O ₂₆	15
Lecithin	ionic	L- α -Phosphatidylcholine	C ₃₅ H ₆₆ NO ₇ P	4

Table 6.3: Class, formula and Hydrophile-Lipophile Balance (HLB)⁴ of surfactant additives added to the 1.5% wt. agar-BM1 gel.

The first series of experiments concerns the gelation dynamics of a 1.5% wt. agar-BM1 gel. The hot and liquid sample is loaded in a pre-heated parallel-plate geometry. The gelation is induced by decreasing the temperature from 50°C to 20°C at a cooling rate of 1°C/min, and monitored following the zero normal force protocol (see Section 2.3.1 in Chapter 2 for more technical details). In the absence of any surfactant, the gelation occurs at $T_g \approx 35.5^\circ\text{C}$ and the storage modulus reaches a terminal value $G'_f \approx 21$ kPa [Fig. 6.15(a)], as already reported in Chapter 3. In the presence of 0.5% wt. Tween 80, the gelation occurs at a similar temperature, but G' experiences a premature drop to reach a much smaller terminal value $G'_f < 1$ kPa [Fig. 6.15(b)]. In the presence of a 0.5% wt. lecithin, the storage modulus G' of the lecithin-loaded agar gel exhibits an even more complex temporal evolution: well after the gelation point, G' drops towards an intermediate plateau value before slowly re-increasing during one hour to reach a value of about 20 kPa [Fig. 6.15(c)].

Paradoxically enough, the 1.5% wt. agar gel loaded with 0.5% wt. of Tween 80 is qualitatively not much softer than the same agar gel without surfactant and seems as

⁴HLB (Hydrophile–Lipophile Balance) is an empirical expression for the relationship of the hydrophilic and hydrophobic groups of a surfactant. The higher the HLB value, the more hydrophilic the surfactant is.

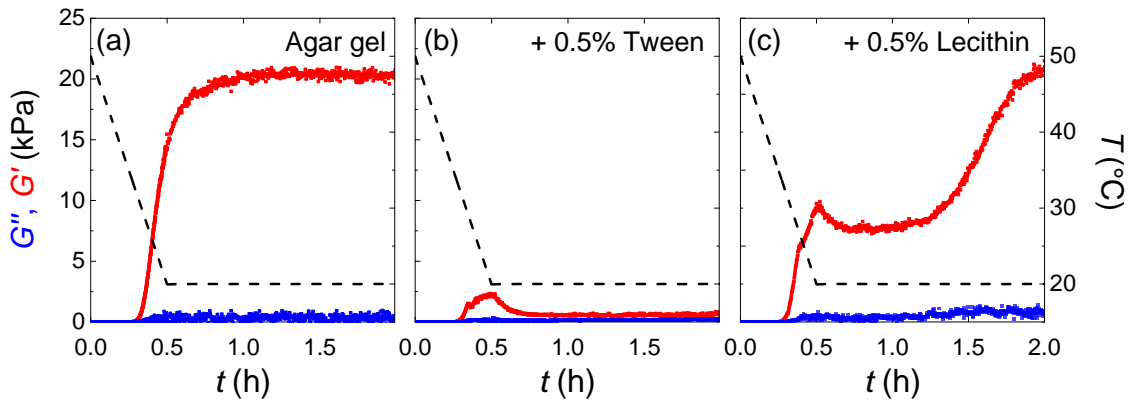


Figure 6.15: Temporal evolution of the storage G' and loss moduli G'' during the gelation of 1.5% wt. agar-BM1 gels: (a) without surfactant, (b) with 0.5% wt. of Tween 80 (b) and (c) with 0.5% wt. lecithin. The gelation is induced by decreasing the temperature from $T = 50^\circ\text{C}$ to 20°C at a cooling rate $\dot{T} = 1^\circ\text{C}/\text{min}$ under zero controlled normal force. Strain amplitude $\gamma = 0.01\%$ and oscillation frequency $f = 1$ Hz.

elastic when probed with the finger, after rising the upper plate. Moreover, the Tween-loaded agar gel displays a microstructure that is extremely similar to that of the agar gel prepared without any additive [compare Fig. 6.16(a) and (b)], which strongly suggests that the presence of Tween 80 only weakly impacts the formation and the microstructure of the agar gel. The low value of the storage modulus G' measured during gelation is most likely due to the gel debonding from the plates of the geometry. Indeed, a hydrophilic surfactant such as Tween 80 (HLB of about 15) usually used for oil-in-water emulsions is likely absorbed both on the agarose molecules and the plastic surfaces, promoting the formation of water films during the agar gelation and preventing the adhesion of the gel with the solid substrate. Such a phenomenon appears as less pronounced for an agar gel loaded with a surfactant of lower HLB such as lecithin since the storage modulus slowly increases toward the expected terminal value $G' \approx 20$ kPa for a gel without any additive. In that framework, the complex evolution of the storage modulus G' reported in Fig. 6.15(c) could be interpreted as a partial debonding (first drop and plateau of G') followed by the slow re-attachment of the agar gel to the plastic plate. The self-assembling of the lecithin molecules in water and the weak adsorption of the hydrophilic aggregates on the plastic surfaces could account for the slow temporal evolution of the adhesive contact after agar

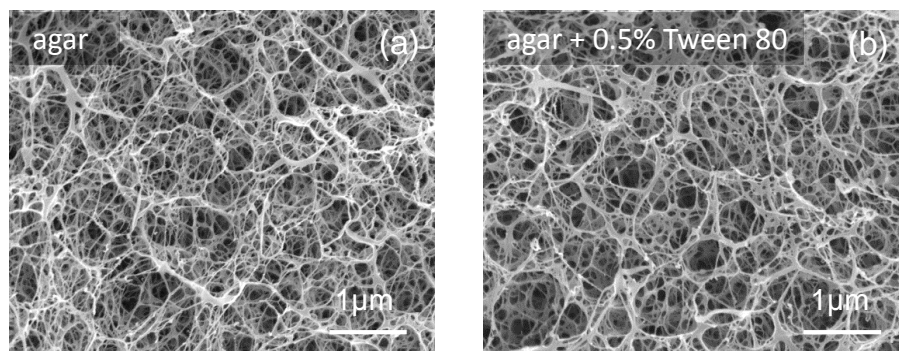


Figure 6.16: Cryo-SEM images of 1.5% wt. agar-BM1 gel without any additive (a), and loaded with 0.5% wt. Tween 80 (b). See Section 2.2.1 in Chapter 2 for the technical details concerning the sample preparation for SEM.

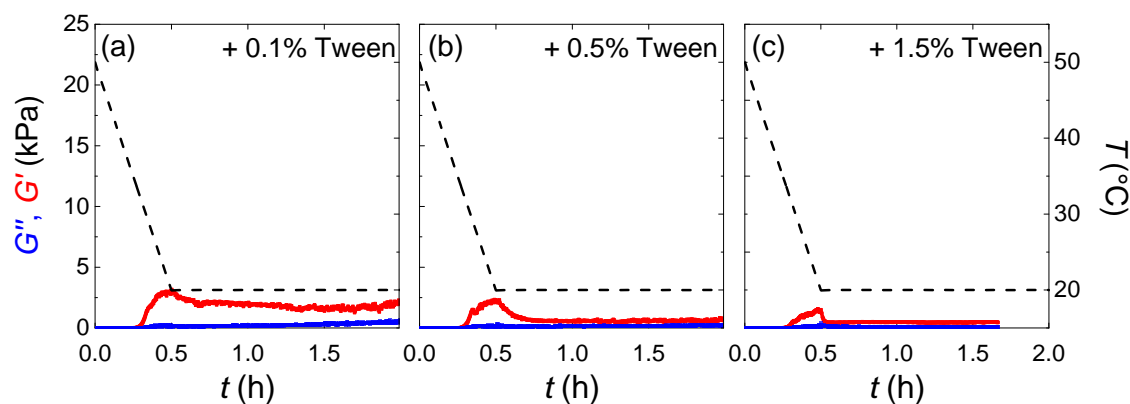


Figure 6.17: Temporal evolution of the storage and loss moduli G' , G'' during the gelation of 1.5% wt. agar-BM1 solutions loaded with Tween 80 at 0.1% wt. (a), 0.5% wt. (b) and 1.5% wt. (c). The gelation is induced by decreasing the temperature from $T = 50^\circ\text{C}$ to 20°C at a cooling rate $\dot{T} = 1^\circ\text{C}/\text{min}$ under the normal force controlled protocol. Strain amplitude $\gamma = 0.01\%$ and oscillation frequency $f = 1$ Hz.

gelation.

I performed a last series of experiments to confirm the impact of Tween 80 on the debonding of agar gels. For this purpose, I repeated the same gelation experiments of 1.5% wt. agar-BM1 solutions loaded this time with both lower or higher concentrations of Tween 80 ranging between 0.1% wt. and 1.5% wt. (Fig. 6.17). In fact, adding amounts of Tween 80 as low as 0.1% wt. is sufficient to induce the rapid debonding of the gel from the plates during the gelation of the sample [Fig. 6.17(a)]. As a consequence, the gel adhesion to a plastic surface is strongly affected by traces of Tween 80, which helps understanding why the Tween-loaded culture media are so sensitive to debonding issues. The issue of surrogate surfactants with a lower HLB might help preventing the gel debonding. However, the addition of Tween 80 to agar gels is essential as it promotes the growth of bacteria in some culture media (Huot, Barrena-Gonzalez, & Petitdemange, 1996) and is mandatory by European Regulation.

6.5 Discussion and conclusion

I have investigated the effect of additives (ions, saccharides and surfactants) on the gelation dynamics, the microstructure, the adhesive properties and the thinning rate of agar(ose) gels in contact with plastic surfaces. Among a wide variety of salts, the “Kosmotropic” anions of the Hofmeister series, e.g. sulfate, favor the gelation of agar solution, which occurs at a higher temperature, whereas the opposite effect is observed for “Chaotropic” anions, e.g. iodide. Within the range of concentrations explored ($< 3\%$ wt.), ions have no significant influence on the gels: neither upon the linear terminal viscoelastic properties, nor on the drying kinetics of the gels. However, anions noticeably strengthen the adhesion between agar gels and plastic (PS) surfaces, which is of key practical interest for biomedical applications. The adhesion between agar gels and plastic surfaces increases with the salt concentration, and markedly depends on the nature of the anion species, while cations have little or no influence on the strength of the adhesive contact. Here again, “Kosmotropic” anions better enhance the adhesion properties of agar gels. Such an effect likely results from ion mediated interactions in aqueous media between the polymers and solid surfaces, although a molecular interpretation is still lacking. In such a context,

the stronger adhesion of agar-BM2 gels compared to agar-BM1 gels reported earlier in the manuscript (see Figure 4.16 in Section 4.3.4, Chapter 4), can be interpreted as a direct consequence of the larger amount of sulfate anions present in agar-BM2 (0.1% wt. of SO_4^{2-} in agar-BM2 vs. 0.06% wt. of SO_4^{2-} in agar-BM1, see Table 2.1 in Chapter 2). Moreover, another agar batch called agar-BM3, even richer in sulfate ions (1.6% wt. of SO_4^{2-} in agar-BM3, see Table 2.1) does not show any long-term detachment, whatever the agar-BM3 concentration and even if cast in smooth glass dishes. In comparison, gel debonding from the lateral wall of the glass dish inevitably occurs during the drying of agar plates made of agar-BM1 or agar-BM2 gels (confidential results). Therefore, the addition of “kosmotropic” ions, e.g. sulfate or phosphate, represents a powerful way to improve the performance of commercial agar-based media.

I have shown also that the addition of minute amounts ($< 0.5\%$ wt.) of non-gelling saccharides to agarose gels only impacts the adhesion properties of the latter for macromolecular additives of large enough molecular weight (> 100 kDa). As a consequence, agaropectin molecules of molecular weight $\overline{M}_w \approx 120$ kDa and present in commercial agar brands are also responsible for lowering the adhesive properties of agar gels. Nonetheless, the addition of minute amounts of non-gelling saccharides to agar gels can be beneficial as it increases the water-holding capacity of the gel, reducing its thinning rate by a factor of two for additive concentrations in the range of 1% wt. to 3% wt. and therefore delaying a possible detachment of the gel plate from the dish. Finally, the addition of surfactants is harmful to the adhesion properties of agar gels in plastic dishes as the adsorption of surfactant molecules on both agarose and solid surfaces may favor the formation of water films at the gel/plastic interface during gelation.

Chapter 7

Conclusion and outlooks

Historically, bioMérieux came to us through Abel Couhert and François Villeval with two specific questions related to the manufacturing and commercial use of agar-based gels for the detection and growth of microorganisms. The first issue was related to the fact that agar gels are subject to water-loss during the manufacturing process, or while being sent to clients. The questions were the following ones: *“How can we prevent the water from being spontaneously released from the gels? Is it linked to the manufacturing process (physics) or to the gel formulation (chemistry)?”*. The second issue was related to the shrinkage and detachment of the gel from the sidewall of the Petri dish, which takes place as the gel is being incubated at constant temperature by the customers and invalidates the test. The question was the following one: *“Can you identify the reason why some gels shrink more than others, and propose a solution to prevent the gels from shrinking?”* My PhD work demonstrates that the techniques and methods described in Chapter 2 namely rheology, interferometry, electron microscopy, a centrifuge technique using a modified spin-coater and the optical flow analysis can bring valuable answers to the aforementioned issues.

Agar gels turned out to be much more delicate to handle and manipulate than I would have expected. Their high deformability and their weak adhesion to solid surfaces coupled to a strong propensity to release water under any external perturbation make most of the measurements very delicate and/or poorly reproducible. Moreover, the contraction of agar samples –and more generally of polysaccharides– at the sol-gel transition also contributes to the challenge of performing high-precision rheological measurements on these gels. In a geometry of constant gap width, the gel contraction is sufficient to either induce the strain hardening of the gel or debond the gel from the plates. I have shown in Chapter 2 that Normal Force Controlled (NFC) rheology is ideally suited to monitor the sol/gel transition of agar gels: the change in the gap width of the geometry compensates in real time for the gel contraction, preventing any artifact while monitoring the gelation. The results obtained with the NFC rheology during my PhD pave the way for a more systematic use of the NFC protocol to study the rheology of non-isochoric phenomena, such as solidification and other phase transitions.

The combined use of the techniques listed above has allowed me to perform a series of benchmark experiments on the gelation of agar gels of the same concentration as the one used to manufacture growth culture media. I have shown in Chapter 3 that the mechanical properties of an agar gel strongly depend upon the time during which the corresponding agar solution is maintained above the gelation temperature. The agarose molecules of an agar solution stored at 80°C experience hydrolysis and intermolecular oxidation after less than a day of incubation. Over longer incubation times, the intermolecular oxidation of agarose molecules further promotes the clustering of the polymers in the sol, leading to the

formation of gels with a coarser microstructure, weaker mechanical properties, and a more ductile behavior. These results, which quantitatively extend the pioneering observations of (Whyte et al., 1984) could serve in the future as a way to tune the mechanical properties of agar-based gels and as a guideline for the design of efficient manufacturing processes of agar-based materials.

In the second part of Chapter 3, I have further applied the NFC rheology to determine the impact of the cooling process of a fresh agar solution on the resulting gel. Surprisingly, the cooling rate does not affect the properties of a gel formed by cooling down a 1.5% wt. agar solution. The viscoelastic properties of the gel are mostly controlled by the terminal temperature at the end of the cooling process, and remain insensitive to a pause during the cooling process. Such a simple and striking result suggests that the gelation of 1.5% wt. agar solution is mainly controlled by a rapid spinodal demixing (Manno et al., 1999). On the contrary, agar sols of agarose concentration larger than 2% wt. are more sensitive to the thermal history, which is probably linked to a gelation scenario involving a competition between a spinodal demixing and a direct gelation (San Biagio et al., 1996). Such results provide a powerful guideline for the manufacturing of culture media in Petri dishes. Indeed, the agar-based sol is poured hot in the Petri dishes moving on a conveyor belt. The dishes are then cooled down at about 2 to 3°C/min by crossing a tunnel inside which both temperature and humidity are controlled. Such a cooling rate is an upper limit, as larger values might lead to a larger contraction of the gel (and possible larger water release) which could promote a faster detachment of the gel from the sidewall of the dish, rendering the culture media unusable. As a matter of fact, the cooling rate of commercial culture media was recently reduced on the production lines in bioMérieux for better performance and longer product life time.

The combined use of traditional rheology and of a modified spinner centrifuge has allowed for a better understanding of the adhesion properties of agar gels in contact with various solid substrates, as reported in Chapter 4. Both methods provide a way for a precise measurement of the critical shear stress associated with the first debonding of an agar gel from a solid surface, in contact of which the gel has been formed. The first debonding of the gel from a solid surface is independent of the chemical nature of the solid surface and mainly controlled by the RMS roughness of the substrate. Actually, the gel adhesion after cooling is strongly linked to the gel contraction that takes place during the sol/gel transition. This sample contraction leads to the formation of intercalated water films when the gelation occurs on a smooth solid surface, which strongly weakens the adhesion. Only the surface imperfections (increase of the surface roughness) allow a dewetting of the metastable water films and the growth of adhesive bridges. When the surface RMS roughness is larger than 20 nm (a characteristic length interpreted as the typical thickness of liquid films), the texture of the random solid surface no longer influences the gel adhesion. Apart from the surface roughness, the gel contraction during the sol/gel transition is another key parameter to control the adhesion of agar gels right after gelation. Increasing either the agar concentration or the cooling rate results in a larger contraction of the sample during the gelation, which promotes the formation of water films at the gel/substrate interface, thus weakening the gel adhesion to the solid substrate. A slow cooling process of the agar solution (about 1°C/min) leads to a smaller contraction and favors both a better adhesion of the gel to the dish and a reduced water-release from the agar-based culture medium. Interestingly, the original centrifuge method also gives the opportunity to determine with a high accuracy the second debonding stress of a gel, i.e. the stress for debonding a gel replaced in contact with the same solid surface after having been debonded a first time. The second debonding stress increases linearly

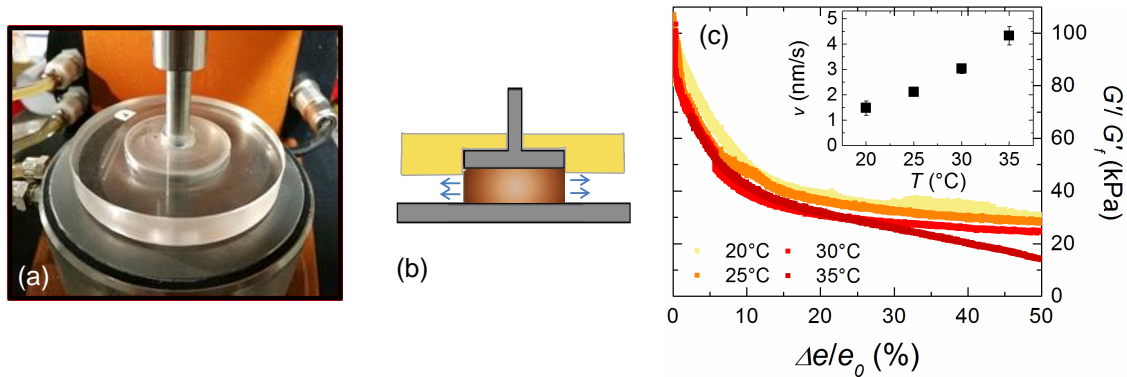


Figure 7.1: (a) View and (b) sketch of the “doughnut”-like geometry used to monitor the slow and uniform drying of an agar gel prepared in a parallel-plate geometry of 40 mm diameter. (c) Evolution of the storage modulus G'/G'_f , normalized by the initial value G'_f , of 1.5% wt. agar-BM2 gels drying at constant temperatures T vs. the relative decrease of the gap width $\Delta e/e_0$ (each color from light yellow to brown corresponds to a constant drying temperature: $T = 20^\circ\text{C}$, 25°C , 30°C and $T = 35^\circ\text{C}$). The gap width e decreases linearly with the drying time t over the whole duration of the experiment and the inset shows the average thinning rate v of the gel as a function of the drying temperature T . SAOS experiments performed with the normal force controlled protocol, an initial gap $e_0 = 500 \mu\text{m}$, a strain amplitude $\gamma = 0.01\%$ and a frequency of 1 Hz.

with the agar concentration and presents lower values than that of the first debonding as a result of the mismatch between the roughness of the gel bottom surface and that of the solid surface. Such a linear concentration dependence of the second debonding stress suggests the removal of water films during the sliding of the gel. An elasto-hydrodynamic effect very recently introduced by Hutt and Persson (Hutt & Persson, 2016) may reasonably account for the rapid removal of the intercalated liquid films when a soft material slides onto a rough solid surface. Finally, the adhesion of the gel increases logarithmically from the moment the gel is put back in contact with the solid surface. Such an effect is even more pronounced for a rough substrate which provides larger channels for draining the water from the gel/substrate interface. A similar slow logarithmic increase of the stress for first gel debonding is also observed after agar gelation. The slow diffusion of interfacial water films through the porous network may reasonably account for the slow increase in the gel adhesion to the solid surface over several hours.

In commercial agar plates, the weak adhesion of agar gels to solid surfaces is often coupled to the loss of water by evaporation. In such a context, the drying dynamics of agar gels cast in circular dishes was investigated in Chapter 5 using a spatio-temporal method to analyse the motion of the gel free surface and detect the precursors of the long term gel detachment, together with interferometric observations to measure the vertical thinning rate of the gel. The surface roughness of the dish wall was shown to play a key role during the drying of the gel: a smooth sidewall allows an homogeneous slip of the gel along the sidewall of the dish and a pure vertical thinning of the gel, whereas a rough sidewall provides a higher adhesion, inhibits any slip of the gel along the sidewall and leads inevitably to the formation of a circular fracture along the edge of the dish. The plastic material used by the bioMérieux company for the commercial Petri dishes displays a moderate roughness of about 10 nm, which allows for the gel to stick and slip along the sidewall, and yet suppresses the gel sliding on the bottom of the dish, which efficiently prevents the long-term detachment of the gel. However, the detachment is still widely observed in some types of commercial plates, which is most likely due to the presence of additives such as surfactant. Interferometric observations further confirm the

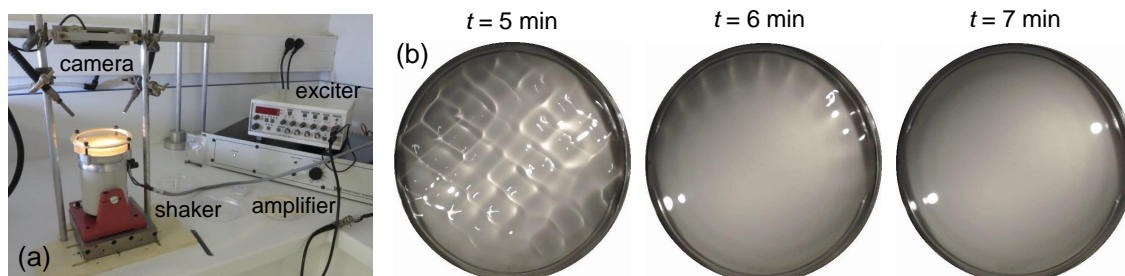


Figure 7.2: (a) View of the shaker (LDS V101, Bruel & Kjaer) coupled to an exciter/amplifier system used to excite Faraday waves at the free surface of a hot 1.5% wt. agar-BM3 solution during cooling to an ambient temperature. (b) Pictures of the upper free surface of the dish during the cooling of the agar solution from 70°C (time $t = 0$) down to 25°C over a duration of about 11 min. Experiments conducted with a vibration frequency of 40 Hz and an acceleration of 2.5 g.

purely vertical thinning of agar gels drying in a smooth plastic dish and provides a key observable to quantify the influence of additives on the drying kinetics of agar(ose) gels.

At this point, we are still missing time-resolved measurements of the gel mechanical properties during the drying process. In a series of preliminary experiments, I have extended the use of the NFC protocol to perform time-resolved monitoring of the linear viscoelastic properties of a gel left to dry at constant temperature. The upper plate of the parallel-plate geometry described in Chapter 2 is topped with a “doughnut-like” lid to ensure a slow and uniform drying of the agar gel along the radial direction [Fig. 7.1(a) and (b)]. As water evaporates, the gap width decreases and an unexpected decrease of the storage modulus of the gel is systematically observed whatever the drying temperature in the range from 20°C to 35°C [Fig. 7.1(c)]. As soon as the water-loss exceeds 5%, the storage modulus G' is divided by a factor of 2 [Fig. 7.1(c)]. Such a surprising result is robust and indeed remains true for various agar concentrations ranging from 0.5% to 3% wt. (Mao, Bouchaudy, Salmon, Divoux, & Snabre, 2017). These changes in the mechanical properties of agar gels under drying are consistent with results obtained from indentation experiments or cryo-SEM observations showing the formation of cellular-like structures after some water evaporation and further highlight the out-of-equilibrium character of the hydrogel microstructure, which is extremely sensitive to any external perturbation. Such preliminary results open new exciting perspectives and constitute another avenue for research.

In Chapter 6, I have investigated the role of various key additives (salts, saccharides and surfactants) commonly present in minute amounts in growth culture media, on the agar(ose) gel properties. The addition of “Kosmotropic” anions of the Hofmeister series favors the gel formation by increasing the gelation temperature by almost 5°C, whereas “Chaotropic” anions delay the gelation by more than 5°C. Within the range of salt concentrations explored ($c < 3\%$ wt.), these ions neither influence the viscoelastic properties of the gel nor the thinning rate of agar gel during drying. Yet, anions markedly strengthen the adhesion of agar gels on plastic (PS) surfaces, which is of key practical interest for biomedical applications. Here again, “Kosmotropic” anions such as sulfate better enhance the adhesion properties of agar gels. The stronger adhesion of some specific agar batches to plastic surfaces, especially agar-BM3, is due to a larger content in sulfate. The addition of sulfate (or potassium or chloride) during the gel preparation thus provides a simple and powerful way to increase the gel adhesion to the plastic dish and to delay any long term detachment, even if the gel is cast in a smooth glass dish, as exemplified by agar-BM3 gels which contains about 16 mg/g of sulfate (instead of 0.6 mg/g in agar-BM1).

Another way of delaying the detachment of the gel from the walls of the dish is to increase the water-holding capacity of the gel without weakening the gel adhesion to the solid surface. Minute amounts of non-gelling saccharides ($< 0.5\%$ wt.) added to agar(ose) gels reduce the thinning rate of gels by a factor of 2 for saccharide concentrations in the range from 1% wt. to 3% wt., which delays the detachment of the gel from the sidewall of the dish. Interestingly, the addition of non-gelling saccharides only impacts the gel adhesion properties for saccharides of large enough molecular weight ($\overline{M}_w > 100$ kDa). As a consequence, agaropectin molecules ($\overline{M}_w \approx 120$ kDa) present in commercial agar plates are partially responsible for the lower adhesion of agar gels to plastic surfaces, compared to agarose gels of the same agarose concentration. Moreover, the addition of hydrophilic surfactants such as Tween 80 with a high HLB is harmful to the adhesion of agar gels in plastic dishes since they favor the formation of intercalated water films during agar gelation.

Of course, the present work leaves many open questions, such as the question of the reversibility of the water-loss in agarose gel, the understanding of the collapse of the gel microstructure when the water evaporates, the lack of reliable values for the Poisson coefficient of agar gels, or the effect of mechanical vibrations on the formation of agar gels. Preliminary experiments, performed on a hot agar solution poured in a dish attached to a shaker [Fig. 7.2(a)] shows a delayed gelation of the peripheral region of the sample, as evidenced by the spatially heterogeneous damping of the Faraday waves visible at the gel free surface, during the gelation. The waves first disappear at the center of the dish during the gelation [Fig. 7.2(b)]. The lower cooling rate of the gel along the periphery of the dish could reduce the gel contraction near the sidewall and induce the formation of liquid films at the gel/wall interface, thus improving the gel adhesion to the sidewall. Such an experimental setup could further be used to test the mechanical resistance of agar gel plates to vibrations and simulate the effects of mechanical disturbances during transport by road of agar-based culture media.

References

- Adelson, E. (1991). Mechanism for motion perception. *Opt. Photonics News*, 24–30.
- Adelson, E. H., & Bergen, J. R. (1985). Spatiotemporal energy models for the perception of motion. *J. Opt. Soc. Am.*, 2, 284–299.
- Adrian, R. (1991). Particle imaging techniques for experimental fluid mechanics. *Annu. Rev. Fluid Mech.*, 23, 261–304.
- Ahmed, J., Guo, H., Yamamoto, T., Kurokawa, T., Takahata, M., Nikajima, T., & Gong, J. P. (2014). Sliding friction of zwitterionic hydrogel and its electrostatic origin. *Macromolecules*, 47, 3101–3107.
- Alvarez, L., Weickert, J., & Sanchez, J. (1981). Reliable estimation of dense optical flow fields with large displacements. *Int. J. Comput. Vision*, 39(1), 41–56.
- Altmann, N., Cooper-White, J. J., Dunstan, D. E., & Stokes, J. R. (2004). Strong through to weak ‘sheared’ gels. *J. Non-Newtonian Fluid Mech.*, 124, 129–136.
- Andrasko, J. (1975). Water in agarose gels studied by nuclear magnetic resonance relaxation in the rotating frame. *Biophys. J.*, 1235–1243.
- Araki, C. (1937). Chemical studies of agar-agar. V. D-galactose and its derivatives. *Nippon Kagaku Kaishi*, 58(12), 1362–1382.
- Araki, C. (1956). Structure of the agarose constituent of agar-agar. *Bull. Chem. Soc. Jpn.*, 29(4), 543–544.
- Araki, C. (1958). Seaweed polysaccharide. *Proc. Fourth Int. Congress Biochem.*, 15–30.
- Armisen, R., & Galatas, F. (1987). Production, properties and use of agar. In D. McHugh (Ed.), (chap. 1). FA.
- Armisen, R., & Galatas, F. (2009). Handbook of hydrocolloids. In G. Phillips & P. Williams (Eds.), (2nd ed., pp. 82–107). Woodhead Publishing.
- Arnott, S., Fulmer, A., & Scott, W. (1974). The agarose double helix and its function in agarose gel structure. *J. Mol. Biol.*, 90, 269–284.
- Ateshian, G. A. (2009). The role of interstitial fluid pressurization in articular cartilage lubrication. *J. Biomech.*, 42(9), 1163–1176.
- Aymard, P., Martin, D. R., Plucknett, K., Foster, T. J., Clark, A. H., & Norton, I. T. (2001). Influence of thermal history on the structural and mechanical properties of agarose gels. *Biopolymers*, 59, 131–144.

- Barham, P., Skibsted, L. H., Bredie, W. L. P., Først, M. B., Møller, P., Risbo, J., ... Mortensen, M. M. (2010). Molecular gastronomy: A new emerging scientific discipline. *Chem. Rev.*, *110*, 2313–2365.
- Barrangou, L., Daubert, C., & Foegeding, E. (2006). Textural properties of agarose gels. 1. rheological and fracture properties. *Food Hydrocolloids*, *20*, 184–195.
- Barron, J. L., Fleet, D. J., & Beauchemin, S. S. (1994). Performance of optical flow techniques. *Int. J. Comput. Vision*, *12*(1), 43–77.
- Bastide, J., Duplessix, R., Picot, C., & Candau, S. (1984). Small-angle neutron scattering and light spectroscopy investigation of polystyrene gels under osmotic deswelling. *Macromolecules*, *17*, 82–93.
- Baumberger, T., Caroli, C., & Martina, D. (2006). Solvent control of crack dynamics in a reversible hydrogel. *Nature Materials*, *5*, 552–555.
- Baumberger, T., Caroli, C., & Ronsin, O. (2003). Self-healing slip pulses and the friction of gelatin gels. *Eur. Phys. J. E*, *11*, 85–93.
- Berthoud, P., Baumberger, T., G'Sell, C., & Hiver, J. M. (1999). Physical analysis of the state- and rate- dependent friction law: Static friction. *Phys. Rev. B*, *59*(22), 14313–14327.
- Bertrand, T., Peixinho, J., Mukhopadhyay, S., & MacMinn, C. (2016). Dynamics of swelling and drying in a spherical gel. *Phys. Rev. Appl*, *6*, 064010.
- Bocquet, L. (2007). Tasting edge effects. *Am. J. Phys*, *75*, 148–150.
- Bonn, D., Denn, M. M., Berthier, L., Divoux, T., & Manneville, S. (2017). Yield stress materials in soft condensed matter. *Rev. Mod. Phys.*, in press.
- Bonn, D., Kellay, H., Prochnow, M., Ben-Djemaa, K., & Meunier, J. (1998). Delayed fracture of an inhomogeneous soft solid. *Science*, *280*, 265–267.
- Bonn, D., Meunier, J., Greffier, O., Al-Kahwaji, A., & Kellay, H. (1998). Bistability in non-newtonian flow: Rheology of lyotropic liquid crystals. *Phys. Rev. E*, *58*, 2215–2218.
- Bowden, F. P., & Tabor, D. (Eds.). (1950). *The friction and lubrication of solids*. Oxford University Press.
- Bracewell, R. N. (1986). *The fast Hartley transform*. New York: Oxford university press.
- Bracewell, R. N., O.Buneman, H.Hao, & J.Villasenor. (1986). Fast two-dimensional Hartley transform. *Proc. IEEE*, *74*, 1282–1283.
- Braudo, E. (1992). Mechanism for galactan gelation. *Food Hydrocolloids*, *6*, 25–43.
- Brenner, T., Nicolai, T., & Johannsson, R. (2009). Rheology of thermo-reversible fish protein isolate gels. *Food Research International*, *42*, 915–924.
- Brigham, J., Gidley, M., Hoffmann, R., & Smith, C. (1994). Microscopic imaging of network strands in agar, carrageenan, locust bean gum and κ -carrageenan/locust bean gum gels. *Food Hydrocolloids*, *8*, 331–344.

- Broedersz, C. P., & MacKintosh, F. C. (2014). Modeling semiflexible polymer networks. *Rev. Mod. Phys.*, *86*, 995–1036.
- Brown, A., Litvinov, R., Discher, D., Purohit, P., & Weise, J. (2009). Multiscale mechanics of fibrin polymer: Gel stretching with protein unfolding and loss of water. *Science*, *325*, 741–744.
- Brzoska, J., Azouz, I. B., & Rondelez, F. (1994). Silanization of solid substrates: a step toward reproducibility. *Langmuir*, *10*, 4367–4373.
- Bureau, L., Baumberger, T., & Caroli, C. (2006). Non-Amontons behavior of friction in single contact. *Eur. Phys. J. E*, *19*, 163–169.
- Callaway, E. (2015). Lab staple agar runs low: Dwindling seaweed harvest imperils reagent essential for culturing microbes. *Nature*, *528*, 171–172.
- Carrillo, J.-M. Y., MacKintosh, F. C., & Dobrynin, A. V. (2013). Nonlinear elasticity: From single chain to networks and gels. *Macromolecules*, *46*, 3679–3692.
- Chambon, F., & Winter, H. (1987). Linear viscoelasticity at the gel point of a crosslinking PDMS with imbalanced stoichiometry. *J. Rheol.*, *31*, 683–697.
- Chaplin, M. F. (2014). Hofmeister series. *Water Structure and Science*. Retrieved from <http://www1.lsbu.ac.uk/water/water-structure-science.html> (London South Bank University)
- Chapman, V. J. (1970). *Seaweed and their uses*. London: Chapman & Hall.
- Charlionet, R., Levasseur, L., & Malandrin, J.-J. (1996). Eliciting macroporosity in polyacrylamide and agarose gels with polyethylene glycol. *Electrophoresis*, *17*, 58–66.
- Chen, Y., Liao, M.-L., Boger, D. V., & Dunstan, D. E. (2001). Rheological characterisation of κ -carrageenan/locust bean gum mixtures. *Carbohydr. Polym.*, *46*(2), 117–124.
- Chui, M., Philips, R., & McCarthy, M. (1995). Measurement of the porous microstructure of hydrogels by nuclear magnetic resonance. *J. Colloid Interface Sci.*, *174*, 336–344.
- Clark, A. H., Richardson, R., Ross-Murphy, S. B., & Stubbs, J. M. (1983). Structural and mechanical properties of agar/gelatin co-gels. small-deformation studies. *Macromolecules*, *16*(8), 1367–1374.
- Clark, A. H., & Ross-Murphy, S. (1987). Structural and mechanical properties of biopolymer gels. *Adv. Polym. Sci.*, *83*, 57–192.
- Clark, A. H., & Ross-Murphy, S. B. (1985). The concentration dependence of biopolymer gel modulus. *British Polymer Journal*, *17*(2), 164–168.
- Cloitre, M., Borrega, R., & Leibler, L. (2000). Rheological aging and rejuvenation in microgel pastes. *Phys. Rev. Lett.*, *85*, 4819–4822.
- Coussot, P., Nguyen, Q. D., Huynh, H. T., & Bonn, D. (2002). Avalanche behavior in yield stress fluids. *Phys. Rev. Lett.*, *88*, 175501.
- Creton, C., & Ciccotti, M. (2016). Fracture and adhesion of soft materials: a review. *Rep. Prog. Phys.*, *79*, 046601.

- Creton, C., Hooker, J., & Shull, K. R. (2001). Bulk and interfacial contributions to the debonding mechanisms of soft adhesives: Extension to large strain. *Langmuir*, *17*, 4948–4954.
- Creton, C., & Leibler, L. (1996). How does tack depend on time of contact and contact pressure? *J. Polym. Sci. Pol. Phys*, *34*(3), 545–554.
- Crosby, A. J., Shull, K. R., Lakrout, H., & Creton, C. (2000). Deformation and failure modes of adhesively bonded elastic layers. *J. Appl. phys*, *85*(5), 2956–2966.
- Dahlquist, C. A. (1969). Treatise on adhesion and adhesives. In R. L. Patrick (Ed.), (Vol. 2, pp. 219–260). Dekker.
- Daniels, K. E., Mukhopadhyay, S., Houseworth, P. J., & Behringer, R. P. (2007). Instabilities in droplets spreading on gels. *Phys. Rev. Lett.*, *99*, 124501.
- Dapp, W. F., Lucke, A., Persson, B. N. J., & Muser, M. H. (2012). Self-affine elastic contact: percolation and leakage. *Phys. Rev. Lett.*, *108*, 244301.
- Davies, E., Hung, Y., Harper, J. B., Hook, J. M., Thomas, D. S., Burgar, I. M., & Lillford, P. J. (2010). Dynamics of water in agar gels studied using low and high resolution ^1H NMR spectroscopy. *Int. J. Food Sci. Technol.*, *45*.
- Dawson, E. Y. (1966). *Marine botany*. New York: Holt, Rinehard and Winston inc. Newyork.
- Dea, I. C. M., McLinnon, A. A., & Rees, D. A. (1972). Tertiary and quaternary structure in aqueous polysaccharide systems which model cell wall cohesion: reversible changes in conformation and association of agarose, carrageenan and galactomannans. *J. Mol. Biol.*, *68*, 153–172.
- Dea, I. C. M., & Rees, D. A. (1987). Affinity interactions between agarose and β -1,4-glycans: a model for polysaccharide associations in algal cell walls. *Carbohydr. Polym.*, *7*, 183–224.
- Deegan, R. D. (2000). Pattern formation in drying drops. *Phys. Rev. E*, *61*(1), 475–485.
- Deegan, R. D., Bakajin, O., Dupont, T. F., Huer, G., Nagel, S. R., & Witten, T. A. (1997). Capillary flow as the cause of ring stains from dried liquid drops. *Nature*, *389*, 526–529.
- De Gennes, P. (1979). *Scaling concepts in polymer physics*. Cornell University Press.
- De Gennes, P., Brochard-Wyart, F., & Quéré, D. (2005). Gouttes, bulles, perles et ondes. In (p. 212-227). Belin.
- Divoux, T., Mao, B., & Snabre, P. (2015). Syneresis and delayed detachment in agar plates. *Soft Matter*, *11*, 3677–3685.
- Dixon, P. T. (1973). *Biology of the rhodophyta* (2nd ed.; Oliver & Boyd, Eds.).
- Djabourov, M., Clark, A. H., Rowlands, D. W., & Ross-Murphy, S. B. (1989). Small-angle x-ray scattering characterization of agarose sols and gels. *Macromolecules*, *22*, 160–180.

- Djabourov, M., Nishinari, K., & Ross-Murphy, S. B. (2013). *Physical gels from biological and synthetic polymers*. Cambridge University Press.
- Duckworth, M., Hong, K. C., & Yaphe, W. (1971). The agar polysaccharides of gracilaria species. *Carbohydr. Res.*, *18*, 1–9.
- Dunn, A. C., Sawyer, W. G., & Angelini, T. E. (2014). Gemini interfaces in aqueous lubrication with hydrogels. *Tribol. Lett.*, *54*, 59–66.
- Ewoldt, R., Johnston, M., & Caretta, L. (2015). Complex fluids in biological systems. In (pp. 207–241). Springer New York.
- Federle, W., Baumgartner, W., & Hölldobler, B. (2004). Biomechanics of ant adhesive pads: frictional forces are rate- and temperature- dependent. *J. Exp. Biol.*, *206*, 67–74.
- Federle, W., Rohoseitz, K., & Hölldobler, B. (2000). Attachment forces of ants measured with a centrifuge: better “wax-runners” have a poorer attachment to a smooth surface. *J. Exp. Biol.*, *203*, 505–512.
- Feke, G., & Prins, W. (1974). Spinodal phase separation in a macromolecular sol-gel transition. *Macromolecules*, *7*, 527–530.
- Flory, P. (1974). Introductory lecture. *Faraday Discuss. Chem. Soc.*, *57*, 7–18.
- Foord, S. A., & Atkins, E. D. T. (1989). New X-ray diffraction results from agarose: Extended single helix structures and implications for gelation mechanism. *Biopolymers*, *28*, 1345–1365.
- Fujii, T., Yano, T., Kumagai, H., & Miyawaki, O. (2000). Scaling analysis of the concentration dependence on elasticity of agarose gel. *Biosci. Biotechnol. Biochem.*, *64*(8), 1618–1622.
- Fuller, K. N. G., & Tabor, D. (1975). The effect of surface roughness on the adhesion of elastic solids. *Proc. R. Soc. A*(345), 327–342.
- Fuse, T., & Goto, F. (1971). Some properties of agarose and agarpectin isolated from various mucilaginous substances of red seaweeds. *Agric. Biol. Chem.*, *35*, 799–804.
- Fuse, T., & Suzuki, T. (1975). Preparation and properties of agar sulfates. *Agric. Biol. Chem.*, *39*, 119–126.
- Gay, C. (2002). Stickiness—some fundamentals of adhesion. *Integr. Comp. Biol.*, *42*, 1123–1126.
- Gibson, J. J. (1950). *The perception of the visual world* (L. Carmichael, Ed.). Boston: The Riverside Press.
- Glicksman, M. (1983). Red seaweed extracts (agar, carrageenan, furcellaran). In M. Glicksman & B. Raton (Eds.), (p. 73–113). CRC Press.
- Gong, J. P. (2006). Friction and lubrication of hydrogels – its richness and complexity. *Soft Matter*, *2*, 544–552.
- Gong, J. P., Higa, M., Iwasaki, Y., Katsuyama, Y., & Osada, Y. (1997). Friction of gels. *J. Phys. Chem. B*, *101*, 5487–5489.

- Gong, J. P., Iwasaki, Y., & Osada, Y. (1999). Friction of gels.3. Friction on solid surfaces. *J. Phys. Chem. B*, *103*, 6001–6006.
- Gong, J. P., Iwasaki, Y., & Osada, Y. (2000). Friction of gels. 5. Negative load dependence of polysaccharide gels. *J. Phys. Chem. B*, *104*, 3423–3428.
- Gong, J. P., & Katsuyama, Y. (2003). Double-network hydrogels with extremely high mechanical strength. *Adv. Mater.*, *15*, 1155–1158.
- Goycoolea, F. M., Richardson, R. K., Morris, E. R., & Gidley, M. J. (1995). Effect of locust bean gum and konjac glucomannan on the conformation and rheology of agarose and κ -carrageenan. *Biopolymers*, *36*, 643–658.
- Grillet, A. M., Wyatt, N. B., & Gloe, L. M. (2012). Polymer gel rheology and adhesion. In J. D. Vicente (Ed.), (p. 59-80). INTECH. (Available from: <http://www.intechopen.com/books/rheology/rheology-and-adhesion-of-polymer-gels>)
- Grindy, S. C., Learsch, R., Mozhdzhi, D., Cheng, J., Barrett, D. G., Guan, Z., ... Holten-Andersen, N. (2015). Control of hierarchical polymer mechanics with bioinspired metal-coordination dynamics. *Nat. Mater.*, *14*, 1210–1217.
- Groot, R. D., Bot, A., & Agterof, W. G. M. (1996). Molecular theory of strain hardening of a polymer gel: Application to gelatin. *The Journal of Chemical Physics*, *104*, 9202–9219.
- Guenet, J.-M., & Rochas, C. (2006). Agarose sols and gels revisited. *Macromol. Symp.*, *242*, 65–70.
- Guisseley, K. (1970). The relationship between methoxyl content and gelling temperature of agarose. *Carbohydr. Res.*, *13*, 247–256.
- Habouzit, D., & Snabre, P. (2010, October). Cocoa butter aging and microstructural changes. In *World food process exhibition*. IPA 2010, Paris.
- Haider, M., & Holmes, M. (1997). A mathematical approximation for the solution of a static indentation tests. *J. Biomechanics*, *7*, 747–751.
- Hands, S., & Peat, S. (1938). Isolation of an anhydro-l-galactose derivative from agar. *Nature*, *142*, 797–798.
- Harris, E. L. V., & Angal, S. (1989). *In protein purification applications: a practical approach* (S. Roe, Ed.). Oxford, New York: Oxford University Press.
- Hayes, W., Keer, L., Herrmann, G., & Mockros, L. (1972). A mathematical analysis for indentation tests of articular cartilage. *J. Biomechanics*, *5*, 541–551.
- Heitz, D., Memin, E., & Schnorr, C. (2010). Variational fluid flow measurements from image sequences: synopsis and perspectives. *Exp. Fluids*, *43*(3), 369–393.
- Hermansson, A. M. (1989). Rheological and microstructural evidence for transient states during gelation of κ -carrageenan in the presence of potassium. *Carbohydr. Polym.*, *10*, 163–181.
- Hermansson, A. M., Eriksson, E., & Jordansson, E. (1991). Effects of potassium, sodium and calcium on the microstructure and rheological behaviour of κ -carrageenan gels. *Carbohydr. Polym.*, *16*, 297–320.

- Heymann, E. (1935). Studies in sol-gel transformations. II. Dilatometric investigations on iron hydroxyde, gelatin, methyl cellulose, silicic acid and viscose. *Trans. Faraday Soc.*, *31*, 462–473.
- Hickson, T., & Polson, A. (1968). Some physical characteristics of the agarose molecule. *Biochemica et Biophysica Acta*, *165*, 43–58.
- Hjerten, S. (1962). A new method for the preparation of agarose for gel electrophoresis. *Biochimica et Biophysica Acta*, *62*, 445–449.
- Hoffman, A. S. (2002). Hydrogels for biomedical applications. *Advan. Drug. Deliv. Rev.*, *54*(1), 3–12.
- Hofmeister, F. (1888). Zur lehre von der Wirkung der Salze. *Arch. Exp. Pathol. Pharmacol.*, *24*, 247–260. (Translated by W. Kunz, J. Henle and B. W. Ninham (2004), About the science of the effect of salts: Franz Hofmeister's historical papers.)
- Horn, B., & Schunck, B. (1981). Determining optical flow. *Artif. Intell.*, *17*, 185–203.
- Huang, N. T., Fiedler, H. E., & Wang, J. J. (1993). Limitation and improvement of PIV. Part 1: Limitation of conventional techniques due to deformation of particle image patterns. *Exp. Fluids*, *15*, 168–174.
- Hubel, D. H., & Wiesel, T. N. (1962). Receptive fields, binocular interaction and functional architecture in the cat's visual cortex. *The Journal of Physiology*, *160*, 106–154.
- Hunt, N., & Grover, L. (2010). Cell encapsulation using biopolymer gels for regenerative medicine. *Biotechnol. Lett.*, *32*, 733–742.
- Huot, E., Barrena-Gonzalez, C., & Petitdemange, H. (1996). Tween 80 effect on bacteriocin synthesis by *Lactococcus lactis* subsp. *cremoris* J46. *Appl. Microbiol.*, *22*, 307–310.
- Hutt, W., & Persson, B. N. J. (2016). Soft matter dynamics: accelerated fluid squeeze-out during slip. *J. Chem. Phys.*, *144*, 124906.
- Iglesias, O., Garcia, A., Roques, M., & Bueno, J. (1993). Drying of water gels: determination of the characteristic curve of agar-agar. *Drying Technol.*, *11*, 571–587.
- Imeson, A. (2010). Food stabilisers, thickeners and gelling agents. In A. Imeson (Ed.), (pp. 31–49). UK: Wiley Blackwell.
- Israelachvili, J. (1992). *Intermolecular and surface forces* (2nd ed.). Academic Press.
- Iwase, E. (1938). Experimental methods in colloid chemistry. In J. Kagaku Koza (Ed.), (Vol. 7, p. 90). Kyoritsu-sha, Tokyo. (in Japanese with English summary)
- Jacobson, B. (2003). The Stribeck memorial lecture. *Tribol. Int.*, *36*, 781–789.
- Kajiya, T., Kaneko, D., & Doi, M. (2008). Dynamic visualization of 'coffee stain phenomenon' in droplets of polymer solution via fluorescent microscopy. *Langmuir*, *24*, 12369–12374.
- Kim, D. H. (1970). Economically important seaweeds, in Chile. 1. Gracilaria. *Botanica Marina*, *13*, 140–162.

- Kunz, W. (2010). Specific ions effects in colloidal and biological systems. *Curr. Opin. Colloid Interface Sci.*, *15*, 34–39.
- Labropoulos, K. C., Niesz, D. E., Danforth, S. C., & Kevrekidis, P. G. (2002). Dynamics rheology of agar gels: theory and experiments. Part 2: gelation behavior of agar sols and fitting of a theoretical rheological model. *Carbohydr. Polym.*, *50*, 407–415.
- Landau, L., & Lifshitz, E. (1970). *Theory of elasticity*. Pergamon Press.
- Larson, R. G. (1999). *The structure and rheology of complex fluids*. Oxford University Press.
- Lee, K.-Y., & Mooney, D. (2001). Hydrogels for tissue engineering. *Chem. Rev.*, *101*, 1869–1879.
- Lee, S., & Song, J. B. (2004). Mobile robot localization using optical flow sensors. *Int. J. Control. Autom.*, *2*(4), 485–493.
- Leger, L., & Creton, C. (2008). Adhesion mechanisms at soft polymer interfaces. *Phil. Trans. R. Soc. A*, *366*, 1425–1442.
- Leocmach, M., Perge, C., Divoux, T., & Manneville, S. (2014). Creep and fracture of a protein gel under stress. *Phys. Rev. Lett.*, *113*, 038303.
- Liang, J. N., Stevens, E. S., Morris, E. R., & Rees, D. A. (1979). Spectroscopic origin of conformation-sensitive contributions to polysaccharide optical activity: Vacuum-ultraviolet circular dichroism of agarose. *Biopolymers*, *18*, 327–333.
- Liu, S., Huang, S., & Li, L. (2016). Thermoreversible gelation and viscoelasticity of κ -carrageenan gels. *J. Rheol.*, *60*, 203–214.
- Lorenz, B., Rodriguez, N., Mangiagalli, P., & Persson, B. N. J. (2014). Role of interfacial fluid flow: theory and some applications. *Eur. Phys. J.*, *37*, 57–70.
- Loussert, C., Bouchaudy, A., & Salmon, J. B. (2016). Drying dynamics of a charged colloidal dispersion in a confined drop. *Physical Review Fluids*, *1*, 084201.
- Maeda, N., Chen, N., Tirrell, M., & Israelachvili, J. N. (2002). Adhesion and friction mechanisms of polymer-on-polymer surface. *Science*, *297*, 379–382.
- Manno, M., Emanuele, E., Martorana, V., Bulone, D., San Biagio, P. L., Palma-Vittorelli, M. B., & Palma, M. U. (1999). Multiple interactions between molecular and supramolecular ordering. *Phys. Rev. E*, *59*, 2222–2230.
- Mao, B., Bentaleb, A., Louerat, F., Divoux, T., & Snabre, P. (2017). Heat-induced aging of agar solutions: Impact on the structural and mechanical properties of agar gels. *Food Hydrocolloids*, *64*, 59–69.
- Mao, B., Bouchaudy, A., Salmon, J. B., Divoux, T., & Snabre, P. (2017). Normal force controlled rheology applied to viscoelastic materials under drying. In *Annual European Rheology Conference*. Copenhagen, Denmark.
- Mao, B., Divoux, T., & Snabre, P. (2016). Normal force controlled rheology applied to agar gelation. *J. Rheol.*, *60*(3), 473–489.

- Martin, A., Buguin, A., & Brochard-Wyart, F. (2001). Dewetting nucleation centers at soft interfaces. *Langmuir*, *17*, 6553–6559.
- Martin, P., & Brochard-Wyart, F. (1998). Dewetting at soft interfaces. *Phys. Rev. Lett.*, *80*(15), 3296–3299.
- Martin, P., Silberzan, P., & Brochard-Wyart, F. (1997). Sessile droplets and a solid/elastomer interface. *Langmuir*, *13*, 4910–4914.
- Martina, D., Creton, C., Dammam, P., Jeusette, M., & Lindner, A. (2012). Adhesion of soft viscoelastic adhesives on periodic rough surfaces. *Soft Matter*, *8*, 5350–5357.
- Marx, V. (2013). Cell culture: A better brew. *Nature*, *496*, 253–258.
- Matsushashi, T. (1990). Food gels. In P. Harris (Ed.), (pp. 1–51). Elsevier Science Publishers LTD. Retrieved from <http://pubs.acs.org/books/references.shtml>
- Matsuo, M., Tanaka, T., & Ma, L. (2002). Gelation mechanism of agarose and κ -carrageenan solutions estimated in terms of concentration fluctuation. *Polymer*, *43*, 5299–5309.
- McCutchen, C. W. (1962). The friction properties of animal joints. *Wear*, *5*(1), 1–17.
- McKenna, S. P., & McGillis, W. R. (2002). Performance of digital image velocimetry processing techniques. *Experiments in Fluids*, *32*, 106–115.
- Medin, A. (1995). *Studies on structure and properties of agarose* (Unpublished doctoral dissertation). Uppsala.
- Meunier, V., Nicolai, T., Durand, D., & Parker, A. (1999). Light scattering and viscoelasticity of aggregating and gelling κ -carrageenan. *Macromolecules*, *32*(8), 2610–2616.
- Mezzenga, R., Schurtenberger, P., Burbidge, A., & Michel, M. (2005). Understanding foods as soft materials. *Nat. Mater.*, *4*, 729–740.
- Mitsuiki, M., Mizuno, A., & Motoki, M. (1999). Determination of molecular weight of agar and effect of the molecular weight on the glass transition. *J. Agric. Food. Chem.*, *47*, 473–478.
- Mohammed, Z., Hember, M., Richardson, R., & Morris, E. (1998). Kinetic and equilibrium processes in the formation and melting of agarose gels. *Carbohydr. Polym.*, *36*, 15–26.
- Moldenaers, P., Mewis, J., & Berghmans, H. (1988). Rheological aspects of gelation in weak gels. In (pp. 420–421). Springer-Verlag Berlin Heidelberg. (Book name: Progress and Trends in Rheology II)
- Morris, E. R., Rees, D. A., & Robinson, G. (1980). Cation specific aggregation of carrageenan helices: Domain model of polymer gel structure. *J. Mol. Biol.*, *138*, 349–362.
- Morris, V. J., & Chilvers, G. (1983). Rheological studies of specific cation forms of κ -carrageenan gels. *Carbohydr. Polym.*, *3*, 129–141.

- Nagasaka, K., & Taneya, S. (2000). Nippon shokuhin kagaku kogaku kaishi. *The Japanese Society for Food Science and Technology*, 47, 670–678. (in Japanese with English summary and figure captions)
- Nakamura, K., Shinoda, E., & Tokita, M. (2001). The influence of compression velocity on strength and structure for gellan gels. *Food Hydrocolloids*, 15, 247–252.
- Nakauma, M., Ishihara, S., Funami, T., Yamamoto, T., & Higashimori, M. (2014). Deformation behavior of agar gel on a soft substrate during instrumental compression and its computer simulation. *Food Hydrocolloids*, 36, 301–307.
- Nakayama, T., Kawasaki, M., Niwa, E., & Hamada, I. (1978). Compression creep behavior and syneresis water of agar-agar and actomyosin gels. *J. Food Sci.*, 43, 1430–1432.
- Narayanan, J., Xiong, J., & Liu, X. (2006). Determination of agarose gel pore size: absorbance measurements vis a vis other techniques. *J Phys Conf Ser*, 28, 83–86.
- Nase, J., Ramos, O., Creton, C., & Linder, A. (2013). Debonding energy of PDMS: a new analysis of a classic adhesion scenario. *Eur. Phys. J. E*, 36, 103–123.
- Naylor, J. (1976). *Production, trade and utilization of seaweeds and seaweed products* (Vol. 159). FAO Fisheries Technical Paper, Rome.
- Newton, L. (1951). *Seaweed utilisation*. Sampson Low, London.
- Nishinari, K., & Fang, Y. (2016a). Relation between structure and rheological/thermal properties of agar. a mini-review on the effect of alkali treatment and the role of agaropectin. *Food Structure*. (In Press)
- Nishinari, K., & Fang, Y. (2016b). Sucrose release from polysaccharide gels. *Food Function*, 7, 2130–2146.
- Nishinari, K., Watase, M., Kohyama, K., Nishinari, N., Oakenfull, D., & Koide, S. (1992). The effect of sucrose on the thermo-reversible gel-sol transition in agarose and gelatin. *Polymer Journal (Tokyo, Japan)*, 24(9), 871–877.
- Nitta, T., Kato, H., Haga, H., Nemoto, K., & Kawabata, K. (2005). Static friction of agar gels: formation of contact junctions at frictional interface. *J. Phys. Soc. Jpn.*, 74(11), 2875–2879.
- Nordqvist, D., & Vilgis, T. (2011). Rheological study of the gelation process of agarose-based solutions. *Food Biophysics*, 6, 450–460.
- Normand, V., Aymard, P., Lootens, D., Amici, E., Plucknett, K., & Frith, W. (2003). Effect of sucrose on agarose gels mechanical behaviour. *Carbohydr. Polym.*, 54, 83–95.
- Normand, V., Lootens, D., Amici, E., Plucknett, K., & Aymard, P. (2000). New insight into agarose gel mechanical properties. *Biomacromolecules*, 1, 730–738.
- Normand, V., Muller, S., Ravey, J. C., & Parker, A. (2000). Gelation kinetics of gelatin: a master curve and network modeling. *Macromolecules*, 33(3), 1063–1071.
- Norziah, M., Foo, S., & Karim, A. (2006). Rheological studies on mixtures of agar (*gracilaria changii*) and κ -carrageenan. *Food Hydrocolloids*, 20, 206–217.

- Omta, A. W., Kropman, M. F., Bakker, S., & Bakker, H. J. (2003). Negligible effect of ions on the hydrogen-bond structure in liquid water. *Science*, *301*, 347–349.
- Ono, T., Sugimoto, T., Shinkai, S., & Sada, K. (2007). Lipophilic polyelectrolyte gels as super-absorbent polymers for nonpolar organic solvents. *Nat. Mater.*, *6*, 429–433.
- Oyen, M. L. (2014). Mechanical characterisation of hydrogel materials. *Int. Mater. Rev.*, *59*(1), 44–59.
- Pauchard, L., & Allain, C. (2003). Stable and unstable evolution during the drying of a polymer solution drop. *Phys. Rev. E*, *68*, 052801.
- Payens, T. A. J., & Snoeren, T. (1972). The effect of simple electrolyte on the sol-gel transition of κ -carrageenan. *J. Electroanal. Chem.*, *37*(291–296).
- Percival, E. G. V., Somerville, J. C., & Forbes, I. A. (1938). Isolation of an anhydro-sugar derivative from agar. *Nature*, *142*, 797–798.
- Pernodet, N., Maaloum, M., & Tinland, B. (1997). Pore sizes of agarose gels by atomic force microscopy. *Electrophoresis*, *18*, 55–58.
- Persson, B. N. J. (1999). Sliding friction. *Surf. Sci. Rep.*, *33*, 83–119.
- Persson, B. N. J., Albohr, O., Tartaglino, U., Volokitin, A. I., & Tosatti, E. (2005). On the nature of surface roughness with application to contact mechanics, sealing, rubber friction and adhesion. *J. Phys. Condens. Matter*, *17*, R1–R62.
- Persson, B. N. J., & Mugele, F. (2004). Squeeze-out and wear: fundamental principles and applications. *J. Phys.: Condens. Matter*, *16*, R295–R355.
- Persson, B. N. J., & Scaraggi, M. (2011). Lubricated sliding dynamics: flow factors and stribeck curve. *Eur. Phys. J. E*, *34*, 113–135.
- Piazza, L., & Benedetti, S. (2010). Investigation on the rheological properties of agar gels and their role on aroma release in agar/limonene solid emulsions. *Food Res. Int.*, *43*, 269–276.
- Piculell, L., & Nilsson, S. (1989). Anion-specific salt effects in aqueous agar agar systems. 1. Effects on the coil-helix transition and gelation of agarose. *J. Phys. Chem.*, *93*, 5596–5601.
- Piechocka, I. K., Bacabac, R. G., Potters, M., MacKintosh, F. C., & Koenderink, G. H. (2010). Structural hierarchy governs fibrin gel mechanics. *Biophys. J.*, *98*, 2281–2289.
- Pouzot, M., Nicolai, T., Benyahia, L., & Durand, D. (2006). Strain hardening and fracture of heat-set fractal globular protein gels. *J. Colloid Interface Sci.*, *293*, 376–383.
- Prasad, A. K. (2000). Particle image velocimetry. *Curr. Sci.*, *79*(1), 51–60.
- Raffel, M., Willert, C., Wereley, C., & Kompenhans, J. (2000). *Particle image velocimetry*. Springer-Verlag Berlin Heidelberg. doi: 10.1007/978-3-540-72308-0
- Rahbani, J., Behzad, A., Khashab, N., & Al-Ghoul, M. (2013). Characterization of internal structure of hydrate agar and gelatin matrices by cryo-SEM. *Electrophoresis*, *34*, 405–408.

- Ramzi, M., Rochas, C., & Guenet, J.-M. (1998). Structure-properties relation for agarose thermoreversible gels in binary solvents. *Macromolecules*, *31*, 6106–6111.
- Rasband, W. S. (1997-2016). *ImageJ* (Tech. Rep.). U. S. National Institutes of Health, Bethesda, Maryland, USA. Retrieved from <https://imagej.nih.gov/ij/>
- Richardson, R., & Goycoolea, F. (1994). Rheological measurement of κ -carrageenan during gelation. *Carbohydr. Polym.*, *24*, 223–225.
- Rinaudo, M. (2008). Main properties and current applications of some polysaccharides as biomaterials. *Polym. Int.*, *57*, 397–430.
- Rinaudo, M., Karimian, A., & Mallas, M. (1979). Polyelectrolyte behavior of carrageenans in aqueous solutions. *Biopolymers*, *18*, 1673–1683.
- Rochas, C., & Lahaye, M. (1989). Average molecular weight and molecular weight distribution of agarose and agarose-type polysaccharides. *Carbohydr. Polym.*, *10*, 289–298.
- Rochas, C., & Rinaudo, M. (1980). Activity coefficients of counterions and conformation in κ -carrageenan systems. *Biopolymers*, *19*(9), 1675–1687.
- Rossetto, H. L., de Souza, M. F., & Pandolfelli, V. C. (2008). Chaotropic substances and their effects on the mechanical strength of portland cement-based materials. *Mater. Res.*, *11*(2), 183–185.
- Rubinstein, M., & Colby, R. H. (2003). *Polymer physics (chemistry)*. Oxford University Press.
- Russ, N., Zielbauer, B., Koynov, K., & Vilgis, T. A. (2013). Influence of nongelling hydrocolloids on the gelation of agarose. *BioMacromolecules*, *14*, 4116–4124.
- Russ, N., Zielbauer, B., & Vilgis, T. (2014). Impact of sucrose and trehalose on different agarose-hydrocolloid systems. *Food Hydrocolloids*, *41*, 44–52.
- San Biagio, P. L., Bulone, D., Emanuele, A., Palma-Vittorelli, M. B., & Palma, M. U. (1996). Spontaneous symmetry-breaking pathways: time-resolved study of agarose gelation. *Food Hydrocolloids*, *10*, 91–97.
- San Biagio, P. L., Madonia, F., Sciortino, F., Palma-Vittorelli, M. B., & Palma, M. U. (1984). Cooperative interaction of polysaccharide molecules in water: A role of connectivity properties of H-bonds within the solvent? *J. Phys. Colloques*, *45*, 225–233.
- Scandiucci de Freitas, P., Wirtz, D., Stolz, M., Göpfert, B., Friederich, N.-F., & Daniels, A.-U. (2006). Pulsatile dynamic stiffness of cartilage-like materials and use of agarose gels to validate mechanical methods and models. *J. Biomed. Mater. Res. B Appl. Biomater.*, *78*, 347–357.
- Schafer, S., & Stevens, E. (1995). A reexamination of the double-helix model for agarose gels using optical rotation. *Biopolymers*, *36*, 103–108.
- Scherer, G. W. (1992a). Drying gels. *J. Non-Cryst. Solids*, *87*, 99–125.
- Scherer, G. W. (1992b). Recent progress in drying of gels. *J. Non-Cryst. Solids*, *148*, 363–374.

- Schmoller, K., Fernández, P., Arevalo, R., Blair, D., & Bausch, A. (2010). Cyclic hardening in bundled actin networks. *Nat. Commun.*, *134*, 1.
- Shchipunov, Y. A. (2002). Lecithin. *Encyclopedia of Surface and Colloid Science*, 2997–3017.
- Siberfeld, T., Rousseau, F., & Reviere, B. (2014). An updated classification of brown algae (ochrophyta, phaeophyceae). *Cryptogamie Algologie*, 117–156.
- Siesler, H. W., Ozaki, Y., Kawata, S., & Heise, H. M. (Eds.). (2002). *Near-infrared spectroscopy: Principles, instrument, applications*. Wiley-VCH, New York.
- Silberzan, P., Leger, L., Ausserre, D., & Benattar, J. (1991). Silanization of silica surfaces. a new method of constructing pure or mixed monolayer. *Langmuir*, *7*, 1647–1651.
- Silverthorne, W., & Sorensen, P. E. (1971). Marine algae as an economic resource. *Marine Technology Society Annual Meeting*, *7*, 523–533.
- Snabre, P., Blaj, O., & Pouligny, B. (2013). Shear-induced diffusion of particles in a granular paste sheared in a large gap Couette cell. In *2nd IMA conference on dense granular flows*. Cambridge, Grande Bretagne.
- Snabre, P., Blaj, O., & Pouligny, B. (2014, September). Analyse spatio-temporelle des trajectoires de particules dans une suspension en écoulement. In *Actes du congrès francophone de techniques lazer, CFTL 2014*. Marseille, France.
- Spandagos, C., Goudoulas, T., Luckham, P., & Matar, O. (2012). Surface tension-induced gel fracture. part 1. fracture of agar gels. *Langmuir*, *28*, 7197–7211.
- Stanley, N. (2006). Food polysaccharides and their applications, second edition. In Taylor & F. Group (Eds.), (pp. 217–238). A.M. Stephens and G.O. Philips and P.A. Williams.
- Stauffer, D., Coniglio, A., & Adam, M. (1982). Gelation and critical phenomena. *Adv. Polym. Sci.*, *44*, 103–158.
- Storm, C., Pastore, J., MacKintosh, F., Lubensky, T. C., & Janmey, P. (2005). Nonlinear elasticity in biological gels. *Nature*, *435*, 191–194.
- Striebeck, R. (1902). Die wesentlichen eigenschaften der gleit-und rollenlager. *Z. Ver. Dtsch. Ing.*, *46*(38), 1341–1348.
- Sun, J.-Y., Zhao, X., Illeperuma, W. R. K., Chaudhuri, O., Oh, K. H., Mooney, D. J., ... Suo, Z. (2012). Highly stretchable and tough hydrogels. *Nature*, *489*, 133–136.
- Suzuki, A., Ishii, R., Yamakami, Y., & Nakano, N. (2011). Surface friction of thermoresponsive poly(N-isopropylacrylamide) gels in water. *Colloid. Polym. Sci.*, *289*, 561–568.
- Suzuki, Y. Y., Tokita, M., & Mukai, S. (2009). Kinetics of water flow through a polymer gel. *Eur. Phys. J. E.*, *29*, 415–422.
- Tagawa, S. (1966). Separation of agar-agar by dimethylsulfoxide into agarose and agaropectin. *J. Shimonoseki Univ. Fish.*, *14*(3), 165.
- Tagawa, S., & Kojima, Y. (1966). On agar-agar and agaropectin in agar prepared from *Garcilaria* harvested in different places. *J. Shimonoseki Univ. Fish.*, *15*, 11.

- Tako, M., & Nakamura, S. (1988). Gelation mechanism of agarose. *Carbohydrate Research*, 180(2), 277–284.
- Tanaka, T., & Fillmore, D. J. (1979). Kinetics of swelling of gels. *J. Chem. Phys.*, 70(3), 1214–1218.
- Tari, O., & Pekcan, O. (2008). Study and drying of κ -carrageenan gel at various temperatures using a fluorescence technique. *Drying Technol.*, 26, 101–107.
- te Nijenhuis, K. (1997). Thermoreversible networks: viscoelastic properties and structure of gels. In (pp. 1–12). Springer-Verlag, Berlin Heidelberg.
- Tokita, M. (2016). Transport phenomena in gel. *Gels*, 2(2), 17–32.
- Tominaga, T., Takedomi, N., Biederman, H., Furukawa, H., Osada, Y., & Gong, J. P. (2008). Effect of substrate adhesion and hydrophobic ion hydrogel friction. *Soft Matter*, 4, 1033–1040.
- Urahama, Y. (1989). Effect of peel load on stringiness phenomena and peel speed of pressure-sensitive adhesive tape. *The Journal of Adhesion*, 31, 47–58.
- Van Vlierberghe, S., Dubruel, P., & Schacht, E. (2011). Biopolymer-based hydrogels as scaffolds for tissue engineering applications: A review. *BioMacromolecules*, 12, 1387–1408.
- Vella, D., Bico, J., Boudaoud, A., Roman, B., & Reis, P. M. (2009). The macroscopic delamination of thin films from elastic substrates. *Proc. Natl. Acad. Sci.*, 106(27), 10901–10906.
- Viasnoff, V., & Lequeux, F. (2002). Rejuvenation and overaging in a colloidal glass under shear. *Phys. Rev. Lett.*, 89, 065701.
- Watase, M., Kohyama, K., & Nishinari, K. (1992). Effects of sugars and polyols on the gel-sol transition of agarose by differential scanning calorimetry. *Thermochimica Acta*, 206, 163–173.
- Watase, M., & Nishinari, K. (1983). Rheological properties of agarose gels with different molecular weights. *Rheol Acta*, 22, 580–587.
- Watase, M., Nishinari, K., Williams, P. A., & Phillips, G. O. (1990). Agarose gels: Effect of sucrose, glucose, urea, and guanidine hydrochloride on the rheological and thermal properties. *J. Agric. Food. Chem.*, 38, 1181–1187.
- Watson, S., Nie, M., Wang, L., & Stokes, K. (2015). Challenges and development of self-assembled monolayer polymer brushes as a green lubrication solution for tribological applications. *RSC Adv.*, 5, 89698–89730.
- Whistler, R. L., & BeMiller, J. N. (1993). *Industrial gums: Polysaccharides and their derivatives*. San Diego: Academic Press.
- Whyte, J., Englar, J., & Hosford, S. (1984). Factors affecting texture profile evaluation of agar gels. *Botanica Marina*, 27, 63–69.
- Woessner, D., Snowden, B. J., & Chiu, Y. C. (1970). Pulsed NMR study of the temperature hysteresis in the agar-water system. *J. Colloid Interface Sci.*, 34(2), 283–289.

- Wu, C., & Yan, C.-Y. (1994). Studies of the swelling and drying kinetics of the thin gelatin gel films by in situ interferometry. *Macromolecules*, *27*, 4516–4520.
- Xie, W. J., & Gao, Y. Q. (2013). A simple theory for the Hofmeister series. *J. Phys. Chem. Lett.*, *4*, 4247–4252.
- Xiong, J.-Y., Narayanan, J., Liu, X.-Y., Chong, T., Chen, S., & Chung, T.-S. (2005). Topology evolution and gelation mechanism of agarose gel. *J. Phys. Chem. B*, *109*, 5638–5643.
- Yamamoto, T., Kurokawa, T., Ahmed, J., Kamita, G., Yashima, S., Furukawa, Y., ... Gong, J. P. (2014). In situ observation of a hydrogel–glass interface during sliding friction. *Soft Matter*, *10*, 5989–5596.
- Yashima, S., Takase, N., Kurokawa, T., & Gong, J. P. (2014). Friction of hydrogels with controlled surface roughness on solid flat substrates. *Soft Matter*, *10*, 3192–3199.
- Young, T. (1805). An essay on the cohesion of fluids. *Phil. Trans. R. Soc. Lond.*, *95*, 65–85.
- Yuan, Y., & Lee, T. R. (2013). Surface science techniques. In G. Bracco & B. Holst (Eds.), (pp. 3–34). Springer.
- Zhang, H., Yoshimura, M., Nishinari, K., Williams, M., Foster, T., & Norton, I. (2001). Gelation behaviour of konjac glucomannan with different molecular weights. *Biopolymers*, *59*, 38–50.
- Zhang, J., Daubert, C., & Foegeding, E. (2007). A proposed strain-hardening mechanism for alginate gels. *J. Food Eng.*, *80*, 157–165.
- Zhang, Y., & Cremer, P. S. (2006). Interactions between macromolecules and ions: the Hofmeister series. *Curr. Opin. Chem. Biol.*, *10*, 658–663.
- Zhao, X. (2014). Multi-scale multi-mechanism design of tough hydrogels: building dissipation into stretchy networks. *Soft Matter*, *10*, 672–687.
- Zhou, S., & Wu, C. (1996). In-situ interferometry studies of the drying and swelling kinetics of an ultrathin poly(N-isopropylacrylamide) gel film below and above its volume phase transition temperature. *Macromolecules*, *29*(14), 4998–5001.
- Zieverink, M., de Rijke, E., de Kruijf, K., & de Kok, P. (2009). Diffusivity and solubility of water in palm oil. In *7th euro fed lipid congress, poster (phys-004)*. Graz, Austria.
- Zrinyi, M., Rosta, J., & Horskay, F. (1993). Studies on the swelling and shrinking kinetics of chemically cross-linked disk-shaped poly(vinyl acetate) gels. *Macromolecules*, *26*, 3097–3102.

**Dynamique de gels à base d'agar en contact avec des surfaces solides:
Gélification, Adhésion, Séchage et Formulation**

Mon projet de thèse a été réalisé en partenariat avec l'entreprise BioMérieux, qui produit des milieux de culture à base de gel d'agar coulés dans des boîtes de Pétri à destination du secteur biomédical. Ces gels, remplis d'eau à 95%, sont susceptibles d'en relâcher par évaporation ou sous l'effet d'une perturbation externe. Le gel se contracte et peut se détacher des parois de la boîte lors de la production ou lors de leur incubation. Ma thèse a consisté à identifier les paramètres clefs qui influent sur la contraction de ces milieux de culture aussi bien au niveau de la composition du gel que des propriétés de surface des parois de la boîte de Pétri. Ce travail expérimental m'a permis d'associer un panel de techniques originales comme la rhéologie à force normale contrôlée, une centrifugeuse, l'interférométrie ou encore la méthode flot optique. J'ai ainsi mis à jour les moteurs du détachement du gel des parois des boîtes et identifier des solutions concrètes pour y remédier.

Mots clés: agar; gel; gélification; contraction; rhéologie; adhésion; détachement; séchage; formulation

**Dynamics of agar-based gels in contact with solid surfaces:
Gelation, Adhesion, Drying and Formulation**

My PhD work was carried out in partnership with the company BioMérieux, a leader in the production of agar-based culture media, cast in Petri dishes and used in microbiology. Being mainly composed of water (>95% wt.), agar gels are naturally prone to solvent-loss by evaporation, either at rest or under an external perturbation. As a result, the gel shrinks and detaches from the sidewall of the dish. The goal of my PhD work was to identify the key parameters driving the gel detachment, in relation with both the gel chemical composition, as well as the dish surface properties. This experimental work has allowed me to use a wide array of techniques such as normal force controlled rheology, interferometric observations, or optical flow analysis applied to the gel deformation. I successfully unravelled the driving forces that lead to the gel detachment from the sidewall of the dish and proposed concrete solutions to be implemented on a commercial scale to prevent it.

Key words: agar; gel; gelation; contraction; rheology; adhesion; debonding; drying; formulation